TU WIEN

DISSERTATION

Neutral Higgs Boson and Z Boson Decays into Pairs of Tau Leptons with the CMS Detector

AUSGEFÜHRT ZUM ZWECKE DER ERLANGUNG DES AKADEMISCHEN GRADES EINES DOKTORS DER TECHNISCHEN WISSENSCHAFTEN UNTER DER LEITUNG VON

Univ.Prof. Dipl.-Phys. Dr.rer.nat. Jochen Schieck

und

Dr. Martin Flechl

als verantwortlich mitwirkender Assistent

am Institut für Hochenergiephysik

der Österreichischen Akademie der Wissenschaften und am Atominstitut der Österreichischen Universitäten (E141)

EINGEREICHT AN DER TECHNISCHEN UNIVERSITÄT WIEN FAKULTÄT FÜR PHYSIK

VON

Dipl.-Ing. Johannes Brandstetter, BSc.

Matrikelnummer 0925541

Bubing 113, 4782 St. Florian

j.brandstetter89@gmail.com

Wien, am 20.März 2018

There is no way around the hard work. Embrace it.

Roger Federer

Abstract

In this thesis, analyses of Z boson and neutral Higgs boson decays into pairs of tau leptons at the Compact Muon Solenoid (CMS) experiment at the CERN Large Hadron Collider (LHC) are studied.

A measurement of the $Z/\gamma^* \to \tau\tau$ cross section in proton-proton collisions at a center-of-mass energy of 13 TeV is presented, using 2015 proton-proton collision data corresponding to an integrated luminosity of 2.3 fb^{-1}. The $Z/\gamma^* \to \tau\tau$ decay is an important standard model process constituting the dominant irreducible background in Higgs boson searches in the di-tau final state. The product of the cross section and branching fraction is measured to be $\sigma(pp \to Z/\gamma^* + X) \times \mathcal{B}(Z/\gamma^* \to \tau\tau) = 1848 \pm 12(\text{stat.}) \pm 67(\text{syst.+lumi.})$ pb, in agreement with the standard model expectation. In addition, the reconstruction and identification efficiency and the energy scale of tau lepton decays to hadron+ν_τ final states are obtained.

A search for additional neutral Higgs bosons decaying to pairs of tau leptons is presented, using 2016 proton-proton collision data recorded at a center-of-mass energy of 13 TeV, corresponding to an integrated luminosity of 35.9 fb^{-1}. The search is performed in the context of the minimal supersymmetric extension of the standard model (MSSM). No significant deviations above the expected standard model background are observed and model-independent upper limits are set on the product of the cross section and the branching fraction. Furthermore, exclusion contours in the m_A-$\tan\beta$ plane for selected MSSM benchmark scenarios are provided.

Finally, upgrade plans that are foreseen to prepare the CMS detector for the high luminosity LHC era are discussed, where special emphasis is put on the identification performance of tau lepton decays to hadron+ν_τ final states.

Kurzfassung

In dieser Arbeit werden Z-Boson- und neutrale Higgs-Boson-Zerfälle zu zwei Tauonen mit Daten analysiert, die vom Compact Muon Solenoid- (CMS-) Experiment am Large Hadron Collider (LHC) aufgezeichnet wurden.

Ein zentrales Element dieser Arbeit ist die Wirkungsquerschnittsmessung des $Z/\gamma^* \to \tau\tau$-Zerfalls. Die dabei analysierten Kollisionsdaten wurden 2015 in Proton-Proton-Kollisionen mit einer Schwerpunktsenergie von 13 TeV aufgezeichnet und entsprechen einer integrierten Luminosität von 2.3 fb^{-1}. Der $Z/\gamma^* \to \tau\tau$-Zerfall ist ein wichtiger, vom Standardmodell der Teilchenphysik vorausgesagter, Prozess. Zum einen dient dieser Zerfall als Standardkanal, um physikalische Eigenschaften der Tauonen zu untersuchen, zum anderen stellt $Z/\gamma^* \to \tau\tau$ den wichtigsten Hintergrundprozess in Analysen dar, die nach Zerfällen von Higgs-Bosonen zu zwei Tauonen suchen. Die Messung liefert ein Ergebnis für das Produkt aus Produktionswirkungsquerschnitt und Zerfallsrate, $\sigma(\text{pp} \to Z/\gamma^* + X) \times \mathcal{B}(Z/\gamma^* \to \tau\tau) = 1848 \pm 12(\text{stat.}) \pm 67(\text{syst.+lumi.})$ pb, und ist in Übereinstimmung mit der theoretischen Vorhersage des Standardmodells. Außerdem bietet diese Messung die Möglichkeit, Rekonstruktionseffizienz und Energieskala von Tauonen des CMS-Detektors zu bestimmen.

Ein weiteres zentrales Element dieser Arbeit ist die Suche nach zusätzlichen neutralen Higgs-Bosonen, die wiederum zu zwei Tauonen zerfallen. Dabei wurden Proton-Proton-Kollisionen analysiert, die 2016 mit einer Schwerpunktsenergie von 13 TeV aufgezeichnet wurden und einer integrierten Luminosität von 35.9 fb^{-1} entsprechen. Die Analyse wurde im Rahmen der minimalen supersymmetrischen Erweiterung des Standardmodels (MSSM) durchgeführt. Das Ergebnis zeigt keine signifikanten Abweichungen von den Vorhersagen des Standardmodells. Als Resultat werden Ausschlussgrenzen auf das Produkt aus Produktionswirkungsquerschnitt und Zerfallsrate gesetzt und Möglichkeiten für die Interpretation der Ergebnisse im Kontext von Theorien jenseits des SM diskutiert.

Zusätzlich werden in dieser Arbeit Weiterentwicklungspläne des CMS Detektors diskutiert, wobei speziell auf die Identifizierung von Tauonen eingegangen wird.

Contents

Introduction

The *Large Hadron Collider* (LHC) at CERN is currently the largest and most powerful particle accelerator, and in combination with sophisticated particle detectors offers unprecedented opportunities to deepen our knowledge of particle physics.

The Higgs boson, discovered in 2012 [1, 2], was the last missing piece of the *Standard Model of Particle Physics* (SM). However, several questions related to this discovery remain concerning, e.g. the exact properties of the discovered Higgs boson or the possibility of additional heavier or lighter Higgs bosons. To address these questions, one of the main tasks at the LHC is thus the further exploration of the Higgs sector where the decay of the Higgs boson into pairs of tau leptons serves as one of the most appealing fermionic final states.

Searches for Higgs bosons decaying into pairs of tau leptons have to deal with various different backgrounds. Many of these backgrounds do not share exactly the same final state as the signal, but rather a similar final state which is misidentified as signal final state. In particular, several backgrounds arise from events in which a quark or gluon jet is misidentified as tau lepton decay. These jets are notoriously difficult to model via simulation. Additionally, due to relatively small misidentification rates, large simulation samples are needed to avoid prohibitively large statistical uncertainties in the modeling. For these reasons, the fake factor method is introduced which relies almost entirely on collision data such that simulation-related uncertainties become negligible and the statistical power of the model scales directly with the collected luminosity without requiring simulation samples to match the latter.

The main part of this thesis is based on the physics results presented in Chaps. 7 and 8. The searches analyze 2015 (2016) proton-proton collision data collected at a center-of-mass energy of 13 TeV. In Chap. 7, a measurement of the inclusive $Z/\gamma^* \to \tau\tau$ cross section is described in detail. As a byproduct, the reconstruction efficiency and the energy scale of tau lepton decays to hadron$+\nu_\tau$ final states are obtained. In Chap. 8, a search for additional neutral Higgs bosons decaying into pairs of tau leptons is summarized. The analysis is carried out in the context of the *Minimal Supersymmetric Extension of the Standard Model* (MSSM).

In this thesis, special emphasis is put on the description and the implementation of the newly developed fake factor method.

The results presented in this thesis are published in:

- CMS Collaboration, Technical Proposal for the Phase-II Upgrade of the CMS Detector, Geneva, CERN-LHC-2015-010, LHCC-P-008, CMS-TDR-15-02, https://cds.cern.ch/record/2020886

- CMS Collaboration, Measurement of the $Z\gamma^* \to \tau\tau$ cross section in pp collisions at $\sqrt{s} = 13$ TeV and validation of τ lepton analysis techniques, 2018, CMS-HIG-15-007, CERN-EP-2017-307, arXiv:1801.03535, Submitted to EPJC

- CMS Collaboration, Search for additional neutral MSSM Higgs bosons in the $\tau\tau$ final state in proton-proton collisions at $\sqrt{s} = 13$ TeV, 2018, CMS-HIG-17-020, arXiv:1803.06553, Submitted to JHEP

Theoretical Overview

The purpose of this chapter is to give an overview of the SM of particle physics. Particular emphasis is put on the concept of spontaneous symmetry breaking as well as summarizing Higgs boson, Z boson and tau lepton properties, which are important theoretical prerequisites for the analyses covered in this thesis.

Supersymmetry (SUSY) is introduced as possible extension of the SM, where the main focus is given to the *Minimal Supersymmetric Extension of the Standard Model* (MSSM) and its incorporation of the Higgs sector.

2.1 The Standard Model

The SM [3–5] was developed in the second half of the last century, with the main formulation being drafted in the 1970s [6] and strengthened by every new particle that was discovered ever since. It encompasses most of the present knowledge of particle physics classifying all particles, which are observed so far, and describing three of the four fundamental interactions, namely the electromagnetic force, the weak force and the strong force. The remaining fourth interaction, gravity, can be described by general relativity, albeit it cannot be incorporated in the current SM. Nevertheless, gravity not being included in the SM does not imply restrictions for describing high-energy processes, since gravitational forces can easily be neglected for subatomic particles and processes at LHC energies.

The SM is a renormalizable quantum field theory, in which spin-1 gauge fields (bosons) mediate the forces and spin-$\frac{1}{2}$ fields (fermions) represent the matter particles. Fundamental principles of the SM are the concept of local gauge invariance and the equivalence between conserved symmetries of the Lagrangian density and conserved currents in particle interactions. The fundamental dynamics of the fields and their interactions

are described by the Lagrangian density

$$\mathcal{L}_{\mathrm{SM}} = \mathcal{L}_{\mathrm{gauge}} + \mathcal{L}_{\mathrm{fermion}} + \mathcal{L}_{\mathrm{Higgs}} + \mathcal{L}_{\mathrm{Yukawa}}. \qquad (2.1)$$

Here, $\mathcal{L}_{\mathrm{gauge}}$ denotes the gauge part of the Lagrangian density, which is built by kinetic terms of the different bosonic gauge fields. $\mathcal{L}_{\mathrm{fermion}}$ comprises the dynamic fermionic terms that include interactions of fermions and gauge bosons. $\mathcal{L}_{\mathrm{Higgs}}$ denotes the dynamic Higgs term, the Higgs potential, mass terms of the gauge bosons and interactions of gauge bosons with the Higgs field. Finally, $\mathcal{L}_{\mathrm{Yukawa}}$ accounts for the fermionic mass terms and interactions of fermions with the Higgs field.

2.1.1 Particles and Interactions

Figure 2.1 illustrates the particle content of the SM. It comprises twelve fundamental spin-$\frac{1}{2}$ fermions and their respective antiparticles, which have the same mass but opposite additive quantum numbers, including electric charge. Fermions can be further categorized into leptons and quarks, both occurring in three generations. Every lepton generation contains one negatively charged lepton, the electron (e), the muon (μ) and the tau lepton (τ), each paired with a corresponding electrically neutral neutrino (ν_{e}, ν_{μ}, ν_{τ}). The three quark generations are the up (u), the charm (c) and the top (t) quark generation, where each quark carries a charge of $+\frac{2}{3}e$ and is paired with the down (d), the strange (s) and the bottom (b) quark, respectively, which have an intrinsic electric charge of $-\frac{1}{3}e$.

The SM is based on a local SU(3)×SU(2)×U(1)[1] gauge symmetry, which implies the presence of spin-1 gauge bosons as carrier particles of the fundamental forces. The SU(3) symmetry reflects the *strong interaction* between the quarks and 8 massless gluon fields, all of which carry color charge. Since leptons do not carry color charge, they do not undergo strong interactions. The corresponding quantum field theory for the strong interaction is *Quantum Chromodynamics* (QCD) [8].
The SU(2)×U(1) gauge symmetry governs the unification of the weak and the electromagnetic force into the *electroweak force*, mediated by the W$^{\pm}$ and Z bosons and the photon, respectively. The electroweak theory predicts the presence of neutral weak cur-

---

[1]In mathematics, SU(n) denotes the *special unitary group* of degree n. It consists of all unitary matrices with determinant 1 and defines a Lie group [7]. The special unitary group is a subgroup of the *unitary group* U(n) that comprises all n × n unitary matrices.
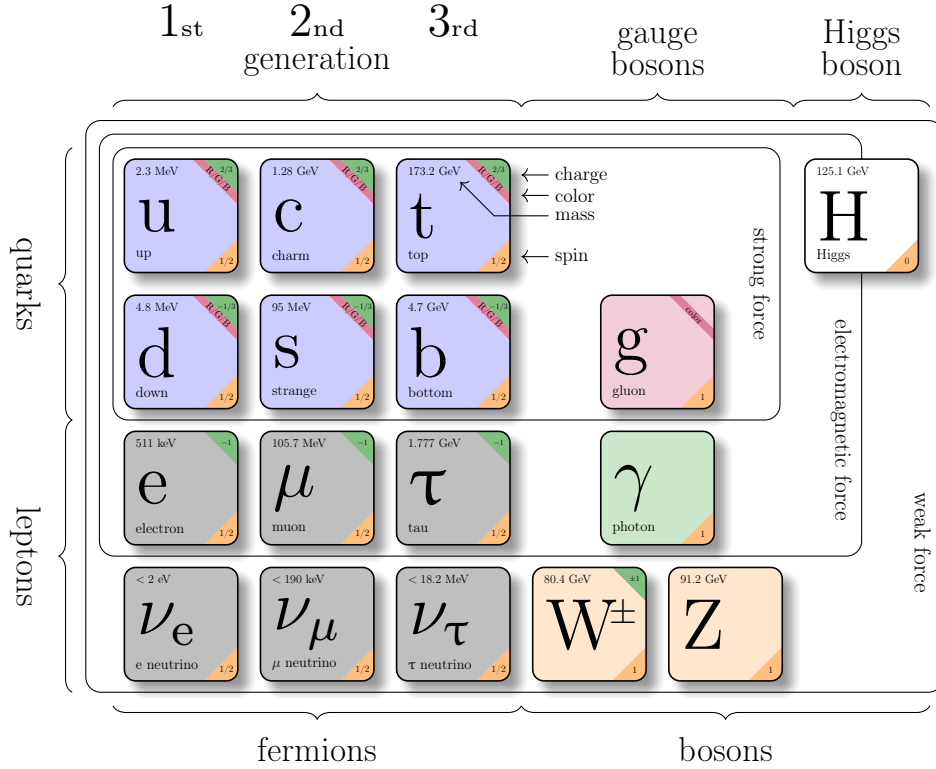
Figure 2.1: Particle and force content of the SM.

rents, which were discovered at the Gargamelle bubble chamber experiment at CERN in 1973 [9]. This was followed by the discovery of the $W^\pm$ and Z bosons at the UA1 and UA2 experiments at CERN [10–13] in 1983. Motivated by observed parity violation in the weak interaction [14], and the absence of right-handed neutrinos [15], the *chirality* operator $\gamma^5 = i\gamma^0\gamma^1\gamma^2\gamma^3$ is introduced, where γ^i $(i = 0, 1, 2, 3)$ are the Dirac matrices [4]. It allows extracting the left- and right-handed components $\Psi_L = \frac{1}{2}(1 - \gamma^5)\Psi$ and $\Psi_R = \frac{1}{2}(1 + \gamma^5)\Psi$ of a fermion field Ψ. As a consequence fermions are devided into *left-handed* and *right-handed* particles, in which left-handed leptons and quarks are grouped into doublets, whereas right-handed fermions form singlets (Tab. 2.1). Right-handed neutrinos are not included in the SM.

Invariance under SU(2)×U(1) transformations introduces four spinor fields $W_{1\mu}$, $W_{2\mu}$, $W_{3\mu}$ and B_μ, where the physical charged $W^\pm_\mu$ bosons, the neutral Z_μ boson and the photon A_μ are found to be a mixture of the gauge fields:

$$W^\pm_\mu = \frac{1}{\sqrt{2}}\left(W^1_\mu \mp iW^2_\mu\right), \tag{2.2}$$

	Generation 1	Generation 2	Generation 3
Leptons	$\begin{pmatrix} \nu_e^L \\ e^L \end{pmatrix}, e^R$	$\begin{pmatrix} \nu_\mu^L \\ \mu^L \end{pmatrix}, \mu^R$	$\begin{pmatrix} \nu_\tau^L \\ \tau^L \end{pmatrix}, \tau^R$
Quarks	$\begin{pmatrix} u^L \\ d'^L \end{pmatrix}, u^R, d^R$	$\begin{pmatrix} c^L \\ s'^L \end{pmatrix}, c^R, s^R$	$\begin{pmatrix} t^L \\ b'^L \end{pmatrix}, t^R, b^R$

Table 2.1: Grouping of leptons and quarks into left-handed and right-handed fermions. d'^L, s'^L and b'^L are superpositions of the mass eigenstates d^L, s^L and b^L [3].

$$Z_\mu = W_\mu^3 \cos\theta_W - B_\mu \sin\theta_W, \tag{2.3}$$

$$A_\mu = W_\mu^3 \sin\theta_W - B_\mu \cos\theta_W. \tag{2.4}$$

Here, θ_W is the so called *Weinberg angle* [6].

2.1.2 Electroweak Symmetry Breaking

The electroweak model, as introduced in Sec. 2.1.1, has some serious shortcomings. Firstly, a Lagrangian density that is invariant under $SU(2) \times U(1)$ gauge transformations forbids massive gauge bosons. Secondly, fermion mass terms of the form

$$-m\bar{\Psi}\Psi = -m(\bar{\Psi}_R \Psi_L + \Psi_L \bar{\Psi}_R), \tag{2.5}$$

where $\bar{\Psi}$ denotes the adjoint of the field Ψ, are composed of left and right handed components that transform differently under $SU(2)$ and $U(1)$ groups, and thus also break gauge invariance. However, the measured masses of the gauge bosons amount to $m_{W^\pm} = 80.385 \pm 0.015$ GeV and $m_Z = 91.1876 \pm 0.0021$ GeV [16], respectively, and the fermion mass spectrum spans over at least six orders of magnitude, whereas only the photon is massless. As a consequence, the electroweak symmetry must be broken.

In the SM, gauge bosons acquire masses by the mechanism of *spontaneous symmetry breaking*, in the following referred to as *Higgs mechanism*, which dynamically breaks the symmetry at low energies and restores it at high energies. It was first introduced by Higgs [17], Englert and Brout [18] and Guralnik, Hagen and Kibble [19] in 1964. In the Higgs mechanism, an additional field is added, which is symmetric under gauge transformations, but acquires a non-zero expectation value in the vacuum state and thus breaks the symmetry. Furthermore, the Goldstone theorem [20] predicts that for each broken generator, i.e. a generator that does not preserve the global symmetry of a system, a new massless scalar particle emerges. For a broken local gauge symmetry,

these additional degrees of freedom can provide the longitudinal polarizations of the massive gauge bosons. A casual phrasing is that the additional degrees of freedom are "eaten" up by the gauge fields which become massive.

In order to break electroweak symmetry, the simplest field to be introduced is a complex SU(2) doublet (*Higgs doublet*)

$$\Phi = \begin{pmatrix} \Phi^+ \\ \Phi^0 \end{pmatrix}, \tag{2.6}$$

where Φ^+ is a charged and Φ^0 a neutral complex scalar field. Taking requirements on the renormalizability and the gauge invariance into account, the Higgs potential has the form

$$V(\Phi^\dagger \Phi) = \lambda(\Phi^\dagger \Phi)^2 - \mu^2(\Phi^\dagger \Phi), \tag{2.7}$$

where two additional parameters, λ and μ, enter the theory. Both are real, $\lambda > 0$ is required for the vacuum to be stable and $\mu^2 > 0$ is chosen in order to induce spontaneous symmetry breaking. A sketch of the Higgs potential is shown in Fig. 2.2.
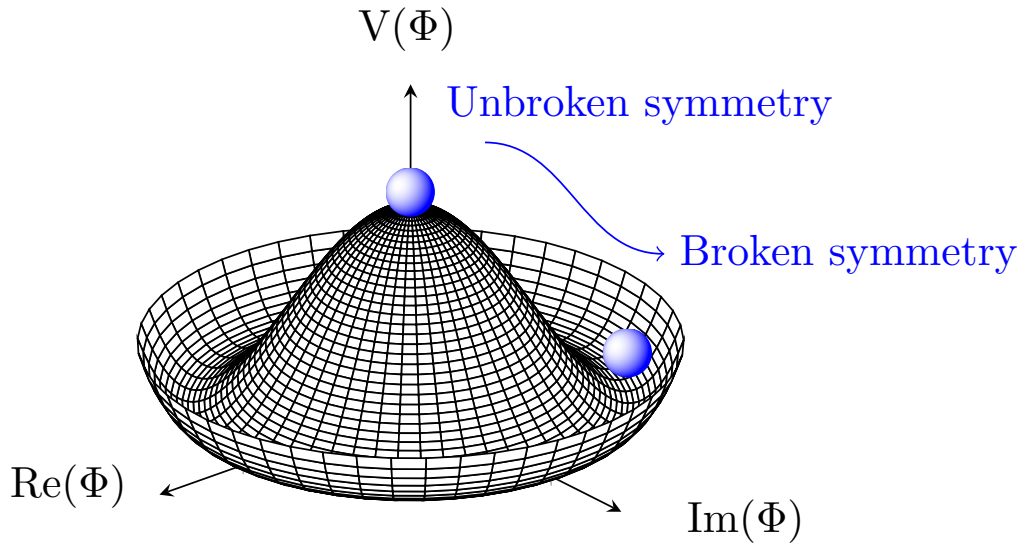
Figure 2.2: Higgs potential. The vacuum expectation value is non-zero. If a ground state is chosen, the symmetry is spontaneously broken.

The potential term in Eq (2.7) has degenerate minima defined by:

$$|\Phi_0|^{\mathrm{min}} = v = \sqrt{\frac{\mu^2}{\lambda}}. \tag{2.8}$$

Without loss of generality the ground state

$$\langle 0 | \Phi | 0 \rangle = \frac{1}{\sqrt{2}} \begin{pmatrix} 0 \\ v \end{pmatrix} \tag{2.9}$$

can be chosen and subsequently Φ can be expanded around the ground state:

$$\Phi = \exp\left(\frac{\mathrm{i}\xi_i \sigma^i}{2v}\right) \frac{1}{\sqrt{2}} \begin{pmatrix} 0 \\ v + \mathrm{H} \end{pmatrix}, \tag{2.10}$$

where σ^i represents the three Pauli matrices, and ξ^i and H are real scalar fields. The Goldstone bosons described by ξ^i are massless, whereas the scalar Higgs boson field H has acquired a mass, namely $m_{\mathrm{H}} = \sqrt{2\mu^2}$. An appropriate gauge transformation allows the Goldstone fields to mix with the gauge boson fields and become the longitudinal components of the $\mathrm{W}^\pm$ and Z fields. At this point it is instructive to count the degrees of freedom before and after electroweak symmetry breaking. Before electroweak symmetry breaking, the total number amounts to 12: the complex Higgs doublet with four, the massless photon field with two and three massless gauge fields with another two degrees of freedom each. After electroweak symmetry breaking, a scalar field H with one degree of freedom has emerged. Additionally, the three massive gauge fields have gained one degree of freedom each. Together with the massless photon, the number of degrees of freedom after electroweak symmetry breaking has not changed and adds up to 12. The Higgs doublet Φ is left containing only one single scalar field H:

$$\Phi = \exp \frac{1}{\sqrt{2}} \begin{pmatrix} 0 \\ v + \mathrm{H} \end{pmatrix}. \tag{2.11}$$

The $\mathrm{W}^\pm$ bosons and Z boson have acquired a mass of $\frac{1}{2}gv$ and $\frac{1}{2}v\sqrt{g^2 + g'^2}$, respectively, while no mass term is assigned to the photon field A_μ. Here, g and g' are the coupling constants of the electroweak interaction. Additionally, the scalar Higgs boson field H has also acquired a mass, namely $m_{\mathrm{H}} = \sqrt{2\mu^2}$.

While gauge boson masses have been introduced by the process of electroweak sym-

metry breaking the masses of leptons and quarks can be generated by *Yukawa couplings*. Yukawa mass terms for a fermion f have the form

$$\mathcal{L}_f = -g_f \left(\Psi^L \Phi \Psi^R + \Psi^R \Phi \Psi^L \right),$$ (2.12)

where Ψ^L is the left-handed component of a spin doublet, Ψ^R the right-handed component of a spin singlet and Φ denotes the complex Higgs doublet. The Yukawa Lagrangian density is gauge invariant, since terms of the form $\Psi^L \Phi \Psi^R$ and $\Psi^R \Phi \Psi^L$ are SU(2) singlets. By Eq. (2.12) a coupling constant g_f is introduced as additional parameter for each fermion generation. The coupling constants of the fermions occur to be proportional to their mass terms

$$m_f = \frac{v}{\sqrt{2}} g_f.$$ (2.13)

Concerning fermions, this means that the Higgs boson predominantly couples to the top quark and to a lesser extent to the bottom quark and to the tau lepton.

A complete derivation of the Higgs mechanism can be found in Ref. [21].

2.2 The Standard Model Higgs Boson

Direct searches for an SM Higgs boson have been performed prior to the LHC era for example at the *Large Electron-Positron* (LEP) Collider at CERN and at the *Tevatron* at Fermilab. The combination of results from the four LEP experiments (ALEPH, DELPHI, L3, OPAL) excluded a SM Higgs boson with a mass of $m_H < 114.4$ GeV at 95% confidence level (CL) [22]. Combined searches at the Tevatron accelerator by the CDF and D0 Collaborations excluded a SM Higgs boson in the mass range 100 GeV $< m_H < 103$ GeV and in the mass range 147 GeV $< m_H < 180$ GeV at 95% CL [23].

It took nearly 50 years from the first proposal of a model with a scalar Higgs boson in 1964 [17] to its discovery at the Large Hadron Collider (LHC), which was announced on July, 4th, 2012 by the ATLAS and CMS collaborations [1,2]. The discovery was based on data corresponding to an integrated luminosity of approximately 5 fb^{-1} collected in 2011 at a center-of-mass energy of 7 TeV and approximately 5-6 fb^{-1} collected at the beginning of 2012 at a center-of-mass energy of 8 TeV. It was driven by the measurements of decays of the Higgs boson into pairs of photons and into pairs of Z bosons, which further decay into four leptons. Both experiments individually reported an ex-

cess with combined significances of more than 5 standard deviations with respect to the background-only hypothesis. Figure 2.3a displays the diphoton invariant mass distribution from the CMS results and Fig. 2.3b displays the invariant mass distribution in the H → ZZ search from the ATLAS results.

At the beginning the newly discovered particle was cautiously referred to as "new scalar boson". However, the couplings consistent with SM expectations, seem to confirm the scaling with mass [24–27], and therefore in 2013, the existence of a Higgs boson was officially announced.

(a)

(b)
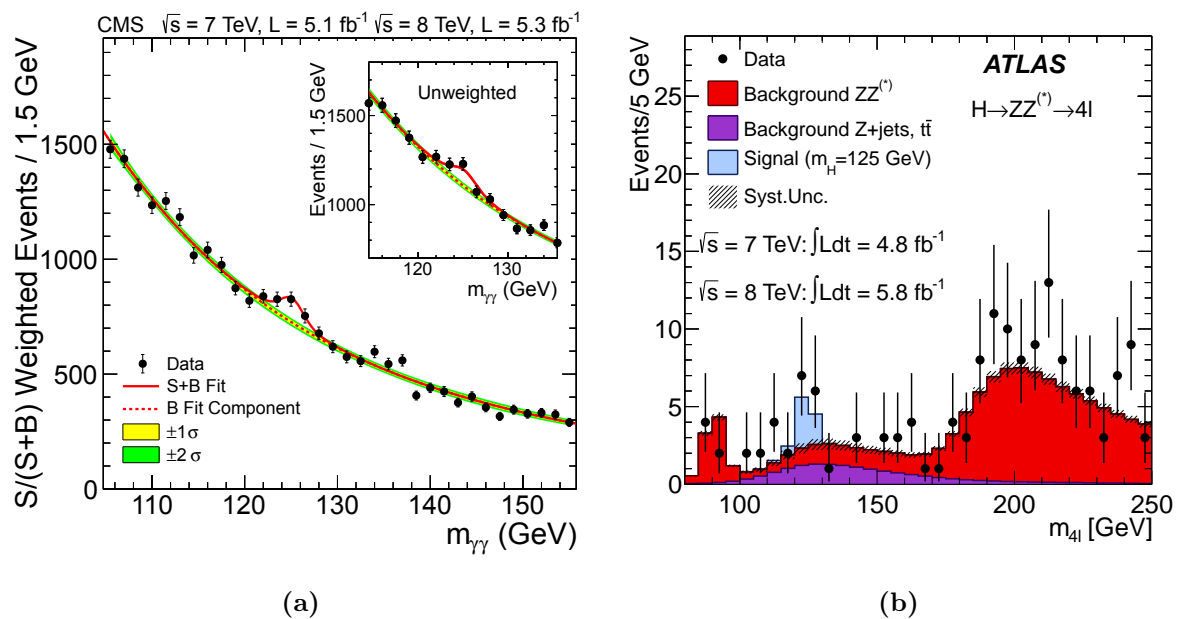
Figure 2.3: Diphoton invariant mass distribution from the CMS H → γγ search [2] (a), and invariant mass distribution from the ATLAS H → ZZ search [1] (b).

2.2.1 Higgs Boson Production Modes

The SM predicts the Higgs boson to be produced in various ways. Leading-order (LO) Feynman diagrams of the four main production modes at the LHC are shown in Fig. 2.4, and the cross sections of the production modes as a function of the center-of-mass energy are displayed in Fig. 2.5. The Higgs boson is predominantly produced via *gluon fusion* (ggF). At lowest order, ggF proceeds through a top quark loop between the gluons and the Higgs boson, since there is no direct coupling between the Higgs boson and the massless gluons, see Fig. 2.4a. In principle, all quarks should be considered in this loop, but in practice only the top and bottom quark loops are relevant in the SM due to the mass dependencies of the Higgs-fermion couplings. *Vector boson fusion*

(VBF) has the second largest production rate that is about a factor 10 smaller than the ggF production rate. However, due to its distinctive signature of a Higgs boson enclosed by two quarks, which hadronize to form jets, see Fig. 2.4b, VBF production plays an important role in Higgs boson physics at the LHC. Production in association with a W or Z boson, which is also called *Higgsstrahlung* (Fig. 2.4c), and production in association with a top quark pair (Fig. 2.4d) can produce multi-lepton and multi-jet final states.
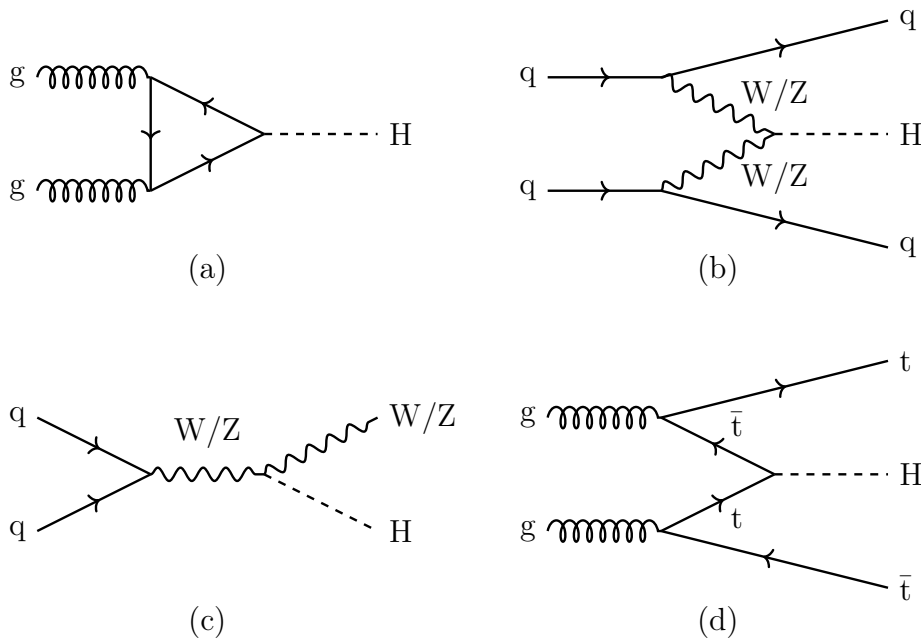
Figure 2.4: Example of LO Feynman diagrams of the four most common SM Higgs boson production modes at the LHC: gluon fusion (a), vector boson fusion (b), W/Z-associated production (c), $t\bar{t}$-associated production (d).

2.2.2 Higgs Boson Decay Modes

Since the Higgs boson interacts with all massive elementary particles many processes exist through which it can decay. The SM branching ratios are summarized in Fig. 2.6. For the decay into fermions (fermion-antifermion pair) the general rule is that the Higgs boson is more likely to decay into heavier fermions due to the fact that the interaction with the Higgs boson is proportional to the fermion mass. The on-shell decay into a top-antitop pair is not possible, since it would require the Higgs boson to have a mass of $m_H > 2m_t$. The most common fermionic decay is hence into a bottom-antibottom pair with a branching ratio of approximately 57.7%. However, due to the overwhelming
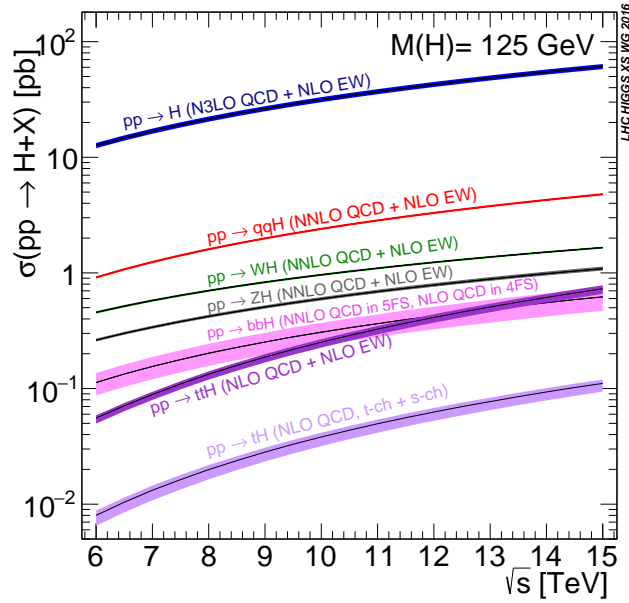
Figure 2.5: Cross section for a SM Higgs boson with a mass of 125 GeV as a function of the center-of-mass energy ($\sqrt{s}$) for a proton-proton collider [28].

background of quark and gluon jets the H → bb decay is very difficult to access. Therefore, H → bb searches mainly target associated production with W/Z bosons due to its relatively clean signature. Decays of the Higgs boson into pairs of tau leptons have the second highest fermionic branching ratio of approximately 6.2%, but the smaller quark and gluon jet background, and therefore the better experimental accessibility with respect to the bb final state, makes Higgs boson decays into pairs of tau leptons the most promising candidate to directly probe Yukawa couplings at the LHC. The first observation of the SM H → ττ decay with a significance of more than 5σ was via combination of ATLAS and CMS Run-1 results of SM H → ττ searches [29]. The first observation of the SM H → ττ decay by a single experiment was reported by CMS [30]. The analysis used 35.9 fb^{-1} of data collected at a center-of-mass energy of 13 TeV in combination with CMS Run-1 data collected at center-of-mass energies of 7 and 8 TeV. Other fermionic decay modes have either an overwhelming quark and gluon jets background (H → cc) or a very small branching ratio due to the relatively small masses of the fermions (H → $\mu\mu$), and thus will require significantly more data for the experiments to become sensitive. Some decay modes, e.g. H → gg, cannot be measured at the LHC at all if SM branching ratios are assumed.

For bosonic decays of the Higgs boson three promising channels exist. Although the branching ratios of 0.227% and 2.64% for H → $\gamma\gamma$ and H → ZZ, respectively, are rela-

tively small, a clean signature characterizes the final states, and thus allows a distinct signal-background separation. Moreover, due to the good energy resolution of the photons in the H → γγ analyses, and for muons and electrons, which comprise the final states in the most-sensitive H → ZZ analyses, these decay channels are best suited for many Higgs boson property measurements. Already LHC Run-1 searches exceeded individual significances of more than 5 standard deviations, see [24–27]. One subtlety is that the Higgs boson does not couple to the photons directly but proceeds through the interfering combination of top quark and W boson loops.

The overall second highest branching ratio for a SM Higgs boson at approximately 21.5% is obtained in the decay into a pair of W bosons. The W bosons can subsequently decay into a quark-antiquark pair or into a charged lepton and the corresponding neutrino. But since the decays into quark-antiquark pairs are difficult to distinguish from quark and gluon jet backgrounds and the decay into leptons cannot be fully reconstructed due to the neutrinos in the final state, the expected H → WW significance is typically slightly weaker than the significance of the H → γγ and H → ZZ channels. The first individual 5σ H → WW observation was reported by ATLAS using the combined Run-1 dataset [31].

Another possibility of a bosonic decay is the H → Zγ decay, which still requires more data for the experiments to become sensitive.
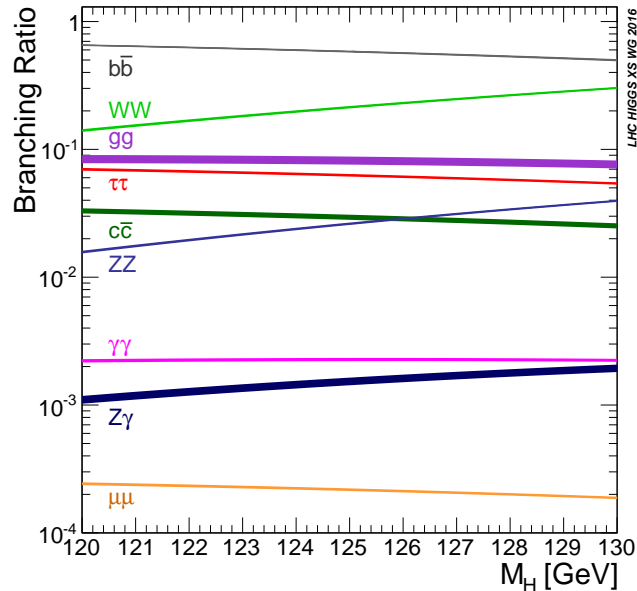

Figure 2.6: SM Higgs boson decay branching ratios at a center-of-mass energy of 13 TeV in the mass range of 120 GeV to 130 GeV [28].

2.2.3 Higgs Boson Properties

The most important properties of the SM Higgs boson are production and decay rates, couplings to fermions and bosons, signal strength, decay width, spin and parity [16]. A summary of combined ATLAS and CMS Run-1 results on production and decay rates as well as couplings and signal strengths can be found in Ref. [29]. Measurements of the spin and parity are reported in Ref. [32, 33].

As described in Sec. 2.1.2, the couplings to vector bosons are a direct consequence of spontaneous symmetry breaking and the couplings to fermions are described by introducing Yukawa couplings. The mass of the SM Higgs boson is one of 19 free parameters that the SM Lagrangian depends on, and whose values have to be established by experiment. The mass of the Higgs boson was the last of these free parameters to be measured, the combined ATLAS and CMS Run-1 result yields $m_{\mathrm{H}} = 125.09 \pm 0.24$ GeV [29].

The 125 GeV SM Higgs boson is predicted to have a small decay width of 4 MeV. This is a relatively small width compared to the widths of the W and Z bosons, which are in the order of a few GeV. Since the Higgs field is a scalar field, it has zero spin. The SM further predicts the Higgs boson to be its own antiparticle, to be CP-even, to have zero electric and zero color charge. So far, no strong deviations from SM predictions for any of these quantities have been observed at the LHC.

2.3 The Z Boson

The Z boson is one of the three intermediate vector bosons of the electroweak interaction with spin 0, no electric charge, a mass of 91.1876 ± 0.0021 GeV and a decay width of 2.4952 ± 0.0023 GeV [16]. Unlike the charged $W^{\pm}$ bosons the neutral Z boson does not alter the electric charge in any interaction, nor does it change other so-called "charges", e.g. strangeness or baryon number. However, the emission or absorption of a Z boson can alter spin, momentum and energy of particles involved in the interaction (*weak neutral current*). An exemplary Feynman graph for a weak neutral current is shown in Fig. 2.7.

Table 2.2 lists the decay modes of the Z boson. It is to note that decays to the three different lepton flavors occur at the same rate within measurement precision (*lepton universality*). Lepton universality is a fundamental assumption of the SM and states that interactions of the three charged leptons are the same despite their different masses and lifetimes.
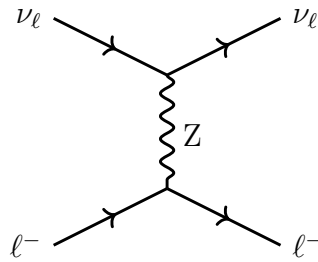
Figure 2.7: A neutral current event in which a charged lepton ($\ell = $ e, μ, τ) changes momentum and (or) energy by the exchange of the neutral Z boson.

Decay Mode	Branching Ratio [%]
e^+e^-	3.363 ± 0.004
$\mu^+\mu^-$	3.366 ± 0.007
$\tau^+\tau^-$	3.370 ± 0.008
Invisible	20.00 ± 0.06
Hadrons	69.91 ± 0.06

Table 2.2: Z boson decay modes and measured branching ratios, the invisible decays comprise the decays to all three neutrino flavors [16].

For H $\to \tau\tau$ analyses the most important irreducible background originates from so-called *Drell-Yan* (DY) [34] processes. DY processes occur in high-energy hadron-hadron scattering where the annihilation of a quark-antiquark pair creates a virtual photon or a Z boson, which subsequently decays into oppositely-charged leptons. In Chap. 7 the DY production of tau lepton pairs ($q\bar{q} \to Z/\gamma^* \to \tau\tau$) is studied and in Chap. 8 the DY process is an important background in the search for additional neutral Higgs bosons decaying to tau lepton pairs.

2.4 The Tau Lepton

The tau lepton is the heaviest member of the lepton family with a mass of 1.777 ± 0.00012 GeV and a proper life time of $2.9 \cdot 10^{-13}$ s [16]. It was discovered in a series of experiments between 1974 and 1977 at the e^+e^- collider at SLAC (Stanford Linear Accelerator Center) [35]. Under the guidance of Martin Lewis Perl the tau lepton was not detected directly, but rather was a series of anomalous events observed, which were of the form $e^+ + e^- \to e^\pm + \mu^\pm$. At least two undetected particles were required to explain the anomalous events, since energy and momentum conservation was not given with only one particle. Thus, it was proposed to explain these anomalies with the

presence of two tau leptons produced in electroweak interactions and their subsequent decays to an electron-muon pair and four undetected neutrinos:

$$\mathrm{e}^+\mathrm{e}^- \rightarrow \tau^+\tau^- \rightarrow \mathrm{e}^\pm \mu^\pm 4\nu.$$

For this discovery Martin Lewis Perl was awarded the Nobel Prize in 1995.

The tau lepton is still not directly detectable in modern collider experiments due to it's short lifetime. Rather it is reconstructed via its decay products. Furthermore, the tau lepton is the only lepton whose mass exceeds the masses of the lightest hadrons, and thus it can decay both into hadrons (τ_h decays) as well as into electrons (τ_e decays) and muons (τ_μ decays), all with associated neutrinos. For searches of heavy bosons with decays into pairs of tau leptons this leads to a total of six possible final states: $\tau_\mathrm{e}\tau_\mathrm{h}$, $\tau_\mu\tau_\mathrm{h}$, $\tau_\mathrm{h}\tau_\mathrm{h}$, $\tau_\mathrm{e}\tau_\mu$, $\tau_\mathrm{e}\tau_\mathrm{e}$, $\tau_\mu\tau_\mu$. A Feynman diagram of the most common decays of the tau lepton is shown in Fig. 2.8, the decay modes and their respective branching ratios are listed in Tab. 2.3. Due to lepton universality the branching ratios to electrons and muons and their respective neutrinos are almost identical. Approximately 65% of the tau lepton decays are to hadrons, whereby most of the decays are a combination of charged and neutral pions. The remaining hadronic decays are split between miscellaneous decay modes including kaons and other hadrons. In practice, one distinguishes between *1-prong* and *3-prong* tau leptons, which directly refers to the number of charged hadrons in the decay , see Sec. 4.2.5.
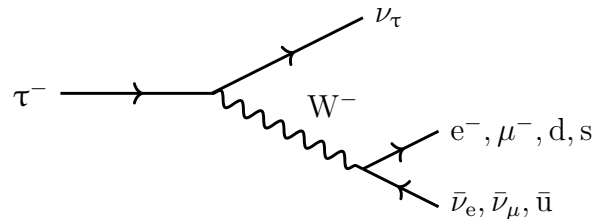
Figure 2.8: Feynman diagram of the most common decays of the negatively charged tau lepton by the emission of a W boson.

2.5 Shortcomings of the Standard Model

Although the SM has demonstrated great success in the last years predicting a huge number of experimental results, it comes with several shortcomings. Roughly spoken, the shortcomings can be divided into plain deficits, that the current formulation is not able to take care of, and theoretical considerations, which at first sight might only

Decay Mode	Branching Ratio [%]
$e^- \bar{\nu}_e \bar{\nu}_\tau$	17.8
$\mu^- \bar{\nu}_\mu \bar{\nu}_\tau$	17.3
$\pi^- \bar{\nu}_\tau$	10.8
$\pi^- \pi^0 \bar{\nu}_\tau$	25.4
$\pi^- \pi^0 \pi^0 \bar{\nu}_\tau$	9.2
$\pi^- \pi^- \pi^+ \bar{\nu}_\tau$	8.9
$\pi^- \pi^- \pi^+ \pi^0 \bar{\nu}_\tau$	2.7
$\pi^- \pi^0 \pi^0 \pi^0 \bar{\nu}_\tau$	1.0
Other hadronic decay modes	6.9

Table 2.3: Decay modes of the tau lepton [16].

appear as non-aesthetic, but have in fact also evoked serious debates.

Not included in the SM, and thus commonly referred to as *beyond the SM* (BSM) phenomena, are e.g. gravity, dark matter and neutrino oscillations. Although negligible at LHC energies, the incompatibility of gravity and the SM will become relevant at the Planck scale at latest ($\Lambda_{\text{Pl}} \sim 10^{18}$ GeV). Associated therewith, the SM can also not address the weakness of gravity relative to the other fundamental interactions. Dark matter is motivated by deviations from the expected galaxy rotation curves, gravitational lensing, formation of galaxy clusters and others [36]. Another prominent BSM phenomenon are neutrino oscillations. In 1998, atmospheric neutrino oscillations were observed by the Super-Kamiokande experiment [37] and in 2001, solar neutrino oscillations were reported by the Sudbury Neutrino Observatory [38]. Neutrino oscillations imply that neutrinos have non-zero masses, which is in direct contradiction to SM assumptions.

Further indications of an incomplete SM originate from theoretical considerations, e.g. matter-antimatter asymmetry, unification of gauge coupling strengths or the question why exactly three generations of particles seem to exist. Another important theoretical issue is the so-called *hierarchy problem*. In the case of the Higgs boson, contributions from fermion and gauge boson loops cause the squared Higgs boson mass to diverge quadratically:

$$\Delta m_{\text{H}}^2 \propto \Lambda_{\text{UV}}^2 + \mathcal{O}(\ln \Lambda_{\text{UV}}), \tag{2.14}$$

where Λ_{UV} is the cut-off scale that can be interpreted as the lowest energy scale, at

which new physics can alter SM predictions. In order to cancel the quadratic divergences by means of renormalization, a lot of *fine-tuning* is required, meaning that parameters have to be adjusted very precisely to match the observations. An important feature of the Higgs boson mass correction is that fermion and boson loops contribute to Δm_{H}^2 with opposite sign. Many BSM solutions to the hierarchy problem have been proposed, one of the most popular theories is supersymmetry. In supersymmetric models every SM fermion has a bosonic superpartner and vice versa. The effect is that the divergent terms in Δm_{H}^2 from each particle or superpartner pair cancel.

2.6 Supersymmetry

As described in Sec. 2.5, the SM suffers from several shortcomings. Motivated by the concept of symmetries in particle physics, SUSY is one of the most appealing BSM theories. SUSY was first proposed in the 1970s when Wess and Zumino identified the characteristic renormalization features of four-dimensional supersymmetric field theories [39]. Motivation for SUSY models are amongst others the intrinsic ability to solve the Hierachy problem, to enable gauge coupling unification and to include dark matter in the SM.

The Haag-Lwhen Wesposzánski-Sohnius theorem [40] states that SUSY is the only non-trivial extension of the Poincaré symmetry consistent with relativistic quantum field theories. Supersymmetry refers to the invariance under transformations between bosonic and fermionic states which are generated by a pair of spin $1/2$ operators Q and $\bar{Q}$ (*Super-Poincaré algebra*):

$$Q\,|\text{Boson}\rangle = |\text{Fermion}\rangle\,, \tag{2.15}$$

$$\bar{Q}\,|\text{Fermion}\rangle = |\text{Boson}\rangle\,. \tag{2.16}$$

The supersymmetric Super-Poincaré algebra has the following anti-commutator relation

$$\{Q_\alpha, \bar{Q}_{\dot{\beta}}\} = 2\sigma^\mu_{\alpha\dot{\beta}}P_\mu, \tag{2.17}$$

where $Q_{\alpha,\beta}$ ($\alpha,\beta \in \{1,2\}$) are *Weyl-Spinors* representing two-component spinors with a defined handedness, P_μ represents the generators of space-time translations and σ^μ the Pauli matrices. Dotted indices denote the components of the corresponding complex conjugated spinors. All other anti-commutator relations between Q operators and between Q and P operators vanish. Equation 2.17 implies that 2 SUSY transforma-

tions yield a space-time translation, or in other words, that the squared Q generators are linked to the four-momentum. Hence, a connection between SUSY and general relativity is possible, which is realized in theories where local gauge invariance under supersymmetric transformations evokes gravitation. Such theories are called supergravitation theories (SUGRA). The simplest supersymmetric model that allows to embed the SM as an effective theory at low energies is the *Minimal Supersymmetric Extension of the Standard Model* (MSSM) [41,42]. The following subsections introduce the MSSM and its incorporation of the Higgs sector.

2.6.1 Minimal Supersymmetric Extension of the Standard Model

The requirements for the MSSM are the introduction of one superpartner degree of freedom for each SM particle degree of freedom. The introduced superpartners, which are referred to as *sparticles*, have identical gauge numbers and Higgs coupling constants, but a spin differing by a unit of $1/2$. Since in the MSSM a single Higgs doublet can neither generate the appropriate masses of all fermions nor does it allow to keep the theory anomaly free, a second Higgs doublet plus superpartners is introduced. The MSSM particle content before electroweak symmetry breaking is listed in Tab. 2.4.

SM particle	Spin	Sparticle	Spin
Leptons		Sleptons	
ν_e^L, e^L, e^R	$1/2$	$\tilde{\nu}_e^L, \tilde{e}^L, \tilde{e}^R$	0
ν_μ^L, μ^L, μ^R	$1/2$	$\tilde{\nu}_\mu^L, \tilde{\mu}^L, \tilde{\mu}^R$	0
$\nu_\tau^L, \tau^L, \tau^R$	$1/2$	$\tilde{\nu}_\tau^L, \tilde{\tau}^L, \tilde{\tau}^R$	0
Quarks		Squarks	
u^L, u^R, d^L, d^R	$1/2$	$\tilde{u}^L, \tilde{u}^R, \tilde{d}^L, \tilde{d}^R$	0
c^L, c^R, s^L, s^R	$1/2$	$\tilde{c}^L, \tilde{c}^R, \tilde{s}^L, \tilde{s}^R$	0
t^L, t^R, b^L, b^R	$1/2$	$\tilde{t}^L, \tilde{t}^R, \tilde{b}^L, \tilde{b}^R$	0
Gauge bosons		Gauginos	
B	1	$\tilde{B}$	$1/2$
W^1, W^2, W^3	1	$\tilde{W}^1, \tilde{W}^2, \tilde{W}^3$	$1/2$
g	1	$\tilde{g}$	$1/2$
Higgs bosons		Higgsinos	
$H_u^0, H_u^+, H_d^0, H_d^+$	0	$\tilde{H}_u^0, \tilde{H}_u^+, \tilde{H}_d^0, \tilde{H}_d^-$	$1/2$

Table 2.4: Particle content of the MSSM. Each SM field has a supersymmetric counterpart with a spin differing by a unit of $1/2$.

Supersymmetric interactions can be derived from any SM vertices by replacing any involved SM particles by their superpartners. In analogy to the SM, electroweak symmetry breaking is realized by the Higgs mechanism. Since the two Higgs doublets in the MSSM have 8 degrees of freedom and three degrees of freedom are absorbed by gauge transformations, which give mass to the W and Z bosons, five physical Higgs boson fields remain. For a CP-conserving MSSM model this results in the electrically neutral fields h^0, H^0 and A^0 and the electrically charged fields H^+ and H^- where the neutral field h^0 is typically associated with the SM Higgs boson. For simplicity h^0, H^0 and A^0 are denoted with h, H and A from now on. If CP is not conserved, the three neutral Higgs bosons are no longer pure CP eigenstates but mixtures of CP-even and CP-odd components. The following descriptions refer to a CP-conserving MSSM model.

If SUSY was an exact symmetry all superpartners would only differ in spin, i.e. every superpartner would have the same mass as the corresponding SM particle (or field). The fact that no SUSY particles have been observed by experiments so far suggests that SUSY is in fact a broken symmetry, in which the superpartner masses are larger than their SM counterparts. In order to ensure for the quadratic divergences to the Higgs boson mass to cancel each other and thus avoid further fine-tuning, the breaking of SUSY has to be *soft*, i.e. the breaking preserves the relation between the couplings, and the symmetry is restored at high energies and therefore is assumed to be in the $\mathcal{O}(\text{TeV})$. The most general soft SUSY-breaking MSSM Lagrangian density introduces 105 free parameters in addition to the 19 SM parameters. Although many of these parameters can be strongly constrained by experiments and theoretical assumptions, several free parameters remain. They comprise mass parameters, trilinear scalar interaction parameters and parameters in the Higgs sector.

The gauge eigenstates which are listed in Tab. 2.4 are not necessarily the eigenstates of the theory. While the mass eigenstates of the first- and second-generation squarks and sleptons states are typically nearly degenerate, the mass splitting in the third generation can be large. Since the electrically neutral wino $\tilde{\text{W}}^3$ and the bino B as well as the neutral Higgsinos carry the same gauge quantum numbers and spin, they mix to four different mass eigenstates - $\tilde{\chi}_1^0$, $\tilde{\chi}_2^0$, $\tilde{\chi}_3^0$ and $\tilde{\chi}_4^0$ - which are called *neutralinos*. Similarly, the charged winos $\tilde{\text{W}}^1$ and $\tilde{\text{W}}^2$ and the charged Higgsinos superimpose to form the mass eigenstates - $\tilde{\chi}_1^\pm$, $\tilde{\chi}_2^\pm$ - which are called *charginos*.

2.6.2 The Higgs Sector of the MSSM

In the Higgs sector of the MSSM, two complex doublet fields are required to generate masses for both *up*-type and *down*-type quarks and leptons. In analogy to the SM (see Eq. 2.6), the two complex SU(2) doublets are defined as:

$$\Phi_{\mathrm{u}} = \begin{pmatrix} \Phi_{\mathrm{u}}^+ \\ \Phi_{\mathrm{u}}^0 \end{pmatrix}, \quad \Phi_{\mathrm{d}} = \begin{pmatrix} \Phi_{\mathrm{d}}^0 \\ \Phi_{\mathrm{d}}^- \end{pmatrix}. \tag{2.18}$$

Again, an appropriate choice of the potential leads to spontaneous symmetry breaking. Without loss of generality, the ground states can be chosen as

$$\langle 0 | \, \Phi_{\mathrm{u}} \, | 0 \rangle = \frac{1}{\sqrt{2}} \begin{pmatrix} 0 \\ v_{\mathrm{u}} \end{pmatrix}, \quad \langle 0 | \, \Phi_{\mathrm{d}} \, | 0 \rangle = \frac{1}{\sqrt{2}} \begin{pmatrix} v_{\mathrm{d}} \\ 0 \end{pmatrix}, \tag{2.19}$$

where v_{u} and v_{d} are the vacuum expectation values of the 2 Higgs doublets and are related to the SM value by

$$v^2 = v_{\mathrm{u}}^2 + v_{\mathrm{d}}^2 = (246 \text{ GeV})^2. \tag{2.20}$$

In order to obtain the physical Higgs fields and their masses, the two Higgs doublets are developed around their vacuum states:

$$\Phi_{\mathrm{u}} = \frac{1}{\sqrt{2}} \begin{pmatrix} \Phi_{\mathrm{u}}^+ \\ v_{\mathrm{u}} + \Phi_{\mathrm{u}} + \mathrm{i}\chi_{\mathrm{u}} \end{pmatrix}, \quad \Phi_{\mathrm{d}} = \frac{1}{\sqrt{2}} \begin{pmatrix} v_{\mathrm{d}} + \Phi_{\mathrm{d}} + \mathrm{i}\chi_{\mathrm{d}} \\ \Phi_{\mathrm{d}}^+ \end{pmatrix}. \tag{2.21}$$

Here, the real parts correspond to the CP-even Higgs bosons and the imaginary parts to the CP-odd Higgs and the Goldstone bosons. Out of the eight initial degrees of freedom (four degrees of freedom for each complex SU(2) doublet), one neutral and two charged Goldstone bosons correspond to the masses of the W$^\pm$ and Z gauge bosons. This leaves five massive Higgs fields, which comprise two neutral CP-even states h and H, one neutral CP-odd state A and a charged Higgs pair H$^\pm$. At tree level all properties of the MSSM Higgs sector can be described by two parameters, which are typically chosen to be the mass of the CP-odd Higgs boson, m_{A}, and the ratio of the vacuum expectation values, $\tan\beta = v_u/v_d$. At tree level the masses of the remaining four Higgs bosons can

be expressed as

$$m_{H^\pm} = m_A^2 + m_W^2, \tag{2.22}$$

$$m_{h,H} = \frac{1}{2}\left(m_A^2 + m_Z^2 \pm \sqrt{(m_A^2 + m_Z^2)^2 - 4m_A^2 m_Z^2 \cos^2 2\beta}\right). \tag{2.23}$$

The LO mass dependency for two different values of $\tan\beta$ is shown in Fig. 2.9. From Eq. 2.23 an upper limit on the mass of the neutral h boson can be derived:

$$m_h \leq m_Z |\cos 2\beta| \leq m_Z. \tag{2.24}$$

This means that at tree level, the mass of the lightest scalar Higgs boson cannot exceed that of the Z boson. However, depending on several other SUSY parameters, the loop corrections to this term can be quite significant and m_h can reach values up to 135 GeV [43]. Since the number of parameters entering such loop calculations is large, it is common to study predictions in scenarios where the relevant parameters are set to fixed values. A selection of different benchmark scenarios can be found in Ref. [44]. For this thesis, the following scenarios are important:

- The m_h^{mod+} scenario [44], which finds regions where in the decoupling region m_h is close to the observed SM-like Higgs boson mass over a wide range of parameter space. A convenient way to perform these modifications is the reduction of the mixing in the stop sector. The observed boson at 125 GeV is interpreted as the h boson within the theoretical uncertainties in m_h of ± 3 GeV.

- The phenomenological hMSSM scenario (habemus MSSM?) [45], which uses the information of the observed boson at 125 GeV and incorporates it by interpreting it as the h boson. The uncertainties in the Higgs boson mass measurements are used to estimate the main radiative corrections and hence the masses of the remaining MSSM Higgs bosons.

In the *decoupling limit*, $m_A \gg m_Z$, the Higgs boson masses are approximately

$$m_h^2 \simeq m_Z^2 \cos^2 2\beta, \tag{2.25}$$

$$m_H^2 \simeq m_A^2 + m_Z^2 \sin^2 2\beta, \tag{2.26}$$

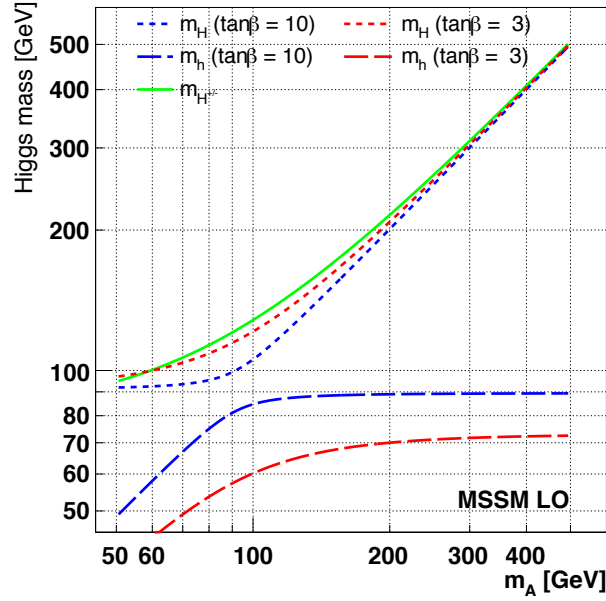$$m_{H^\pm}^2 \simeq m_A^2 + m_W^2, \tag{2.27}$$

Figure 2.9: Values of the masses at LO of the neutral Higgs bosons H, h and the charged Higgs boson $H^{\pm}$ as a function of the pseudoscalar mass m_A for two different values of $\tan\beta$ [46].

and thus $m_A^2 \approx m_H^2 \approx m_{H^{\pm}}^2$. "Decoupling" refers to the fact that the H boson decouples from the W and Z bosons and the h boson has couplings similar to the SM Higgs boson. Fermionic couplings of the h boson also become SM-like, while for the neutral H and A bosons couplings to down-type quarks, e.g. bottom quarks, and electron, muon or tau leptons get enhanced by a factor, which primarily depends on $\tan\beta$, whereas couplings to up-type fermions are suppressed by the same amount.

For values of $m_A \geq 300$ GeV, the MSSM is close to the decoupling limit. The h boson usually takes the role of the SM-like Higgs boson and H and A are nearly degenerate in mass. The enhanced couplings to down-type quarks and charged leptons raise particular interest in searches for additional heavy neutral Higgs bosons in the $\tau\tau$ and bb final states. Furthermore, the enhanced coupling to bottom quarks has consequences in the production. Namely, compared to SM Higgs production b-associated production dominates over ggF production at large values of $\tan\beta$ and in ggF production the kinematic properties of the Higgs bosons change at large values of $\tan\beta$, since the contribution of bottom quarks to the fermion loop increases. A LO Feynman diagram for b-associated production of the heavy neutral A and H bosons is shown in Fig. 2.10.
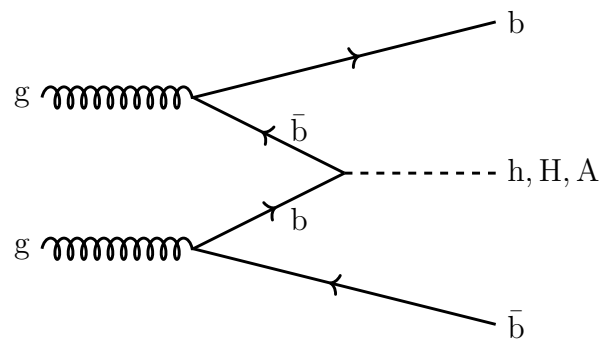
Figure 2.10: Example LO Feynman diagram for the production of heavy neutral Higgs bosons in association with b quarks.

Experimental Setup

The *European Organization for Nuclear Research* (CERN, French: L'Organisation européenne pour la recherche nucléaire) is situated at the French-Swiss border near Geneva. It is home to the world's largest and most powerful particle accelerator and collider, the LHC. In Sec. 3.1, an overview of the LHC is given and in Sec. 3.2, the Compact Muon Solenoid (CMS) experiment is introduced. For further reading Refs. [47, 48] are recommended. In this chapter, the CMS subdetector systems are described as used for the 2015 and 2016 data taking periods, which are relevant for this thesis.

3.1 The Large Hadron Collider

Built in the former LEP tunnel in Switzerland and France, the LHC has a circumference of 26.7 kilometers and is constructed between 70 and 150 meters below the surface. The LHC started to operate at a center-of-mass energy of 0.9 TeV and 2.3 TeV in 2009 for proton-proton (pp) collisions. The 2009 run period was mostly used for testing the subsystems of the LHC and calibration of the experiments. In 2010 and 2011, the center-of-mass energy was increased to 7 TeV and the first physics results were published (start of LHC Run-1). In 2012, the center-of-mass energy was again increased to 8 TeV before the LHC was closed and upgraded for two consecutive years. Since 2015, the LHC is accelerating and colliding protons at a center-of-mass energy of 13 TeV (LHC Run-2). Apart from pp collisions, the LHC is also capable of accelerating heavy ion beams and producing ion-ion as well as proton-ion collisions.

Before proton (or ion) beams are accelerated to their final energies they undergo a series of pre-acceleration steps to reach enough energy to be injected into the LHC. A sketch of the per-acceleration steps is shown in Fig. 3.1. Protons are obtained from hydrogen atoms and are linearly accelerated in the *Linac2* to up to 50 MeV. Subsequently, the

protons are injected in the *Proton Synchrotron Booster* (PSB) which accelerates them to up to 1.4 GeV. After the PSB, the *Proton Synchrotron* (PS) accelerates the protons up to 25 GeV and finally, the *Super Proton Synchroton* (SPS) accelerates them to the LHC injection energy of 450 GeV. The bunches are transferred to and accumulated in the LHC. Once the injection phase is terminated, the colliding beams reach their final energies and afterwards circulate for many hours under normal operating conditions.
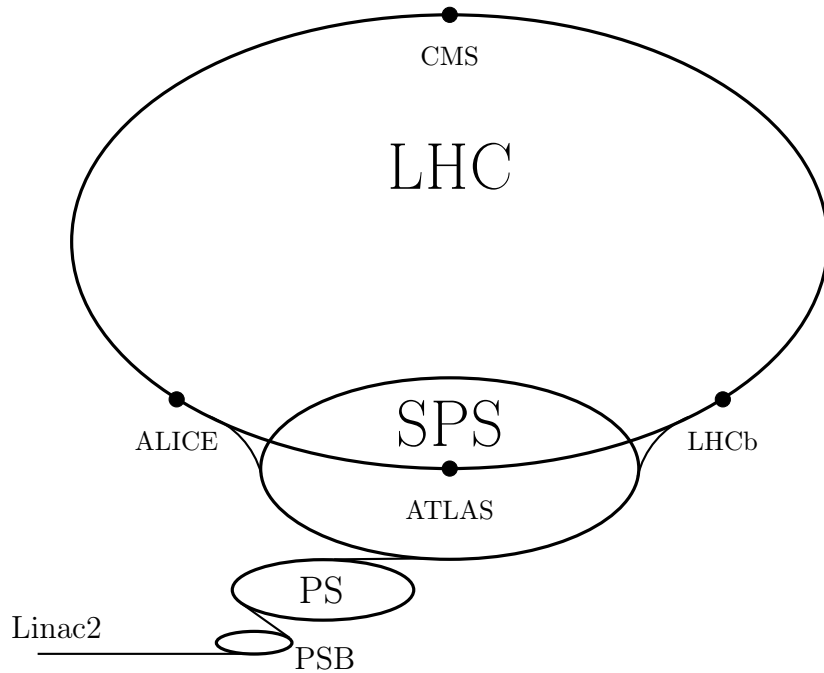

Figure 3.1: Illustration of the LHC accelerator complex consisting of Linac2, PSB, PS, SPS and LHC, as well as the four large experiments.

Focusing on the LHC, Fig. 3.2 illustrates a simplified layout of the accelerator and its main facilities. The injected beams travel into opposite directions and are brought to collision at point 1 (ATLAS [49]), at point 2 (ALICE [50]), at point 5 (CMS [48]) and at point 8 (LHCb [51]). The two multipurpose experiments ATLAS and CMS are designed for a variety of physics analyses with the main intention to search for the Higgs boson and to look for physics beyond the SM, whereas the LHCb experiment is dedicated to the search for CP violation and other measurements in B hadron decays. The ALICE experiment is built to mainly study quark-gluon plasma production in heavy-ion collisions. The LHC also consists of beam cleaning regions (point 3 and point 5), radio frequency (RF) cavities for acceleration (point 4) and the beam dump (point 6). 1232 niobium-titanium superconducting dipole magnets are required to keep the beams circulating. Each magnet is 14.3 m long and generates magnetic fields up to 8.4 T. The magnets cooled by superfluid helium operate at a temperature of 1.9 K.
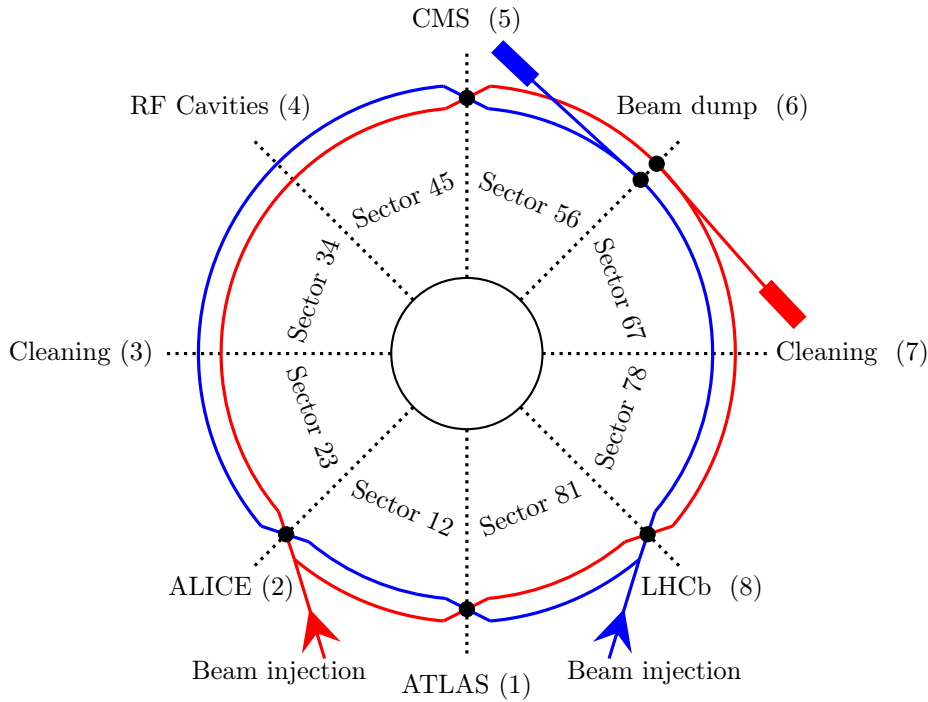
Figure 3.2: Illustration of the LHC layout and its main facilities. The four collision regions are the ATLAS, ALICE, CMS and LHCb experiments. The injection, cleaning, acceleration and dumping of the beams is also sketched.

Colliders are characterized by the so called *instantaneous luminosity* $\mathcal{L}$ that is defined as

$$\mathcal{L} = \nu_{\mathrm{n}}\frac{\mathrm{N_b}\mathrm{n_p^2}}{4\pi\sigma_x\sigma_y}\mathrm{F}, \tag{3.1}$$

where ν_{n} denotes the revolution frequency, $\mathrm{N_b}$ the number of proton bunches, $\mathrm{n_p}$ the number of protons per bunch and σ_x and σ_y the beam size in horizontal and vertical directions, respectively. F is a reduction factor which accounts for the reduction of the effective beam size due to the beam crossing angle at the interaction points. The LHC is designed to operate at an instantaneous luminosity of 10^{34} cm^{-2}s^{-1}, which translates to 10^{34} collisions per second and per cm^2 of cross section. In 2015 and 2016, the LHC operated with approximately 2200 bunches per beam with up to $1.3 \cdot 10^{11}$ protons per bunch, which were circulating at the same time and brought to collision every 25 ns. The achieved peak luminosities are $0.51 \cdot 10^{34}$ cm^{-2}s^{-1} and $1.53 \cdot 10^{34}$ cm^{-2}s^{-1} in 2015 and 2016, respectively [52].

The luminosity integrated over time is a measure of the collected amount of data. Since 1 barn equals 10^{-24} cm^2, the unit *inverse femtobarn* (fb^{-1}) is commonly used in high energy physics. Accordingly, an integrated luminosity of 1 fb^{-1} corresponds to the oc-

curance of (on average) 1 event of a process which has a cross section of 1 fb. Figure 3.3 displays the integrated luminosity over time for the 2015 and 2016 run periods.

The number of *pileup* (PU) events describes the average number of proton-proton collisions per bunch-crossing, and thus for a constant number of beam bunches a growing instantaneous luminosity goes hand in hand with an increasing number of PU events. In 2015, the average number of PU interactions was $\langle \mu \rangle = 14$ while in 2016, the average number was $\langle \mu \rangle = 27$ (see Fig. 3.4).
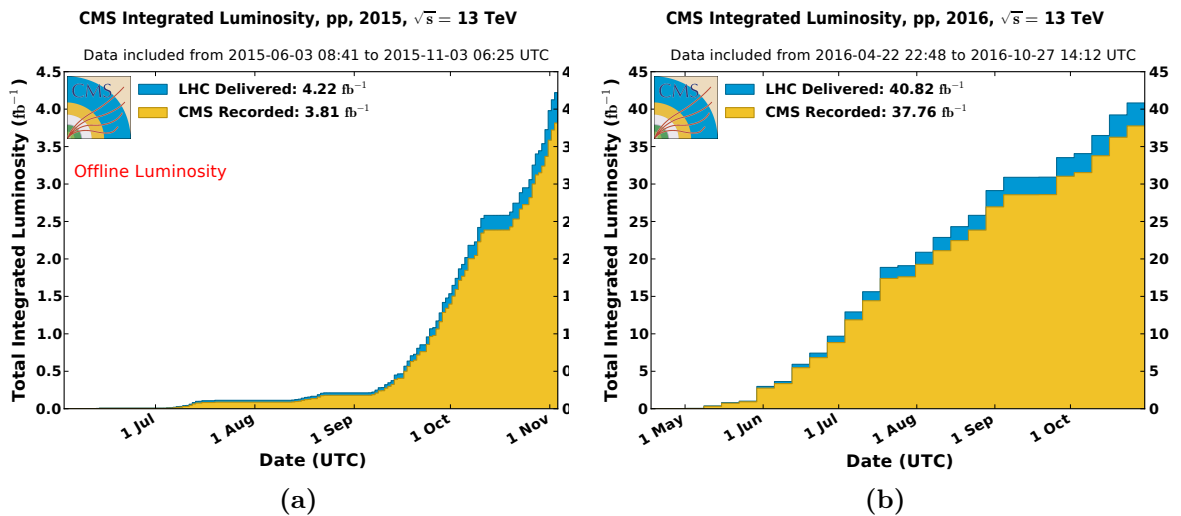
Figure 3.3: Integrated luminosity over time delivered by the LHC and recorded by CMS for the 2015 (a) and 2016 (b) run periods at a center-of-mass energy of 13 TeV [52].

3.2 The CMS Experiment

Located on French territory, in a cavern approximately 100 meters below the surface of France, the CMS detector is one of two multipurpose experiments at the LHC [48,53]. It is designed for a broad physics program, among others Higgs boson searches and BSM physics. In Fig. 3.5, the structure of the CMS detector is displayed exhibiting the typical onion-like structure of particle detectors at colliders. The central feature of the CMS apparatus is a superconducting solenoid which provides a magnetic field of 3.8 Tesla. The solenoid encloses the inner parts of the CMS detector, which are from the inside out: a silicon pixel and strip tracker, a lead tungstate crystal *electromagnetic calorimeter* (ECAL), and a brass and scintillator *hadron calorimeter* (HCAL). The ECAL is composed of a barrel and two endcap detectors, the HCAL is organized into barrel, endcap and forward sections. Muons are detected in ionization chambers which are embedded in the steel flux-return yoke outside the solenoid.
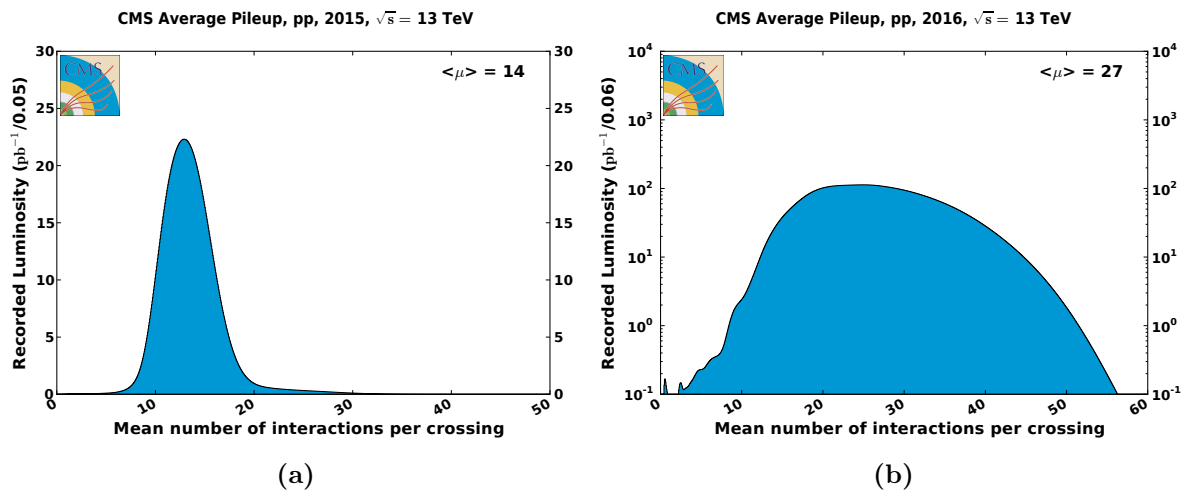
Figure 3.4: Mean number of interactions per bunch crossing for the 2015 (a) and 2016 (b) run periods at a center-of-mass energy of 13 TeV, assuming a minimum bias cross section of 80 mb [52].
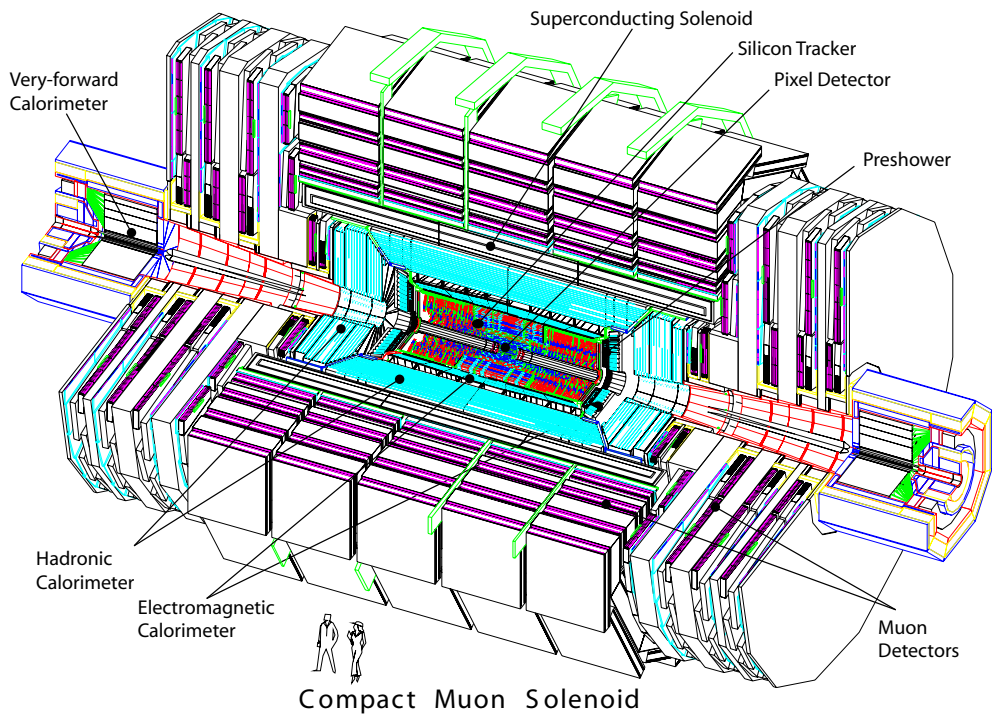

Figure 3.5: Cut-away view of the CMS detector [48].

3.2.1 Conventions

The point of collision for two partons is denoted as *primary vertex* (PV). The PV is inside the *beam spot* (BS) which approximates the overlap region of the two proton bunches. Besides the PV, information about *secondary vertices* (SVs) can be extracted if long-lived particles, like B mesons, travel a certain distance before decaying.

The coordinate system used in CMS is right-handed and is centered at the *interaction point* (IP). The x axis points towards the center of the LHC ring, the y axis points vertically upwards and the z axis points along the beam pipe. It is common to use spherical coordinates instead of cartesian ones, where the azimuthal angle ϕ is defined in the $x - y$ plane and the polar angle θ is measured with respect to the z axis. Instead of the polar angle θ the *pseudorapidity* $\eta = -\ln\tan(\theta/2)$ is commonly used. The measurement of momentum in the transverse plane, denoted as p_{T}, is of particular interest due to boost invariance with respect to the z direction. Similarly, the transverse energy E_{T} is measured from the values of x and y components.

3.2.2 Tracking System

The innermost part of the CMS detector, closest to the beam axis, is the silicon tracking system consisting of *silicon pixel* and *silicon strip* detectors. Its main task is to efficiently and accurately measure the trajectories of charged particles originating from collisions, i.e. electrons, muons and charged hadrons. The magnetic field is almost homogeneous within the volume of the tracker. It is used to measure the curvature of the tracks induced by the Lorentz force of charged particles in a magnetic field and subsequently to determine the particle momentum. Moreover, the tracks are used to identify the PVs of a bunch crossing as well as SVs from the decays of long-lived particles. In nominal operation conditions, in the order of thousand particles traverse the tracker volume every 25 ns. Thus, a fast and radiation-resistant tracker with high granularity is needed which has led to the choice of silicon detectors as the CMS tracking system. The silicon detectors ensure efficient tracking up to $|\eta| < 2.5$. Signals from the pixel and the strip detectors are clustered and subsequently build *hits*, which are characterized by a position and a corresponding uncertainty. The 1440 silicon pixel detector modules are surrounded by 15148 silicon strip detector modules which in total cover an area of roughly 200 m^2. For nonisolated particles with $|\eta| < 1.4$ and a transverse momentum of $1 < p_{\mathrm{T}} < 10$ GeV, track uncertainties are typically 1.5% in p_{T} and 25-90 μm in the transverse and 45-150 μm in the longitudinal impact parameter [54]. Isolated particles with $|\eta| < 1.4$ and a transverse momentum of $p_{\mathrm{T}} = 100$ GeV have typical

track uncertainties of 3% in p_T and 10 (30) μm in the transverse (longitudinal) impact parameter [54].

An illustration of the CMS inner tracking system is sketched in Fig. 3.6. The innermost pixel detectors comprise three layers in the barrel region (BPix) and two in the endcap region (FPix). The arrangement of the BPix and FPix layers is such that a minimum of three hits is ensured in most of the regions with $|\eta| < 2.5$. The pixel detector modules are surrounded by silicon strip detector modules comprising four layers of tracker inner barrels (TIB) and three layers of tracker inner disks (TID) in each endcap. The alignment of the strips, which are 10-20 cm long and 80-180 μm wide, is parallel to the beam direction in the barrel and radial in the endcaps. The TIB/TID are surrounded by the tracker outer barrel (TOB) consisting of six barrel layers and the tracker end-caps (TEC) consisting of nine endcap layers.
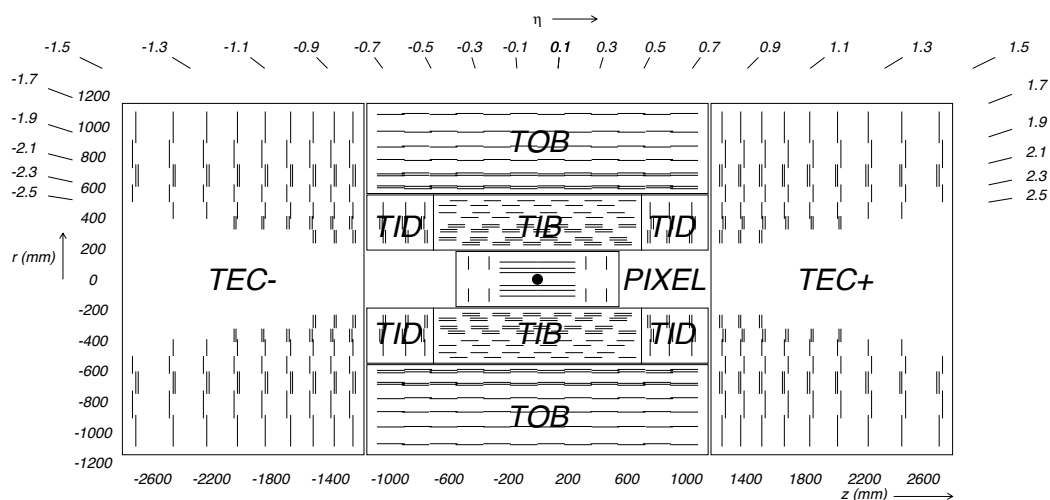
Figure 3.6: Layout of the inner tracking system which consists of silicon pixel detectors in the three innermost layers surrounded by silicon strip detectors [48].

3.2.3 Electromagnetic Calorimeter

The purpose of the ECAL is to measure the energy of electrons and photons with high accuracy. Its design was driven by the need for accurate photon and electron reconstruction, especially since the decay of the Higgs boson into two photons is one of the benchmark discovery channels at the LHC. The main material used for the construction of the ECAL is *lead tungstate*, $PbWO_4$, which is an extremely dense but

optically clear material that scintillates when photons and electrons pass through. The energetic electrons and photons produce an electromagnetic shower by generating a cascade of lower-energy particles, in which electrons and photons dominantly undergo bremsstrahlung and pair production, respectively. The electromagnetic shower continues until either the energy of the photons falls below the pair production threshold or ionization processes start to dominate. The atoms in the lead tungstate crystals are ionized by the charged particles in the shower. The subsequent de-excitation of the atoms yields the emission of scintillation light which is converted to an electric current by photodiodes.

The radiation length of lead tungstate is 0.89 cm. This means that since the length of the implemented crystals is 23 cm and 22 cm in the barrel and the endcap, respectively, almost the entire electron and photon energy is deposited within these crystals. Furthermore, lead tungstate has a rapid light yield where 80% of the light yield is within the time of one bunch crossing (25 ns). These properties of lead tungstate allow the CMS ECAL to have excellent granularity, timing precision and energy resolution. The energy resolution $\sigma(E)/E$ can be parametrized as

$$\frac{\sigma(E)}{E} = \sqrt{\left(\frac{S}{\sqrt{E}}\right)^2 + \left(\frac{N}{E}\right)^2 + C^2} \,, \tag{3.2}$$

where S describes the instrumental noise, N represents stochastic effects, which are caused by shower fluctuations, and C stands for intercalibration errors.

An illustration of the CMS ECAL is sketched in Fig. 3.7. The ECAL is separated into a barrel (EB) and two endcap (EE) regions. Avalanche photodiodes and vacuum phototriodes are used for detecting the scintillating light in the EB and EE, respectively. Altogether the ECAL covers a region of $|\eta| < 3.0$, of which the EB covers the pseudorapidity range $|\eta| < 1.479$. It consists of 61200 crystals with a front face of $22 \cdot 22$ mm^2 and a length of 23 cm corresponding to 25.8 times the radiation length. The two EE detectors consist of 7300 crystals which have a front face of $28.6 \cdot 22$ mm^2 and a length of 22 cm corresponding to 24.9 times the radiation length. For extra spatial precision, in front of each EE, in the region $1.653 < |\eta| < 2.6$, two preshower detectors (ES) are installed that are made of two discs of lead interleaved with two layers of silicon strip detectors. They allow to better distinguish between single high energetic photons and less interesting close pairs of low-energy photons.

For unconverted or late-converting photons an energy resolution of approximately 1% and 2.5% is achieved in the EB and the EE, respectively. For the remaining photons an

energy resolution of 2.5% and between 3% and 4% is achieved in the EB and the EE, respectively [55]. For electrons the energy resolution varies from 1.7% for well-measured electrons in the EB to 4.5% for electrons in the EE, which can lose a significant fraction of their energy due to bremsstrahlung [56].
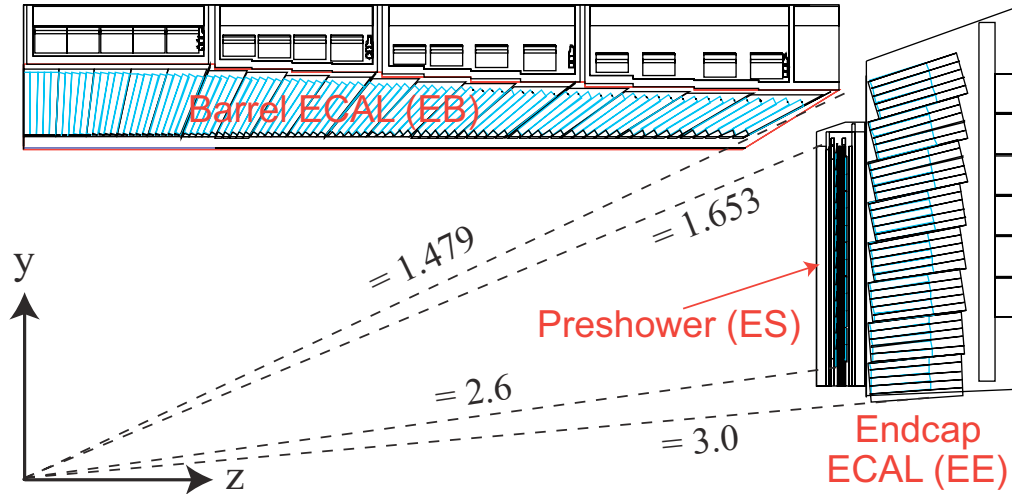

Figure 3.7: Layout of the CMS ECAL [53].

3.2.4 Hadronic Calorimeter

The HCAL surrounds the ECAL calorimeter and is designed to measure the energy of hadrons, such as protons, neutrons, pions or kaons. The HCAL is assembled from several absorbing brass layers which are interleaved with alternating layers of scintillators. The hadron showers cause pulses in the scintillators which are then forwarded to hybrid photodiodes. The choice to use brass as an absorber in most of the HCAL is driven by its short nuclear interaction length of 16.4 cm, which is needed since the overall space is limited due to the compact CMS design, where the solenoid contains most of the inner parts of the detector.

An illustration of the CMS HCAL is sketched in Fig. 3.8. It is subdivided into four subsystems, namely the hadron barrel (HB), the hadronic endcap (HE), the hadronic outer barrel (HO) and the hadronic forward calorimeter (HF). The HB covers a range up to $|\eta| < 1.3$ consisting of 16 absorber layers which corresponds to a depth of 5.8 and 10.6 times the interaction lengths at $|\eta| = 0$ and at $|\eta| = 1.3$, respectively. However, the HB alone does not provide a sufficient containment of the hadron showers due to the limited space between ECAL and solenoid. Thus, it is supported by the HO which uses

the magnet coil as an absorber and increases the total depth of the calorimeter system
up to a minimum of 11.8 times the interaction lengths [48]. The main importance of
the HO arises for sampling highly penetrating or late starting showers. The HEs cover
the range $1.3 < |\eta| < 3.0$ that contains about 34% of all the particles produced [48]
providing approximately a depth of 10 interaction lengths. Finally, the high pseudo-
rapidity region $3.0 < |\eta| < 5.0$ is instrumented with the HF calorimeter. An accurate
coverage of the high η region is of particular importance since several interesting final
state topologies predict jets with large η values. Since the HF calorimeters experience
the highest particle flux, radiation-hard quartz fibres embedded in a steel absorber are
used.

The read-out of the HCAL is structured in individual towers with a cross section of
$\Delta\eta \times \Delta\vartheta = 0.087 \times 0.087$ and $\Delta\eta \times \Delta\vartheta = 0.17 \times 0.17$ for $|\eta| < 1.6$ and $|\eta| > 1.6$,
respectively [57]. The combined energy resolution σ of ECAL and HCAL was measured
in a pion beam and found to be approximately

$$\frac{\sigma}{E} = \frac{110\%}{\sqrt{E}} \oplus 9\% \ , \tag{3.3}$$

where the energy E is expressed in GeV [58].
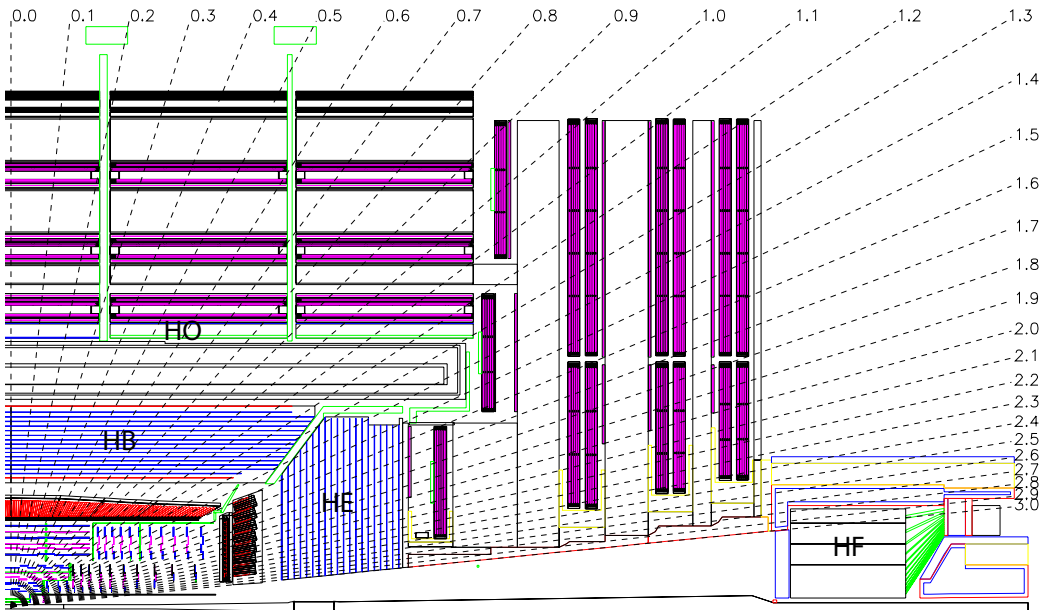
Figure 3.8: Layout of the CMS HCAL [48].

3.2.5 Muon Systems

Since muons can penetrate several meters of material without interacting they are typically not stopped by any of the CMS calorimeters, unlike most other particles. Hence, the gaseous chambers designed to detect muons are placed outside the solenoid. They cover the range $|\eta| < 2.4$ [48]. Muons are about 200 times more massive than electrons, and therefore lose less energy via bremsstrahlung. Typically muons leave hits in the tracker, pass the calorimeters and the solenoid, where they loose a small fraction of their energy, and finally are detected in the muon systems.

A layout of the CMS muon systems is given in Fig. 3.9. In the central region up to $|\eta| < 1.2$, drift tubes (DT) are positioned in four cylindrical layers between the plates of the magnet return yoke which ensures a nearly homogeneous magnetic field. Altogether 250 DTs exist where every DT has an average size of 2 times 2.5 meters consisting of 12 aluminium layers. Each layer is further subdivided into several tiny tubes where every tube has a cross section area of 13×42 mm^2 and contains a stretched wire inside a gaseous volume of argon and carbon dioxide gas. Whenever particles pass by, electrons are knocked off the gas atoms and move towards the positively charged wire. This yields an electric current, which, combined with the information of the drift time between impact of the passing particles and received signal, allows to determine the coordinates of the particles.

In the endcap region ($0.9 < |\eta| < 2.4$), particle rates are higher and the magnetic field is less homogeneous compared to the barrel region. Hence, cathode strip chambers (CSC) are deployed that are characterized by having a fast response, being radiation hard and having a fine segmentation. The wedge-shaped CSCs consist of several arrays of positively charged wires crossed with negatively charged copper strips. Electrons that are knocked off by passing muons move towards the anode wires, whereas positive ions move away from the wires towards the copper cathodes. Due to the perpendicular positioning of strips and wires a determination of the coordinates of the particles is possible.

Resistive plate chambers (RPC) are installed in the range $|\eta| < 1.6$ augmenting both DTs and CSCs. They comprise parallel anode and cathode plates and a gaseous volume in between, where the muon ionization is detected by arrays of metallic strips running parallel to the beam axis. Although RPCs have poorer resolution than DTs and CSCs, their response time is very quick (about 1 ns). Thus, RPCs are used as dedicated and independent muon trigger providing an unambiguous identification of particle bunches. The muon system standalone measurement provides a p_T resolution of $9\% - 11\%$ for

muons with $p_T < 200$ GeV and $|\eta| < 2.4$. The best possible resolution is achieved by combining hits in the tracker with assignments from the muon chambers, as described in Chap. 4. The resulting resolution for muons with 20 GeV $< p_T < 100$ GeV amounts to $1.3\% - 2\%$ and less than 6% in the barrel and the endcap, respectively [59].
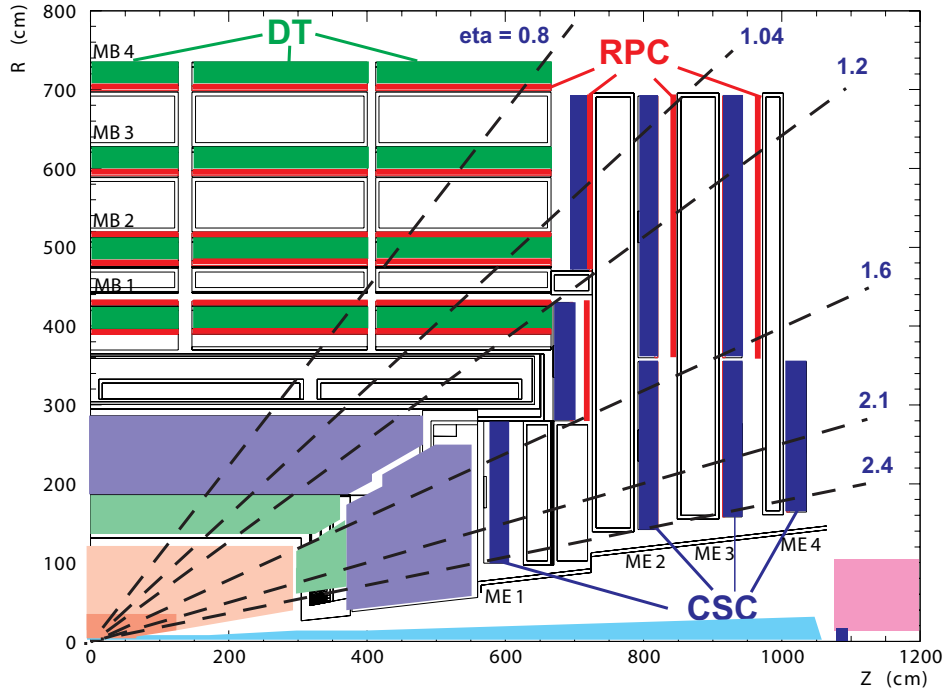

Figure 3.9: Layout of the CMS muon systems [53].

3.2.6 Trigger Systems and Data Acquisition

To date, proton bunches cross inside the CMS detector every 25 ns at a rate of 40 MHz. Since for the *data acquisition* (DAQ) it is neither feasible to read out every event nor to write every event - which is of $\mathcal{O}(MB)$ - to disk, a sophisticated *trigger system* is required. The recorded rate is brought down to $\mathcal{O}(1$ kHz$)$ using a two-tiered trigger system [60]. The *Level-1* (L1) trigger, built from custom hardware, combines information from the calorimeters and muon detectors and reduces the rate to around 100 kHz. The *high-level trigger* (HLT) comprises a farm of processors that run a fast event reconstruction software. The HLT further reduces the event rate to around 1 kHz allowing the remaining events to be written to disk for subsequent offline analysis.

The L1 trigger is designed to ensure a fixed latency of 3.2 μs within which a decision whether to keep or to discard an event must be taken. If the event is accepted the

full detector information is read out. The L1 trigger comprises trigger primitives from ECAL and HCAL and from the muon detectors, respectively, which are processed in several steps before being combined in the global trigger (GT). The architecture of the L1 trigger is sketched in Fig. 3.10. The L1 calorimeter trigger consists of two stages, the regional calorimeter trigger (RCT) and the global calorimeter trigger (GCT). The RCT receives information from over 8000 ECAL and HCAL towers concerning transverse energies and quality flags, and processes this information in parallel. The output e/γ candidates and E_T sums are sent to the GCT which sorts the e/γ candidates, classifies jets as central, forward or tau jets and calculates global quantities. For muons each of the three muon systems participates in L1 muon triggering, where front-end trigger electronics identify track segments from the hit informations which are registered in multiple detector planes. The global muon trigger (GMT) collects information of regional track finders and merges muon candidates which are found by more than one subsystem. Finally, the GT combines informations from the GCT and the GMT and issues a decision whether to keep or to discard the event. The decision is sent to the tracker (TRK), ECAL, HCAL and muon systems (MU) via the trigger, timing and control (TTC) system.
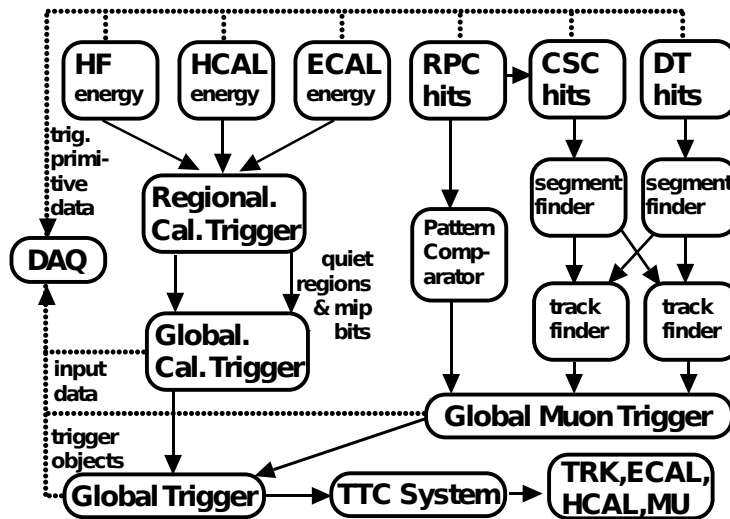
Figure 3.10: Overview of the CMS L1 trigger system [60].

The HLT is the second trigger stage and uses the complete detector information. Compared to the L1 trigger, hit patterns from the tracker are included, and thus a more accurate determination of object momentum and particle identification is possible. In

addition, the algorithms used in the HLT are more sophisticated and are close to the algorithms of the full object reconstruction. This requires a standard processor farm of several thousand CPUs where various trigger algorithms run at the same time. The collection of such trigger algorithms is referred to as *trigger menu*. Upon completion of HLT triggering, accepted events are sent to archival storage. Events are grouped into a set of nearly exclusive streams corresponding to the different *paths* in the trigger menu, e.g. a *SingleMuon* or *SingleElectron* dataset comprises events where at least one muon or electron, respectively, is found fulfilling relevant requirements.

Although the CMS trigger system reduces the amount of data quite significantly, several petabytes of data are produced every year. Combined with the even larger amount of simulated events, the need for dedicated storage and computing resources is obvious. Thus, together with other LHC experiments a global tiered data storage and analysis network has been installed which is known as the *Worldwide LHC Computing Grid* (WLCG) [61]. The *Tier 0* centers, located at CERN and in Budapest, perform a full event reconstruction. All data is then further distributed to at least one of the thirteen *Tier 1* centers which are responsible for large-scale reprocessing and safe-keeping of proportional shares. Finally, *Tier 2* centers produce simulated events and provide analyses specific resources for individual scientists who access the Tier 2 facilities through local computing resources.

Object Reconstruction and Simulation

This chapter describes the simulation and reconstruction of proton-proton collision events at the CMS detector. In order to estimate SM backgrounds and to interpret obtained results, most analyses partially rely on predictions of Monte Carlo (MC) event simulation, as described in Sec. 4.1.

In Sec. 4.2, the reconstruction of collision events with the CMS detector is explained. In order to optimally reconstruct a set of particles, the information from all CMS subdetectors is utilized. Emphasis is given to the algorithms which are relevant to the analyses in this thesis, as well as to common aspects of event selection.

4.1 Event Simulation

The probabilistic nature of particle physics is taken into account by MC methods, where pseudo-random numbers are generated according to probability density functions of physics models [62]. Based on the factorization theorem [63], the generation of simulated events can be split into several steps: the *hard subprocess*, *parton showers*, the *hadronization* of quark and gluon jets, the *underlying event* and the *decay* to long-lived particles. These steps are illustrated in Fig. 4.1. The full generation of simulated events furthermore contains PU interactions and the interactions of stable particles with the detector material.

The hard subprocess results from collisions of constituents of colliding particle beams. The momenta of the colliding constituents are selected by sampling from *parton distribution functions* (PDFs) that define the probability for a constituent (parton: quark or gluon) to carry a certain fraction of the proton momentum. Since the hard subprocess involves a large momentum transfer and both incoming and outgoing particles are asymptotically free, the hard subprocess can be computed using perturbative QCD [65]. The re-
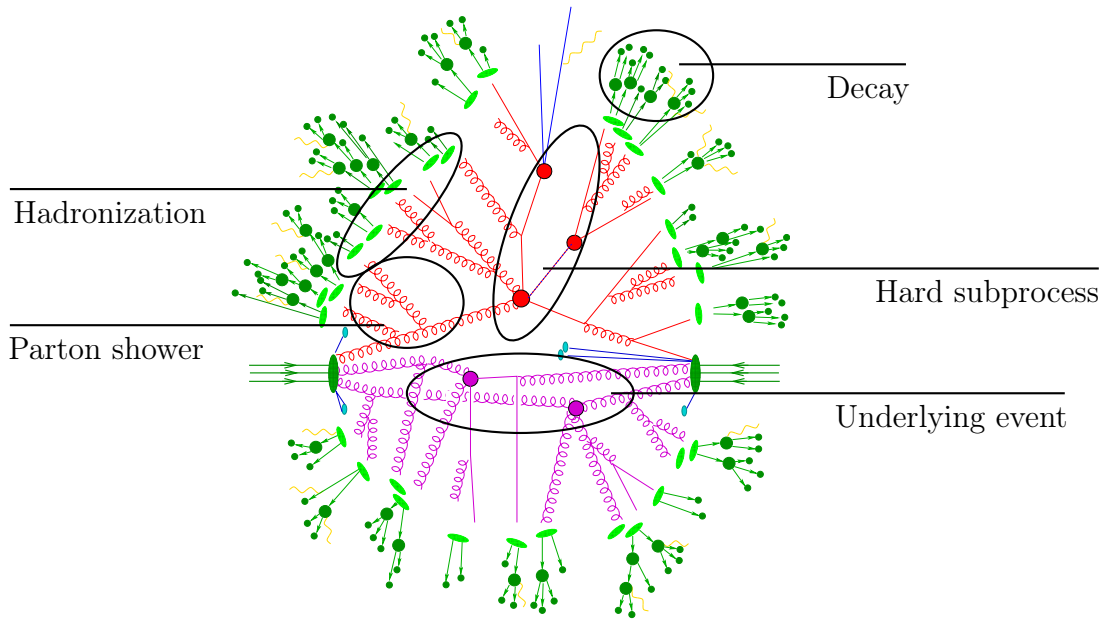
Figure 4.1: Illustration of the components of proton-proton collisions as simulated in MC event generators. Figure (modified) taken from Ref. [64].

quired matrix element calculations are implemented at the lowest order (LO) of perturbation theory in the PYTHIA [66] and HERWIG++ [67] generators, which are able to model the kinematics of a wide range of processes. More dedicated LO generators, such as MADGRAPH [68], are capable of calculating matrix elements with a higher number of final state partons. Furthermore, next-to-leading order (NLO) calculations, which yield a more accurate description with reduced uncertainties, are implemented in some generators, e.g. POWHEG [69–73] and aMC@NLO [74]. MADGRAPH_aMC@NLO [75] unifies MADGRAPH and aMC@NLO generators, where processes are simulated at LO for any user-defined processes and at NLO for QCD corrections to SM processes, respectively.

As the hard subprocess involves large momentum transfers, the engaged partons are accelerated. Just as accelerated electric charges emit photons, the accelerated colored initial and final state partons of the hard subprocess emit QCD radiation in the form of gluons. These gluons can further split into gluon pairs or quark-antiquark pairs. The resulting parton showers can be seen as higher order corrections to the hard subprocess. However, it is not feasible to calculate these corrections exactly. Instead, an approximation scheme associates the dominant contributions with collinear parton splitting or soft gluon emission. The process continues until the individual partons reach a minimum energy threshold that yields non-perturbative interactions [76, 77]. At this

stage hadronization leads to the formation of final state hadrons, and the generators have to rely on models based on current non-perturbative QCD techniques.

In addition to the hard subprocess, extra hadron production occurs which cannot be ascribed to showering from the colored partons. This extra activity, known as underlying event, arises from interactions between other proton constituents not involved in the hard subprocess. The underlying event typically gives rise to soft QCD interactions that have to be incorporated in the generator.

To simulate the decay of unstable particles dedicated packages can be interleaved with the generators of the hard subprocess. For instance, EVTGEN [78] models the decay of hadrons and TAUOLA [79] the decay of τ_h. The last step of the event generation involves the detector simulation. The GEANT4 [80] software package is used to fully simulate the detector geometry, the magnetic field, the interaction of the final state particles with the detector material and the electronic read-out. The detector simulation provides events in the same format as the CMS DAQ system, such that simulated events and data can directly be compared.

4.2 Object Reconstruction

4.2.1 Tracks and Vertices

The trajectories of charged particles are exploited to obtain their momenta and positions. The track reconstruction at CMS is performed with the *combinatorial track finder* (CTF) algorithm [81], which is an extension of the Kalman filter [82] proceeding in four steps:

Firstly, a seed provides initial track candidates by only using 2 or 3 hits each. Secondly, the seed trajectories along the flight path are extrapolated, where the aim is to search for additional hits that can be added to the initial seed. Then, the tracks are fitted to provide the best possible estimate of the parameters of each track. Finally, quality flags are set and tracks failing specified criteria are discarded.

These steps are repeated up to six times, and in each step hits that are found to match with identified tracks are removed.

After the complete set of tracks is reconstructed, the vertices of each interaction can be determined. In order to reconstruct primary vertices, tracks are required to fulfill certain quality criteria, e.g. the number of associated hits in the inner tracking system and the normalized χ^2 of the trajectory fit or the impact parameter with respect to the

nominal beam spot [54]. By means of a *deterministic annealing algorithm* [83], selected tracks are clustered to primary vertex candidates, where each vertex candidate is required to be separated by a minimum distance from the closest neighbor. For vertices containing at least two tracks, the *adaptive vertex fitter* [84] determines the best fit of the vertex position as well as the fit quality.

In the following analyses (Chaps. 7 - 8) the vertex candidate with the largest summed squared p_{T} of tracks associated with the vertex is chosen as the vertex corresponding to the hard subprocess. All other vertices are considered to come from additional soft scattering vertices at collision time (PU).

4.2.2 Muon Reconstruction

Since muons are typically the only particles traversing the muon chambers, they can be identified with high accuracy [59]. Additionally, due to their electric charge muons leave a track in the tracking system. Reconstruction starts by independently reconstructing tracks in the muon chambers (*standalone muon tracks*) and tracks in the inner tracking system (*tracker muon tracks*) [53]. Based on the standalone muon and tracker muon tracks, a combined track collection (*global muon tracks*) is constructed. Whenever a link is established, the track parameters are refitted taking the combination of hits in the inner and outer detectors into account. Quality criteria are applied on the multiplicity of hits, on the number of matched segments and on the quality of the global muon track fit, which is quantified through a χ^2 criterion.

In order to distinguish muons produced in decays of electroweak gauge or Higgs bosons from those produced within jets, an additional isolation criterion is applied. The *relative isolation* I_{rel} is defined within an isolation cone of $\Delta R = \sqrt{(\Delta\eta)^2 + (\Delta\phi)^2}$:

$$I_{\mathrm{rel}}^{\mu} = \frac{I^{\mu}}{p_{\mathrm{T}}^{\mu}} = \frac{\overset{\text{charged, non-PU}}{\sum} p_{\mathrm{T}} + \max\left(0, E_{\mathrm{T}}^{\mathrm{neutral}} + E_{\mathrm{T}}^{\mathrm{photon}} - \Delta\beta \overset{\text{charged, PU}}{\sum} p_{\mathrm{T}}\right)}{p_{\mathrm{T}}^{\mu}}, \quad (4.1)$$

where $p_{\mathrm{T}}^{\mathrm{charged}}$ corresponds to the p_{T} of all charged hadronic candidates, $E_{\mathrm{T}}^{\mathrm{neutral}}$ and $E_{\mathrm{T}}^{\mathrm{photon}}$ to the transverse energy of all neutral hadron and photon candidates, respectively. An estimate of the neutral PU contribution is made based on the charged PU contribution $\sum E_{\mathrm{T}}(\mathrm{PU})$, multiplied by $\Delta\beta$, which is a parameter to estimate the ratio of neutral to charged components of the hadronization and is typically set to 0.5. The isolation cone ΔR usually has a size between 0.3 and 0.5.

4.2.3 Electron Reconstruction

Electrons are characterized by a charged track and by producing showers and getting stopped in the ECAL [56]. Therefore, the associated energy deposits in the ECAL cells are exploited to reconstruct energy clusters, which are related to tracks in the silicon tracker. The energy loss due to bremsstrahlung is accounted for by summing up energy deposits in the ECAL emitted tangent to the track. Dedicated *supercluster* algorithms are applied for combining the ECAL clusters from both the initial electron and the bremsstrahlung photons. Additional requirements are employed to remove electrons that originate from photon conversions. To distinguish electrons from hadrons that mimic electron signatures, a multivariate (MVA) approach based on boosted decision trees (BDTs) is used. The BDTs are trained on simulated events, which contain either genuine or false electrons and are based on observables quantifying the quality of the electron track, the compactness of electron clusters and the matching of the track momentum and direction with the sum and position of energy deposits in the ECAL. The relative isolation I_{rel} is defined as for the muons, see Eq. (4.1).

4.2.4 The Particle-Flow algorithm

The PF algorithm [57] was employed for the first time by the ALEPH experiment at LEP [85] and is now strongly affecting the design of possible future detectors for e^+e^- colliders. However, prior to the LHC area the intricacy of possible final states arising from proton-proton collisions was considered to curb the advantages of PF approaches. The identification of particles from the hard subprocess was expected to be seriously downgraded due to boosts at higher center-of-mass energies and high particle densities caused by hadronic showers. Nevertheless, it turned out the CMS subdetectors are sufficiently segmented to provide good separation for individual particles, and hence a global event description which identifies all particles becomes possible.

The current PF procedure applied at CMS is the following: Firstly, charged tracks in the tracker and in the muon chambers are reconstructed and energy deposits in the calorimeter cells are clustered. Then, neighboring cells are aggregated into the clusters, and charged tracks and energy clusters are linked to blocks and potential bremsstrahlung photons are added to the tracks. The particle identification proceeds as follows:

- If a global muon is compatible with a track element concerning position and momentum, the global muon is designated as PF muon and corresponding en-

ergy deposits in the calorimeters are subtracted from the relevant clusters. Electrons are designated as PF electrons and corresponding ECAL clusters are subtracted if the fitted tracks and ECAL clusters are compatible with standalone candidate electrons that are obtained by electron reconstruction as described in Sec. 4.2.3. The compatibility is assessed by refitting the tracks and applying a multivariate discriminator against charged hadrons.

- The remaining tracks are assigned to charged hadrons where the momentum is obtained from the fit. If the cluster energies exceed the track momenta, this is interpreted as the overlap of neutral particles. However, if the energy excess is larger than the total ECAL energy linked to tracks, it is assigned to a PF photon.

- Finally, all remaining clusters, which are not linked to any tracks, are assigned to photons and neutral hadrons, respectively.

4.2.5 Tau Reconstruction

Hadronic decays of tau leptons are reconstructed using the *hadrons+strips* (HPS) algorithm [86–88], which distinguishes individual τ_h decay modes. Figure 4.2 illustrates the HPS algorithm for a τ_h decay into one charged particle and two neutral hadrons. The underlying principle of the HPS algorithm is to separately reconstruct charged hadrons and neutral pions, both constituents of jets, and to subsequently combine this information. The neutral pions are reconstructed by clustering the PF photons and PF electron pairs within rectangular strips, which are narrow in the η- but wide in the ϕ-direction. This accounts for the broadening of energy deposits in the ECAL when one of the photons produced in $\pi^0 \to \gamma\gamma$ decays converts within the tracking detector. Electrons are taken into account since the probability of photon conversion into e^+e^- pairs is sizable. Strips that contain one or more electron or photon constituents and pass an additional p_T cut on the sum of electrons and photons are kept for further processing.

Based on the observed number of strips and charged particles, the τ_h candidate is considered to be one of the following decay modes:

- A single charged particle without any strips: $h^\pm$.

- A combination of a single charged particle and one strip: $h^\pm\pi^0$.

- A combination of a single charged particle and two strips: $h^\pm\pi^0\pi^0$.

- A combination of three charged particles: $h^\pm h^\mp h^\pm$.

During LHC Run-1, strips with a fixed size of 0.05×0.2 in the η-ϕ plane were deployed, which is superseded by an improved version of strip reconstruction for data taking for LHC Run-2. In this improved version, the strip size is variable as a function of the highest-p_T photon or electron (Fig. 4.3), which accounts for electromagnetic energy leakage of the τ_h decay. For instance, photons and electrons may go outside the fixed window size after energy losses due to multiple conversions or bremsstrahlung. Further details on HPS reconstruction are given in Ref. [88].
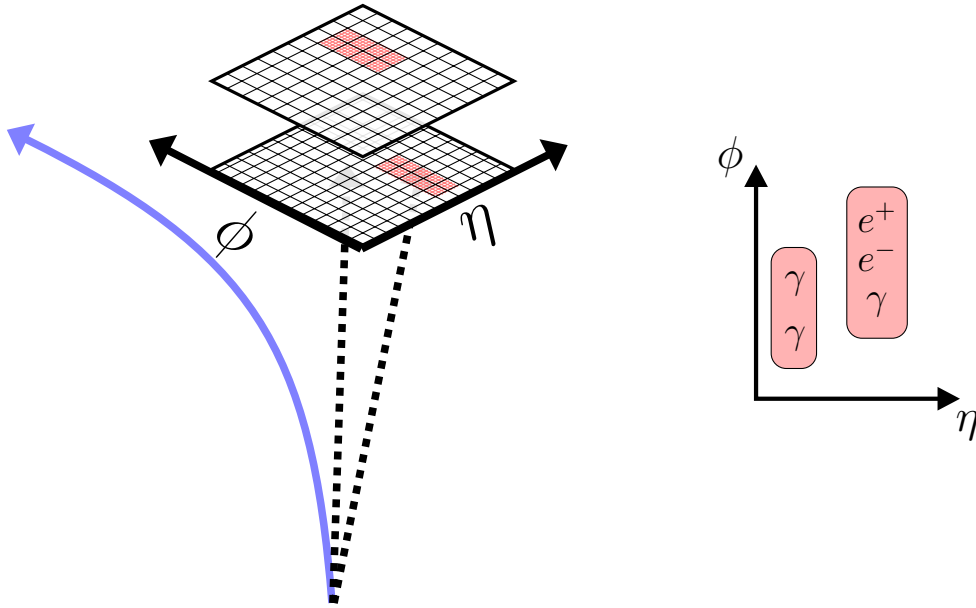
Figure 4.2: Illustration of the HPS algorithm for a τ_h decay into one charged particle and two neutral hadrons. The neutral hadrons are reconstructed by clustering the PF photons and the PF electron pairs.

The main handles to distinguish τ_h decays from quark or gluon jets and electrons are BDT-based τ_h identification (ID) discriminants [88], whereas cutoff-based discriminants are used in order to separate τ_h from muons [86].

For the large background of quark and gluon jets, isolation requirements yield a significant discrimination power. The isolation is computed by summing up the scalar p_T values of photons and charged particles originating from the PV. An isolation cone size of $\Delta R = 0.5$ is used, which is centered around the τ_h direction. The BDT input variables are complemented by the scalar p_T sum of charged particles, which do not originate from the PV, by variables that provide sensitivity to the lifetime of the τ_h and by the reconstructed τ_h decay modes. Furthermore, the *transverse impact parameter*, defined as the distance of the closest approach to the beam-line of the highest p_T track

(a)   (b)
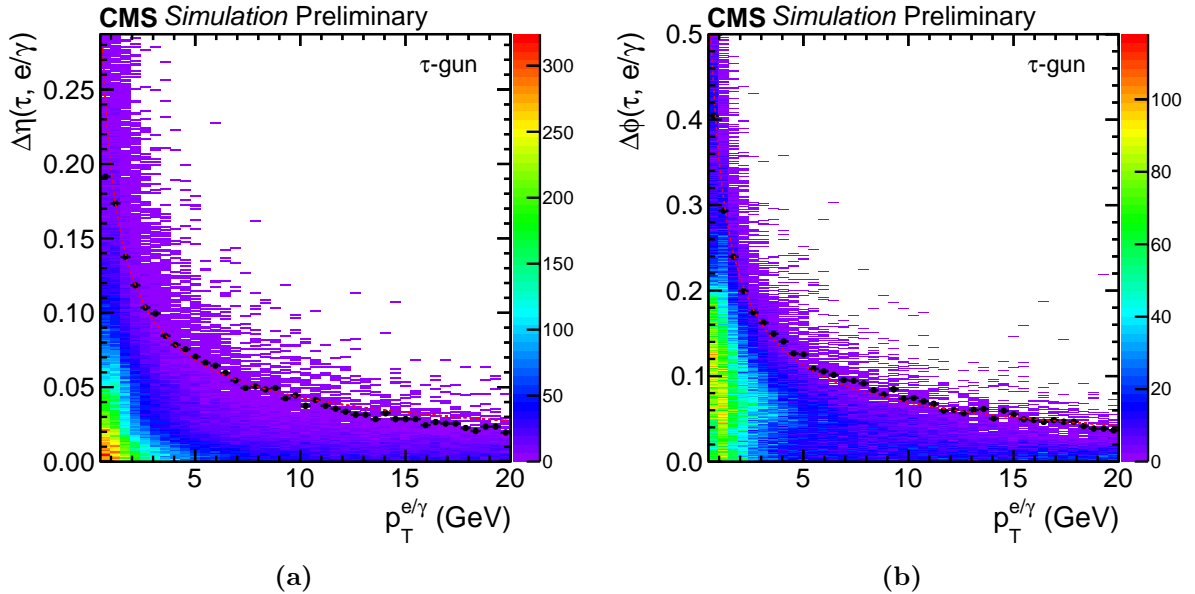
Figure 4.3: Distance in η (a) and ϕ (b) between τ_h and the highest-p_T photon or electron [88]. Decay products of large-p_T τ_h candidates tend to be boosted in the τ_h flight direction motivating the deployment of a p_T-dependent strip size, in order to reduce background contributions for high-energetic τ_h decays.

of the τ_h, is used for any decay mode. For reconstructed 3-prong τ_h decays a fit of the three tracks to a common SVs is attempted, and the distance to the PV is added to the BDT input variables. The BDTs are trained on simulation samples of genuine τ_h decays and jets. Requirements on the output correspond to different *working points* (WPs) targeting minimal, moderate and tight constraints on the ID efficiency and the misidentification probability of the reconstructed τ_h candidate. The six available WPs are `VeryLoose`, `Loose`, `Medium`, `Tight`, `VeryTight` and `VeryVeryTight`. Figure 4.4 illustrates the ID efficiency and the misidentification probability as a function of the p_T of the genuine τ_h and the jet, respectively.

In order to separate τ_h candidates from electrons a different BDT-based discrimination is performed [86]. Isolated electrons have a high probability to be misidentified as τ_h decays in the $h^{\pm}$ decay mode. In addition, the bremsstrahlung photons that are emitted by electrons crossing the tracker often mimic π^0s in the reconstruction. The chosen BDT input variables comprise observables that quantify the matching between the sum of energy depositions in the ECAL and the momentum of the leading track of the τ_h candidate, and observables that distinguish electromagnetic and hadronic showers.

The cutoff-based discriminator against muons deploys a matching of the leading track of the τ_h candidate with energy deposits in the ECAL and HCAL, as well as with track segments in the muon detectors.
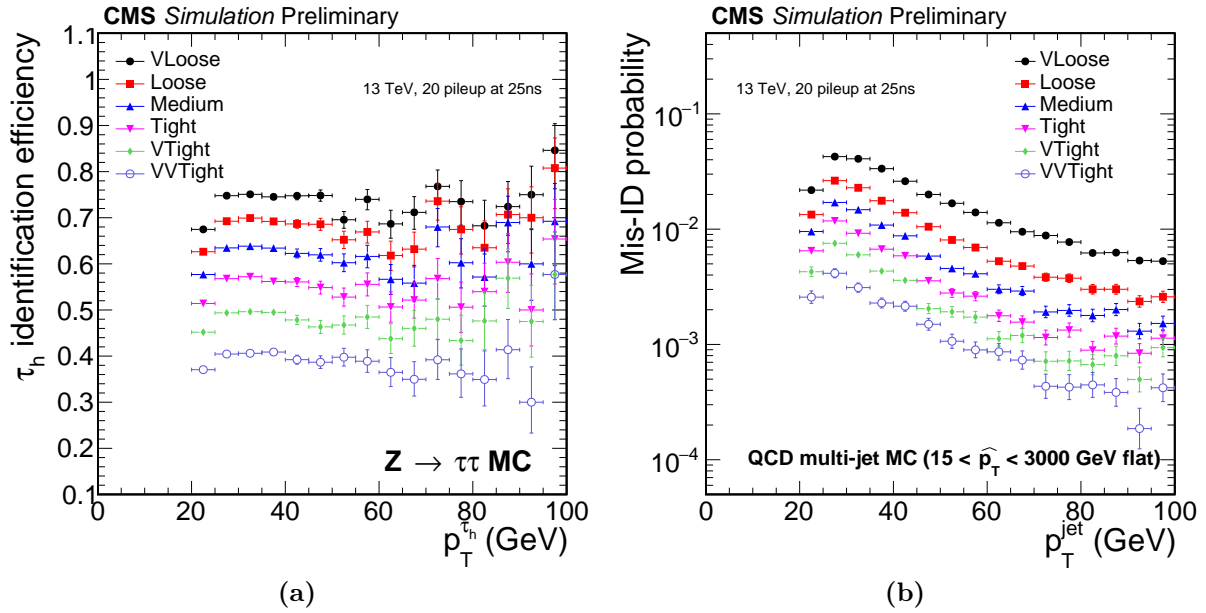
Figure 4.4: ID efficiency (a) and misidentification probability (b) for six different WPs of τ_h candidates as a function of p_T [88].

4.2.6 Jet Reconstruction

Quarks and gluons are produced in abundance at the LHC. However, due to confinement in the strong interaction, they are not observed directly since they fragment and hadronize almost immediately, leading to a relatively collimated high-multiplicity spray of particles called "jet". The properties of such a jet are related to the properties of the partons that initiate it. In the analyses described in this thesis, jets are reconstructed from PF candidates using the anti-k_T jet algorithm [89]. Clustering algorithms commonly define a distance d_{ij} between every pair of objects (i, j) and a distance between each object and the beamline d_{iB}:

$$d_{ij} = \min(p_{T_i}^{2p}, p_{T_j}^{2p}) \cdot \frac{\Delta R_{ij}^2}{R^2} \tag{4.2}$$

$$d_{iB} = p_{T_i}^{2p}, \tag{4.3}$$

where ΔR is the separation distance in the η-ϕ plane and R is a fixed distance parameter, which is set to $R = 0.4$ in the following analyses; p defines the behavior of the clustering algorithm and takes the value -1 for the anti-k_T algorithm. The algorithm proceeds by identifying the smallest of the d_{ij} and d_{iB} parameters. If the smallest parameter is a d_{ij} parameter, the objects i and j are combined into a single object and the process repeats. If it is a d_{iB} parameter instead, the object with label i is assumed

to be a final state jet, and thus removed from the list. The advantage of the anti-k_T algorithm is that it tends to cluster jets around the highest p_T particle, which leads to cone-like jet areas in the η-ϕ plane.

In order to take PU interactions in the jet reconstruction into account, charged hadrons that are associated with vertices other than the PV are removed from the list of PF candidates [90]. Reconstructed jets are required to pass a set of minimal identification criteria that aim to reject jets arising from calorimeter noise [90]. Furthermore, jets are required not to overlap with identified electrons, muons or τ_h candidates within a range of $\Delta R = 0.5$ in the described analyses.

Due to a number of experimental facts, e.g. non-linear calorimeter response, detector noise or overlap with non-instrumented regions, the energy of reconstructed jets may systematically differ from the energy of the underlying particle jet. To account for these effects, dedicated *jet energy correction* factors are derived, which are sequentially applied to the four-momenta of reconstructed jets in data and simulated events [91]. In doing so, the jets are corrected for the p_T and η dependencies of the jet energy response as well as for energy contributions from PU interactions.

4.2.6.1 Identification of b Jets

The identification of jet flavors is rather challenging at detector-level since the signatures of jets are very similar. Jets originating from up, down or strange quarks cannot be distinguished from each other, whereas they can be discriminated to some extent from gluon jets if variables are exploited that are sensitive to jet shape and jet substructure [90].

On the contrast, jets that originate from the hadronization of bottom quarks can be distinguished from other-flavor jets due to their large masses of about 5 GeV and their long lifetimes ($\tau \approx 1.5$ ps). B hadrons typically travel a distance set by the scale $L = c\tau \approx 450$ μm before decaying, and thus any charged decay products produce tracks with a measurable impact parameter d_0 with respect to the PV (Fig. 4.5).

The *Combined Secondary Vertex* (CSV) algorithm [92] combines information about displaced tracks, the long lifetime of B hadrons, the high particle multiplicity and the informations of SVs associated to the jet using MVA techniques. The CSV algorithm was further optimized during Run-2 and the current version, which is also used in the following analyses, is referred to as CSVv2 [93].

One should also mention that for some extent a separation of jets originating from charm quarks is also possible since the mass and the lifetime of the charm quark differ

from those of up, down and strange quarks. However, the separation power is lower than for b jets.
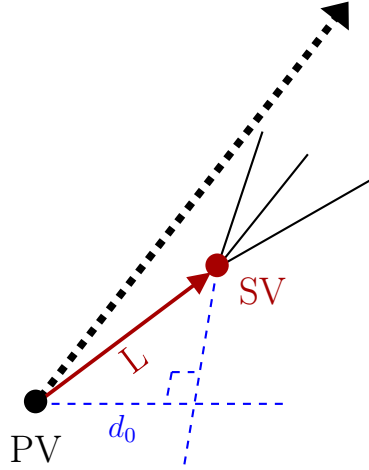
Figure 4.5: Illustration of the impact parameter d_0. The red line marks the flight distance of the B meson and the dashed blue line indicates the impact parameter of the SV with respect to the PV. The dashed black line sketches an additional light jet originating from the PV.

4.2.7 Missing Transverse Energy

The only SM particles which neither decay nor interact within any subdetector are neutrinos. Thus, their presence can be inferred as a momentum imbalance in the transverse plane assuming all detected particles are evaluated. The negative vectorial sum of the $\vec{p}_\mathrm{T}$ of all visible particles in an event is referred to as *missing transverse momentum* $\vec{E}_\mathrm{T}^\mathrm{miss}$, while the scalar $E_\mathrm{T}^\mathrm{miss}$ is quantified as *missing transverse energy*.

The $\vec{E}_\mathrm{T}^\mathrm{miss}$ reconstructed using a PF technique (PF $\vec{E}_\mathrm{T}^\mathrm{miss}$) is used in the majority of CMS analyses [94]. The PF $\vec{E}_\mathrm{T}^\mathrm{miss}$ performance can be degraded by a number of factors, e.g. minimum energy thresholds in the calorimeter read-out, non-instrumented detector regions, reconstruction inefficiencies or PU interactions. Dedicated techniques have hence been developed to correct both the response and the resolution of the PF $\vec{E}_\mathrm{T}^\mathrm{miss}$ [94]. The PF $\vec{E}_\mathrm{T}^\mathrm{miss}$ is used in the analyses described in Chap. 8.

An alternative algorithm is the MVA $\vec{E}_\mathrm{T}^\mathrm{miss}$, which is based on a set of MVA regressions and provides improved $\vec{E}_\mathrm{T}$ measurement in the presence of multiple PU interactions. It is computed as a correction to the hadronic recoil $\vec{u}_\mathrm{T}$, which is defined as the vectorial sum of all transverse momenta except that of the vector boson. Firstly, a correction to $\vec{u}_\mathrm{T}$ is derived by training a BDT to match $\vec{u}_\mathrm{T}$ in simulated events. Then, a second BDT is trained to predict $\vec{u}_\mathrm{T}$ on a dataset where the direction of $\vec{u}_\mathrm{T}$ has already been corrected. The corrected $\vec{u}_\mathrm{T}$ is then added to the vector boson momentum

$\vec{q}_{\mathrm{T}}$ in the transverse plane. Momentum conservation in the transverse plane requires $\vec{u}_{\mathrm{T}} + \vec{q}_{\mathrm{T}} + \vec{E}_{\mathrm{T}}^{\mathrm{miss}} = 0$. The kinematic definitions are summarized in Fig. 4.6. The MVA $\vec{E}_{\mathrm{T}}^{\mathrm{miss}}$ is used in the analysis described in Chap. 7.
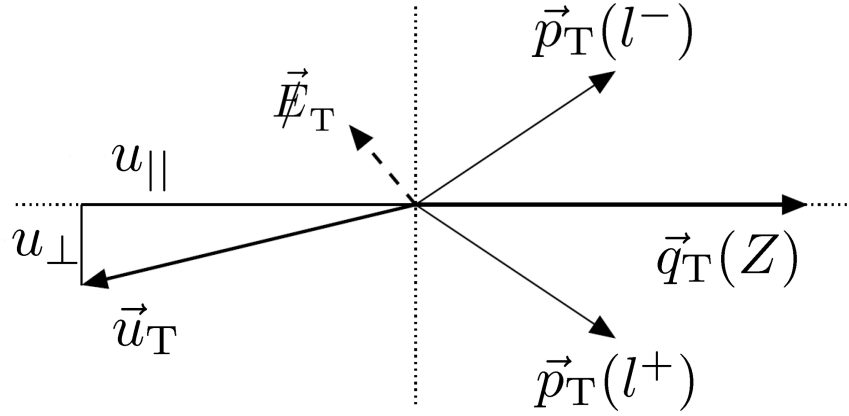
Figure 4.6: Illustration of Z $\rightarrow$ ll event kinematics in the transverse plane [94]. The notation $\vec{\not{E}}_{\mathrm{T}}$ is equivalent to $\vec{E}_{\mathrm{T}}^{\mathrm{miss}}$.

Phase-II Upgrade of the CMS Detector

This chapter gives an overview of the LHC upgrade plans with special emphasis on the HL-LHC area and the required updates on the CMS detector. Within the scope of the CMS upgrade plans, τ_h ID studies are discussed. The presented physics results are based on the Refs. [95, 96].

5.1 LHC and CMS Upgrade Plans
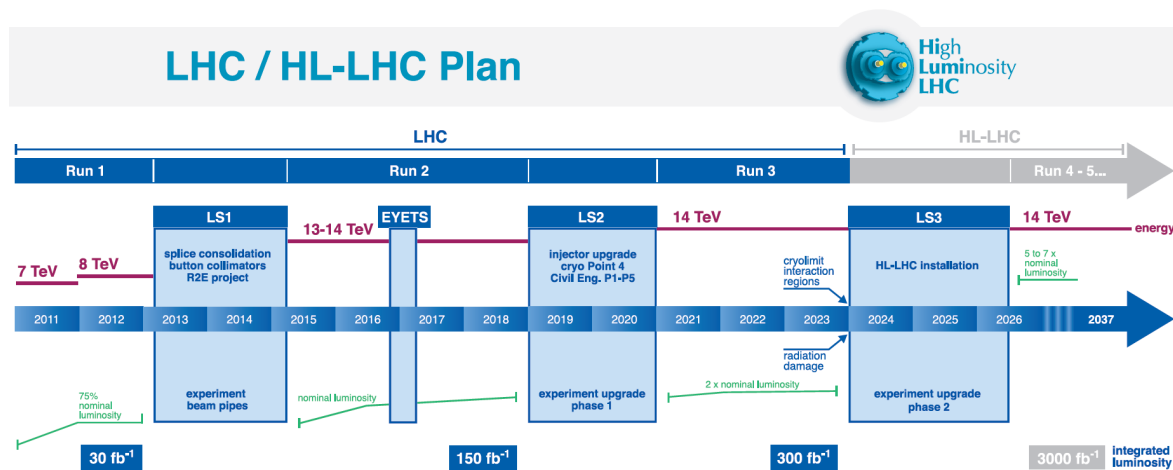
Figure 5.1: Illustration of the LHC upgrade plans [96].

A sketch of the LHC upgrade plans is shown in Fig. 5.1. The LHC is designed to operate at an instantaneous luminosity of 10^{34} cm^{-2}s^{-1}. Already in Run-1, a peak luminosity of 7.7×10^{33} cm^{-2}s^{-1} was achieved [52], which is 77% of the design luminosity. During the first long shutdown, LS1, which started in 2013 and ended in the beginning of 2015, the bunch spacing was reduced from 50 ns to 25 ns. As a result, in 2016, the design luminosity was surpassed for the first time achieving a value of 1.53×10^{34} cm^{-2}s^{-1} [52]. In the

second long shutdown, LS2, further improvements on the injector chain are planned, and an integrated luminosity of over 300 fb^{-1} is foreseen to be provided by the LHC by the end of 2023. To maintain its performance the CMS detector is undergoing a series of staged upgrades in the period from LS1 to the end of LS2. The so-called *CMS Phase-I Upgrade*, documented in Ref. [97], comprises a new L1 trigger installation in 2015, a new HF electronics installation during the winter shutdown 2015-2016, an installation of a new pixel detector during the winter shutdown 2016-2017 and a new HCAL barrel and endcap installation in LS2.

After Run-3, the quadrupoles that focus the beams at the ATLAS and CMS experiments are expected to have strongly suffered from radiation exposure, and thus are close to the end of their expected lifetimes. In the third long shutdown, LS3, they are intended to be replaced with quadrupole triplets that lead to narrower ("squeezed") beams, and additional crab cavities will be added to further optimize the bunch overlap in the detector regions. These changes are intended to yield a significant increase of the LHC luminosity. In the following HL-LHC era, also referred to as *Phase-II*, the proposed operation scenario is to level the instantaneous luminosity at $5 \times 10^{34} \mathrm{cm}^{-2} \mathrm{s}^{-1}$ from a potential peak value of $2 \times 10^{35} \mathrm{cm}^{-2} \mathrm{s}^{-1}$. The LHC will potentially deliver 250 fb^{-1} per year over a 10 year period. The strong increase in instantaneous luminosity goes hand in hand with a substantial rise of PU interactions.

5.2 CMS Phase-II Detector Upgrade

At a nominal operation scenario of a leveled luminosity of $5 \times 10^{34} \mathrm{cm}^{-2} \mathrm{s}^{-1}$, a mean value of 140 PU interactions is expected. This leads to possible radiation damage as well as growing demands on the different subdetectors and computing modules. To counteract the performance degradation of the detector, the CMS Phase-II upgrade program involves detailed studies of the conceptual design and the expected performance of different upgrade scenarios. Performance studies, which are based on a combination of detailed measurements and use as input Run-1 data and the exposure of test components to expected radiation levels, have shown that the key components for the HL-LHC detector upgrade are the replacement of the tracker, the calorimeter and the muon endcaps. The upgrade plans are supplemented by DAQ, software and computing improvements as well as updated beam radiation protection and luminosity measurements. Next a short overview of the upgrade plans of the tracker and calorimeter endcaps is given since their upgrades mainly influence the following studies. More information can be found in Ref. [95].

Tracker

By reaching LS3, the tracker will already have suffered severe radiation damage, and hence must be completely replaced in order to maintain proper track reconstruction performance. To handle the much higher number of PU interactions, the granularity of both the pixel system and the outer tracker will be significantly increased.

For the pixel system smaller pixels and thinner sensors will be applied. The improved impact parameter resolution and two-track separation will yield enhanced b-tagging performance as well as improved τ_h decay and track reconstruction. Furthermore, 10 additional pixels discs in the forward region will help to extend the η coverage, to support the larger η coverage of the calorimeter.

In the outer tracker increased granularity will be achieved by shortening the length of the silicon sensor strips. Several additional design improvements to achieve a much lighter Outer Tracker are planned, which in return will provide improved p_T resolution and a lower rate of photon conversions.

Calorimeter Endcaps

The replacement calorimeter of the ECAL and HCAL endcaps is called *High Granularity Calorimeter* (HGCAL), designed to cover the endcap and forward regions ($|\eta| > 1.479$). The replacement of the current endcap and forward detectors will become inevitable due to their high radiation exposure. The HGCAL consisting of tungsten and copper plates interleaved with silicon sensores and scintillators will feature a combined electromagnetic and hadronic section. The HGCAL comprises three parts: the *endcap electromagnetic* (EE), the *front hadronic* (FH) and the *backing hadronic* (BH) calorimeters, which together cover roughly ten interaction lengths. The EE and the FH calorimeters are foreseen to operate at $-30°C$ using CO_2 to mitigate silicon radiation damage, and for the BH calorimeter lower operation temperatures are considered as well. A schematic view of the HGCAL is shown in Fig. 5.2.

5.3 Detector Performance Studies

In order to evaluate the performances of the proposed detector upgrades, different scenarios have been simulated using GEANT4:

- Phase-I detector conditions without radiation aging at an average rate of 50 PU interactions, which corresponds to an instantaneous luminosity of 10^{34} cm^{-2}s^{-1}. The scenario is referred to as "PHASE I 50 PU".
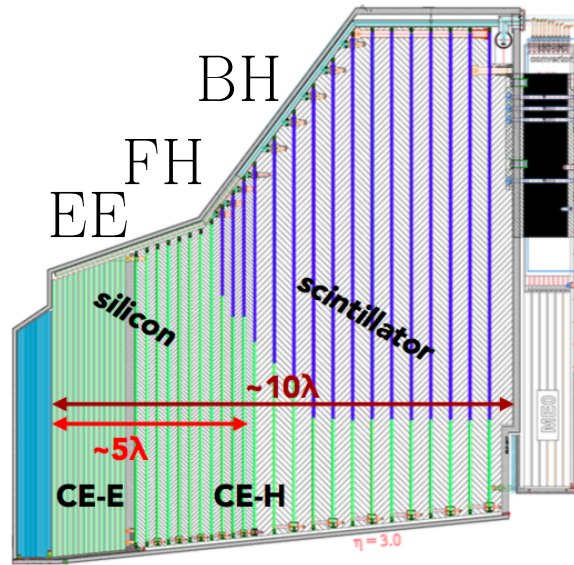
Figure 5.2: Schematic view of the HGCAL design. The electronic section (EE) is referred to as CE-E and the hadronic section (FH and BH) as CE-H. Figure taken from Ref. [98].

- Phase-I detector conditions with modelling of radiation damage effects at an integrated luminosity of 1000 fb^{-1} at an average of 140 PU interactions, which corresponds to an instantaneous luminosity of 5×10^{34} cm^{-2}s^{-1}. The scenario is referred to as "PHASE I Aging 140 PU".

- Phase-II detector conditions at an average of 140 PU interactions (5×10^{34} cm^{-2}s^{-1}). The performance of the new sub-detectors is assumed not to degrade with radiation, whereas an aging of 1000 fb^{-1} is included for the barrel calorimeters, since their active elements are not planned to be replaced. The scenario is referred to as "PHASE II 140 PU".

5.3.1 Tau Performance Studies

The presented tau performance studies are based on the reconstruction algorithm described in Sec. 4.2.5. However, this algorithm has not yet been optimized to HL-LHC running conditions, and thus presented results can be seen as conservative lower estimates of the tau performance. The two main performance aspects are the *tau isolation* and the *electron rejection*, which are deployed to reject the background of quark and gluon jets and electrons, respectively, which are falsely identified as τ_h. Since muon identification for τ_h decays has an efficiency of more than 99% and a misidentification rate of about 10^{-4} by "normal" techniques, extra τ_h anti-muon discrimination has been neglected for these upgrade studies.

5.3.1.1 Tau Isolation Performance

The products of τ_h decays are typically more isolated than τ_h candidates that are misreconstructed from quark or gluon jets. Therefore, the sum of momenta around the isolation cone of the τ_h candidate is an important handle to decrease the τ_h misidentification rate. The studies focus on the case where only charged particles are used for isolation p_T sum calculations. This approach is justified since previous CMS measurements have established that the charged isolation is the dominant source for discrimination against jets and that it is relatively PU robust [87]. The estimation of contributions from neutral hadrons is more difficult and will be subject of future studies.

The τ_h candidates considered for the isolation calculations are required to pass the following criteria:

- generated visible (i.e. without neutrinos) $p_T > 20$ GeV,

- generated visible $|\eta| < 2.3$.

In order to be considered as reconstructed τ_h the candidates must fulfill:

- match to a generated τ_h within $\Delta R < 0.5$,

- reconstructed $p_T > 20$ GeV,

- reconstructed $|\eta| < 2.3$.

Additionally, the reconstructed τ_h candidate is tested to pass the isolation requirement. This translates to the absolute p_T sum of all tracks within a cone of $\Delta R < 0.5$ around the reconstructed τ_h direction to be smaller than a given value. It is to note that the τ_h isolation efficiency decreases with the number of PU interactions since a larger number of PU yields more passing tracks, and thus a larger isolation sum. Therefore, the maximally allowed p_T sum was increased to 3.5 GeV and 4 GeV in the "PHASE II 140 PU" and "PHASE I Aging 140 PU" scenario, respectively, to yield similar efficiencies in all three scenarios. The τ_h isolation efficiencies for the three different scenarios are shown in Fig. 5.3.

The jet misidentification rate complements the isolation performance studies. It quantifies the probability that a true jet will be reconstructed as τ_h candidate. To be considered for the misidentification rate calculation, a jet has to fulfill the following criteria:
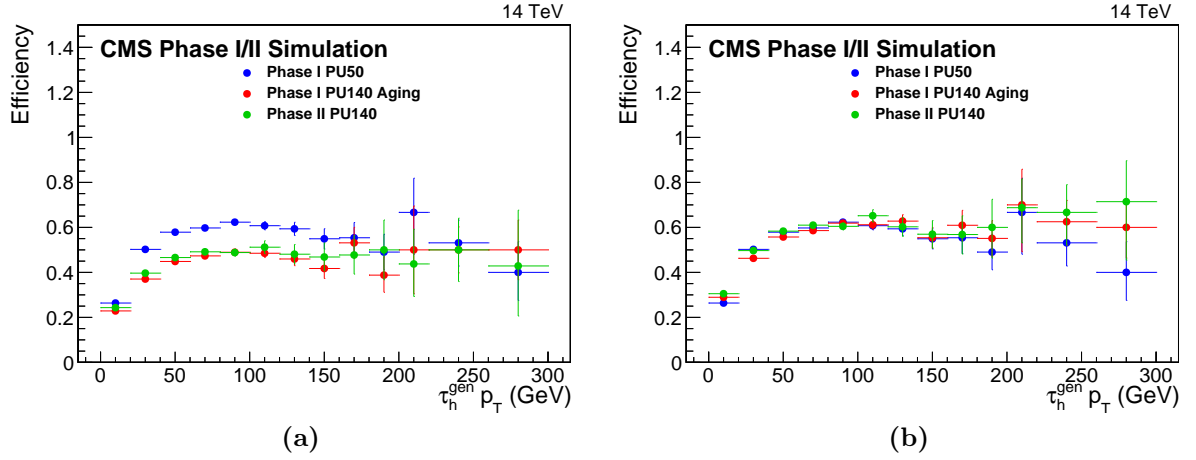
Figure 5.3: τ_h isolation efficiency using the same isolation criterion (a) and for a tuned isolation selection to yield similar signal efficiencies in all three scenarios (b) [95].

- generated jet with $p_T > 20$ GeV and $|\eta| < 2.3$,

- match to a reconstructed jet within $\Delta R < 0.5$,

- distance along z-axis between primary vertex and the jet constituents is smaller than 0.2 cm.

Among those, a jet is counted as misidentified τ_h candidate if

- the generated jet is matched to a reconstructed τ_h candidate with $p_T > 20$ GeV and $|\eta| < 2.3$,

- the τ_h candidate passes the charged isolation selection.

The probability for a jet to be reconstructed as τ_h candidate and to pass the charged isolation requirement is shown in Fig. 5.4.

The τ_h ID efficiency for the "PHASE 1 50 PU" scenario is comparable to the Run-1 and Run-2 performances for similar working points (50-60%) [87,88]. The increase of jets passing the ID requirements in the "PHASE I Aging 140 PU" scenario can be partly ascribed to the looser isolation requirements, but still shows 2-3 times higher misidentification rates if the τ_h isolation criterion is kept the same. If the τ_h isolation criterion is changed in order to keep the ID efficiency the same for all three scenarios, the misidentification rate shows significantly higher rates for the "PHASE I Aging 140

PU", whereas in the "PHASE II 140 PU" it would partly recover the misidentification rates of the "PHASE I 50 PU" scenario. The reason for the misidentification rate to increase in the aging scenario is twofold. On the one hand the tracking efficiency is decreased due to the radiation damage, and on the other hand the decrease is caused by the larger number of PU interactions, as discussed above. The Phase-II tracker upgrade recovers a part of the lost tracker efficiency, and thus the fractions of misidentified jets will become closer to the "PHASE 1 50 PU" scenario.

Figure 5.4: Jet misidentification rate using the same isolation criterion (a) and for a tuned isolation selection to yield similar signal efficiencies in all three scenarios (b) [95].

5.3.1.2 Electron Rejection Performance

The rejection of electrons is an important part of the tau ID performance, as described in Sec. 4.2.5. Due to different running conditions and different detector scenarios the BDT-based discrimination is retrained in all three scenarios. In particular, in the "PHASE II 140 PU" scenario the Phase-II calorimeter strongly alters the important BDT input variables, e.g. ECAL and HCAL energy deposits. In all cases the discriminator is trained separately for the barrel and the endcap regions due to the different instrumentation. For the training of the endcap region in the "PHASE II 140 PU" scenario a new set of variables is exploited since the initial set of variables relies on a separate ECAL and HCAL endcap calorimeter. Typical HGCAL variables with a high discrimination power are e.g. the shower width along $|\eta|$ or the fraction of the energy loss in the hadronic part of the HGCAL.

In Fig. 5.5a, the performance of the BDT discriminator for all three scenarios combining barrel and endcap region is shown, Fig. 5.5b compares the performance for the

barrel region, only. The performance is severely degraded for the "PHASE I aged 140 PU" scenario, whereas the "PHASE II 140 PU" scenario can almost regain the performance of the "PHASE 1 50 PU" scenario. Figures 5.5c-d show the fraction of generated τ_h decays that pass the electron rejection discriminator for a chosen working point, as well as the fraction of electrons that are reconstructed and identified as τ_h decays. The performance is degraded in the "PHASE I aged 140 PU" scenario, whereas the Phase-II detector strongly decreases the fraction of misidentified electrons. This indicates the potential of the Phase-II detector upgrade although more studies are needed to fully adapt electron rejection to HL-LHC conditions.
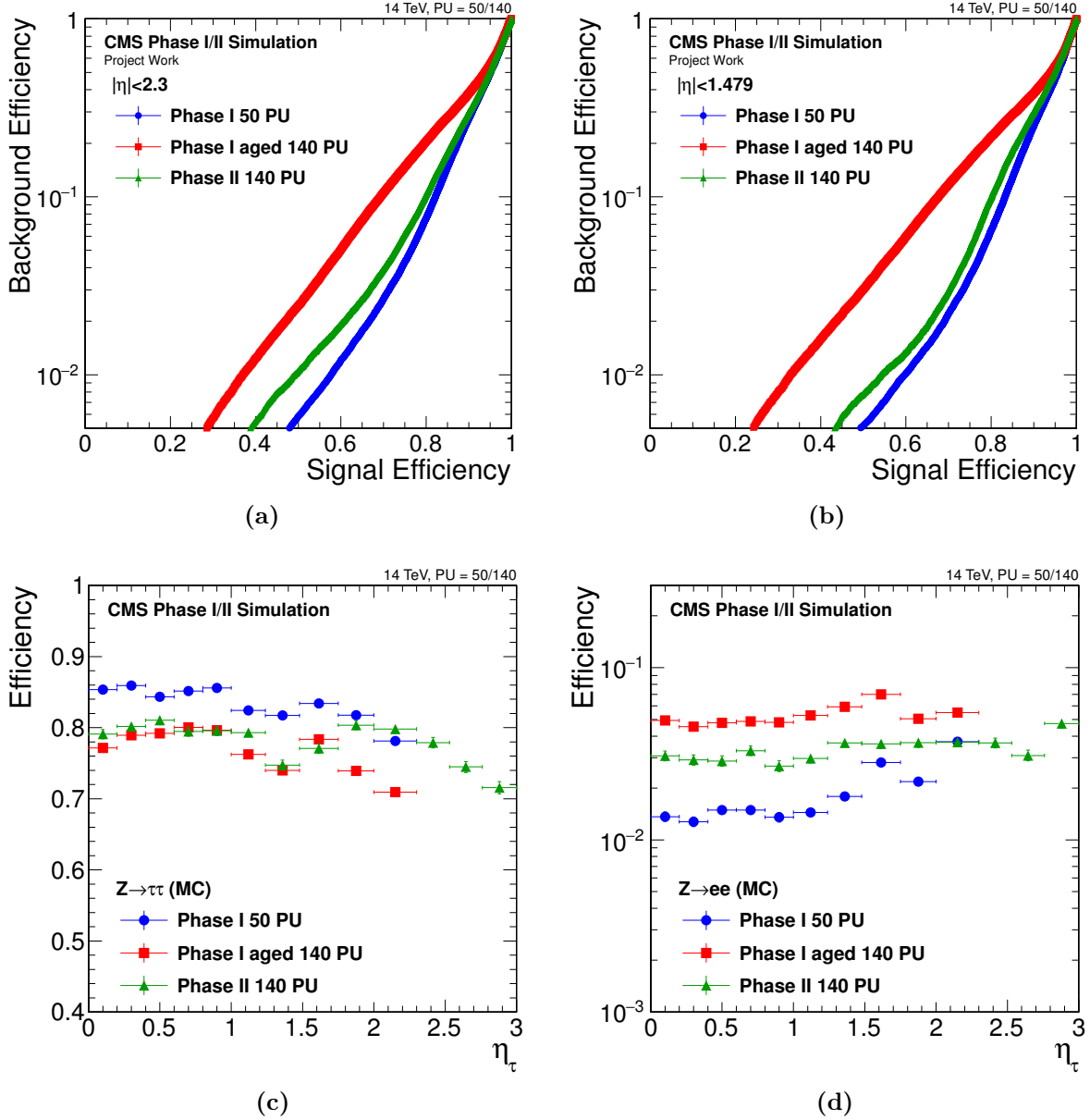
Figure 5.5: Performance of the electron rejection combining barrel and endcap region (a) and for the barrel region only (b). Efficiency of true generated τ_h decays to be reconstructed as τ_h decay (c). Probability of electrons from $Z \rightarrow ee$ events to be misidentified as τ_h decays (d) [95].

Introduction to the Relevant Analyses

The purpose of this chapter is to motivate the analyses presented in Chaps. 7 -8 and to summarize past analyses that are related to these results. $Z/\gamma^* \to \tau\tau$ results comprise Tevatron, ATLAS and CMS measurements at different center-of-mass energies. Presented MSSM H/A analyses involve LEP and Tevatron as well as ATLAS and CMS Run-1 measurements complemented by existing Run-2 results.

6.1 $Z/\gamma^* \to \tau\tau$ Measurements

The study of DY production of tau lepton pairs ($q\bar{q} \to Z/\gamma^* \to \tau\tau$) is important for several reasons. The $Z/\gamma^* \to \tau\tau$ process constitutes the dominant irreducible background in SM $H \to \tau\tau$ analyses as well as in various searches for new resonances that decay into a pair of tau leptons. Furthermore, $Z/\gamma^* \to \tau\tau$ is the standard candle for tau physics since it allows to study the τ_h reconstruction and ID efficiency as well as to measure the τ_h energy scale (ES). At the LHC, the DY production cross section for $m_{\ell\ell} > 50$ GeV exceeds the SM Higgs production cross section by about three orders of magnitude. It is crucial not only to understand the $Z/\gamma^* \to \tau\tau$ production very precisely but also to be able to model distributions of important observables in various kinematic regions.

6.1.1 $Z/\gamma^* \to \tau\tau$ Cross Section

The DY production cross section of tau lepton pairs was previously measured in proton-antiproton collisions by the CDF and D0 Collaborations at the Tevatron at a center-of-mass energy of 1.96 TeV [99–101] and at the LHC by ATLAS and CMS at a center-of-mass energy of 7 TeV [102, 103]. Assuming lepton universality the $Z/\gamma^* \to \mu\mu$ and $Z/\gamma^* \to$ ee cross section measurements are also relevant. For these final states, corre-

sponding ATLAS and CMS analyses at a center-of-mass energy of 13 TeV can be found in Refs. [104–106], whereas no study of the $Z/\gamma^* \to \tau\tau$ cross section at a center-of-mass energy of 13 TeV has been performed prior to the analysis presented in Chap. 7.

The DY production cross section increases with the center-of-mass energy. A summary plot of several different cross section measurements at various different center-of-mass energies is shown in Fig. 6.1. The results agree well with NNLO theory predictions computed with the program FEWZ [107, 108] for all center-of-mass energies.
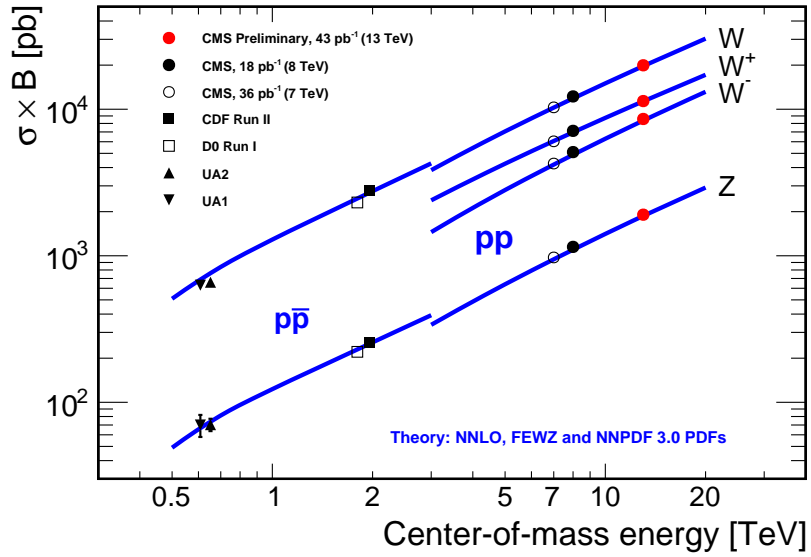
Figure 6.1: Measurements of the total Z (as well as W^+, W^-, W) production cross sections times branching fractions into pair of leptons versus center-of-mass energies for various experiments [104].

6.1.2 Tau Lepton Performance

As a byproduct of the $Z/\gamma^* \to \tau\tau$ cross section, the τ_h ID efficiency and τ_h ES are measured. The τ_h ES is defined as the ratio of the reconstructed τ_h energy to the true energy of the visible tau decay products as obtained from MC generators.

The τ_h ID efficiency and ES have also been investigated in Ref. [88] where results are obtained using the same dataset as for the $Z/\gamma^* \to \tau\tau$ cross section measurement (integrated luminosity of 2.3 fb^{-1} at a center-of-mass energy of 13 TeV). The τ_h ID efficiency can be obtained in different ways, where the most accurate measurements use a *tag-and-probe* method in $Z/\gamma^* \to \tau_\mu\tau_h$ events or exploit the ratio of $Z/\gamma^* \to \tau_\mu\tau_h$ and $Z/\gamma^* \to \mu\mu$ events. Resulting data-to-simulation correction factors depend on the WP of the BDT based ID discriminant, see Sec. 4.2.5, and commonly have uncertainties of $3-5\%$.

The τ_h ES is determined by using simulation and producing different $Z/\gamma^* \to \tau_\mu \tau_\mathrm{h}$ shape templates where the energy of the reconstructed τ_h is varied between -6% and 6% in steps of 0.1%. The distributions are fitted to data separately for different decay modes to obtain the data-to-simulation correction factors. Resulting τ_h ES correction factors are close to unity and have uncertainties of roughly 1%.

6.1.3 The Fake Factor Method

Besides the above mentioned physics results, another aim of the analysis is to introduce and validate new tau lepton analysis techniques, namely the fake factor method. The fake factor method is developed to estimate backgrounds arising from events in which a quark or gluon jet is misidentified as τ_h decay in the $\tau_\mathrm{e}\tau_\mathrm{h}$, $\tau_\mu\tau_\mathrm{h}$, $\tau_\mathrm{h}\tau_\mathrm{h}$ final state. In the scope of this analysis, the fake factor is applied for the first time in a CMS analysis comprising final states of decays into pairs of tau leptons. The fake factor method is developed such that it can be used in similar (future) analyses, see Chap. 8. Furthermore, analysis specific cross checks are conducted to evaluate the method.

6.2 MSSM H/A analyses

As described in Sec. 2.6.2, the Higgs sector of the MSSM predicts five physical Higgs bosons. At large values of $\tan\beta$ the enhanced coupling to down-type quarks and charged leptons makes searches for additional heavy neutral Higgs bosons decaying into pairs of tau leptons particularly interesting.

Searches in the context of the MSSM for additional heavy neutral Higgs bosons in the di-tau final state were performed in $\mathrm{e}^+\mathrm{e}^-$ collisions at LEP [109] and in proton-antiproton collisions at the Tevatron [110–113]. Past LHC Run-1 ATLAS and CMS searches for additional heavy neutral Higgs bosons comprise b quark [114, 115], di-muon [116, 117] and di-tau [118–121] final states. The larger mass and therefore the larger coupling with respect to the di-muon decay, and the smaller quark and gluon jet background, and therefore the better experimental accessibility, with respect to the b quark decay, give $\mathrm{A}/\mathrm{H} \to \tau\tau$ analyses a leading role in this field. Figure 6.2 summarizes different exclusion limits at 95% confidence level (CL) in the MSSM $\mathrm{m}_\mathrm{h}^{\mathrm{mod}+}$ scenario, as obtained by selected CMS analyses that have been performed on the Run-1 dataset. The blue lines indicate the exclusion limits obtained in the $\mathrm{A}/\mathrm{H} \to \tau\tau$ analysis [122], which make up the dominant limits for moderate and large values of $\tan\beta$.

The increase of the LHC center-of-mass energy to 13 TeV at the beginning of Run-2
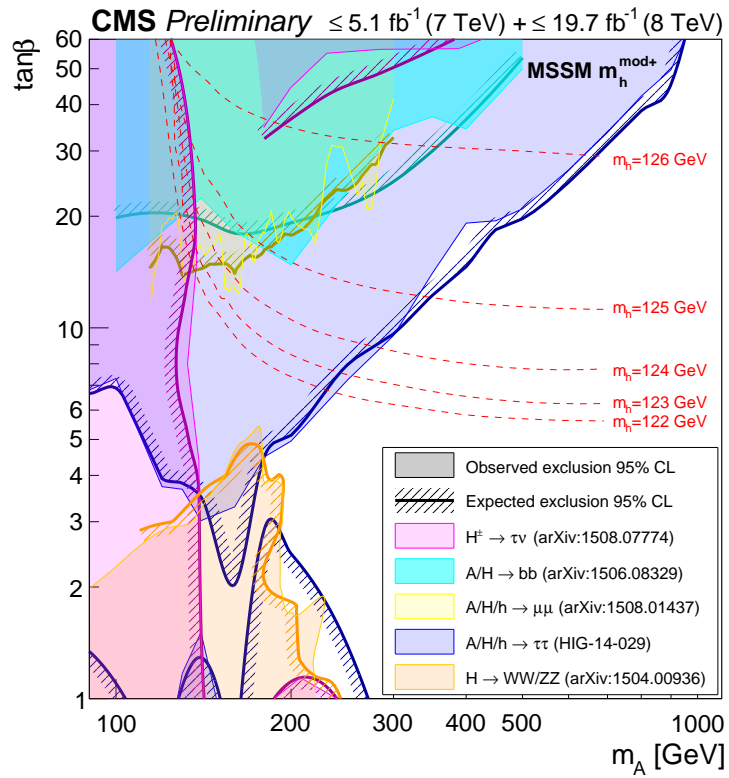
Figure 6.2: Exclusion limits at 95% CL in the MSSM $m_h^{\mathrm{mod+}}$ scenario for selected CMS Run-1 analyses [123].

enables to access and probe even higher Higgs boson masses. As a result, already by analyzing the LHC 2015 dataset, which is relatively small compared to the dataset collected during Run-1, ATLAS and CMS were able to surpass Run-1 $A/H \to \tau\tau$ sensitivity at high masses. Since no signal was found new exclusion limits were set [124, 125]. Furthermore, CMS produced a preliminary follow-up result using 12.9 fb^{-1} of the 2016 dataset [126] and the latest ATLAS results already take into account the complete 2016 dataset [127]. In both analyses no signal was found and the exclusion limits were further pushed towards higher mass points. Figure 6.3a and Figure 6.3b show the obtained ATLAS exclusion limits for ggF and b-associated production, respectively. Figure 6.3c illustrates the observed and expected 95% CL upper limits on $\tan\beta$ in the m_A-$\tan\beta$ plane in the MSSM $m_h^{\mathrm{mod}+}$ scenario [127]. The obtained upper limits are compared to the CMS results presented at the end of Chap. 8.

(a)

(b)

(c)
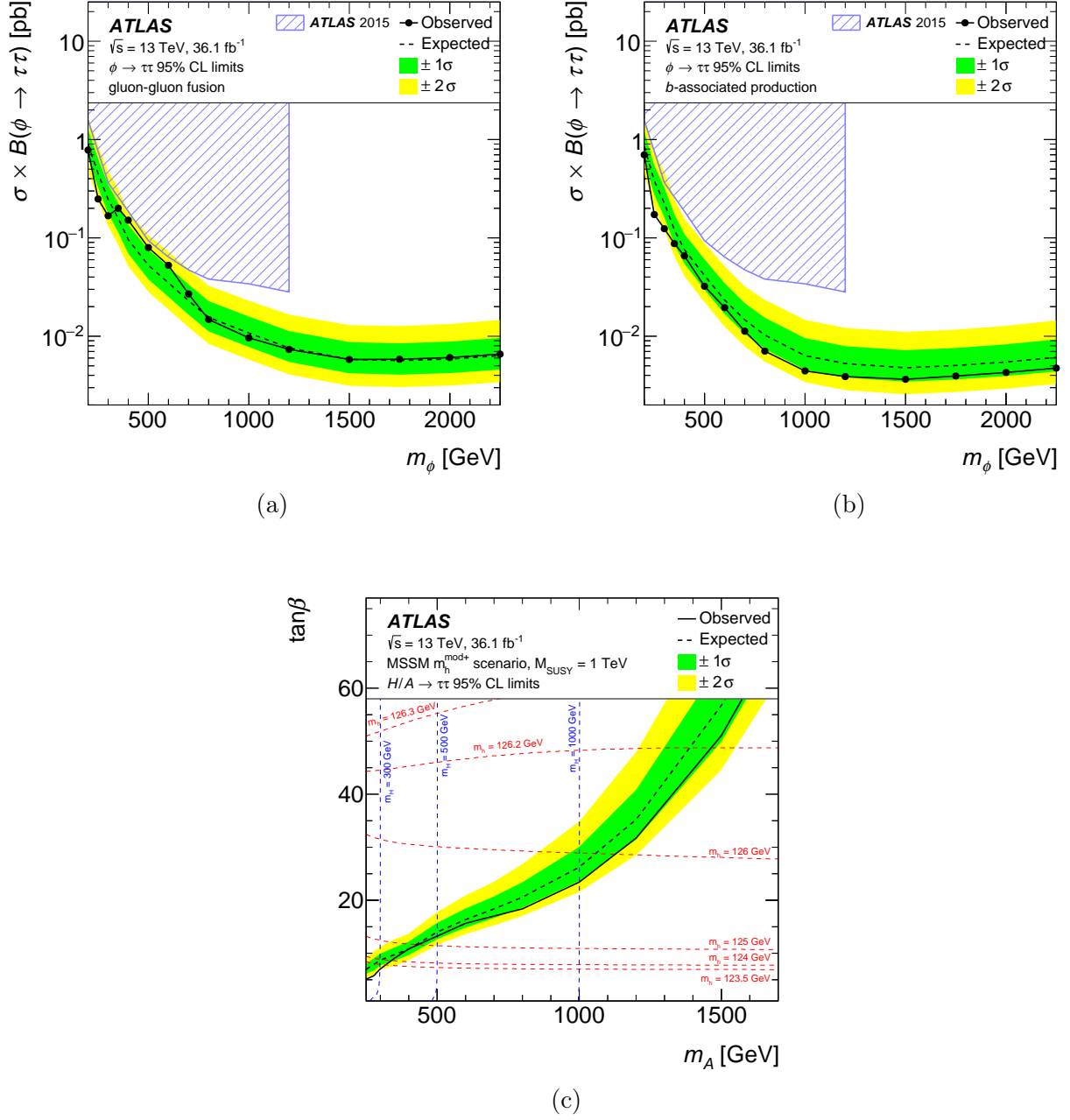
Figure 6.3: The observed and expected upper limits on the ggF (a) and b-associated production (b) at 95% CL. The expected and observed 95% CL upper limits on $\tan\beta$ as function of m_A in the MSSM m_h^{mod+} scenario (c) [127].

Measurement of the $Z/\gamma^* \rightarrow \tau\tau$ Cross Section in pp Collisions at $\sqrt{s} = 13$ TeV and Validation of τ Lepton Analysis Techniques

In this chapter, a measurement of the inclusive $\mathrm{pp} \rightarrow Z/\gamma^* + X \rightarrow \tau\tau$ cross section is presented. The estimation of one of the most relevant backgrounds is described in detail. The author carried out the analysis in the $\tau_e\tau_h$, $\tau_\mu\tau_h$ and $\tau_h\tau_h$ final states and implemented the fake factor method. The results of the analysis have been submitted for publication [128].

The analysis is based on the 2015 proton-proton collision dataset recorded by the CMS experiment at 25 ns bunch spacing at a center-of-mass energy of 13 TeV, corresponding to an integrated luminosity of 2.3 fb^{-1}. Information on the 2015 run period is summarized in Sec. 3.1.

The event selection comprises the $\tau_e\tau_h$, $\tau_\mu\tau_h$, $\tau_h\tau_h$, $\tau_e\tau_\mu$ and $\tau_\mu\tau_\mu$ final states. The $\tau_e\tau_e$ final state is not considered since it was found to be the least sensitive final state in previous studies [129]. The validity of the newly introduced fake factor method is evaluated in event categories that are used in previous $H \rightarrow \tau\tau$ analyses at the LHC.

The mass of the tau lepton pair, from now on denoted as $m_{\tau\tau}$, is estimated by the SV_{FIT} algorithm [130]. The SV_{FIT} algorithm is based on a likelihood approach and takes as input the momentum sums of the visible decay products of both tau leptons, the reconstructed $\vec{E}_T^{miss}$ and an event-by-event estimate of the $\vec{E}_T^{miss}$ resolution.

The signal is obtained via a simultaneous fit of the $m_{\tau\tau}$ distribution in all final states.

7.1 Event Selection

Objects are reconstructed as described in Sec. 4.2. To estimate the momentum imbalance in the transverse plane, the MVA $\vec{E}_{\mathrm{T}}^{\mathrm{miss}}$ is used, see Sec. 4.2.7. Reconstructed jets (b jets) are required to fulfill $p_{\mathrm{T}} > 30$ GeV (20 GeV) and $|\eta| < 4.7$ (2.4).

The selected events are recorded by a single-electron trigger in the $\tau_{\mathrm{e}}\tau_{\mathrm{h}}$ final state, a single-muon trigger in the $\tau_{\mu}\tau_{\mathrm{h}}$ and $\tau_{\mu}\tau_{\mu}$ final states, triggers based on the presence of two τ_{h} candidates in the $\tau_{\mathrm{h}}\tau_{\mathrm{h}}$ final state and triggers based on the presence of both an electron and a muon in the $\tau_{\mathrm{e}}\tau_{\mu}$ final state.

The *signal region* (SR) for each final state is defined by the following selection criteria.

In the $\tau_{\mathrm{e}}\tau_{\mathrm{h}}$ ($\tau_{\mu}\tau_{\mathrm{h}}$) final state, selected offline events are required to contain an electron (a muon) of $p_{\mathrm{T}} > 24$ GeV (19 GeV) and $|\eta| < 2.1$, and a τ_{h} with $p_{\mathrm{T}} > 20$ GeV and $|\eta| < 2.3$. The light lepton l (electron in the $\tau_{\mathrm{e}}\tau_{\mathrm{h}}$ final state, muon in the $\tau_{\mu}\tau_{\mathrm{h}}$ final state) is required to pass an isolation requirement of $I^{\mathrm{l}} < 0.1 \cdot p_{\mathrm{T}}^{\mathrm{l}}$, computed according to Eq. (4.1). The selected τ_{h} is required to have a charge opposite to that of the light lepton and pass a `Tight` WP of the MVA-based τ_{h} ID discriminant. Additionally, in the $\tau_{\mathrm{e}}\tau_{\mathrm{h}}$ ($\tau_{\mu}\tau_{\mathrm{h}}$) final state, the τ_{h} is required to pass a tight (loose) MVA-based discriminant against electrons and a loose (tight) cut-based discriminant against muons. Events that contain additional electrons or muons, passing minimal kinematic, identification and isolation requirements, are rejected in order to reduce backgrounds from $Z/\gamma^* \to \mathrm{ee}$, $Z/\gamma^* \to \mu\mu$ and diboson events. A transverse mass cut of $m_{\mathrm{T}}^{\mathrm{l}} < 40$ GeV is applied to reduce backgrounds originating from W+jets and $t\bar{t}$ production. The transverse mass $m_{\mathrm{T}}^{\mathrm{l}}$ is defined as

$$m_{\mathrm{T}}^{\mathrm{l}} = \sqrt{2 p_{\mathrm{T}}^{\mathrm{l}} E_{\mathrm{T}}^{\mathrm{miss}} \left(1 - \cos \Delta\phi \right)}, \tag{7.1}$$

where $\Delta\phi$ denotes the angle in the transverse plane between the light lepton momentum and the $\vec{E}_{\mathrm{T}}^{\mathrm{miss}}$ vector.

In the $\tau_{\mathrm{h}}\tau_{\mathrm{h}}$ final state, events are required to contain two selected τ_{h} candidates with $p_{\mathrm{T}} > 40$ GeV and $|\eta| < 2.1$ that satisfy a `Very Tight` MVA-based ID requirement, have opposite-sign electric charge and satisfy loose criteria on the discriminants used to separate τ_{h} from electrons and muons. As in the $\tau_{\mathrm{e}}\tau_{\mathrm{h}}$ and $\tau_{\mu}\tau_{\mathrm{h}}$ final states, events containing additional electrons or muons are rejected.

In the $\tau_{\mathrm{e}}\tau_{\mu}$ final state, the offline selection requires an electron with $p_{\mathrm{T}} > 13$ GeV and $|\eta| < 2.5$, and a muon with $p_{\mathrm{T}} > 10$ GeV and $|\eta| < 2.4$, where either the electron or

the muon is required to pass a threshold of $p_T > 18$ GeV. Furthermore, the electron-muon pair is required to have opposite-sign electric charge and each lepton has to satisfy the isolation criterion $I^l < 0.15 \cdot p_T^l$. Events containing an additional electron or muon are rejected. The $t\bar{t}$ background is reduced by requiring a cut on the topological discriminant $D_\zeta > -20$ GeV, where D_ζ is defined as:

$$D_\zeta = P_\zeta^{\text{miss}} - 0.85 \cdot p_\zeta^{\text{vis}}, \qquad P_\zeta^{\text{miss}} = \vec{p}_T^{\;\text{miss}} \cdot \hat{\zeta}, \qquad P_\zeta^{\text{vis}} = (\vec{p}_T^{\;\text{e}} + \vec{p}_T^{\;\mu}) \cdot \hat{\zeta}. \qquad (7.2)$$

Here, $\vec{p}_T^{\;\text{e}(\mu)}$ denotes the transverse momentum vector of the electron (muon) and $\hat{\zeta}$ the bisectional direction between the electron and the muon in the transversal plane. The reconstruction of the projections P_ζ^{miss} and P_ζ^{vis} is illustrated in Fig. 7.1a. The D_ζ distribution for events selected in the $\tau_e\tau_\mu$ final state is shown in Fig. 7.1b.

<div align="center">(a)   (b)</div>
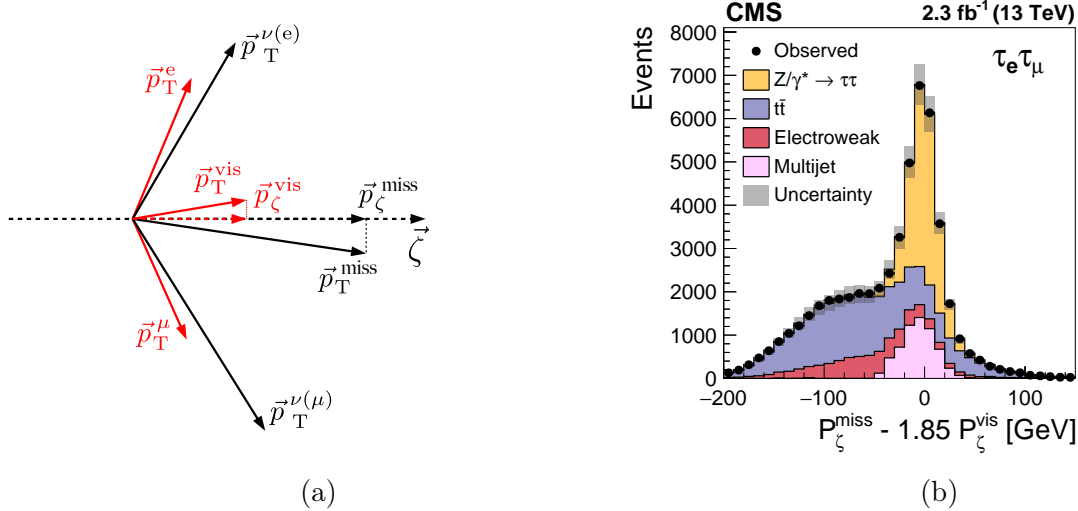
Figure 7.1: Reconstruction of the projections P_ζ^{miss} and P_ζ^{vis} (a) and distribution of $D_\zeta = P_\zeta^{\text{miss}} - 0.85 \cdot P_\zeta^{\text{vis}}$ (b) for events selected in the $\tau_e\tau_\mu$ final state [128].

In the $\tau_\mu\tau_\mu$ final state, the leading and the trailing muon are required to satisfy $p_T > 20$ GeV and $p_T > 10$ GeV, respectively. Both muons are required to be within $|\eta| < 2.4$ and to fulfill $I^\mu < 0.15 \cdot p_T^\mu$. Furthermore, the two muons have to be of opposite-sign electric charge and fulfill $m_{\mu\mu} < 80$ GeV, in order to reduce the large background arising from DY production of muon pairs. A BDT is trained to separate the $Z/\gamma^* \to \tau\tau$ signal from the large $Z/\gamma^* \to \mu\mu$ background, where, among other observables, the ratio of the p_T of the dimuon system to the scalar sum of the two muons, the pseudorapidity of the dimuon system or E_T^{miss} are used as input.

7.2 Event Simulation

MC simulation samples are used to model the $Z/\gamma^* \to \tau\tau$[1] signal and the $Z/\gamma^* \to ee$, $Z/\gamma^* \to \mu\mu$, W+jets, $t\bar{t}$, single top quark and diboson (WW, WZ, ZZ) background processes. The $Z/\gamma^* \to \ell\ell$ ($\ell = e, \mu, \tau$) and W+jets events are modeled using LO matrix element calculations, implemented in the program MADGRAPH_aMC@NLO [75], diboson events are modeled using NLO matrix element calculations, implemented in MADGRAPH_aMC@NLO, and $t\bar{t}$ and single top quark events are generated using NLO calculations, implemented in the program POWHEG v2 [69–73]. SM ggF and VBF H $\to \tau\tau$ events, generated for a Higgs boson mass of $m_H = 125$ GeV at NLO in POWHEG, complement the background processes. To increase the sample size in regions of high signal purity, additional samples have been generated with different numbers of additional jets for $Z/\gamma^* \to \ell\ell$ and W+jets events.

All samples are produced based on the NNPDF3.0 [131–133] PDFs. Parton showers and parton hadronization are modeled using PYTHIA 8.212 [66] with the CUETP8M1 [134] underlying event tune.

The cross sections used to normalize $Z/\gamma^* \to \ell\ell$, W+jets and $t\bar{t}$ events are at NNLO accuracy and the cross sections for single top quark and diboson events are at NLO accuracy to the generation.

7.2.1 Data-to-Simulation Corrections

A PU reweighting is applied to all simulation samples in order to obtain similar PU distributions between data and simulation. For the 2015 run period, an average number of 12 PU events is observed, see Fig. 3.4a.

Further corrections are derived. In order to account for the differences between data and simulation in the electron and muon tracking efficiency and in the electron and muon efficiency of the identification and isolation requirements of these two lepton flavors, a tag-and-probe technique with $Z \to ee$ and $Z \to \mu\mu$ events is applied, as described in Ref. [135]. In a similar way, a tag-and-probe method is applied to $Z \to \tau\tau$ events in the $\tau_\mu\tau_h$ final state to obtain corrections for the efficiency of triggering τ_h decays and for the τ_h ID efficiency.

The distribution of the τ_h decay modes is reweighted to match the τ_h decay mode distribution observed in data. The weights are computed such that the combined yield of τ_h decays reconstructed as $h^\pm$, $h^\pm\pi^0$, $h^\pm\pi^0\pi^0$ and $h^\pm h^\mp h^\pm$ is kept constant and are

---

[1]$Z/\gamma^* \to \ell\ell$ ($\ell = e, \mu, \tau$) events, like W+jets events, contain different numbers of additional jets in the final state. Due to simplicity the notation $Z/\gamma^* \to \ell\ell$ is used instead of $Z/\gamma^* \to \ell\ell$+jets.

applied to reconstructed τ_h candidates that are matched to *generated* τ_h decays in simulated $Z/\gamma^* \to \tau\tau$ events. Here, "generated" refers to the final state τ_h produced by MC event generators before entering the detector simulation. To account for residual differences in the $e \to \tau_h$-misidentification rate, corrections are further applied to $Z \to ee$ events in the $\tau_e\tau_h$ final state in which an electron is reconstructed as τ_h. Finally, for each exclusive event category, as described in Tab. 7.1, a $Z/\gamma^* \to \tau\tau$ reweighting factor is derived based on differences between data and simulation in $Z/\gamma^* \to \mu\mu$ events.

In order to improve the modeling of the kinematic properties of the top quarks in $t\bar{t}$ events, a reweighting is applied based on the p_T spectra of the top and the anti-top quark [136,137]. For $Z/\gamma^* \to \ell\ell$ events the dilepton mass and p_T spectrum is reweighted based on weights obtained from studies of $Z/\gamma^* \to \mu\mu$ events.

Jet energy corrections in bins of jet p_T and η are applied to correct the jet energies to the true particle or parton energy. This is necessary since the detector response to particles is not linear and hence it is not straightforward to translate the measured jet energy to the true energy of the particles or partons. Additionally, residual data-to-simulation corrections are derived and applied to the simulated samples. Data-to-simulation corrections have further been obtained to correct the b jet ID efficiency in simulation, where $t\bar{t}$ and Z+jets events are used to determine efficiency and misidentification rate for real b jets and for jets originating from light quarks, respectively.

A correction is applied to the direction and magnitude of the $\vec{E}_T^{miss}$ vector based on differences in data and simulation estimates of the hadronic recoil in $Z/\gamma^* \to \mu\mu$ events. The $\vec{E}_T^{miss}$ corrections are applied to samples where a well-defined direction and magnitude of $\vec{E}_T^{miss}$ exists, i.e. $Z/\gamma^* \to \ell\ell$, W+jets and SM $H \to \tau\tau$ samples.

Corresponding uncertainties on all described corrections have been incorporated into the uncertainty model, as summarized in Sec. 7.5.

7.3 Estimation of the Misidentified-τ_h Background with the Fake Factor Method

In the final states containing a τ_h, i.e. $\tau_e\tau_h$, $\tau_\mu\tau_h$ and $\tau_h\tau_h$, a large fraction of the background contribution arises from quark or gluon jets misidentified as τ_h decays. To avoid confusion the term "misidentified-τ_h" in this thesis is attributed only to jets that are falsely reconstructed and classified as τ_h.

For the statistical inference of the signal the misidentified-τ_h backgrounds in these final states are estimated using the fake factor method. The main processes contributing to the misidentified-τ_h background, namely the QCD multijet, the W+jets and the $t\bar{t}$ pro-

cess contain specific mixtures of gluon-, light-quark- (u, d, s) and heavy-quark-initiated (c, b) jets, with different probabilities to be misidentified as τ_h decay. Figure 7.2 illustrates the τ_h misidentification rates for simulated quark and gluon jets of different flavor.

The main challenge of an unbiased background modeling by the fake factor method is to take various kinematic properties of the (fake) τ_h candidates as well as the misidentified-τ_h background composition into account.
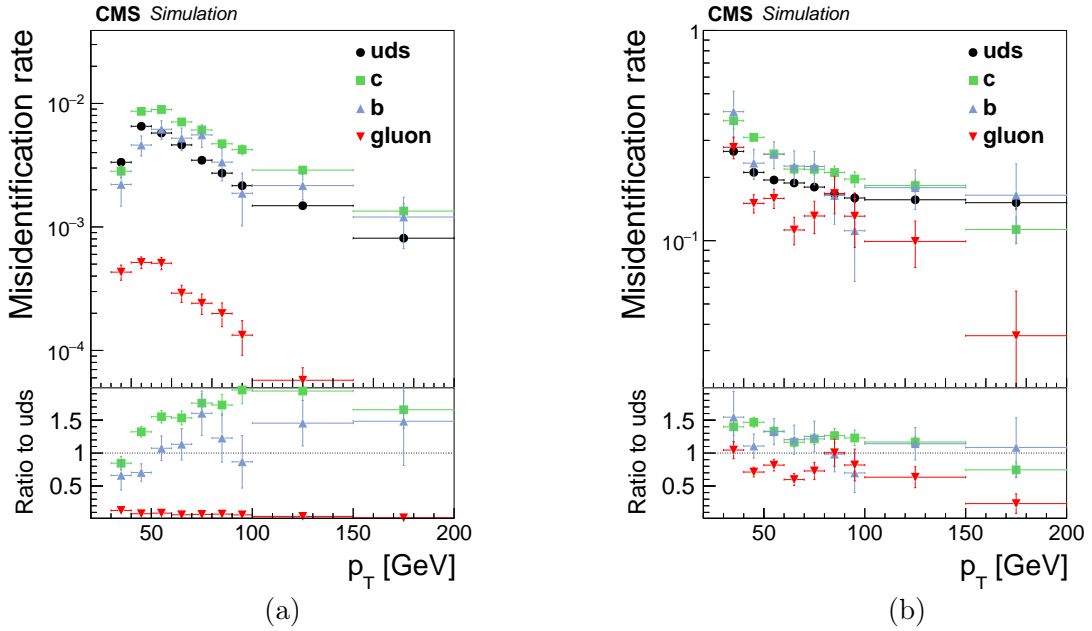
Figure 7.2: Misidentification rates for simulated quark and gluon jets of different flavor. The rates are shown as a function of jet p_T, for jets passing $p_T > 20$ GeV and $|\eta| < 2.3$ (a), and for jets passing in addition the `VeryLoose` τ_h ID criteria (b) [128].

7.3.1 Idea of the Fake Factor Method

The fake factor method is designed to estimate the number of events for a certain background process which arises due to jet $\to \tau_h$-misidentification in a region which only differs from the SR by a modified τ_h ID requirement. This region is referred to as *application region* (AR). In this implementation, the τ_h-identification is required to fulfill the `VeryLoose` but not the `Tight` (`VeryTight`[2]) WP of the discriminant in the $\tau_e\tau_h/\tau_\mu\tau_h$ ($\tau_h\tau_h$) final state. The AR is thus orthogonal to the SR and primarily populated by events with jets misidentified as τ_h. The contamination of the sample in

---

[2]For simplicity, the `Tight` WP of the τ_h ID is used in the following description. Please note that in the $\tau_h\tau_h$ final state this always refers to the `VeryTight` WP.

the AR by events with genuine τ_h or misidentified electrons or muons is of $\mathcal{O}(10\%-15\%)$ in the $\tau_\mathrm{e}\tau_\mathrm{h}$ and $\tau_\mu\tau_\mathrm{h}$ final states and of $\mathcal{O}(5\%)$ in the $\tau_\mathrm{h}\tau_\mathrm{h}$ final state. Figure 7.4 displays the background composition in the AR for the $\tau_\mathrm{e}\tau_\mathrm{h}$, $\tau_\mu\tau_\mathrm{h}$ and $\tau_\mathrm{h}\tau_\mathrm{h}$ final states. To obtain an estimate for the number of background events originating from this background in the SR, the number of events in the AR is weighted with the ratio (fake factor) of events that fulfill the `Tight` WP ($n_\mathtt{Tight}$) over events that fulfill the `VeryLoose` but fail the `Tight` WP ($n_\mathtt{!Tight}^\mathtt{VeryLoose}$) of the τ_h ID discriminant. The fake factor for a specific background i

$$\mathrm{FF}_i = \frac{n_\mathtt{Tight}}{n_\mathtt{!Tight}^\mathtt{VeryLoose}}, \qquad i \in \mathrm{QCD}, \mathrm{W+jets}, \mathrm{t\bar{t}} \tag{7.3}$$

is obtained from a dedicated *determination region* (DR_i). Contributions from other backgrounds than i are estimated from simulation and subtracted from the numerator and the denominator of Eq. (7.3). The underlying assumption for the extrapolation from DR_i to the AR/SR is that the fake factor is the same in both regions. If the assumption is mildly violated corrections for this discrepancy are determined. The fake factors are independently derived for backgrounds due to QCD multijet, W+jets and $\mathrm{t\bar{t}}$ events, and are estimated in bins of the p_T of the τ_h candidate, in categories of the τ_h decay mode (1-prong, 3-prong), and the jet multiplicity ($\mathrm{N_{jet}} = 0$ and $\mathrm{N_{jet}} \geq 1$). A weighted fake factor FF is obtained from

$$\mathrm{FF} = \sum_i w_i \cdot \mathrm{FF}_i, \qquad w_i = \frac{\mathrm{N}_\mathrm{AR}^i}{\sum_j \mathrm{N}_\mathrm{AR}^j}, \qquad i,j \in \mathrm{QCD}, \mathrm{W+jets}, \mathrm{t\bar{t}}, \tag{7.4}$$

where N_AR^i denotes the expected number of events for background i in the AR. The predicted number of misidentified-τ_h events, $\mathrm{N}_{\mathrm{jet}\to\tau_\mathrm{h}}$, in a given range of a kinematic variable (e.g. $m_{\tau\tau}$) is obtained by:

$$\mathrm{N}_{\mathrm{jet}\to\tau_\mathrm{h}} = \mathrm{N}_\mathrm{AR} \times \sum_i w_i \cdot \mathrm{FF}_i, \tag{7.5}$$

where the weighted fake factor FF is applied on an event-by-event basis. The fake factor method is illustrated in Fig. 7.3.

Besides QCD multijet, W+jets and $\mathrm{t\bar{t}}$ background processes, also $Z/\gamma^* \to \ell\ell$ ($\ell = \mathrm{e}, \mu, \tau$) events have non-negligible misidentified-τ_h background contributions. But since the analyzed data do not provide a way of measuring fake factors for $Z/\gamma^* \to \ell\ell$ events with

sufficient statistical accuracy, the fake factors measured in W+jets events are used in-
stead. The validity of this procedure is justified by studies of simulated $Z/\gamma^* \to \ell\ell$ and
W+jets events, which indicate a similar flavor composition of the jets as well as similar
fake factors. Corresponding uncertainties are incorporated into the uncertainty model.

$$\text{FF} = \sum_i w_i \cdot \text{FF}_i$$

$$w_i = \frac{\text{N}^i_{\text{AR}}}{\sum_j \text{N}^j_{\text{AR}}}$$

$$i \in \text{QCD},\ \text{W}+\text{jets},\ \text{t}\bar{\text{t}}$$
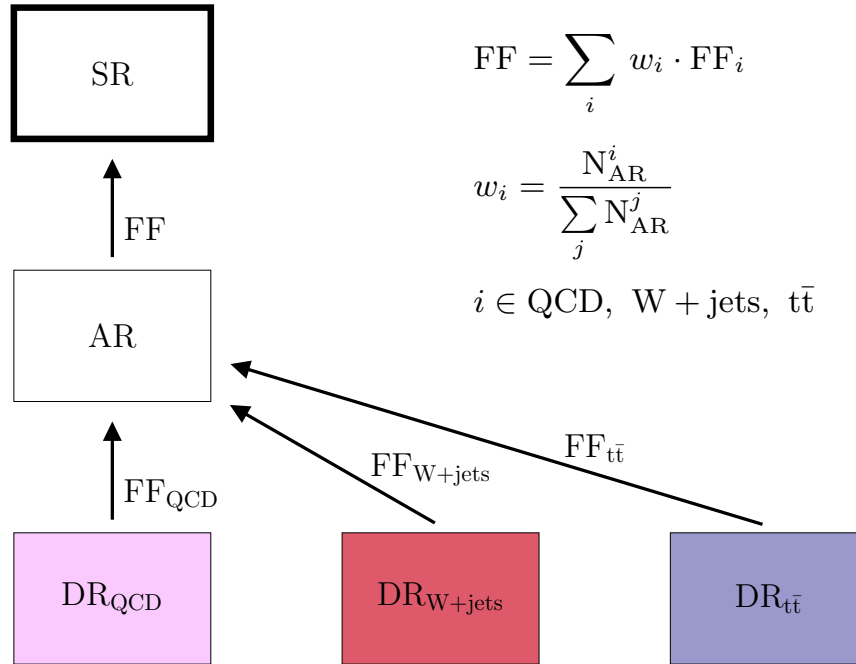
Figure 7.3: Illustration of the fake factor measurement and application for the estimation
of QCD multijet, W+jets, and $\text{t}\bar{\text{t}}$ events.
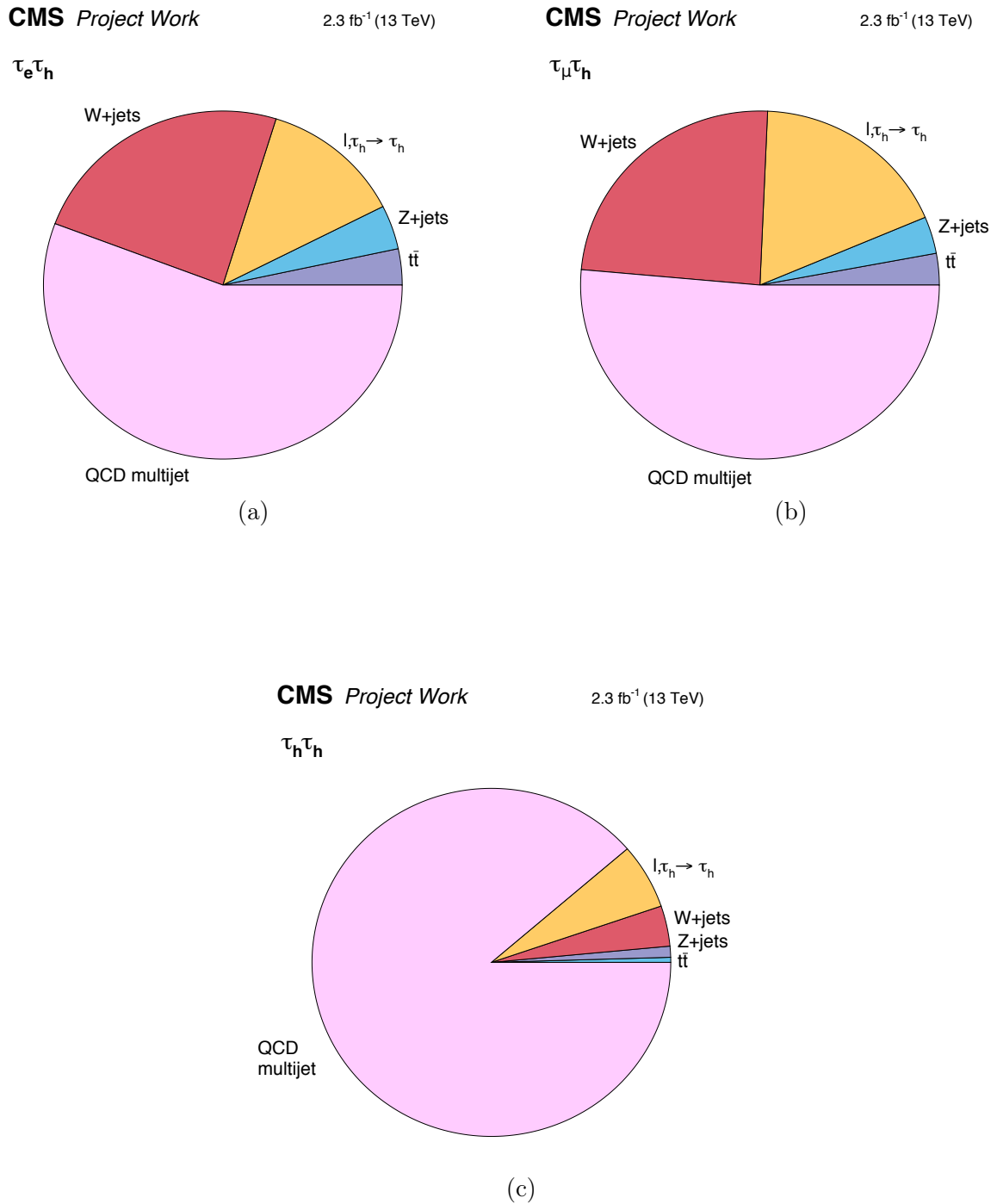
Figure 7.4: Fraction of misidentified-τ_h backgrounds in the inclusive AR that are due to QCD multijet, W+jets, $Z/\gamma^* \to \ell\ell$+jets, and $t\bar{t}$ production in the $\tau_e\tau_h$ (a), $\tau_\mu\tau_h$ (b) and $\tau_h\tau_h$ (c) final states. The yellow part displays the contributions from events with genuine τ_h decays or misidentified electrons or muons.

7.3.2 Fake Factor Measurements

7.3.2.1 QCD Multijet Fake Factors

The QCD multijet determination region (DR_{QCD}) for the $\tau_e\tau_h$ and $\tau_\mu\tau_h$ final states is characterized by the same event selection as the SR, except for the following requirements:

- The electric charges of the selected light lepton and the τ_h candidate are required to be the same, i.e. $q_l \cdot q_{\tau_h} > 0$ (SR: opposite-sign electric charge).

- The isolation of the light lepton has to be in the range $0.05 \cdot p_T^l < I^l < 0.15 \cdot p_T^l$ (SR: $I^l < 0.10 \cdot p_T^l$).

The motivation for these selection cuts is to enhance QCD multijet events with respect to all other events. In addition, events with poorly isolated light leptons ($I^l > 0.15 \cdot p_T^l$) are rejected as large isolation values lead to a bias of the fake factor measurement, see Sec. 7.3.4.1. For low values of lepton isolation ($I^l < 0.05 \cdot p_T^l$), the events are contaminated with a significant fraction of non-QCD multijet contributions, mainly W+jets events, and are thus rejected. The FF_{QCD} measurement is sketched in Fig. 7.5. Corresponding corrections that are needed to account for differences between the SR and DR_{QCD} are described in Sec. 7.3.4.1. The fake factors determined in DR_{QCD} are shown in Fig. 7.6.

For the $\tau_h\tau_h$ final state, the DR_{QCD} requirement is that the electric charges of the two τ_h candidates are the same. Since in this final state other misidentified-τ_h backgrounds are very small compared to the QCD multijet background, it can be assumed at good approximation that the fake factors derived in DR_{QCD} can be applied to all events in the AR. To avoid any kinematic bias, one of the two reconstructed τ_h candidates is selected at random and considered as candidate for the FF_{QCD} measurement. The second τ_h candidate has to fulfill the nominal `VeryTight` requirement.

7.3.2.2 W+jets Fake Factors

The W+jets determination region (DR_{W+jets}) for the $\tau_e\tau_h$ and $\tau_\mu\tau_h$ final states is characterized by the same event selection as the SR, except for the following requirements:

- The transverse mass m_T^l, as defined in Eq. (7.1), is required to be above 70 GeV (SR: $m_T^l < 40$ GeV).

- There is no b jet allowed in the event (SR: any number of b jets allowed).
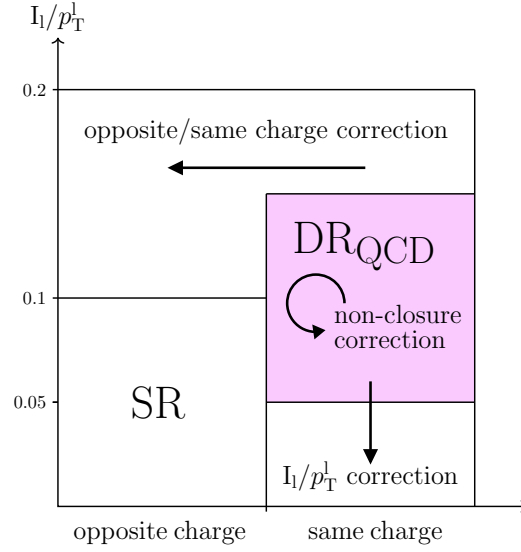
Figure 7.5: Illustration of DR_{QCD} for the $\tau_e\tau_h$ and $\tau_\mu\tau_h$ final states. The indicated corrections are described in Sec. 7.3.4.1.

The high m_T^l values are motivated by the fact that in W+jets events the much larger mass of the W boson typically results in a neutrino traveling in the opposite direction as the lepton in the transverse plane, and therefore W+jets events tend to have larger values of m_T^l. The contamination arising from $t\bar{t}$ events is reduced by vetoing events that contain at least one b jet. The FF_{W+jets} measurement is sketched in Fig. 7.7a, the corresponding corrections are described in Sec. 7.3.4.2. The fake factors determined in DR_{W+jets} are shown in Fig. 7.8a-d.

7.3.2.3 $t\bar{t}$ Fake Factors

The $t\bar{t}$ determination region ($DR_{t\bar{t}}$) is the same for the $\tau_e\tau_h$ and $\tau_\mu\tau_h$ final states. $DR_{t\bar{t}}$ is characterized by the same event selection as for the SR, except for the following requirements:

- There is at least one b jet required (SR: no requirement on the number of b jets).

- In addition to an isolated muon as defined in the $\tau_\mu\tau_h$ final state selection, an electron with $p_T > 13$ GeV, $|\eta| < 2.5$ and $I^e < 0.10 \cdot p_T^e$ is required (SR: events that contain a third lepton are vetoed).

The $FF_{t\bar{t}}$ measurement is sketched in Fig. 7.7b, the fake factors for the $\tau_\mu\tau_h$ final state determined in $DR_{t\bar{t}}$ are shown in Fig. 7.8e-f.
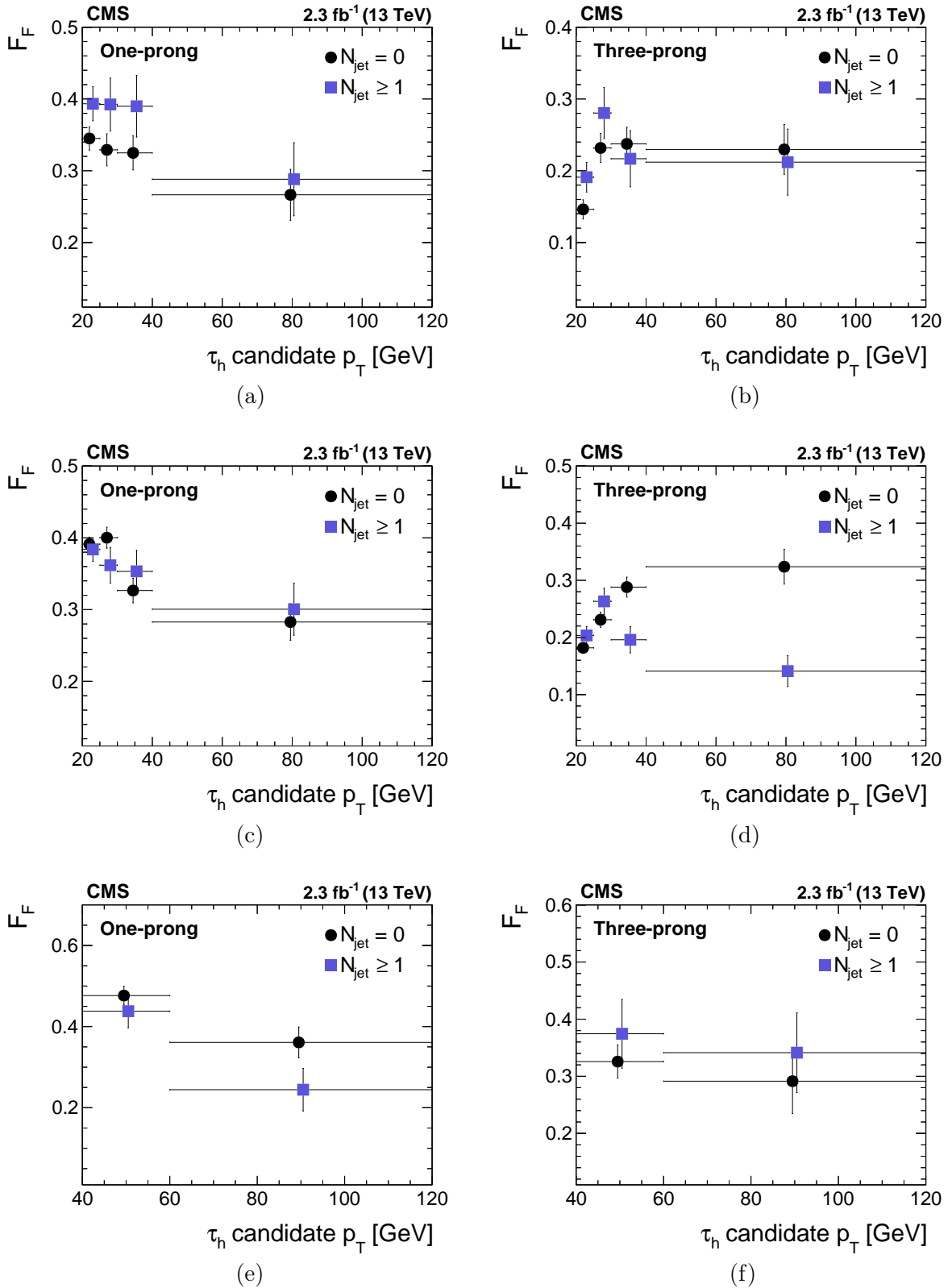
Figure 7.6: The fake factor values measured in QCD multijet events in the $\tau_e\tau_h$ (a, b), $\tau_\mu\tau_h$ (c, d), and $\tau_h\tau_h$ (e, f) final states, shown in bins of jet multiplicity, τ_h decay mode, and p_T [128]. For better readability the abscissae of the points are offset.
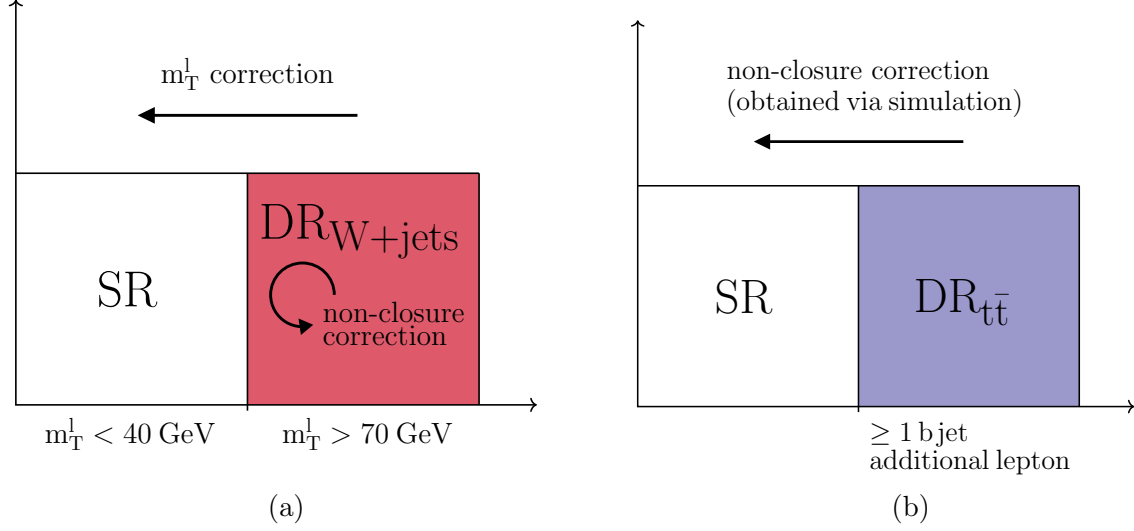
Figure 7.7: Illustration of DR_{W+jets} (a) and $DR_{t\bar{t}}$ (b). The indicated corrections are described in Secs. 7.3.4.2 and 7.3.4.3.

7.3.3 Estimation of Misidentified-τ_h Background Composition

The fake factor applied to a given event in the AR is a weighted average of the values measured in DR_{QCD}, DR_{W+jets} and $DR_{t\bar{t}}$, as described in Eq. (7.4). In the $\tau_e\tau_h$ and $\tau_\mu\tau_h$ final states, the relative contribution w_i from background i in the AR is determined through a *maximum likelihood* (ML) fit to distributions binned in m_T^l and categories of the τ_h decay mode (1-prong, 3-prong). The template representing the QCD multijet background contribution is taken from data in the AR, where the light lepton satisfies a modified isolation criterion of $0.05 \cdot p_T^l < I^l < 0.15 \cdot p_T^l$ and contributions from other processes are subtracted based on simulation. The template distributions for other backgrounds are taken from simulation. These are W+jets, $t\bar{t}$ and $Z/\gamma^* \to \ell\ell$ backgrounds that contain a misidentified-τ_h, as well as $t\bar{t}$, $Z/\gamma^* \to \ell\ell$ and diboson backgrounds containing genuine τ_h decays or misidentified light leptons (as shown in yellow in Fig. 7.4). The fractions w_{QCD}, w_{W+jets}, $w_{Z/\gamma^*\to\ell\ell}$ and $w_{t\bar{t}}$ are determined in the fit for every bin in m_T^l and τ_h decay mode such that

$$w_{QCD} + w_{W+jets} + w_{Z/\gamma^*\to\ell\ell} + w_{t\bar{t}} = 1. \tag{7.6}$$
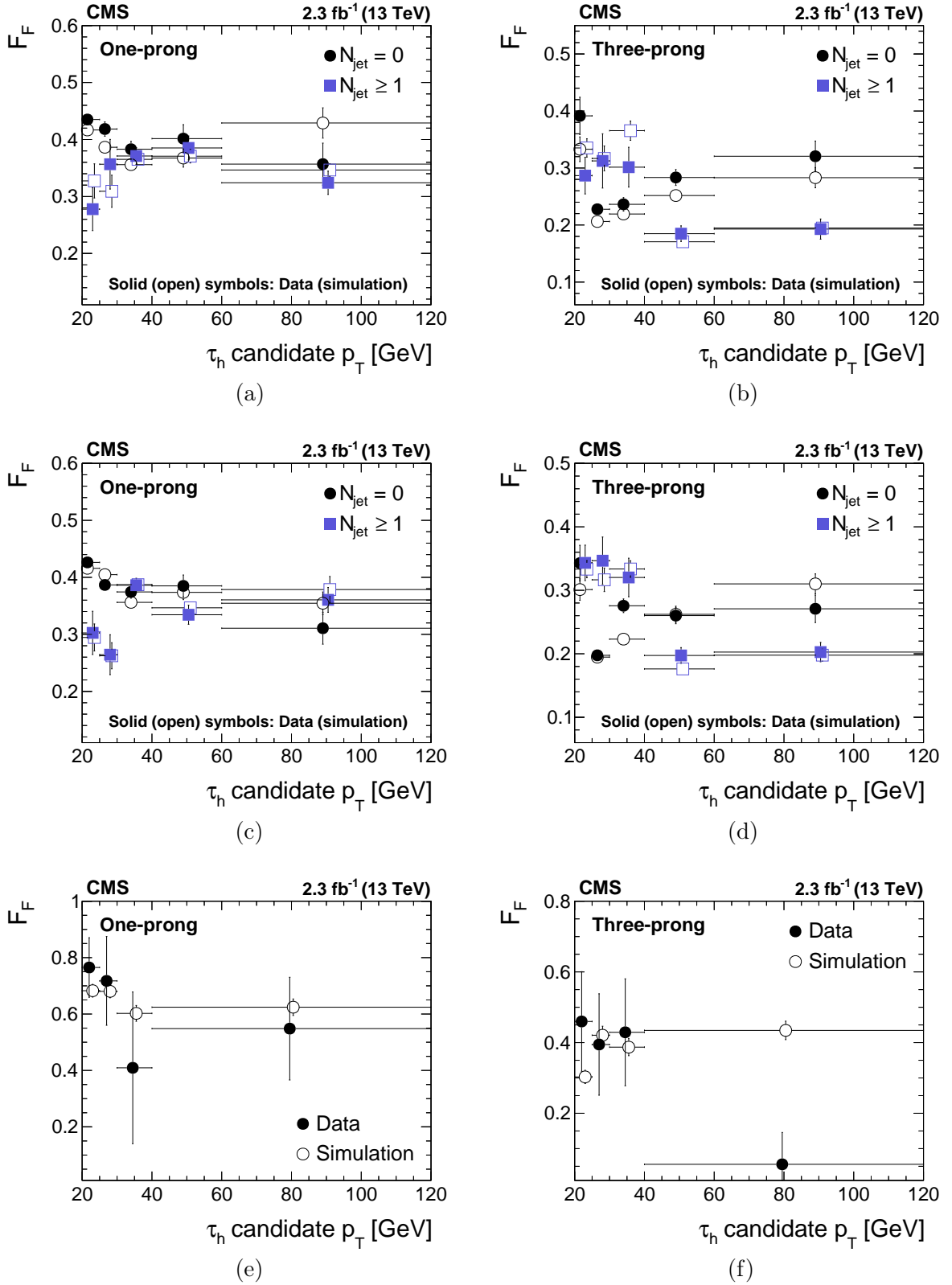
Figure 7.8: The fake factor values measured in W+jets events in the $\tau_e\tau_h$ (a, b) and $\tau_\mu\tau_h$ (c, d) final states and in $t\bar{t}$ events (e, f), shown in bins of jet multiplicity, τ_h decay mode, and p_T [128]. For better readability the abscissae of the points are offset.

From the resulting misidentified-τ_h background prediction in a range of a kinematic variable (e.g. $m_{\tau\tau}$), contributions from events in the AR with genuine τ_h decays or misidentified electrons or muons are subtracted using simulation.

For the exclusive event categories listed in Tab. 7.1, fractions are extracted using simulation, except for the QCD multijet background which is estimated by the difference of observed data events minus the expectation of all other background processes. This gives more robust results in low-statistics regions and the results are compatible with the template fit.

In the $\tau_h\tau_h$ final state, one of the two reconstructed τ_h candidates is selected at random and is required to fulfill the `VeryLoose` but not `VeryTight` ID criterion, whereas the other τ_h candidate has to fulfill the nominal `VeryTight` ID criterion. For QCD multijet events in which both τ_h candidates are due to misidentification in all but a negligible fraction of events, this procedure assures that combinatorial effects are taken into account correctly. For the other misidentified-τ_h backgrounds, typically one of the two τ_h candidates has been correctly identified while the other is a misidentified jet - the fraction of events with two misidentified jets is at most a few percent and thus well below the associated systematic uncertainties. In order to correctly estimate the backgrounds with one misidentified-τ_h, backgrounds are added by simulation if the selected τ_h candidate is matched to a generated τ_h, an electron or a muon. This is done for all simulation samples and, combined with the FF estimate, yields an unbiased estimate of the misidentified-τ_h background.

7.3.4 Fake Factor Corrections

The misidentified-τ_h background estimate in the SR using the raw fake factors described in Sec. 7.3.2.1 can be imperfectly modeled in terms of normalization and shape due to:

- Differences between SR and DR which affect the fake factor measurement, e.g. a different composition in terms of gluon-, light-quark- and heavy-quark-initiated jets.

- Any residual differences, e.g. due to the finite binning of the fake factors or dependencies on variables that are not used to model the fake factors.

Corrections are derived to account for these differences.

7.3.4.1 QCD Multijet Fake Factor Corrections

In the $\tau_e\tau_h$ and $\tau_\mu\tau_h$ final states, some of the properties of the light lepton in the event are correlated with the τ_h ID. This requires to correct the fake factor dependency as a function of I^l/p^l_T in order to extrapolate the fake factors to the SR. In addition, a small difference is observed depending on whether the fake factor is measured in a region where the light lepton and the τ_h have the same- or opposite-sign electric charge. In total, three (two) corrections are derived in the $\tau_e\tau_h/\tau_\mu\tau_h$ ($\tau_h\tau_h$) final state:

- A nonclosure correction, as a function of the visible mass (m_{vis}).

- An I^l/p^l_T-dependent correction (only in the $\tau_e\tau_h$ and $\tau_\mu\tau_h$ final states).

- A correction for the extrapolation from the same-sign (DR_{QCD}) to the opposite-sign electric charge region (SR).

The nonclosure correction as a function of m_{vis} is derived in the same region that is used to extract raw QCD multijet fake factors, see Sec. 7.3.2.1. The misidentified-τ_h background is estimated as function of m_{vis} using the raw fake factors and compared to the observed background distribution. The ratio of the two is smoothed with a Gaussian kernel of variable width in order to limit the statistical fluctuations and applied as multiplicative correction. The QCD multijet nonclosure correction for the $\tau_\mu\tau_h$ final state is shown in Fig. 7.9a, corresponding nonclosure corrections for the $\tau_e\tau_h$ and the $\tau_h\tau_h$ final state can be found in Apps. A.1.1 - A.1.2.

The I^l/p^l_T-dependent correction is derived in a same electric charge region. The misidentified-τ_h background is estimated as function of I^l/p^l_T, applying the fake factors corrected for the nonclosure correction described above, and compared to the observed background distribution. The ratio of the two, smoothed with a Gaussian kernel of variable width (see Fig. 7.9b for the $\tau_\mu\tau_h$ final state and App. A.1.1 for the $\tau_e\tau_h$ final state), is applied as an additional multiplicative correction. For the lowest bin in terms of I^l/p^l_T, the events are contaminated with a significant fraction of non-QCD multijet events, mainly W+jets events, at a level of up to 50%. This contamination is subtracted based on simulation and an additional associated uncertainty is propagated to the fake factor correction, see Sec. 7.5.1 for fake factor related uncertainties . Since the correction is derived in a same-sign electric charge region and applied in the opposite-sign electric charge SR, it is implicitly assumed that there is no significant correlation between the dependency of the fake factor on I^l/p^l_T and the relative electric charges.

The extrapolation to the opposite-sign electric charge region is derived as a function of m_{vis} in a region with $0.1 < I^l/p_{\mathrm{T}}^l < 0.2$ for the $\tau_e\tau_h$ and $\tau_\mu\tau_h$ final states, and a second τ_h that fulfills the `VeryLoose` but fails the `VeryTight` ID requirement in the $\tau_h\tau_h$ final state. First, raw fake factors are derived in this region with a same electric charge requirement and then corrected for nonclosure as a function of m_{vis}. These corrected fake factors are then applied in the same region except for an opposite-sign electric charge requirement, and the estimated misidentified-τ_h background is compared to the observed background distribution. The ratio of the two as a function of m_{vis}, smoothed with a Gaussian kernel of variable width, is shown in Fig. 7.9c for the $\tau_\mu\tau_h$ final state and in Apps. A.1.1 - A.1.2 for the $\tau_e\tau_h$ and $\tau_h\tau_h$ final states. The contamination of the sample in opposite-sign electric charge region by events with genuine τ_h or misidentified electrons or muons is of $\mathcal{O}(25\%)$ in the $\tau_e\tau_h$ and $\tau_\mu\tau_h$ final states and of $\mathcal{O}(5\%)$ in the $\tau_h\tau_h$ final state.

7.3.4.2 W+jets Fake Factor Corrections

For selected W+jets events the τ_h ID is anti-correlated with m_{T}^l. This correlation is created by requiring a minimum p_{T} on the light lepton, which, for low-m_{T}^l events, favors events with a hard recoil of the W boson. This is only possible in the presence of one or more relatively hard jets, leading to less isolated τ_h candidates at low transverse momentum since the tau ID is strongly correlated to the difference of the p_{T} of the τ_h and the p_{T} of the associated jet. In total, two types of corrections are derived:

- A nonclosure correction, as a function of m_{vis}.

- A correction depending on m_{T}.

The nonclosure correction is derived in the same region as used to extract the raw W+jets fake factors, see Sec. 7.3.4.2. The misidentified-τ_h background is estimated as a function of m_{vis} using raw fake factors and compared to the observed background distribution. The ratio of the two, smoothed with a Gaussian kernel of variable width (see Fig. 7.9d for the $\tau_\mu\tau_h$ final state and App. A.1.1 for the $\tau_e\tau_h$ final state) is applied as a multiplicative correction.

The m_{T}^l-dependent correction is derived from simulated W+jets events. For this purpose, the raw fake factors and the nonclosure correction are re-derived from simulation and applied to estimate the W+jets misidentified-τ_h background as a function of m_{T}

(a)

(b)

(c)

(d)

(e)

(f)
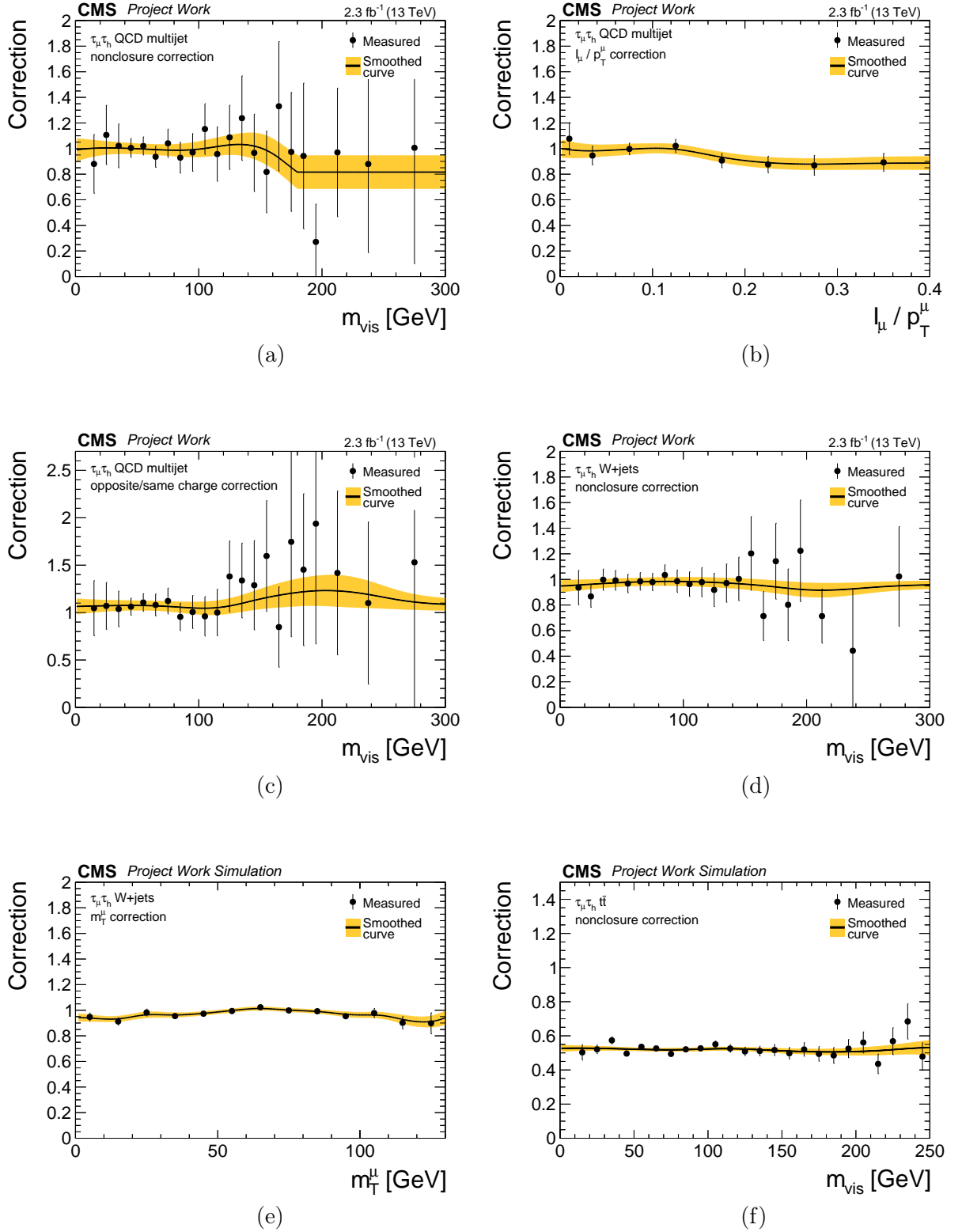
Figure 7.9: Fake factor corrections in the $\tau_\mu\tau_h$ final state containing corrections for the raw FF_{QCD}: nonclosure correction in m_{vis} (a), I^μ/p_T^μ correction (b) and opposite-sign/same-sign electric charge correction (c), corrections for the raw FF_{Wjets}: nonclosure correction in m_{vis} (d) and m_T^μ correction (e) and a nonclosure correction for the raw $FF_{t\bar{t}}$ (f).

in simulated samples. It is compared to the actual simulated background and the ratio of the two, smoothed with a Gaussian kernel of variable width (see Fig. 7.9e for the $\tau_\mu\tau_\mathrm{h}$ final state and App. A.1.1 for the $\tau_\mathrm{e}\tau_\mathrm{h}$ final state) is applied as an additional multiplicative correction. It has been checked that this correction obtained from simulation can be applied on data by comparing the fake factors in $Z/\gamma^* \to \mu\mu$ events as a function of the dimuon m_T in data and simulation. They are compatible within uncertainties.

7.3.4.3 $t\bar{t}$ Fake Factor Corrections

Requiring both a muon and an electron (see Sec. 7.3.2.3) leads to a bias that needs to be accounted for by an adequate nonclosure correction: in $\mathrm{DR}_{t\bar{t}}$, the τ_h candidate will typically be a jet originating from a B meson, since both W bosons decay leptonically (as strongly suggested by the requirement of an electron and a muon in $\mathrm{DR}_{t\bar{t}}$). However, in the SR, a significant fraction of jets misidentified as τ_h are light jets originating from hadronic W boson decays, and thus the jet composition differs between $\mathrm{DR}_{t\bar{t}}$ and SR. The nonclosure correction in m_vis is derived from simulated $t\bar{t}$ events. For this purpose, the raw fake factors are re-derived from simulation and applied to estimate the $t\bar{t}$ background as a function of m_vis in the SR. It is compared to the actual simulated background and the ratio of the two, smoothed with a Gaussian kernel of variable width (see Fig. 7.9f) is applied as a multiplicative correction.

7.3.5 Validation of the Fake Factor Estimate

The modeling of the misidentified-τ_h background is validated in two ways: The misidentified-τ_h background estimate is compared to data in a dedicated control region containing events with a lepton pair of same-sign electric charge (SS validation region). In addition, the agreement of the background estimate is checked in several exclusive event categories, as listed in Tab. 7.1.

7.3.5.1 Validation in Control Regions

The SS validation region is characterized by the same event selection as for the SR, except for the requirement on the lepton pair to have the same electric charge. In order to avoid an overlap with the SS validation region the selection of $\mathrm{DR}_{\mathrm{QCD}}$ is altered: $0.1 < I^\mathrm{l}/p_\mathrm{T}^\mathrm{l} < 0.2$ for the $\tau_\mathrm{e}\tau_\mathrm{h}$ and $\tau_\mu\tau_\mathrm{h}$ final states, and a second τ_h that fulfills the `VeryLoose` but fails the `VeryTight` ID requirement in the $\tau_\mathrm{h}\tau_\mathrm{h}$ final state. Corre-

sponding QCD multijet fake factors as well as the misidentified-τ_h background composition in the SS validation region have been re-derived . The $m_{\tau\tau}$ distribution in the SS validation region in the $\tau_e\tau_h$, $\tau_\mu\tau_h$ and $\tau_h\tau_h$ final states is shown in Fig. 7.10. The data are compared to the sum of misidentified-τ_h background, $Z/\gamma^* \to \tau\tau$ signal, and other backgrounds in which the reconstructed τ_h is either due to a genuine τ_h or a misidentified electron or muon. A simultaneous ML fit to the observed $m_{\tau\tau}$ distributions is performed, similar to the fit described in Sec. 7.6.1. The $Z/\gamma^* \to \tau\tau$ signal as well as the background contributions are shown for the values of nuisance parameters obtained from the ML fit to the data (*post-fit* distributions). A good agreement is observed between the data and the background prediction in the SS validation region, which confirms the validity of the misidentified-τ_h estimate obtained through the fake factor method.

7.3.5.2 Validation in Event Categories

Category	Selection
0-jet	No jets and no b jets.
1-jet, low Z boson p_T	At least one jet, no b jets, $p_T^Z < 50$ GeV,
	and event not selected in 2-jet VBF category.
1-jet, medium Z boson p_T	At least one jet, no b jets, $50 < p_T^Z < 100$ GeV,
	and not selected as 2-jet VBF.
1-jet, high Z boson p_T	At least one jet, no b jets, $p_T^Z > 100$ GeV,
	and not selected as 2-jet VBF.
2-jet VBF	At least one pair of jets, no b jets.
1 b jet	Exactly one b jet.
2 b jet	Exactly two b jets.

Table 7.1: Event categories used to validate the modeling of backgrounds. Similar categories have been used in previous CMS H $\to \tau\tau$ analyses. [128]
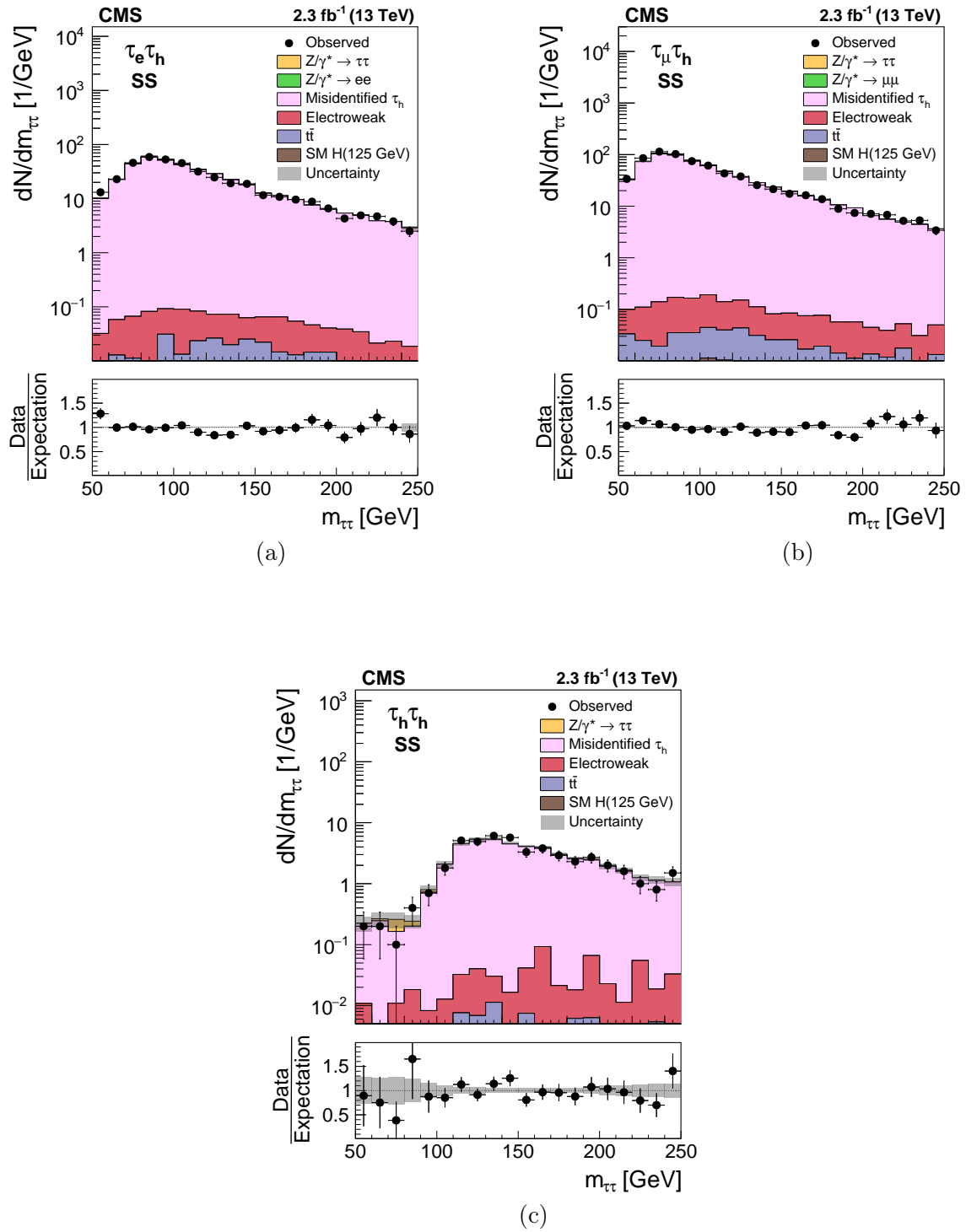
Figure 7.10: Post-fit distributions of $m_{\tau\tau}$ in the SS validation regions for the $\tau_e\tau_h$ (a), $\tau_\mu\tau_h$ (b) and $\tau_h\tau_h$ (c) final states compared to expected background contributions [128].

The event categories presented in Tab. 7.1 are based on the jet multiplicity, p_T of the tau lepton pair and the multiplicity of b jets. The transverse momentum of the Z boson (p_T^Z) is reconstructed by adding the momentum vectors from the visible τ decay products and the reconstructed $\vec{E}_T^{\text{miss}}$ in the transverse plane. The m_{jj} and $\Delta\eta_{jj}$ variables are used in the SM H $\rightarrow \tau\tau$ analysis to select VBF Higgs signal events, and refer to the mass and to the separation in η of the two jets of highest p_T in events containing two or more jets, respectively [30].

In order to account for different misidentified-τ_h background compositions in different exclusive event categories, the fractions w_{QCD}, w_{Wjets} and $w_{t\bar{t}}$ are determined separately for each category. Distributions of $m_{\tau\tau}$ for the $\tau_\mu\tau_h$ final state are shown in Figs. 7.11 - 7.12. Corresponding distributions for the $\tau_e\tau_h$ and $\tau_h\tau_h$ final states can be found in Apps. A.1.3 - A.1.4. A simultaneous ML fit to the observed $m_{\tau\tau}$ distributions is performed independently for each category. The procedure is similar to the fit described in Sec. 7.6.1. The good agreement in all exclusive categories in the $\tau_e\tau_h$, $\tau_\mu\tau_h$ and $\tau_h\tau_h$ final states further confirms the reliability of the fake factor method.

7.4 Estimation of Other Backgrounds

Besides the misidentified-τ_h background in the $\tau_e\tau_h$, $\tau_\mu\tau_h$ and $\tau_h\tau_h$ final states, three other sizeable backgrounds exist:

- The QCD multijet background in the $\tau_e\tau_\mu$ and $\tau_\mu\tau_\mu$ final states.

- The $t\bar{t}$ background in the $\tau_e\tau_\mu$ final state.

- $Z/\gamma^* \rightarrow \mu\mu$ background in the $\tau_\mu\tau_\mu$ final state.

In the $\tau_e\tau_\mu$ and the $\tau_\mu\tau_\mu$ final states, background contributions from QCD multijet events are estimated in a control region that contains events with an electron and a muon or two muons of same electric charge, respectively. To arrive at an estimate of the QCD multijet background in the SR, the yield in the same charge region is scaled by a suitable extrapolation factor that is defined by the ratio of eμ or $\mu\mu$ pairs with opposite electric charge to those with same electric charge (OS/SS ratio). This ratio is obtained in events in which at least one lepton passes an inverted isolation criterion of $I^l < 0.15 \cdot p_T^l$ and both leptons satisfy a relaxed isolation criterion of $I^l < 0.6 \cdot p_T^l$. The requirement $I^l < 0.15 \cdot p_T^l$ ensures that the isolated sideband region (SB1) does not overlap with the SR. Since the measured OS/SS ratio is found to depend on the lepton kinematics the ratio is measured as function of p_T of the two leptons l and l'
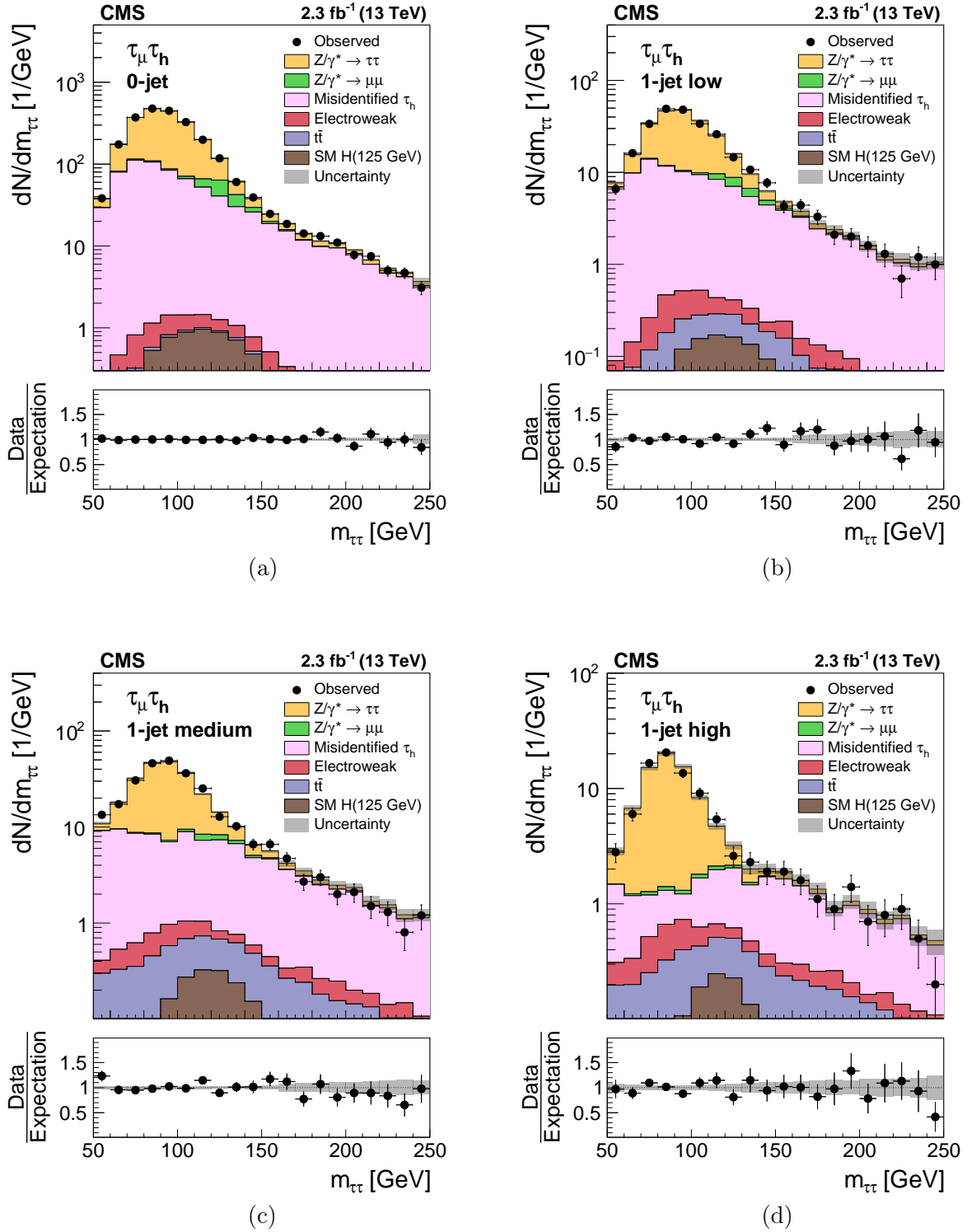
Figure 7.11: Post-fit distributions of $m_{\tau\tau}$ in different exclusive event categories in the $\tau_\mu\tau_h$ final state: 0-jet (a), 1-jet low (b), 1-jet medium (c) and 1-jet high Z boson p_T (d) [128].
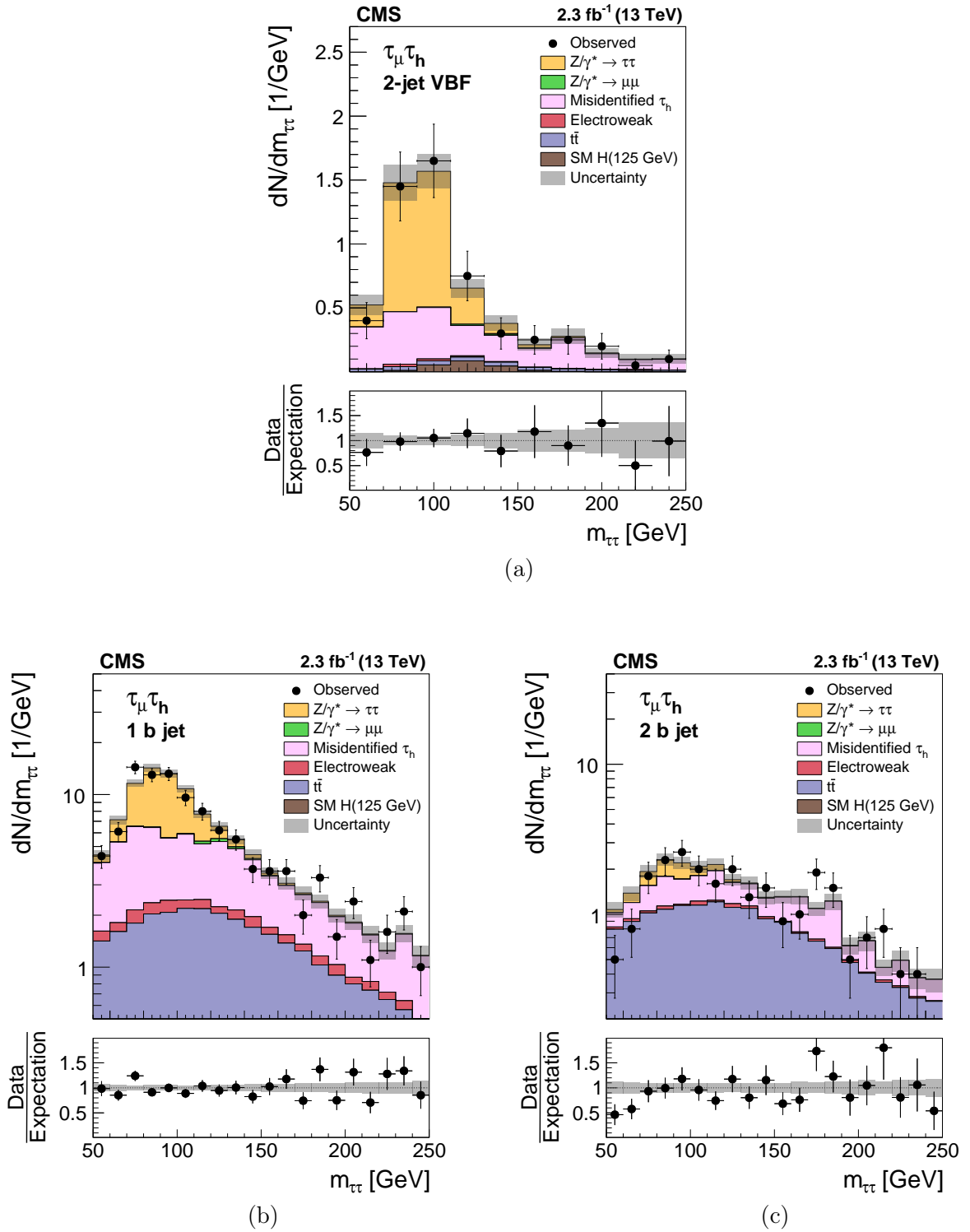
Figure 7.12: Post-fit distributions of $m_{\tau\tau}$ in different exclusive event categories in the $\tau_\mu\tau_h$ final state: 2-jet VBF (a), 1 b jet (b) and 2 b jet (c) [128].

and their separation $\Delta R(l,l') = \sqrt{(\eta_l - \eta_{l'})^2 + (\phi_l - \phi_{l'})^2}$ in the $\eta - \phi$ plane. The systematic uncertainty arising from the upper limit on I^l/p_T^l is estimated by taking the difference between the OS/SS ratio in SB1 and in a different isolation sideband region (SB2) that is defined by requiring at least one of the two leptons to pass the condition $I^l > 0.6 \cdot p_T^l$. Contributions to SB1 and SB2 from backgrounds other than QCD multijet production are subtracted using simulation.

For the modeling of the $t\bar{t}$ background the $m_{\tau\tau}$ distribution is taken from simulation, while the $t\bar{t}$ event yield in the SR is determined from data. This is true for the $t\bar{t}$ background in the $\tau_e\tau_\mu$ and the $\tau_\mu\tau_\mu$ final states, and in the $\tau_e\tau_h$, $\tau_\mu\tau_h$ and $\tau_h\tau_h$ final states, for the part of the $t\bar{t}$ background that is not described by the fake factor method, namely background contributions that are either due to genuine τ_h or due to misidentification of an electron or muon as τ_h. For this purpose, events in a $t\bar{t}$ enriched control region are required to satisfy selection criteria that are similar to the requirements for the SR in the $\tau_e\tau_\mu$ final state, except for an inverted D_ζ cut, $D_\zeta < -40$ GeV, and the requirement $E_T^{miss} > 80$ GeV. The observed $t\bar{t}$ event yield in this control region is a 1.01 ± 0.07 multiple of the expectation from simulation and is applied as scale factor to simulated $t\bar{t}$ events in the SR.

The $Z/\gamma^* \to \mu\mu$ background and contributions from remaining minor backgrounds, e.g. backgrounds from single top quark and diboson production, are estimated using simulation.

7.5 Systematic Uncertainties

The systematic uncertainties that can alter the normalization and the $m_{\tau\tau}$ mass spectrum in $Z/\gamma^* \to \tau\tau$ signal or background processes can be categorized into theory-related and experimental sources. The latter can be further subdivided into those associated with the fake factor method and uncertainties associated with the reconstruction of physical objects and with remaining background estimates.

7.5.1 Fake Factor-Specific Uncertainties

Fake factor-related systematic uncertainties comprise statistical uncertainties on the fake factor measurement and uncertainties on the relevant corrections and estimated fractions:

- Statistical uncertainties in the fake factor measurement in $\mathrm{DR_{QCD}}$, $\mathrm{DR_{W+jets}}$ and $\mathrm{DR_{t\bar{t}}}$, see e.g. Figs. 7.6 and 7.8 for the $\tau_\mu\tau_\mathrm{h}$ fake factors. Due to their statistical nature, they are uncorrelated, except for $\mathrm{FF_{t\bar{t}}}$ where the same measurement is used for the $\tau_\mathrm{e}\tau_\mathrm{h}$ and $\tau_\mu\tau_\mathrm{h}$ final states. Overall they constitute five nuisance parameters for the $\tau_\mathrm{e}\tau_\mathrm{h}$ and $\tau_\mu\tau_\mathrm{h}$ final states and one nuisance parameter for the $\tau_\mathrm{h}\tau_\mathrm{h}$ final state.

- Systematic uncertainties related to the $\mathrm{FF_{QCD}}$ corrections, see e.g. Fig. 7.9 for the $\tau_\mu\tau_\mathrm{h}$ final state. The uncertainties are added in quadrature for each final state individually, hence adding one nuisance parameter per final state:

  - Uncertainty in the nonclosure correction.
  - Uncertainty in the $I^\mathrm{l}/p_\mathrm{T}^\mathrm{l}$-dependent correction (only in the $\tau_\mathrm{e}\tau_\mathrm{h}$ and $\tau_\mu\tau_\mathrm{h}$ final states).
  - Uncertainty in the extrapolation from the same-sign ($\mathrm{DR_{QCD}}$) to the opposite-sign electric charge region (SR) .

- Systematic uncertainties related to the $\mathrm{FF_{W+jets}}$ corrections, see e.g. Fig. 7.9 for the $\tau_\mu\tau_\mathrm{h}$ final state. The uncertainties are added in quadrature for each final state individually, hence adding one nuisance parameter each for the $\tau_\mu\tau_\mathrm{h}$ and $\tau_\mathrm{e}\tau_\mathrm{h}$ final state:

  - Uncertainty in the nonclosure correction.
  - Uncertainty in the m_T^l-dependent correction.

- Systematic uncertainties related to the $\mathrm{FF_{t\bar{t}}}$ corrections. The uncertainty in the nonclosure correction is the same for the $\tau_\mathrm{e}\tau_\mathrm{h}$ and the $\tau_\mu\tau_\mathrm{h}$ final state and is fully correlated, adding one nuisance parameter in total.

- Systematic uncertainties in the fraction of W+jets, Z+jets and $t\bar{t}$ events with one misidified-τ_h in the AR, adding one nuisance parameter for the $\tau_\mathrm{h}\tau_\mathrm{h}$ final state.

Uncertainties in the misidentified-τ_h background composition in the AR are obtained by changing w_QCD, $w_\mathrm{W+jets}$, $w_\mathrm{t\bar{t}}$ and $w_{\mathrm{Z}/\gamma^* \to \ell\ell}$ within their respective uncertainties. Since the changes on the overall fake factor shape and yield are negligible and well covered with the respective uncertainties in the fake factor measurements, these uncertainties are not considered. As outlined in Sec. 7.3.1, measured fake factors in W+jets events are used to estimate the $Z/\gamma^* \to \ell\ell$ misidentified-τ_h background. Studies of simulated

$Z/\gamma^* \rightarrow \ell\ell$ and W+jets events yield similar fake factors with maximum deviations of 30%. These deviations are taken into account as up and down variations on the fraction of $Z/\gamma^* \rightarrow \ell\ell$ events that are covered with W+jets fake factors.

All uncertainties enter as shape uncertainties. Figure 7.13 shows the $m_{\tau\tau}$ distributions for the misidentified-τ_h background as well as the resulting pre-fit uncertainties in the $\tau_e\tau_h$, $\tau_\mu\tau_h$ and $\tau_h\tau_h$ final states.
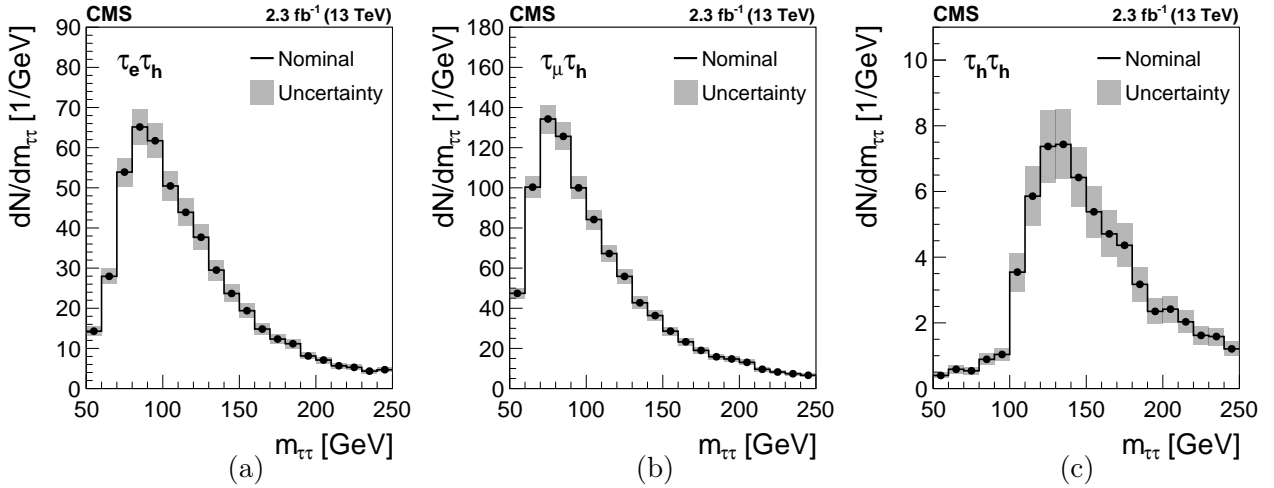
Figure 7.13: Distributions of $m_{\tau\tau}$ for the expected misidentified-τ_h background in the $\tau_e\tau_h$ (a), $\tau_\mu\tau_h$ (b) and $\tau_h\tau_h$ (c) final states [128]. The pre-fit fake factor-related systematic uncertainties are represented by the grey shaded band.

7.5.2 Other Uncertainties

The uncertainties not related to the fake factor method are summarized in Tab. 7.2. A 3% change in the τ_h ES affects the $Z/\gamma^* \rightarrow \tau\tau$ signal yield by 3, 3 and 17% in the $\tau_e\tau_h$, $\tau_\mu\tau_h$ and $\tau_h\tau_h$ final states, respectively. The τ_h ID and trigger efficiency is measured with an uncertainty of 6% [88]. The e $\rightarrow \tau$ misidentification rates are measured with 13% and 29% accuracy in the ECAL barrel and the endcap regions, respectively. The uncertainty on the $t\bar{t}$ background distribution is taken into account by changing the weights that are applied to the $t\bar{t}$ MC samples in order to improve the modeling of the top p_T distribution. The uncertainty corresponds to 100% of the correction. Due to the topological D_ζ cut the affect on the signal yield is relatively strong in the $\tau_e\tau_\mu$ final state (6%) and small (1%) in the other final states. The uncertainties in the yields of single top quark and diboson simulation samples are $\approx 15\%$. The yields of simulated W+jets samples that are used in the $\tau_e\tau_\mu$ and $\tau_\mu\tau_\mu$ final states are known to an accuracy of 15%. The SM Higgs boson production is assigned an uncertainty of 30%. This

reflects the experimental uncertainty in the $H \to \tau\tau$ rate measured at a center-of-mass energy of 13 TeV [30]. The theoretical uncertainty in the product of acceptance and efficiency for the $Z/\gamma^* \to \tau\tau$ signal amounts to $\approx 2\%$ in the $\tau_e\tau_h$, $\tau_\mu\tau_h$, $\tau_e\tau_\mu$ and $\tau_\mu\tau_\mu$ final states and to $\approx 6\%$ in the $\tau_h\tau_h$ final state.

The table also quantifies the impact that each systematic uncertainty has on the $Z/\gamma^* \to \tau\tau$ cross section measurement. It is defined as the percent change in the cross section measurement when individual sources are varied by one standard deviation relative to their nominal value. The impacts are computed for post-fit values of the nuisance parameters. The largest impact is observed for the uncertainty on the integrated luminosity and the uncertainty on the normalization of the $Z/\gamma^* \to ee$ ($Z/\gamma^* \to \mu\mu$) process, followed by electron, muon and τ_h ID and trigger efficiencies. The impact of the integrated luminosity uncertainty is smaller than the 2.3% uncertainty in the integrated luminosity measurement [138]. This is caused by correlations of the luminosity nuisance parameter with other nuisance parameters. The $Z/\gamma^* \to ee$ and $Z/\gamma^* \to \mu\mu$ production cross sections are left unconstrained in the fit, such that the integrated luminosity does not get further constrained by the large $Z/\gamma^* \to \mu\mu$ background in the $\tau_\mu\tau_\mu$ final state.

7.6 Results

7.6.1 Signal Extraction

The product of cross section times branching ratio, $\sigma\,(pp \to Z/\gamma^* + X) \times \mathcal{B}\,(Z/\gamma^* \to \tau\tau)$, is obtained through a simultaneous ML fit to the observed $m_{\tau\tau}$ distributions in the $\tau_e\tau_h$, $\tau_\mu\tau_h$, $\tau_h\tau_h$, $\tau_e\tau_\mu$ and $\tau_\mu\tau_\mu$ final states. The likelihood function to extract the signal is of the form

$$\mathcal{L}(\text{data}|\xi \cdot s(\theta) + b(\theta)) = \prod_i \mathcal{P}(k_i|\xi \cdot s_i(\theta) + b_i(\theta)) \times \prod_j \mathcal{C}(\hat{\theta}_j|\theta_j), \qquad (7.7)$$

where i labels all bins of the input distributions with event numbers k_i in all final states and all control regions, and j denotes all nuisance parameters. The term ξ corresponds to a scaling parameter for a given signal s_i, b_i to the prediction of all backgrounds in bin i and θ_j to a given nuisance parameter. The probability to observe k_i events in a

Source	Applies to	Shape	Change in yield	Impact
Integrated luminosity	Simulation estimates	$-$	2.3%	1.9%
τ_h ID and trigger	Simulation estimates	$-$	$6-12\%$	1.5%
τ_h ES	Simulation estimates	$\checkmark$	$3-17\%$	$< 0.1\%$
Rate of e misidentified as τ_h	Z/$\gamma^* \to$ ee	$-$	$13-29\%$	0.4%
Rate of μ misidentified as τ_h	Z/$\gamma^* \to \mu\mu$	$-$	30%	0.2%
Electron ID and trigger	Simulation estimates	$-$	2%	1.5%
Electron ES	Simulation estimates	$\checkmark$	$< 1\%$	0.2%
Muon ID and trigger	Simulation estimates	$-$	2%	1.6%
E_T^{miss} response and resolution	Simulation estimates	$-$	$< 1\%$	0.2%
Z/$\gamma^* \to$ ee, $\mu\mu$	Z/$\gamma^* \to$ ee, $\mu\mu$	$-$	Unconstrained	1.8%
QCD multijet	QCD multijet in $\tau_e\tau_\mu$, $\tau_\mu\tau_\mu$	$\checkmark$	20%	0.2%
t$\bar{\text{t}}$	t$\bar{\text{t}}$	$-$	7%	1.0%
Shape of t$\bar{\text{t}}$	t$\bar{\text{t}}$	$\checkmark$	$1-6\%$	$< 0.1\%$
SM H	SM H	$-$	30%	$< 0.1\%$
Single top quark	Single top quark	$-$	15%	$< 0.1\%$
Diboson	Diboson	$-$	15%	0.2%
W+jets	W+jets in $\tau_e\tau_\mu$, $\tau_\mu\tau_\mu$	$-$	15%	$< 0.1\%$
PDF	Signal	$-$	1%	1.0%
Scale dependence	Signal	$-$	$\leq 6\%$	0.5%
UE and parton showers	Signal	$-$	1%	1.0%

Table 7.2: Experimental and theoretical uncertainties in the Z/$\gamma^* \to \tau\tau$ cross section measurement [128]. The relative change in the yield corresponds to a one standard deviation change in a corresponding source of uncertainty. Fake factor specific uncertainties are not listed.

given bin i is expressed by the Poisson distribution:

$$\mathcal{P}(k_i | \xi \cdot s_i(\theta) + b_i(\theta)) = \frac{(\xi \cdot s_i(\theta) + b_i(\theta))^{k_i}}{k_i!} \exp\left(-(\xi \cdot s_i(\theta) + b_i(\theta))\right). \qquad (7.8)$$

The function $\mathcal{C}(\hat{\theta}_j | \theta_j)$ corresponds to the probability density function used to implement the uncertainty that is related to the nuisance parameter θ_j, where $\hat{\theta}_j$ is the estimate for θ_j from the fit to the data. The incorporation of the nuisance parameters, treated by the frequentist paradigm [139, 140], distinguishes between:

- Systematic uncertainties that affect the normalization but not the $m_{\tau\tau}$ distribution. They are represented by the Gamma function if they are statistical in origin and by log-normal probability density functions, if otherwise.

- Systematic uncertainties that affect the $m_{\tau\tau}$ distribution (shape uncertainties) are represented by Gaussian probability density functions and are incorporated in the fit via the technique described in Ref. [141].

The number of background events $b_i(\theta)$ in bin i is the sum of all background processes, as described in Secs. 7.3 - 7.4. Correlations among final states as well as between the $Z/\gamma^* \to \tau\tau$ signal and backgrounds are taken into account through relationships among final states, processes and nuisance parameters in the ML fit.

The best fit value $\hat{\xi}$ of the *parameter of interest* (POI) denotes the value that maximizes the likelihood function $\mathcal{L}(\text{data} | \xi \cdot s(\theta) + b(\theta))$ in Eq. (7.7). The result of the fit gives the best-fit values for the nuisance parameters, $\hat{\theta}_j$, and their uncertainties $\hat{\sigma}_{\theta_j}$. In order to quantify the best-fit values of the nuisance parameters with respect to the pre-fit values the corresponding *pulls* are calculated:

$$\text{pull}(\theta_j^{\text{pre}}) = \frac{\hat{\theta}_j - \theta_j^{\text{pre}}}{\hat{\sigma}_{\theta_j}}, \qquad (7.9)$$

, where θ_j^{pre} denotes the pre-fit nuisance parameters. To obtain a 68% CI on the POI, the *profile likelihood ratio* (PLR) [139, 140] $\lambda(\xi)$ is used, which is defined as:

$$\lambda(\xi) = \frac{\mathcal{L}(\text{data} | \xi \cdot s(\hat{\theta}_\xi) + b(\hat{\theta}_\xi))}{\mathcal{L}(\text{data} | \hat{\xi} \cdot s(\hat{\theta}_{\hat{\xi}}) + b(\hat{\theta}_{\hat{\xi}}))}, \qquad (7.10)$$

where $\hat{\theta}$ indicates the obtained best-fit values from the fit to the data and $\hat{\xi}$ indicates that the fit has been performed for ξ fixed to its best-fit value. The 68% CI is defined by

the values of ξ for which $-2\ln\lambda(\xi)$ increases by one unit relative to its minimum. This procedure is justified since the distribution $-2\ln\lambda(\xi)$ approaches a $\chi^2(1)$ distribution in the limit of a large data sample.

The likelihood scan for the cross section ξ is illustrated in Fig. 7.14 for the combined fit of all five final states. Nuisance parameters θ_k corresponding to uncertainties that are ignored in a given likelihood scan are fixed at values $\hat{\theta}_k$ that produce the best fit to the data. This procedure is reflected in the "Stat. + syst. uncertainty" and "Stat. uncertainty" curves where the nuisance parameters corresponding to the integrated luminosity, and to other systematic uncertainties, are successively fixed in the ML fit.
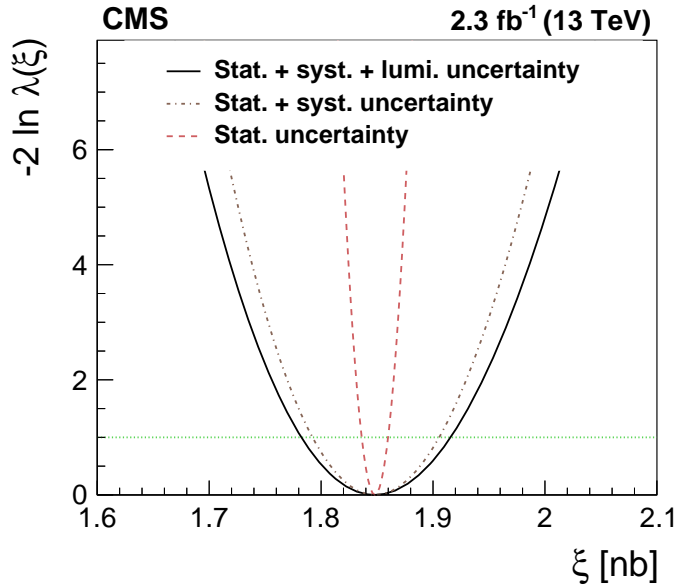
Figure 7.14: Dependence of $-2\ln\lambda(\xi)$ on the cross section ξ [128]. $\lambda(\xi)$ is computed for the simultaneous ML fit to the observed $m_{\tau\tau}$ distributions in all final states. The three curves correspond to the case that only statistical uncertainties, in addition systematic uncertainties and all uncertainties are included in the fit. The horizontal line at $-2\ln\lambda(\xi) = 1$ is used to determine the 68% CI on ξ.

Post-fit distributions of $m_{\tau\tau}$ for selected events in the inclusive SR are shown in Fig. 7.15 for the $\tau_e\tau_h$, $\tau_\mu\tau_h$ and $\tau_h\tau_h$ final states and in Fig. 7.16 for the $\tau_e\tau_\mu$ and $\tau_\mu\tau_\mu$ final states. The post-fit distribution and the corresponding uncertainties are derived based on the pulls and uncertainties of the individual nuisance parameters in the ML fit.
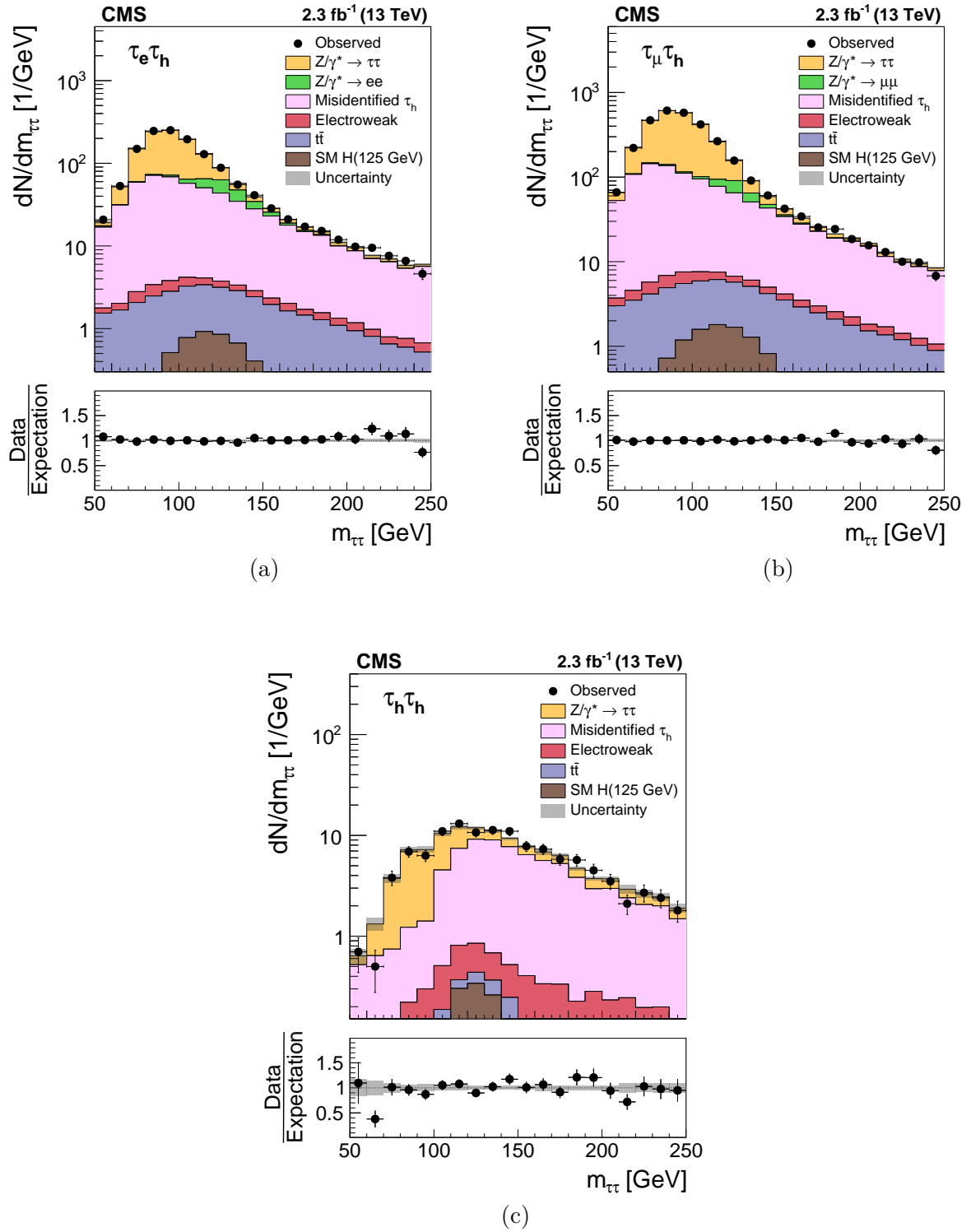
Figure 7.15: Post-fit distributions of $m_{\tau\tau}$ in the $\tau_e\tau_h$ (a), $\tau_\mu\tau_h$ (b) and $\tau_h\tau_h$ (c) final states [128].
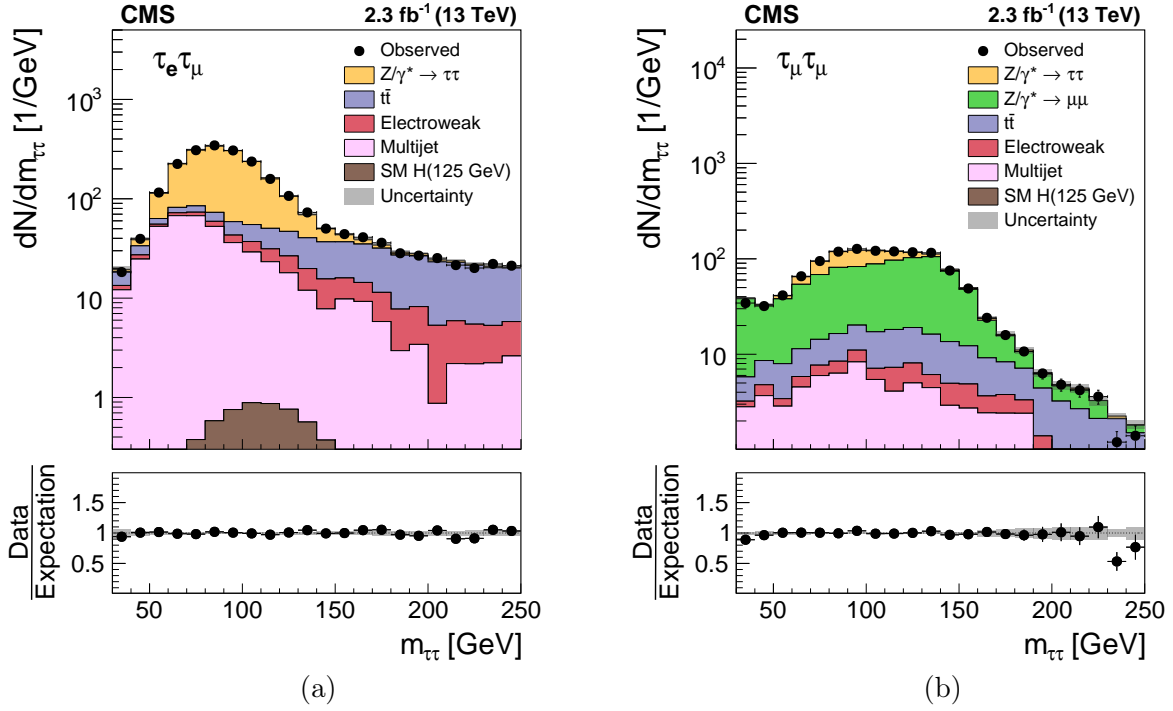
Figure 7.16: Post-fit distributions of $m_{\tau\tau}$ in the $\tau_\mu\tau_e$ (a) and $\tau_\mu\tau_\mu$ (b) final states [128].

7.6.2 Cross Section and Likelihood Contours

The pp → Z/γ* + X → ττ cross section is obtained within the mass window 60 GeV < $m_{\tau\tau}$ < 120 GeV. In the $\tau_e\tau_h$, $\tau_\mu\tau_h$, $\tau_e\tau_\mu$ and $\tau_\mu\tau_\mu$ final states, contributions from Z/γ* → ττ events that have a mass outside this window are at the level of a few percent. However, in the $\tau_h\tau_h$ channel, the contribution is about 40%. This is caused by the high p_T threshold (p_T > 40 GeV) for the two τ_h candidates. Signal events that contain two τ_h with p_T > 40 GeV either contain a high-p_T Z boson or a τ_h pair above the mass of the Z boson. Since only a small fraction of signal events pass either of these two conditions, the Z/γ* → ττ event yield is small, see Fig. 7.15c, and a large fraction of signal events contain tau lepton pairs outside the mass window 60 GeV < $m_{\tau\tau}$ < 120 GeV. The measured cross section is shown in Fig. 7.17. A ML fit to the observed $m_{\tau\tau}$ distributions is performed in the five individual final states as well as a simultaneous ML fit in the combination of all final states. For the latter the resulting cross section with uncertainties decomposed into statistical, systematic and luminosity-related uncertainties amounts to:

$$\sigma(\text{pp} \to \text{Z}/\gamma^*+\text{X}) \times \mathcal{B}(\text{Z}/\gamma^* \to \tau\tau) =$$

$$1848 \pm 12 \text{ (stat.)} \pm 57 \text{ (syst.)} \pm 35 \text{ (lumi.) pb} . \qquad (7.11)$$

Channel	$\sigma(pp \to Z/\gamma^*+X) \times \mathcal{B}(Z/\gamma^* \to \tau\tau)$ [pb]
$\tau_e\tau_h$	1799 ± 29 (stat.) ± 120 (syst.) ± 34 (lumi.)
$\tau_\mu\tau_h$	1784 ± 17 (stat.) ± 117 (syst.) ± 34 (lumi.)
$\tau_h\tau_h$	1477 ± 137 (stat.) ± 270 (syst.) ± 30 (lumi.)
$\tau_e\tau_\mu$	1851 ± 19 (stat.) ± 58 (syst.) ± 34 (lumi.)
$\tau_\mu\tau_\mu$	1967 ± 121 (stat.) ± 92 (syst.) ± 37 (lumi.)

Table 7.3: Cross section $\sigma(pp \to Z/\gamma^*+X) \times \mathcal{B}(Z/\gamma^* \to \tau\tau)$ measured individually in the $\tau_e\tau_\mu$, $\tau_\mu\tau_h$, $\tau_h\tau_h$, $\tau_e\tau_\mu$ and $\tau_\mu\tau_\mu$ final states [128].

The result is compatible with the theory prediction of 1845^{+12}_{-6} (scale) ± 33 (PDF) pb, computed at NNLO accuracy [142] using the NNPDF3.0 PDFs [133].
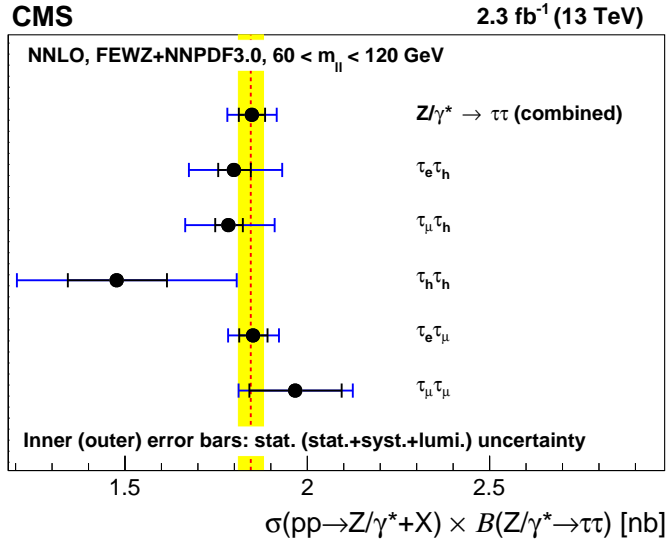
Figure 7.17: The inclusive cross section $\sigma(pp \to Z/\gamma^*+X) \times \mathcal{B}(Z/\gamma^* \to \tau\tau)$ measured in five individual final states and in the combination of all final states [128].

The results on the cross section measurement in the five individual final states are summarized in Tab. 7.3. The obtained values are compatible with each other. The largest deviation is observed in the $\tau_h\tau_h$ channel and amounts to a little more than one standard deviation with respect to the combined result.. Event yields for $Z/\gamma^* \to \tau\tau$ signal events and backgrounds in the five individual final states are listed in App. A.1.5.

A simultaneous ML fit to the $m_{\tau\tau}$ distributions observed in the $\tau_e\tau_h$, $\tau_\mu\tau_h$, $\tau_h\tau_h$, $\tau_e\tau_\mu$ and $\tau_\mu\tau_\mu$ final states is used to measure the τ_h ID efficiency and the τ_h ES. For this measurement, the single POI ξ is replaced by a three-component vector, $\vec{\xi} = (\xi_1, \xi_2, \xi_3)$, with ξ_1 corresponding to $\sigma\left(\text{pp} \to \text{Z}/\gamma^* + \text{X}\right) \times \mathcal{B}\left(\text{Z}/\gamma^* \to \tau\tau\right)$, ξ_2 to the τ_h ID efficiency and ξ_3 to the τ_h ES. The likelihood function in Eq. (7.7) is then fitted as function of the three POIs. The nuisance parameters corresponding to the τ_h ID efficiency and the τ_h ES are removed for this fit. The likelihood contours for the joint parameter estimation are shown in Fig. 7.18. The third POI (the one that is not shown in a given likelihood contour) is profiled, i.e. its value is chosen such that the likelihood function $\mathcal{L}$ reaches its local maximum, for the given values of the other two POIs. Also shown in the plot are contours for which $-2\ln\ \sigma(\xi)$ exceeds its minimum value by 2.30 and 6.18 units, corresponding to a coverage of 68% and 95% in the two-dimensional plane. The measured values of the τ_h ID efficiency and the τ_h ES are quoted as data-to-simulation scale factors (SFs). The corresponding 68% CIs are obtained for the values of the respective parameter for which $-2\ln\lambda(\vec{\xi})$ increases by one unit relative to its minimum, when profiling the other two POIs in the fit. The resulting SFs amount to 0.979 ± 0.022 and 0.986 ± 0.009 for the τ_h ID efficiency and for the τ_h ES, respectively. Both SFs are compatible with unity within two standard deviations. It is to note that this τ_h ID efficiency measurement is the most precise measurement at the CMS experiment so far.
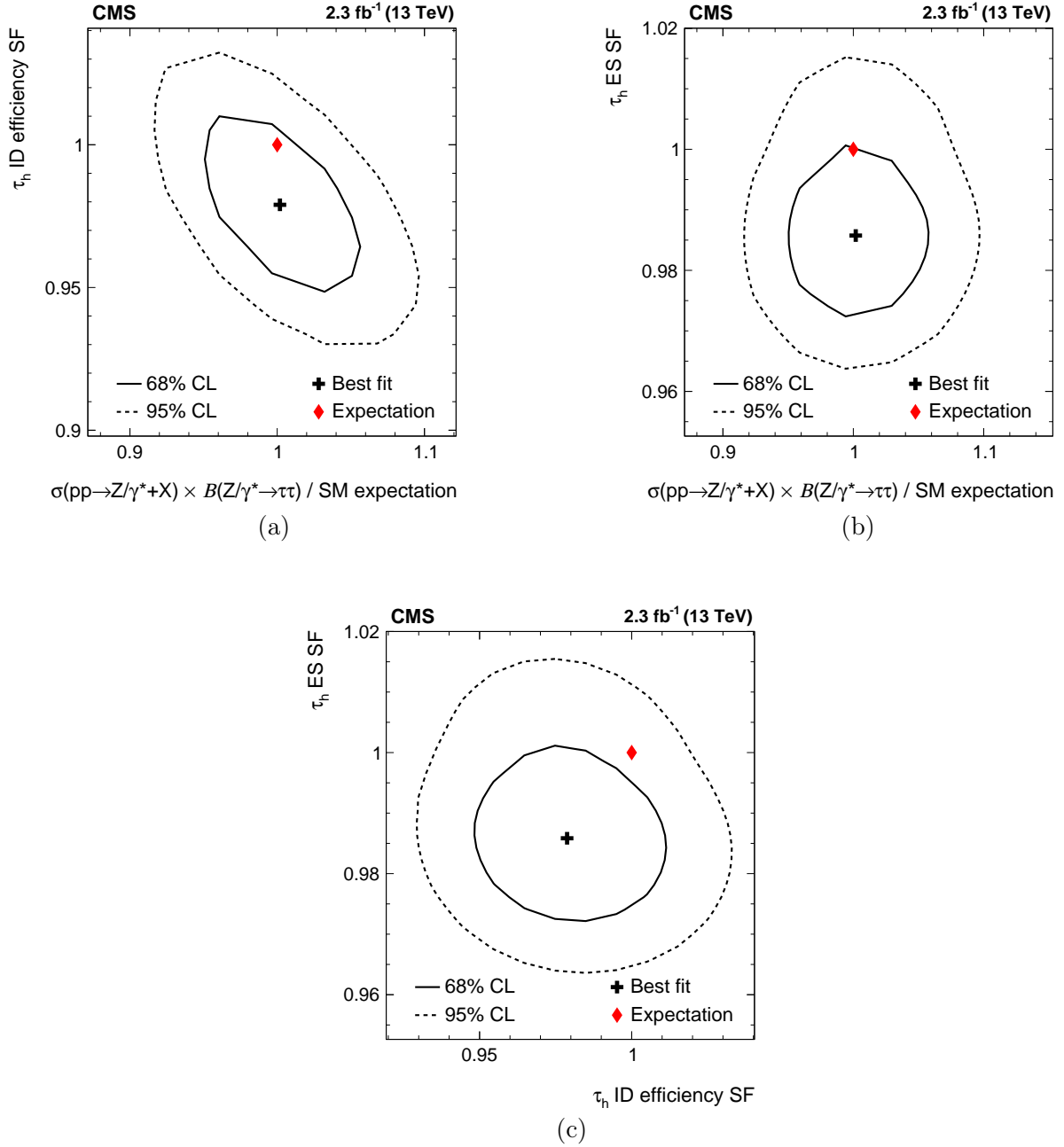
Figure 7.18: 2D likelihood contours for the joint parameter estimation of $\sigma(pp \to Z/\gamma^*+X) \times \mathcal{B}(Z/\gamma^* \to \tau\tau)$ and the τ_h ID efficiency (a), $\sigma(pp \to Z/\gamma^*+X) \times \mathcal{B}(Z/\gamma^* \to \tau\tau)$ and the τ_h ES (b), and the τ_h ES and the τ_h ID efficiency (c) [128].

Search for Additional Neutral MSSM Higgs Bosons in the $\tau\tau$ Final State in Proton-Proton Collisions at $\sqrt{s} = 13\,\text{TeV}$

In this chapter, a search for additional neutral Higgs bosons in the $\tau\tau$ final state is presented. The analysis strategies, the background estimation, and the discussion of systematic uncertainties are described in detail. The author carried out the analysis in the $\tau_{\text{e}}\tau_{\text{h}}$, $\tau_{\mu}\tau_{\text{h}}$ and $\tau_{\text{h}}\tau_{\text{h}}$ final states, estimated one of the most relevant backgrounds with the fake factor method and performed a dedicated cross-check analysis in the $\tau_{\text{e}}\tau_{\text{h}}$ and $\tau_{\mu}\tau_{\text{h}}$ final states. The results of the analysis have been submitted for publication [143].

The analysis is based on the 2016 proton-proton collision dataset recorded by the CMS experiment at 25 ns bunch spacing at a center-of-mass energy of 13 TeV, corresponding to an integrated luminosity of 35.9 fb^{-1}. Information on the 2016 run period is summarized in Sec. 3.1.

The event selection comprises the $\tau_{\text{e}}\tau_{\text{h}}$, $\tau_{\mu}\tau_{\text{h}}$, $\tau_{\text{h}}\tau_{\text{h}}$ and $\tau_{\text{e}}\tau_{\mu}$ final states. The expected sensitivity for the $\tau_{\text{e}}\tau_{\text{e}}$ and $\tau_{\mu}\tau_{\mu}$ final states is small compared to the other four final states, and therefore they are not considered in this analysis.

The final discriminative variable that is used for signal extraction is the *total transverse mass* of the tau lepton pair, $m_{\text{T}}^{\text{tot}}$ [118], defined as

$$m_{\text{T}}^{\text{tot}} = \sqrt{m_{\text{T}}^2(E_{\text{T}}^{\text{miss}}, \ell_1) + m_{\text{T}}^2(E_{\text{T}}^{\text{miss}}, \ell_2) + m_{\text{T}}^2(\ell_1, \ell_2)}, \tag{8.1}$$

where $\ell = \text{e}, \mu, \tau$ and the transverse mass $m_{\text{T}}(1, 2)$ between two objects (1,2) is given by

$$m_{\text{T}}(1, 2) = \sqrt{2p_{\text{T}}(1)p_{\text{T}}(2) \cdot (1 - \cos\Delta\phi(1, 2)}, \tag{8.2}$$

so that $m_{\mathrm{T}}(E_{\mathrm{T}}^{\mathrm{miss}}, \mathrm{l})$, where $\mathrm{l} = \mathrm{e}, \mu$, is equivalent to the transverse mass defined in Eq. (7.1).

8.1 Event Selection and Categorization

Objects are reconstructed as described in Sec. 4.2. To estimate the momentum imbalance in the transverse plane, the PF $\vec{E}_{\mathrm{T}}^{\mathrm{miss}}$ is used, see Sec. 4.2.7. Reconstructed jets (b jets) are required to fulfill $p_{\mathrm{T}} > 30$ GeV (20 GeV) and $|\eta| < 4.7$ (2.4). The selected events are recorded by a single-electron trigger in the $\tau_{\mathrm{e}}\tau_{\mathrm{h}}$ final state, a single-muon trigger in the $\tau_{\mu}\tau_{\mathrm{h}}$ final state, triggers based on the presence of two τ_{h} candidates in the $\tau_{\mathrm{h}}\tau_{\mathrm{h}}$ final state and triggers based on the presence of both an electron and a muon in the $\tau_{\mathrm{e}}\tau_{\mu}$ final state.

In the $\tau_{\mathrm{e}}\tau_{\mathrm{h}}$ ($\tau_{\mu}\tau_{\mathrm{h}}$) final state, selected offline events are required to contain an electron (a muon) of $p_{\mathrm{T}} > 26$ GeV (23 GeV) and $|\eta| < 2.1$, and a τ_{h} with $p_{\mathrm{T}} > 30$ GeV and $|\eta| < 2.3$. The electron (muon) is required to pass an isolation requirement of $I^{\mathrm{e}(\mu)} < 0.1$ $(0.15) \cdot p_{\mathrm{T}}^{\mathrm{e}(\mu)}$, computed according to Eq. (4.1). The selected τ_{h} is required to have an electric charge opposite to that of the light lepton and pass the `Tight` WP of the MVA-based τ_{h} ID discriminant. Additionally, in the $\tau_{\mathrm{e}}\tau_{\mathrm{h}}$ ($\tau_{\mu}\tau_{\mathrm{h}}$) final state, the τ_{h} is required to pass a tight (loose) MVA-based discriminant against electrons and a loose (tight) cut-based discriminant against muons. Events that contain additional electrons or muons, passing minimal kinematic, identification and isolation requirements, are rejected in order to reduce backgrounds from $\mathrm{Z}/\gamma^{*} \rightarrow \mathrm{ee}$, $\mathrm{Z}/\gamma^{*} \rightarrow \mu\mu$ and diboson events. A transverse mass cut of $m_{\mathrm{T}} < 70$ GeV is applied to reduce backgrounds originating from W+jets and $\mathrm{t}\bar{\mathrm{t}}$ production.

In the $\tau_{\mathrm{h}}\tau_{\mathrm{h}}$ final state, events are required to contain two selected τ_{h} candidates with $p_{\mathrm{T}} > 40$ GeV and $|\eta| < 2.1$ that satisfy a `Medium` ID criterion, have opposite-sign electric charge and satisfy minimal criteria on the discriminants used to separate τ_{h} from electrons and muons. As in the $\tau_{\mathrm{e}}\tau_{\mathrm{h}}$ and $\tau_{\mu}\tau_{\mathrm{h}}$ final states, events containing additional electrons or muons are rejected.

In the $\tau_{\mathrm{e}}\tau_{\mu}$ final state, the offline selection requires an electron with $p_{\mathrm{T}} > 13$ GeV and $|\eta| < 2.5$, and a muon with $p_{\mathrm{T}} > 10$ GeV and $|\eta| < 2.4$, where either the electron or the muon is required to pass a threshold of $p_{\mathrm{T}} > 24$ GeV. Furthermore, the electron-muon pair is required to have opposite-sign electric charge and each lepton has to satisfy the isolation criterion $I^{\mathrm{e}(\mu)} < 0.15(0.20) \cdot p_{\mathrm{T}}^{\mathrm{e}(\mu)}$. Events containing an additional electron or muon are rejected. The $\mathrm{t}\bar{\mathrm{t}}$ background is reduced by requiring a cut on the topological discriminant $D_{\zeta} > -50$ GeV.

To further increase the sensitivity of the analysis, selected events in every final state are categorized into a *b-tag* and a *no b-tag* category. The b-tag category is designed to target Higgs boson production in association with b quarks and requires that events contain at least one b-tagged jet. All other events are assigned to a no b-tag category. In the $\tau_e\tau_h$ and $\tau_\mu\tau_h$ final states, these event categories are further split into two subcategories based on m_T^l:

- Tight-m_T: $m_T^l < 40$ GeV

- Loose-m_T: 40 GeV $< m_T^l < 70$ GeV.

In the $\tau_e\tau_\mu$ final state, a subcategorization is introduced based on the D_ζ variable:

- Low-D_ζ: -50 GeV $< D_\zeta < -10$ GeV

- Medium-D_ζ: -10 GeV $< D_\zeta < 30$ GeV

- High-D_ζ: $D_\zeta > 30$ GeV.

Most of the signal events in the respective final states fall into the tight-m_T and medium-D_ζ subcategories. However, the loose-m_T and low-/high-D_ζ subcategories increase the signal acceptance, particularly for high-mass hypotheses, and are hence added to the analysis with respect to previous analyses [125, 126]. In the $\tau_h\tau_h$ final state, no further subcategorization is applied.

In total 16 event categories enter the statistical analysis. An illustration of the complete event categorization is shown in Fig. 8.1. Additionally, Z $\rightarrow \mu\mu$ and t$\bar{\text{t}}$ control regions are introduced, as described in Sec. 8.4. In Fig. 8.2, the inclusive m_T^μ and D_ζ distributions are shown for the $\tau_\mu\tau_h$ and $\tau_\mu\tau_e$ final state, respectively, before applying any event subcategorization. A detailed discussion of the different background compositions is given in Secs. 8.3 - 8.4.

8.2 Event Simulation

The MC event generators used for the modeling of signal and background processes are very similar to the generators described in Sec. 7.2. The Z/$\gamma^* \rightarrow \ell\ell$ and W+jets background processes are modeled using the MADGRAPH_aMC@NLO event generator at LO accuracy. Additional Z/$\gamma^* \rightarrow \ell\ell$ and W+jets samples have been generated with different numbers of additional jets. Diboson events are modeled using the
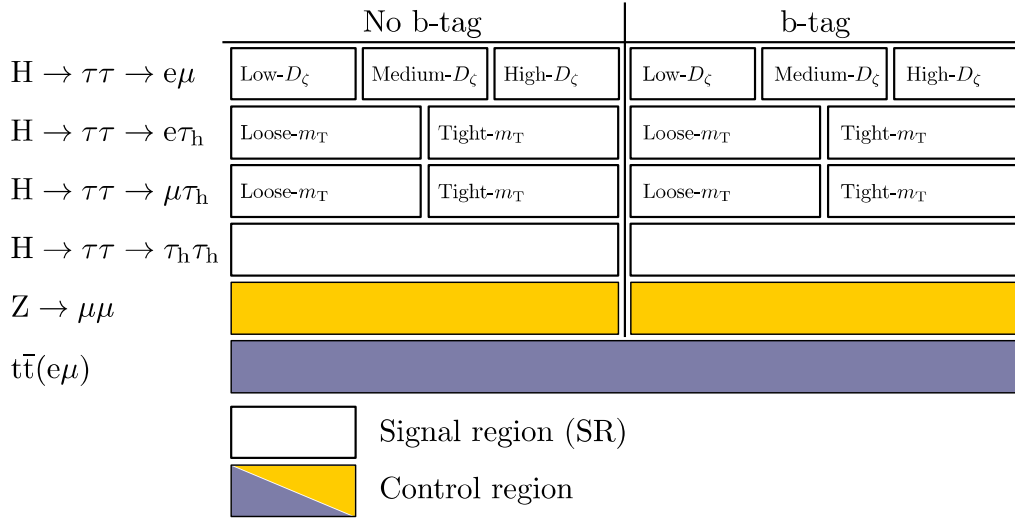
Figure 8.1: Overview of the sixteen signal subcategories and three background control regions [143]. All displayed subcategories enter the statistical analysis described in Sec. 8.6.1.
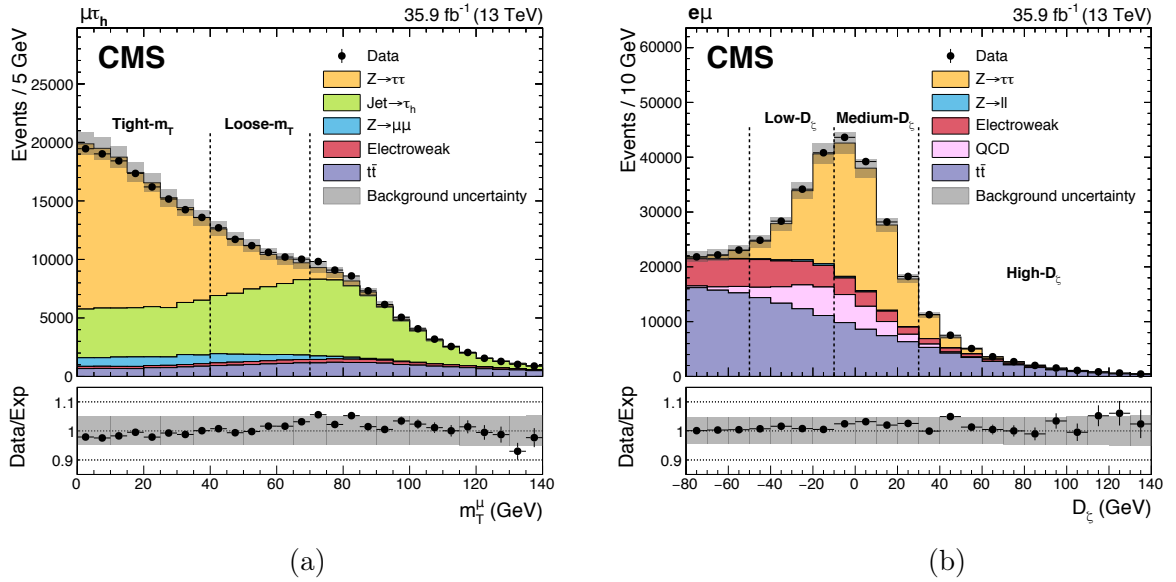
Figure 8.2: Observed and expected distributions of D_ζ (a) and m_T^μ (b) in the $\tau_e\tau_\mu$ and $\tau_\mu\tau_h$ final states, respectively [143]. The distributions are shown before applying a ML fit as used for the signal extraction, see Sec. 8.6.1. No shape affecting uncertainties are displayed. The definition of the subcategories is indicated by the dashed vertical lines.

MADGRAPH_aMC@NLO event generator at NLO accurancy, single top quark and
$t\bar{t}$ processes are modeled using NLO calculations, implemented in POWHEG v2. SM
Higgs boson processes complement the backgrounds. They include ggF, VBF and as-
sociated vector boson production (ZH, WH) and are modeled with POWHEG.

The targeted Higgs boson production process in association with b quarks is modeled
with MADGRAPH_aMC@NLO at NLO accuracy. The ggF signal process is simulated
at LO using PHYTIA 8.212. To improve the modeling of the ggF signal, the Higgs
boson p_T distribution is reweighted using POWHEG at NLO precision. The p_T spectra
corresponding to the t quark, the b quark as well as the tb interference contributions
to the initial loop are calculated individually following Refs. [144–146].

All samples are produced based on the NNPDF3.0 [131–133] set of PDFs, parton shower
and hadronization are modeled using PYTHIA 8.212 [66] with the CUETP8M1 [134]
underlying event tune.

The cross sections for $Z/\gamma^* \to \ell\ell$, W+jets and $t\bar{t}$ events are computed at NNLO accu-
racy and the cross sections for single top quark and diboson events are computed at
NLO accuracy to the generation.

8.2.1 Data-to-Simulation Corrections

Several corrections are derived to account for differences between data and simula-
tion. The corrections comprise most of the ones described in Sec. 7.2.1, but are mea-
sured using the 2016 dataset, including PU reweighting, lepton ID and isolation scale
factors, τ_h ID scale factors, scale factors for b tagged jets, a reweighting of the top
quark p_T in $t\bar{t}$ events and of the Z boson p_T in $Z/\gamma^* \to \ell\ell$ events, as well as fake rate
and fake energy scale corrections for light leptons being misidentified as τ_h.

8.3 Estimation of the Misidentified-τ_h Background with the Fake Factor Method

The misidentified-τ_h background in the $\tau_e\tau_h$, $\tau_\mu\tau_h$ and $\tau_h\tau_h$ final states is estimated
using the fake factor method, as introduced in Sec. 7.3. The large increase in collision
data, which amounts to an increase in integrated luminosity of roughly a factor of
15, allows to extend the method in order to exploit its statistical power in high-p_T
regions. However, it is to note that the general concept of the method stays the same.
For further description, it is useful to define an inclusive SR which has the same final
state event selection as listed in Sec. 8.1, except no requirements on the number of b
jets.

8.3.1 Changes with respect to the $Z/\gamma^* \to \tau\tau$ Cross Section Analysis

The most obvious changes concern the fitting of the p_T dependence of the measured fake factors, the treatment of the $t\bar{t}$ fake factors and the refinement of the method in the $\tau_h\tau_h$ final state.

Small modifications are introduced to estimate the misidentified-τ_h background composition in the AR. Fractions of the different misidentified-τ_h backgrounds are derived separately in all four exclusive event subcategories in the $\tau_e\tau_h$ and $\tau_\mu\tau_h$ final states and in the two exclusive subcategories in the $\tau_h\tau_h$ final state. The background composition in the AR is shown for the $\tau_\mu\tau_h$ final state in Fig. 8.3. Fractions of the misidentified-τ_h backgrounds are obtained in bins of τ_h p_T (in contrast to m_T^l in Ref. [128]) and τ_h decay mode (1-prong, 3-prong). The fraction of the QCD multijet background is determined by subtracting the sum of all processes modeled with simulation from the observed data. All other fractions are obtained from simulation.

8.3.2 Uncorrected Fake Factors

In the $\tau_e\tau_h$ and $\tau_\mu\tau_h$ final states, the determination region $\mathrm{DR_{QCD}}$ has the following requirements with respect to the inclusive SR:

- The electric charges of the selected light lepton and the τ_h candidate are required to be the same.

- The isolation of the light lepton has to be in the range $0.05 \cdot p_T^l < I^l < 0.15 \cdot p_T^l$.

- The transverse mass m_T^l is required to be below 40 GeV.

For $\mathrm{DR_{QCD}}$ in the $\tau_h\tau_h$ final state, two τ_h candidates with same electric charge are required.

In the $\tau_e\tau_h$ and $\tau_\mu\tau_h$ final states, the determination region $\mathrm{DR_{W+jets}}$ has the following requirements with respect to the inclusive SR:

- The transverse mass m_T^l is required to be above 70 GeV.

- No b jets are allowed in the event.

Due to the large nonclosure observed in $t\bar{t}$ fake factors, see Fig. 7.9f, which is mostly caused by the different jet composition between the AR and the SR, $t\bar{t}$ fake factors are
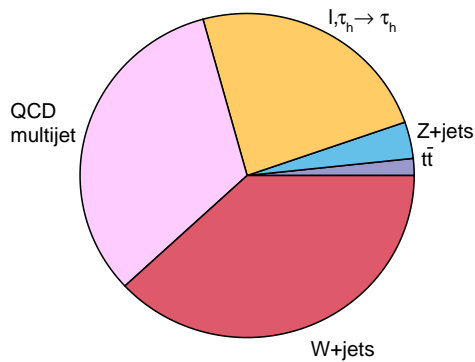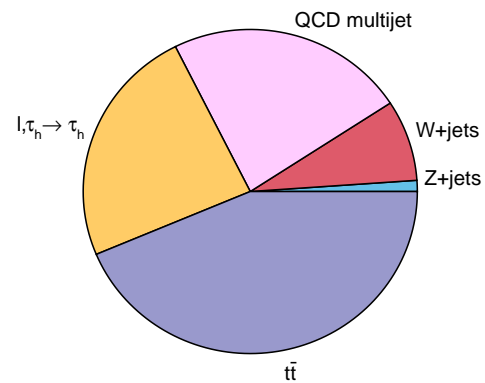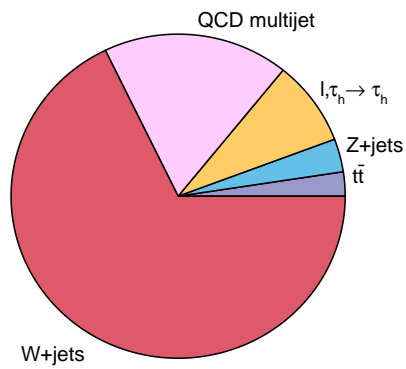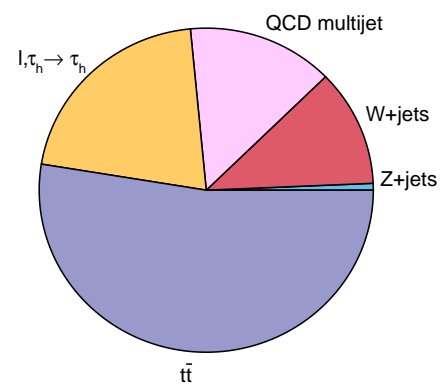
Figure 8.3: Fraction of misidentified-τ_h backgrounds in the AR in four exclusive event categories in the $\tau_\mu\tau_h$ final state [143]. Backgrounds in the AR are due to QCD multijet, W+jets, $Z/\gamma^* \to \ell\ell + $ jets, and $t\bar{t}$ production. The yellow part displays the contributions from events with genuine τ_h decays or misidentified electrons or muons.

derived in the inclusive SR using simulation. This is done separately for the $\tau_e\tau_h$ and $\tau_\mu\tau_h$ final states, and scale factors to correct data-simulation differences are obtained in a control region that is characterized by the same event selection as the inclusive SR, except for:

- At least one b jet is required.

- At least one isolated muon and one isolated electron are required.

It has been checked that the obtained correction factors do not depend on p_T within uncertainties. The corrections consist of four scale factors, giving the data-to-simulation ratio for the $t\bar{t}$ fake factors:

- $\tau_\mu\tau_h$ final state, 1-prong: 0.81

- $\tau_\mu\tau_h$ final state, 3-prong: 0.74

- $\tau_e\tau_h$ final state, 1-prong: 0.68

- $\tau_e\tau_h$ final state, 3-prong: 0.82

The difference between data and simulation is taken as an estimate for the uncertainty on the correction and incorporated in the uncertainty model, as discussed in Sec. 8.5.

The increase in integrated luminosity allows to use a finer binning in p_T when measuring the fake factors. The p_T dependency is fit with a Landau function plus a first- or second-order polynomial. The choice of the order of the used polynomial function depends on the convergence behavior of the fit. Corresponding uncertainties are derived using toys, where every point is allowed to vary randomly within its uncertainties and for every variation the obtained points are fitted. Uncertainties are extracted for the 68% envelope of the toys for every bin in jet multiplicity and τ_h decay mode. The obtained fake factors are shown in Figs. 8.4 - 8.5.

8.3.3 Misidentified-τ_h Backgrounds in the $\tau_h\tau_h$ Final State

In the $\tau_h\tau_h$ final state, one has to deal with the ambiguity of potentially having two jets misidentified as τ_h in the event. For QCD multijet events, both τ_h candidates are due to misidentification in all but a negligible fraction of events. In Sec. 7.3.3, the fake τ_h candidate is selected at random. This procedure is modified by considering every event for which one τ_h fulfills the nominal `Medium` ID requirement, and the other τ_h
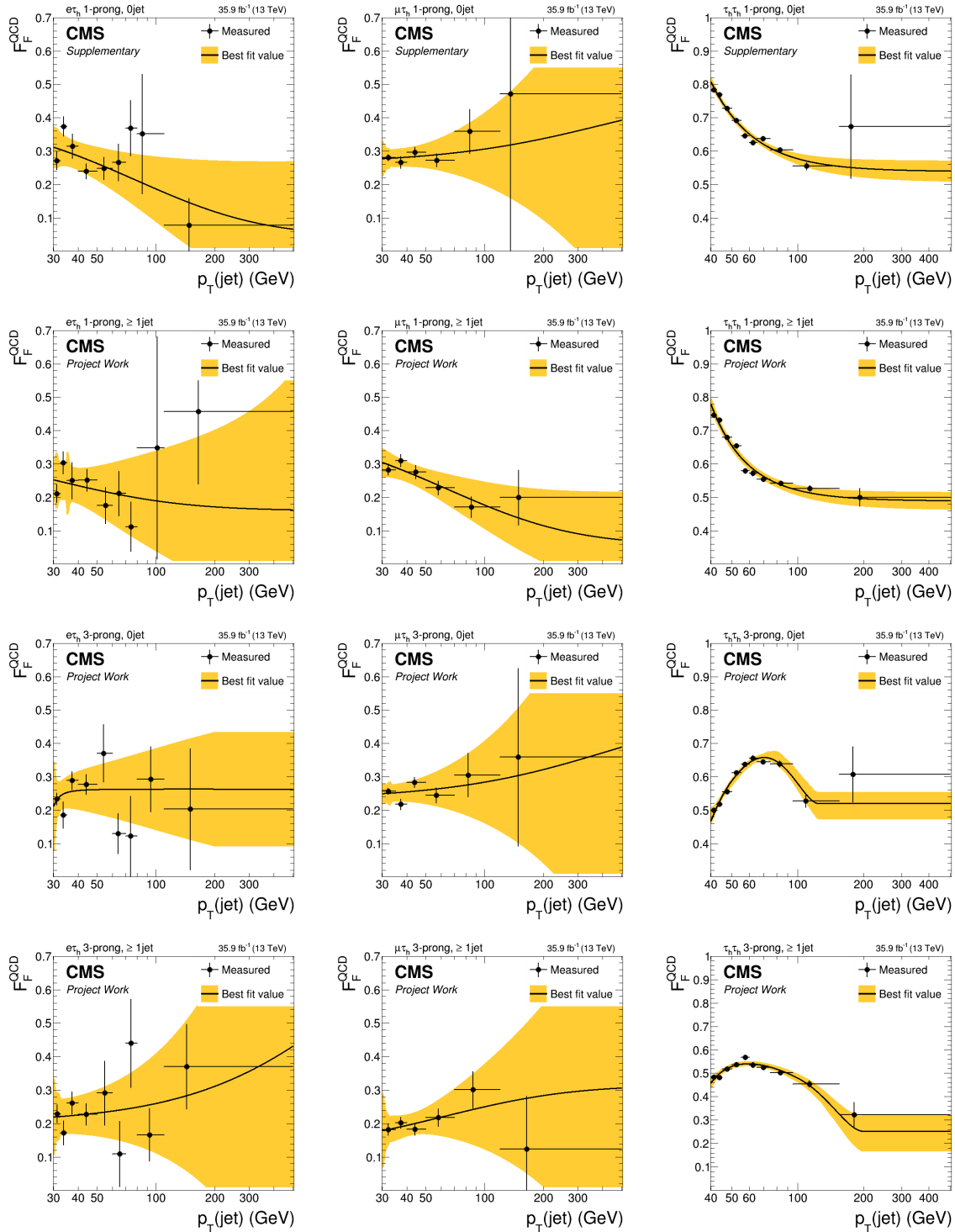
Figure 8.4: The fake factors as obtained in QCD multijet events in the $\tau_e\tau_h$ (left column), $\tau_\mu\tau_h$ (center), and $\tau_h\tau_h$ (right column) final states [143]. The fake factors are measured in bins of jet multiplicity and τ_h decay mode, and fitted with a Landau function plus a first- or second-order polynomial.
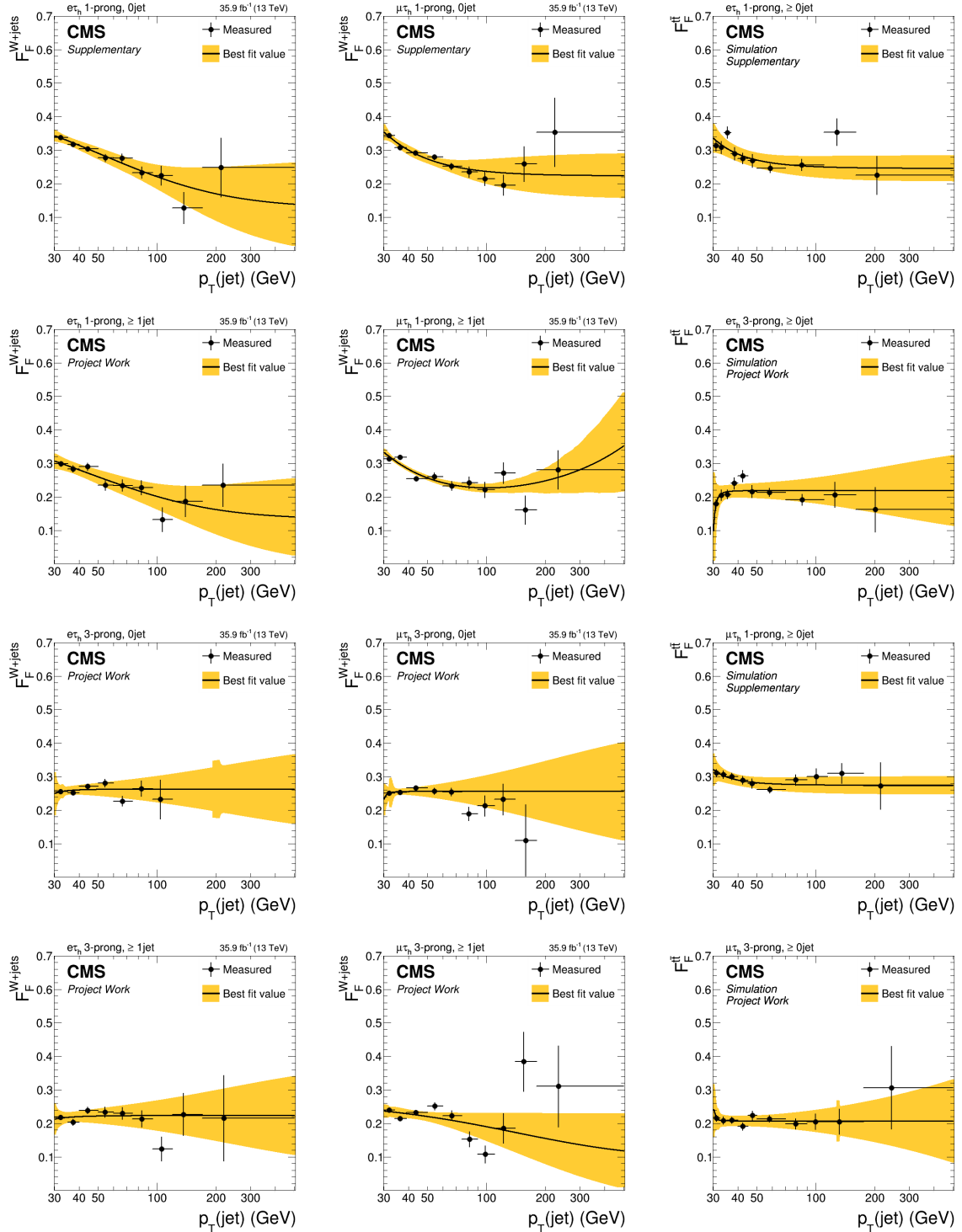
Figure 8.5: The fake factors as obtained in W+jets events in the $\tau_e\tau_h$ (left column) and $\tau_\mu\tau_h$ (center) final states, and the fake factors as obtained in simulated $t\bar{t}$ events in the $\tau_e\tau_h$ and $\tau_\mu\tau_h$ final states (right column) [143]. The W+jets fake factors are measured in bins of jet multiplicity and τ_h decay mode, and fitted with a Landau function plus a first- or second-order polynomial. The $t\bar{t}$ fake factors are measured inclusively in jet multiplicity and in bins of τ_h decay mode, and are fitted with a Landau function plus a first-order polynomial.

the `VeryLoose` but not the `Medium` ID requirement. A weight of 0.5 is applied to take the combinatorial effect into account. For the other background processes, as already described in Sec. 7.3.3, typically one of the τ_h candidates has been correctly identified while the other one is a misidentified jet. In the vast majority of these events selected in the AR, the correctly identified τ_h fulfills the `Medium` ID requirement whereas the mis-identified jet fulfills the `VeryLoose` but not the `Medium` ID requirement. Since there is no significant combinatorial effect, these events are taken into account with a weight of 1.0. The amount of events for which this is the case is estimated with their expected fractions. Corresponding uncertainties are incorporated in the uncertainty model, as discussed in Sec. 8.5. This procedure allows to estimate the complete misidentified-τ_h background in the $\tau_h\tau_h$ final state with the fake factor method.

In the $\tau_h\tau_h$ final state, an additional correction depending on the p_T of the isolated τ_h candidate (the τ_h that fulfills the nominal `Medium` ID) is applied to the QCD multijet fake factors in DR_{QCD}. This is in analogy to the lepton isolation corrections that are applied to the QCD multijet fake factors in the $\tau_e\tau_h$ and $\tau_\mu\tau_h$ final states, and corrects for correlations between the isolation of the two τ_h. The correction is derived as follows. The misidentified-τ_h background in DR_{QCD} as a function of p_T of the isolated τ_h candidate is estimated using the raw fake factors corrected for nonclosure as a function of m_{vis}. The estimate is compared to the observed background distribution. The ratio of the two is smoothed with a Gaussian kernel of variable width in order to limit the statistical fluctuations and is applied as multiplicative correction. The p_T correction is shown in Fig. 8.6.

8.3.4 Fake Factor Corrections

A full list of the corrections that are applied to the raw fake factors measured in DR_{QCD}, DR_{W+jets} and $DR_{t\bar{t}}$ is given in Tab. 8.1. The corrections are derived in the same way as described in Sec. 7.3.4, except for the newly introduced $p_T^{\tau_h}$-dependent correction in the $\tau_h\tau_h$ final state and the data-to-simulation scale factors measured in simulated $t\bar{t}$ events. Figure 8.7 shows corrections for the raw QCD multijet, W+jets and $t\bar{t}$ fake factors measured in the $\tau_\mu\tau_h$ final state.

8.3.5 Cross-Check Analysis in the $\tau_e\tau_h$, $\tau_\mu\tau_h$ Final States

In order to check the validity of the fake factor method, a dedicated cross-check analysis for the QCD multijet and W+jets backgrounds in the $\tau_e\tau_h$ and $\tau_\mu\tau_h$ final states is performed. Remaining backgrounds are taken from simulation.
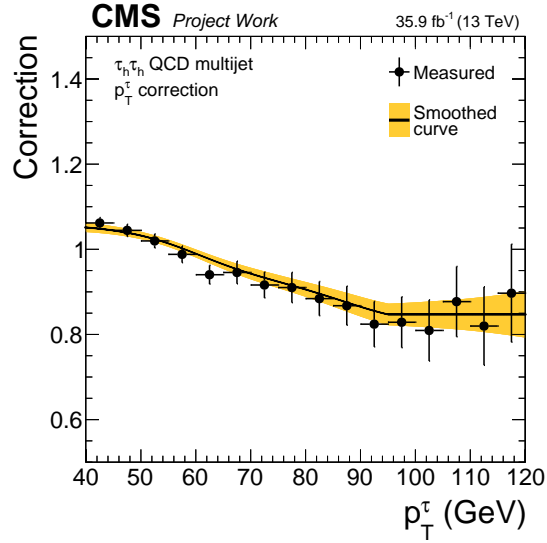
Figure 8.6: QCD multijet fake factor correction as a function of the p_T of the isolated τ_h candidate.

	Correction	Dependency	Control region	$\tau_e\tau_h$	$\tau_\mu\tau_h$	$\tau_h\tau_h$
	Nonclosure	m_{vis}	DR_{QCD}	✓	✓	✓
FF_{QCD}	$p_T^{\tau_h}$-dependent	$p_T^{\tau_h}$	DR_{QCD}			✓
	$\dfrac{I^l}{p_T^l}$-dependent	$\dfrac{I^l}{p_T^l}$	DR_{QCD} (w/o $\dfrac{I^l}{p_T^l}$)	✓	✓	
	Opposite-sign/ same-sign charge	m_{vis}	Orthogonal isolation/ID	✓	✓	✓
FF_{W+jets}	Non-closure	m_{vis}	DR_{W+jets}	✓	✓	
	m_T^l-dependent	m_T^l	From simulation	✓	✓	
$FF_{t\bar{t}}$	Non-closure	m_{vis}	$DR_{t\bar{t}}$	✓	✓	
	Data/Simulation	None	$t\bar{t}$ enriched sideband	✓	✓	

Table 8.1: Summary of fake factor corrections applied to the raw fake factors FF_{QCD}, FF_{W+jets}, and $FF_{t\bar{t}}$. Here, isolation refers to the isolation of the light lepton in the $\tau_e\tau_h$ and $\tau_\mu\tau_h$ final states and ID to the identified τ_h candidate in the $\tau_h\tau_h$ final state.
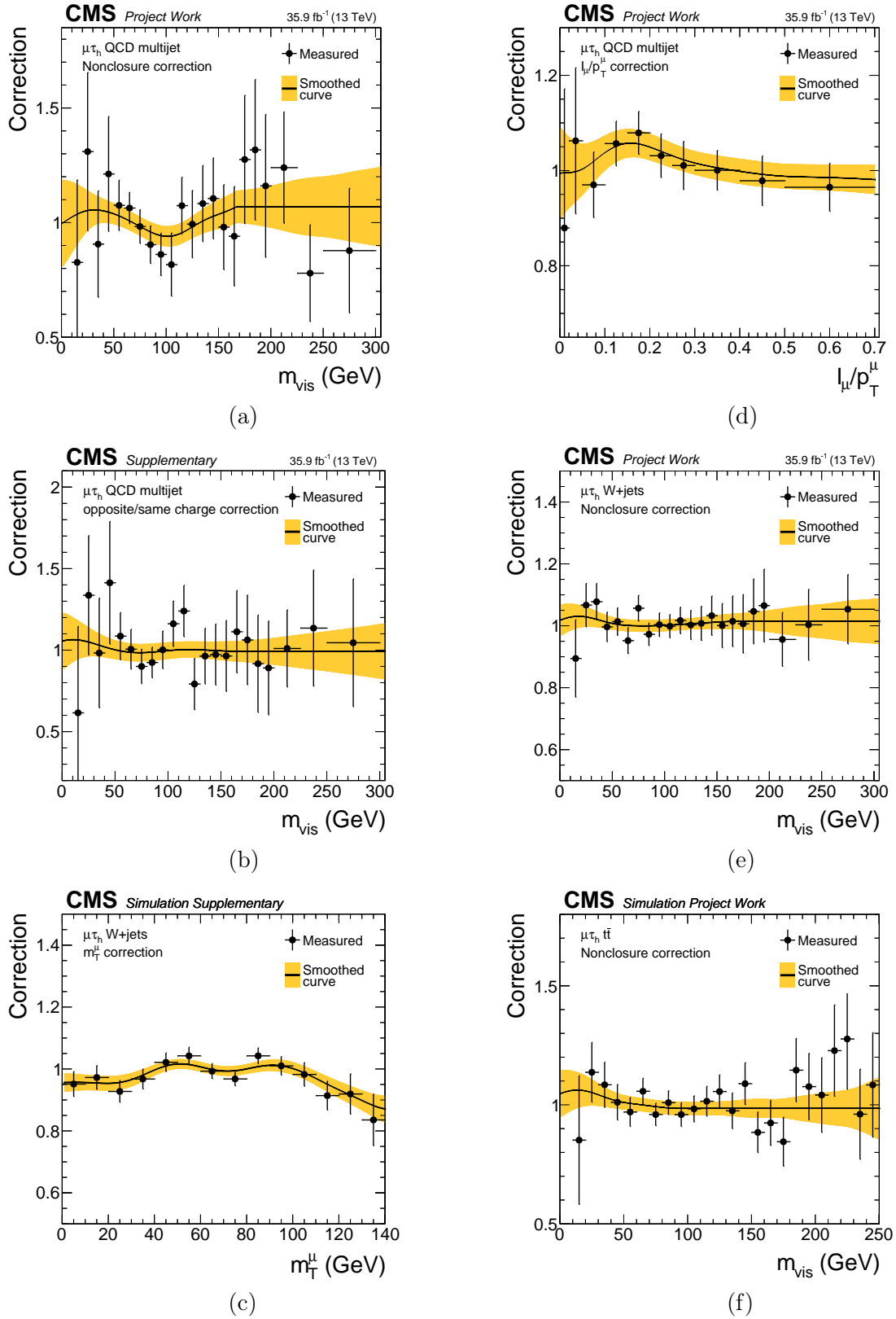
Figure 8.7: Fake factor corrections in the $\tau_\mu \tau_h$ final state containing corrections for the raw FF_{QCD}: nonclosure correction in m_{vis} (a), I^μ/p_T^μ correction (b) and opposite-sign/same-sign electric charge correction (c), corrections for the raw FF_{Wjets}: nonclosure correction in m_{vis} (d) and m_T^μ correction (e) and a simulation-based nonclosure correction for the raw $FF_{t\bar{t}}$(f) [143].

The prediction of the W+jets background is obtained using two dedicated control regions (CRs) which have the same event selection as the corresponding SRs, except for an $m_{\mathrm{T}}^{\mathrm{l}} > 70$ GeV requirement. Additionally, the light lepton and τ_{h} are required to be of opposite-sign (OS) and same-sign (SS) electric charge, respectively. The estimation of the normalization of W+jets events is then obtained as follows:

$$
\begin{aligned}
N_{\mathrm{data}}'^{\mathrm{SS}} &= N_{\mathrm{QCD}}^{\mathrm{SS}} + N_{\mathrm{W+jets}}^{\mathrm{SS}} \\
N_{\mathrm{data}}'^{\mathrm{OS}} &= f_{\mathrm{QCD}}^{\mathrm{OS/SS}} \cdot N_{\mathrm{QCD}}^{\mathrm{SS}} + f_{\mathrm{W+jets}}^{\mathrm{OS/SS}} \cdot N_{\mathrm{W+jets}}^{\mathrm{SS}},
\end{aligned}
\tag{8.3}
$$

where $N_{\mathrm{data}}'^{\mathrm{SS(OS)}}$ denotes the number of events in the corresponding CRs, after all other backgrounds than QCD multijet and W+jets are subtracted using simulation. The extrapolation factor $f_{\mathrm{W+jets}}^{\mathrm{OS/SS}}$ between the two CRs is obtained from simulation, and the extrapolation factor $f_{\mathrm{QCD}}^{\mathrm{OS/SS}}$ is extracted from a fit to the data using a third CR, where in addition to the SS electric charge requirement the isolation of the light lepton is inverted.

From Eq. (8.3) an estimate of $N_{\mathrm{W+jets}}^{\mathrm{SS}}$ can be derived. The final W+jets normalization $N_{\mathrm{W+jets}}^{\mathrm{OS}}$ is then obtained using

$$
N_{\mathrm{W+jets}}^{\mathrm{OS}} = N_{\mathrm{W+jets}}^{\mathrm{SS}} \cdot f_{\mathrm{W+jets}}^{\mathrm{OS/SS}} \cdot f_{\mathrm{W+jets}}^{\mathrm{CR/SR}},
\tag{8.4}
$$

where $f_{\mathrm{W+jets}}^{\mathrm{CR/SR}}$ is the ratio of simulated W+jets events in the OS SR and the OS CR. The event numbers in Eq. (8.3) as well as the extrapolation factors $f_{\mathrm{W+jets}}^{\mathrm{OS/SS}}$ and $f_{\mathrm{W+jets}}^{\mathrm{CR/SR}}$ are obtained individually for each event subcategory.

The shape of the final discriminating variable, $m_{\mathrm{T}}^{\mathrm{tot}}$ is taken from simulation.

The shape and the normalization to estimate the QCD multijet background are obtained from CRs that have the same event selection as the corresponding SRs, except for an SS electric charge requirement on the τ_{h} and the respective light lepton. The non-QCD multijet backgrounds are subtracted using simulation, except for W+jets events where the normalization $N_{\mathrm{W+jets}}^{\mathrm{OS}}$ and the extrapolation factor $f_{\mathrm{QCD}}^{\mathrm{OS/SS}}$ are obtained as described above.

To control the normalization of W+jets and QCD multijet events two additional CRs per $\tau_{\mathrm{e}}\tau_{\mathrm{h}}$ and $\tau_{\mu}\tau_{\mathrm{h}}$ final state are included in the ML fit, namely the OS W+jets CR and the SS QCD multijet CR.

Figure 8.8 illustrates the post-fit distributions of $m_{\mathrm{T}}^{\mathrm{tot}}$ in the $\tau_{\mathrm{e}}\tau_{\mathrm{h}}$ and $\tau_{\mu}\tau_{\mathrm{h}}$ final states

using the simulation-based cross-check background estimates. To obtain the post-fit distributions a simultaneous ML is performed, as described in Sec. 8.6, in which the fake factor-specific uncertainties are replaced with uncertainties that are specifically derived for the cross-check analysis. The figures also compare the overall background estimate to the fake factor method. The good agreement in all categories shows the reliability of the fake factor method.
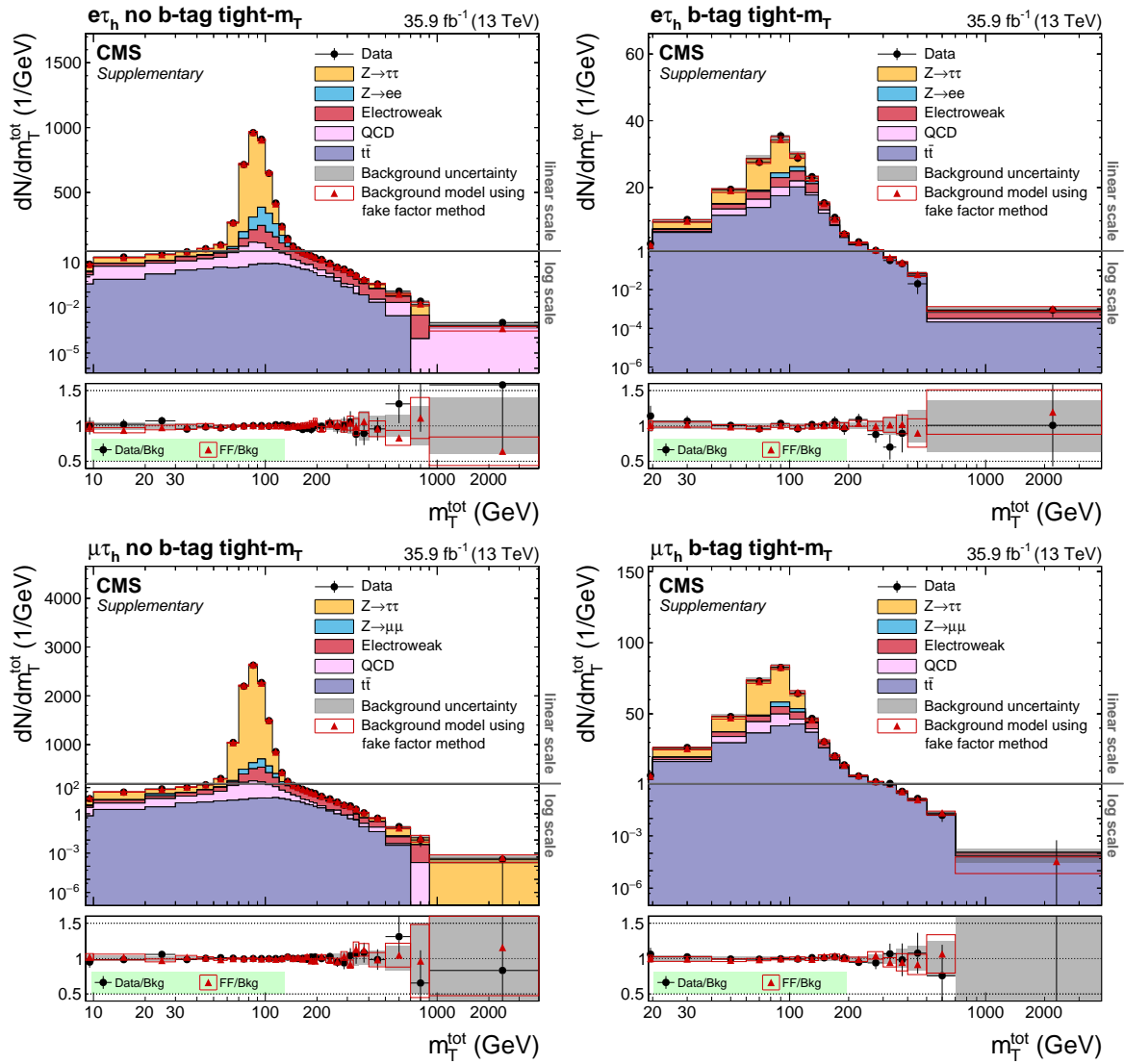
Figure 8.8: Post-fit distributions of m_T^{tot} in the $\tau_e\tau_h$ (top) and $\tau_\mu\tau_h$ (bottom) final states, using the simulation-based cross-check [143]. For both final states the most sensitive Tight-m_T event subcategories are shown. The triangles correspond to the background estimate obtained when the fake factor method is used.

8.4 Estimation of Other Backgrounds

Besides the misidentified-τ_h background in the $\tau_e\tau_h$, $\tau_\mu\tau_h$ and $\tau_h\tau_h$ final states, three other sizeable backgrounds exist:

- The $Z/\gamma^* \to \tau\tau$ background in all four final states. It is estimated from simulation together with a dedicated $Z/\gamma^* \to \mu\mu$ CR used to constrain the DY normalization. Additionally, the $Z/\gamma^* \to \tau\tau$ background estimation in the $\tau_e\tau_h$, $\tau_\mu\tau_h$ and $\tau_h\tau_h$ final states is cross-checked by comparing it to the prediction that is obtained from the "$\mu \to \tau$ embedding" method, as deployed during the LHC Run-1 analyses, see e.g. in Ref. [129, 147]. Good agreement is observed between the corrected simulation and the embedding method, which confirms the validity of the modeling of the $Z/\gamma^* \to \tau\tau$ background.

- The $t\bar{t}$ background in all four final states. Its shape is estimated from simulation and is normalized in a dedicated $t\bar{t}$-enriched CR.

- The QCD multijet background in the $\tau_e\tau_\mu$ final state.

Note that in the $\tau_e\tau_h$, $\tau_\mu\tau_h$ and $\tau_h\tau_h$ final states this only applies to the background components that are not described by the fake factor method, namely background contributions that are either to genuine τ_h or due to misidentification of an electron or muon as τ_h.

Contributions from remaining backgrounds are estimated from simulation with data-to-simulation corrections applied.

8.4.1 Additional Control Regions

The normalization uncertainty of the $Z/\gamma^* \to \tau\tau$ background in the event subcategories is constrained by including a dedicated $Z/\gamma^* \to \mu\mu$ CR in the ML fit.

The selection of the $Z/\gamma^* \to \mu\mu$ CR is aligned with the selection of the $\tau_\mu\tau_h$ final state, as described in Sec. 8.1. Instead of a muon-τ_h pair, a $\mu\mu$ pair with most isolated muons is chosen where one muon is required to pass the single muon trigger. Both muons are required to have $p_T^\mu > 10$ GeV where at least one muon is required to fulfill $p_T^\mu > 24$ GeV. Additionally, the visible mass of the di-muon system is required to fulfill 70 GeV $< m_{vis} < 110$ GeV. The yields of the $Z/\gamma^* \to \mu\mu$ and $Z/\gamma^* \to \tau\tau$ contributions are correlated with each other in order to correctly account for systematic uncertainties that are common to both processes and affect the normalization. The $Z/\gamma^* \to \mu\mu$

yield is divided into a no b-tag and b-tag category to keep the $Z/\gamma^* \to \mu\mu$ CR and $Z/\gamma^* \to \tau\tau$ SR phase space as similar as possible. Differing acceptance effects are taken into account by varying the factorization and the renormalization scale and deriving uncertainties on the ratio of the $Z/\gamma^* \to \tau\tau$ yield in the SR over the $Z/\gamma^* \to \mu\mu$ yield in the corresponding CR.

The modeling of the $t\bar{t}$ background is controlled in a dedicated $t\bar{t}$-enriched region. The region has the same final state selection as applied in the $\tau_e\tau_\mu$ final state, see Sec. 8.1, except for additional $D_\zeta < -50$ GeV and $E_T^{\mathrm{miss}} > 80$ GeV cuts making the region orthogonal to the SRs. The purity of the selected events in this region amounts to 85% where the remaining events mostly originate from single-top and diboson processes. The $t\bar{t}$ normalization in this region is correlated with all SRs in the $\tau_e\tau_\mu$ final state, and $t\bar{t}$ background contributions that are not described by the fake factor method in the $\tau_e\tau_h$, $\tau_\mu\tau_h$ and $\tau_h\tau_h$ final states. The deployed $t\bar{t}$ CR is inclusive but binned in m_T^{tot}, and thus both normalization and shape effects are taken into account.

8.4.2 QCD Multijet Modeling in the $\tau_e\tau_\mu$ Final State

In the $\tau_e\tau_\mu$ final state, the shape of the QCD multijet background in the opposite-sign (OS) electric charge SR is estimated in a CR in which electron and muon are required to be of same-sign (SS) electric charge. This shape is normalized by a OS/SS ratio that is measured in an isolation sideband region (SB) which is defined by the requirement that both leptons satisfy a relaxed isolation, $I^l < 0.4 \cdot p_T^l$, and to avoid overlap with the SR at least one lepton is required to fail the nominal isolation requirement, $I^e > 0.15 \cdot p_T^e$ or $I^\mu > 0.20 \cdot p_T^\mu$. The OS/SS ratio is measured as function of p_T of the leading lepton, p_T of the subleading lepton and the separation $\Delta(e,\mu)$ between both leptons in the $\eta - \phi$ plane. Contributions from backgrounds other than QCD multijet are subtracted based on simulation.

To account for differences in the OS/SS ratio of the different categories, dedicated scale factors are introduced which extrapolate yields from the inclusively selected sample to individual event categories.

Finally, to also take differences between the SR and the SB region into account, an additional scale factor is derived from simulation.

8.5 Systematic Uncertainties

The uncertainties that enter the statistical model, as described in Sec. 8.6.1, can be split into theoretical uncertainties and experimental uncertainties. For better readability the systematic uncertainties are further split into those associated with the fake factor method and other uncertainties, as it is done in Sec. 7.5.

8.5.1 Fake Factor-Specific Uncertainties

The fake factor-related uncertainties can be summarized to:

- Statistical uncertainties in the fake factor determination in DR_{QCD}, DR_{W+jets} and $DR_{t\bar{t}}$ given by the fit uncertainty on the p_T fit, see Figs. 8.4 - 8.5. Due to their statistical nature they are uncorrelated and hence constitute twelve nuisance parameters for the $\tau_e\tau_h$ and $\tau_\mu\tau_h$ final states and four nuisance parameters for the $\tau_h\tau_h$ final state.

- Systematic uncertainties related to the FF_{QCD} corrections, see e.g. Fig. 8.7 for the $\tau_\mu\tau_h$ final state. The uncertainties are added in quadrature for each final state individually, hence adding one nuisance parameter per final state:

  - Uncertainty in the nonclosure correction.

  - Uncertainty in the I^l/p_T^l-dependent correction ($\tau_e\tau_h$ and $\tau_\mu\tau_h$ final states).

  - Uncertainty in the correction depending on the p_T of the identified τ_h candidate ($\tau_h\tau_h$ final state), see Fig. 8.6.

  - Uncertainty in the extrapolation from the same-sign (DR_{QCD}) to the opposite-sign electric charge region (SR).

- Systematic uncertainties related to the FF_{W+jets} corrections, see e.g. Fig. 8.7 for the $\tau_\mu\tau_h$ final state. The uncertainties are added in quadrature for each final state individually, hence adding one nuisance parameter each for the $\tau_\mu\tau_h$ and $\tau_e\tau_h$ final state:

  - Uncertainty in the nonclosure correction.

  - Uncertainty in the m_T^l-dependent correction.

  - Uncertainty in the usage of FF_{W+jets} to estimate the misidentified-τ_h $Z/\gamma^* \to \ell\ell$ background.

- Systematic uncertainties related to the $\mathrm{FF}_{t\bar{t}}$ corrections, see e.g. Fig. 8.7f for the $\tau_\mu\tau_\mathrm{h}$ final state. The uncertainties are added in quadrature for each final state individually, hence adding one nuisance parameter each for the $\tau_\mu\tau_\mathrm{h}$ and $\tau_\mathrm{e}\tau_\mathrm{h}$ final state:

  - Uncertainty in the nonclosure correction.

  - Uncertainty in the data-to-simulation correction factors.

- Systematic uncertainties in the fraction of W+jets, $Z/\gamma^* \to \ell\ell$ and $t\bar{t}$ events with one misidentified-τ_h in the AR, adding three nuisance parameters for the $\tau_\mathrm{h}\tau_\mathrm{h}$ final state.

- Systematic uncertainties related to the subtraction of genuine τ_h backgrounds and backgrounds due to misidentification of electrons and muons as τ_h in the AR.

All uncertainties are shape uncertainties, except for the uncertainty in the background subtraction in the AR. In contrast to Sec. 7.5.1, shape uncertainties are factorized into a pure shape and a pure normalization part. The shape uncertainties are normalized to the same area as the nominal shape, and the normalization terms are added in quadrature for each subcategory in each final state and enter the ML fit as normalization uncertainties. This is done separately for the statistical uncertainties on the fake factor measurement and the systematic uncertainties on the corrections.

All uncertainties are dominantly statistical in nature and therefore are treated as uncorrelated across channels, except for the uncertainty on the $t\bar{t}$ corrections which are derived in the same control region for the $\tau_\mathrm{e}\tau_\mathrm{h}$ and $\tau_\mu\tau_\mathrm{h}$ final states.

8.5.2 Other Uncertainties

This section summarizes systematic uncertainties that are not related to the fake factor method. A full description can be found in Ref. [143]. A list of these uncertainties is shown in Tab. 8.2. The uncertainties can be split into normalization and shape uncertainties.

The normalization uncertainties are as follows:

- Uncertainty related to the measurement of the integrated luminosity [148].

- Uncertainties in the measurement of ID, isolation and trigger efficiencies for electrons and muons.

- Uncertainties in the measurement of τ_h misidentification probabilities of electrons ($e \to \tau_h$) and muons ($\mu \to \tau_h$). The uncertainties are applied to $Z/\gamma^* \to ee$ and $Z/\gamma^* \to \mu\mu$ events in the $\tau_e\tau_h$, $\tau_\mu\tau_h$ and $\tau_h\tau_h$ final states.

- The uncertainty in the τ_h ID efficiency per τ_h candidate. It is factorized into a part that is correlated and a part that is uncorrelated across the final states.

- The uncertainty in the jet energy scale depends on the final state and subcategory affecting the number of events entering each subcategory.

- A uncertainty in the response and resolution of E_T^{miss} is applied to samples where a well-defined direction and magnitude of $\vec{E}_T^{\mathrm{miss}}$ exists, i.e. all signal samples, $Z/\gamma^* \to \ell\ell$ and W+jets samples. For other backgrounds, e.g. $t\bar{t}$, single top or diboson backgrounds, jet energy scale and unclustered energy scale variations are also propagated to E_T^{miss}.

- Uncertainties in the cross section of single top, diboson and W+jets processes.

- Due to the dedicated $Z/\gamma^* \to \mu\mu$ and $t\bar{t}$ CRs, no theoretical uncertainties on the normalization are needed. However, uncertainties are applied to $Z/\gamma^* \to \ell\ell$ and $t\bar{t}$ events to account for the extrapolation from the CRs to the SR.

- In the $\tau_e\tau_\mu$ final state, for the estimation of the QCD multijet background an overall 30% uncertainty is applied on the extrapolation from the CR to the SR. Additionally, category dependent uncertainties are derived on the OS/SS ratios.

- Theoretical uncertainties in the acceptance of signal events that are produced in association with b quarks. The uncertainties are obtained by varying the renormalization and factorization scales, and the internal generator matching scale $\mathcal{Q}_{\mathrm{sh}}$ related to parton showering [28].

- For the model-dependent interpretations, see Sec. 8.6.2, uncertainties associated to the MSTW2008 [149] set of PDFs are calculated, as recommended in Refs. [149, 150].

- For the set of results in which the SM Higgs boson production is included in the ML fit, uncertainties in the production cross section due to different choices of the renormalization and factorization scales, and due to different choices of PDFs and α_s, are taken into account. The uncertainties are derived following the procedure described in Ref. [28].

The shape uncertainties are as follows:

- Uncertainties are applied on the τ_h ES. They are split into three independent uncertainties depending on the τ_h decay mode (decay into a single charged hadron with and without pions, and decay into three charged hadrons).

- For the high τ_h p_T regime in the $\tau_\mathrm{e}\tau_\mathrm{h}$, $\tau_\mu\tau_\mathrm{h}$ and $\tau_\mathrm{h}\tau_\mathrm{h}$ final states, an additional uncertainty is applied.

- In the $\tau_\mathrm{e}\tau_\mathrm{h}$ final state, an uncertainty in the ES of electrons that are misidentified as τ_h decays is derived. Different values are applied to 1-prong decay mode τ_h candidates with and without neutral pions, respectively.

- In the $\tau_\mathrm{e}\tau_\mu$ final state, an electron ES uncertainty is applied. In the $\tau_\mathrm{e}\tau_\mathrm{h}$ final state, this uncertainty is negligible.

- Uncertainty in the top quark p_T correction in simulated $t\bar{t}$ events. The uncertainty corresponds to 100% of the correction.

- Uncertainties related to the reweighting of the dilepton mass and p_T spectrum of $Z/\gamma^* \to \ell\ell$ events. Overall five uncertainties are derived including the muon ES and the $t\bar{t}$ cross section uncertainty. The remaining three uncertainties arise from the statistical uncertainties in the measured weights that are found to be non-negligible in three bins.

- In the $\tau_\mathrm{e}\tau_\mu$ final states, uncertainties are applied to events containing jet $\to$ e and jet $\to \mu$ misidentifications. The size of the uncertainties depends on the p_T of the jet, and are at least 10%.

8.6 Results

8.6.1 Signal Extraction

For the statistical inference of the signal, a likelihood function of the same form as outlined in Eq. (7.7) is used. Please note that the notation of the scaling parameter for the signal that is introduced in Chap. 7 as ξ is changed to μ, in compliance with the common notation for SM Higgs boson and BSM searches. Therefore, in this chapter

Uncertainty	$\tau_e\tau_\mu$	$\tau_e\tau_h$	$\tau_\mu\tau_h$	$\tau_h\tau_h$	Process	Shape
Integrated luminosity	✓	✓	✓	✓	MC	–
e/μ-trigger, ID, isolation	✓	✓ / –	– / ✓	–	MC	–
Jet $\to$ e mis-ID	✓	–	–	–	MC	✓
Jet $\to \mu$ mis-ID	✓	–	–	–	MC	✓
e $\to \tau_h$ mis-ID	–	✓ / –	–	– / ✓	Z $\to$ ee	–
$\mu \to \tau_h$ mis-ID	–	–	✓ / –	– / ✓	Z $\to \mu\mu$	–
τ_h-trigger	–	–	–	✓	MC	–
τ_h-ID	–	✓	✓	– / ✓	MC	–
τ_h-ID (high p_T)	–	✓	✓	✓	MC	✓
τ_h energy scale	–	✓	✓	✓	MC	✓
e $\to \tau_h$ energy scale	–	✓	–	–	Z $\to$ ee	✓
e energy scale	✓	–	–	–	MC	✓
Jet energy scale	✓	✓	✓	✓	MC	–
b tagging	✓	✓	✓	✓	MC	–
E_T^{miss} resp./res.	✓	✓	✓	✓	MC	–
Sideband extrapolation	✓	✓	✓	✓	Z $\to \tau\tau$	
	✓	✓	✓	✓	Z $\to$ ll	–
	✓	✓	✓	✓	$t\bar{t}$	
	✓	–	–	–	QCD	
Bkgr. in signal categories		✓	✓	✓	Diboson	
	✓	✓	✓	✓	Single t	–
		–	–	–	W+jets	
Top quark p_T reweighting	✓	✓	✓	✓	$t\bar{t}$	✓
Z reweighting of LO MC	✓	✓	✓	✓	Z $\to \ell\ell$	✓
b-associated signal acceptance	✓	✓	✓	✓	Signal	–
PDF/scale	✓	✓	✓	✓	Signal, SM Higgs	–

Table 8.2: Overview of the systematic uncertainties that are used in the ML fit, as described in Sec. 8.6.1 [143]. The label "MC" refers to all processes that have been obtained from simulation. Fake factor-specific uncertainties are not shown.

the likelihood function used to describe the statistical inference reads:

$$\mathcal{L}(\text{data}|\mu \cdot s(\theta) + b(\theta)) = \prod_i \mathcal{P}(k_i|\mu \cdot s_i(\theta) + b_i(\theta)) \times \prod_j \mathcal{C}(\hat{\theta}_j|\theta_j). \qquad (8.5)$$

In order to assess the compatibility of the observed data and the expectation, pre-fit and post-fit m_T^{tot} distributions in the individual subcategories are studied. The post-fit distributions and the corresponding uncertainties are based on the constraints and pulls of the individual nuisance parameters of the ML fit. In Figs. 8.9 - 8.10, the m_T^{tot} distributions are shown for the most sensitive event subcategories. The fit is performed for a signal-plus-background $(s + b)$ MSSM $m_H^{\text{mod}+}$ hypothesis that corresponds to the values $m_A = 700$ GeV and $\tan\beta = 20$.

The largest background contributions are due to the irreducible $Z/\gamma^* \to \tau\tau$ events, the misidentified-τ_h events and, in the b-tag subcategories, $t\bar{t}$ events. A full list of the observed number of events and the relative background contributions is given in App. A.2.6.

No significant excess of events is observed in the investigated Higgs boson mass region between 90 GeV and 3.2 TeV. In the following section the upper limits on the presence of a signal and the possible interpretations of the data are discussed.

8.6.2 Exclusion Limits and Likelihood Scans

Model-Independent Exclusion Limits

To obtain model-independent exclusion limits, the *modified frequentist approach* as described in Refs. [151, 152] is used. A test statistic q_μ is defined that is based on the PLR introduced in Sec. 7.6.1:

$$q_\mu = -2\ln \frac{\mathcal{L}(\text{data}|\mu \cdot s(\hat{\theta}_\mu) + b(\hat{\theta}_\mu))}{\mathcal{L}(\text{data}|\hat{\mu} \cdot s(\hat{\theta}_{\hat{\mu}}) + b(\hat{\theta}_{\hat{\mu}}))}, \qquad (8.6)$$

and allows to obtain 95% CL upper limits on the product of cross section times branching ratio for ggF and b-associated production, respectively. The limits are derived assuming a single resonance, ϕ, and using the narrow-width approximation for the signal hypothesis. In order to obtain limits for ggF production, the b-associated production is profiled and vice versa. This means that contributions of the respective second signal process are allowed to float freely in the ML fit, and thus are chosen such that the likelihood function $\mathcal{L}$ reaches its maximum in the $s + b$ fit.
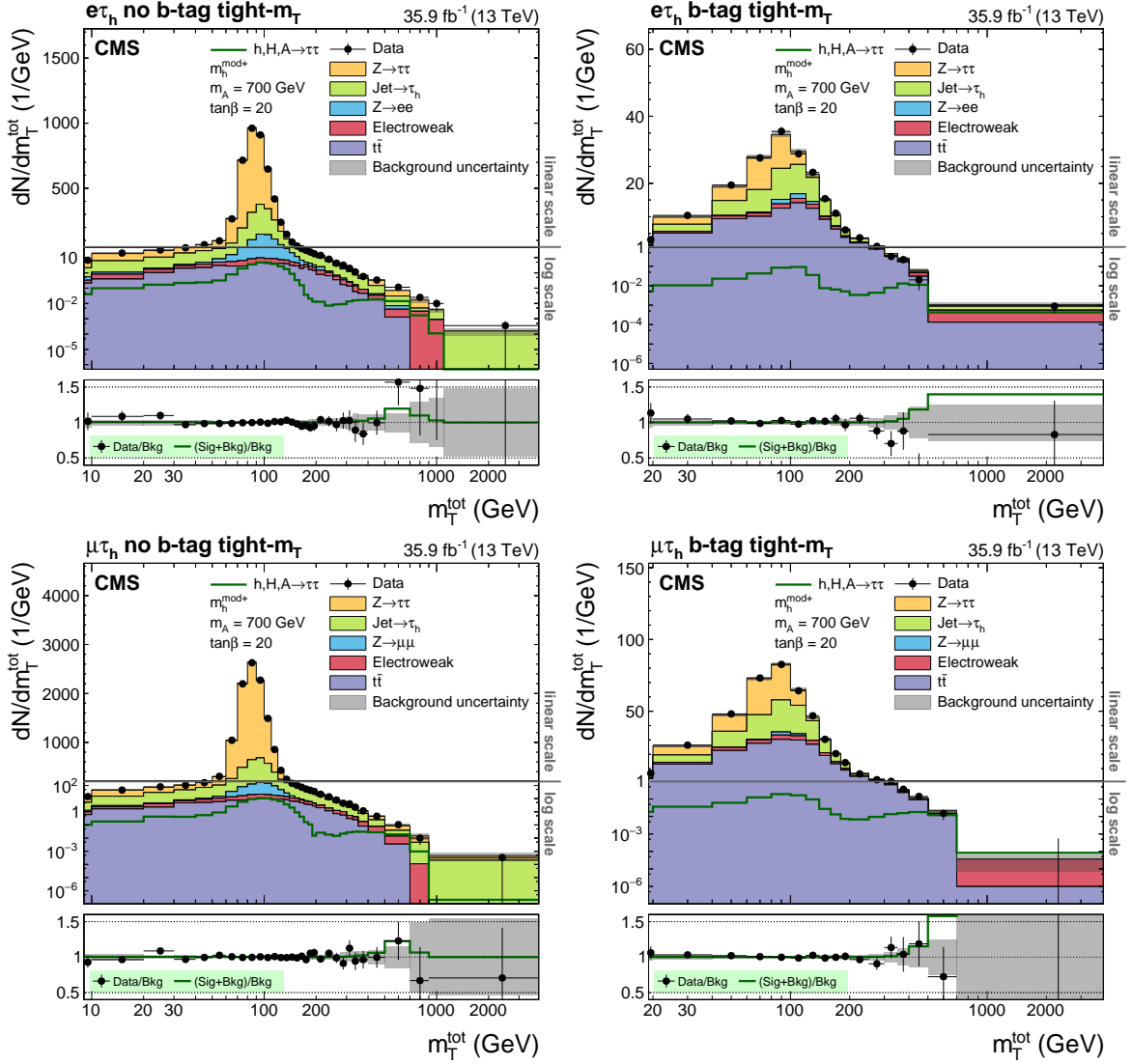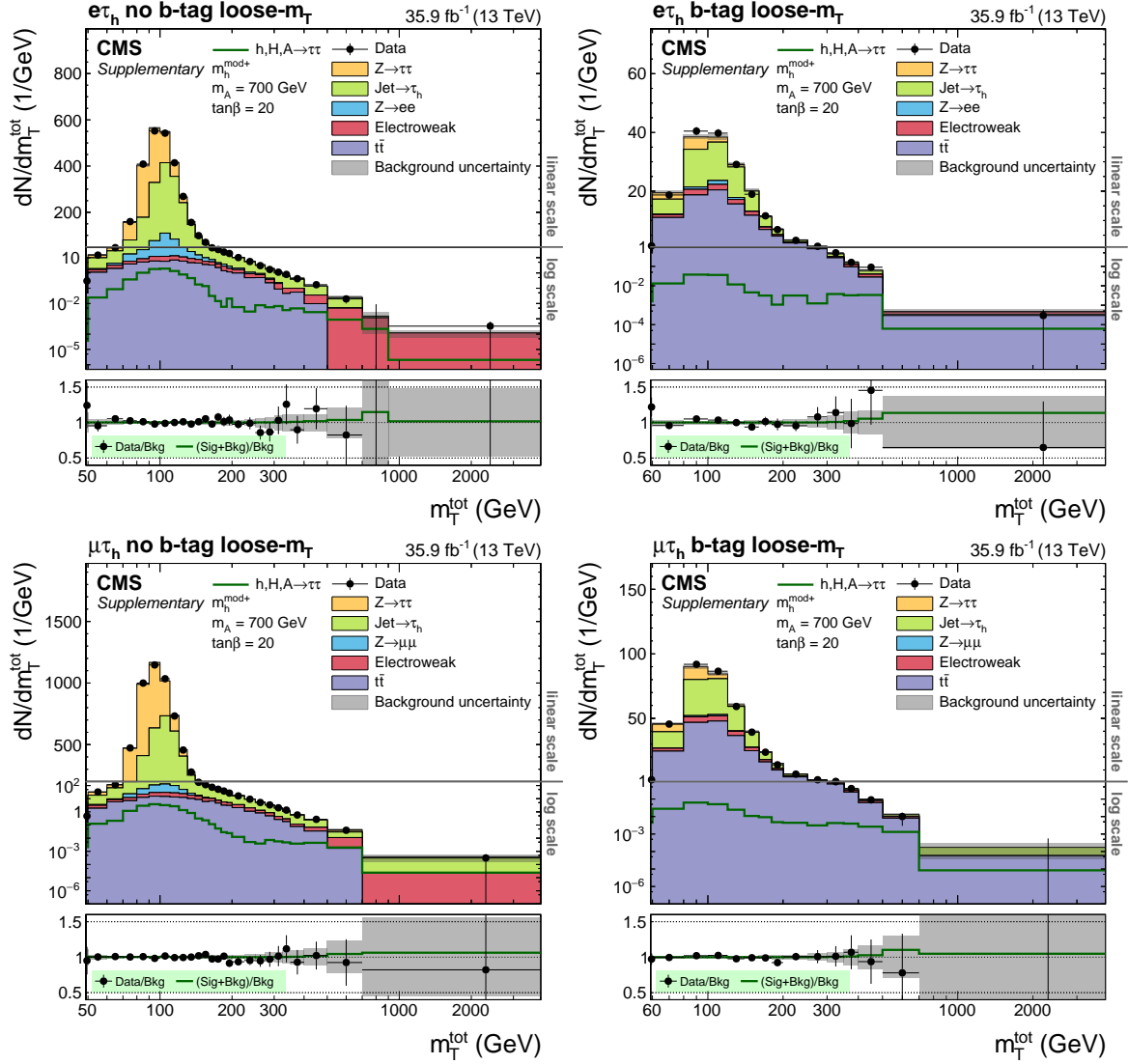
Figure 8.9: Post-fit distribution of $m_{\mathrm{T}}^{\mathrm{tot}}$ in the $\tau_e\tau_h$ (top) and $\tau_\mu\tau_h$ (bottom) final state [143]. For both final states the most sensitive Tight-m_{T} event subcategories are shown. The change from logarithmic to linear scale on the vertical axis is indicated by the gray horizontal line.
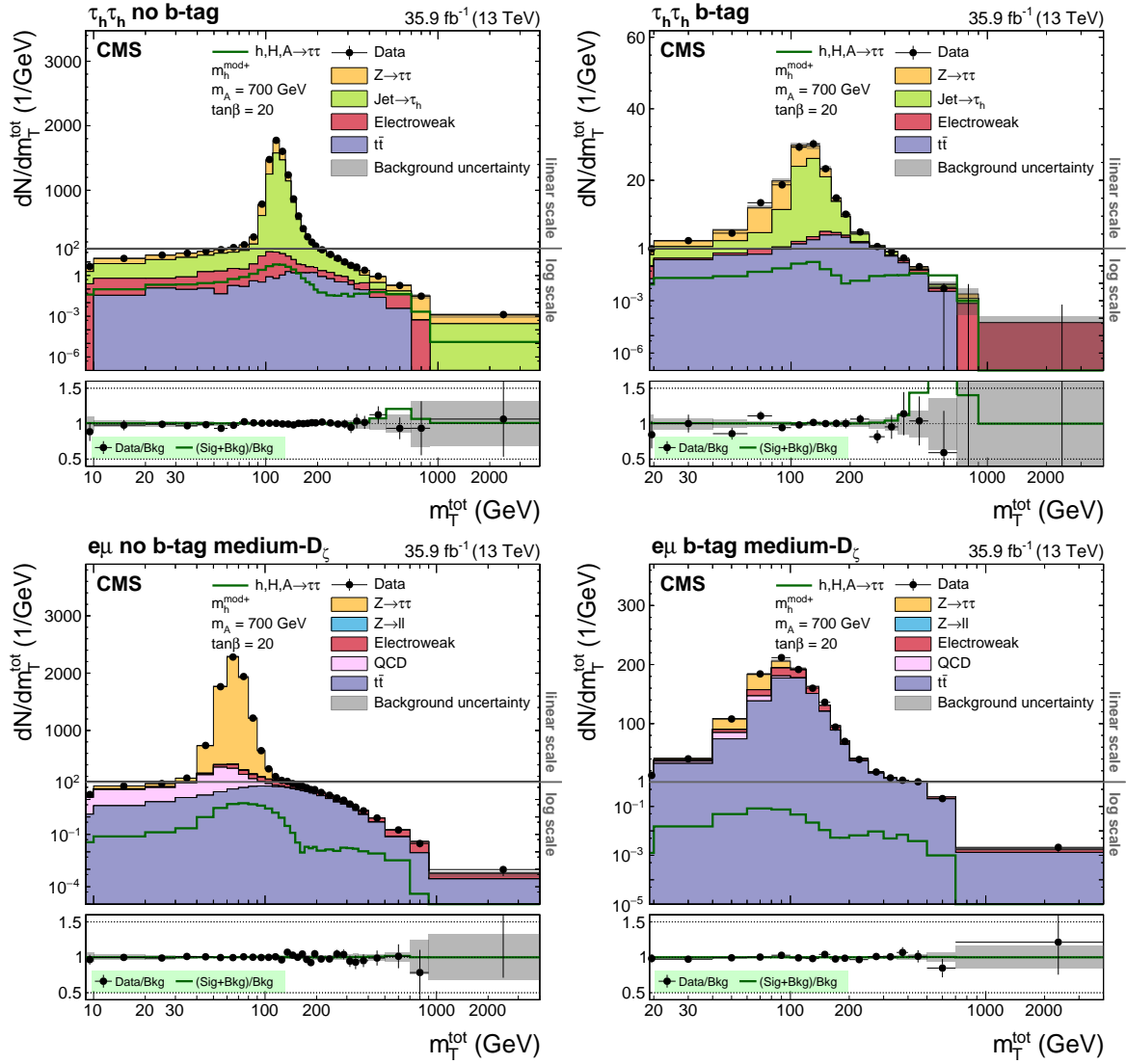
Figure 8.10: Post-fit distribution of m_T^{tot} in the $\tau_h\tau_h$ (top) and $\tau_\mu\tau_e$ final state (bottom) [143]. For the $\tau_\mu\tau_e$ final state the most sensitive Medium-D_ζ event subcategories are shown. The change from logarithmic to linear scale on the vertical axis is indicated by the gray horizontal line.

Expected and observed 95% CL upper limits are shown in Fig. 8.11. Here, the SM Higgs boson is added to the background. The exclusion limit around the SM Higgs boson mass of 125 GeV is approximately 7 pb for ggF production. The corresponding product of cross section times branching ratio for the SM Higgs boson amounts to 3 pb [28]. This suggests that the analysis is close to becoming sensitive to the SM Higgs boson and hence motivates adding it to the backgrounds. For b-associated production the exclusion limit around 125 GeV is approximately 4 pb, the corresponding product of cross section times branching ratio for the SM Higgs boson is 0.03 pb [28]. In App. A.2.5, limits are shown where the SM Higgs boson has not been added to the SM background. As outlined in Sec. 8.2, the p_T spectrum of the Higgs boson for ggF and b-associated production is estimated at NLO precision. This yields differences in sensitivity at low mass points for which the Higgs boson p_T significantly affects the p_T of its decay products. For ggF production expected exclusion limits are shown for the cases where only the b quark and only the t quark, respectively, are taken into account in the ggF loop.

Also shown in Fig. 8.11 are the expected 95% CL upper limits split by final states. For ggF production, the $\tau_\mu\tau_\mathrm{h}$ final state is most sensitive in the low-mass regime ($m_\phi < 300$ GeV), and the $\tau_\mu\tau_\mathrm{h}$ and $\tau_\mathrm{h}\tau_\mathrm{h}$ final states have roughly the same sensitivity for the medium and high mass regime. For b-associated production, the $\tau_\mathrm{h}\tau_\mathrm{h}$ final state is the most sensitive for masses larger than $m_\phi > 200$ GeV. The upper limits obtained from the cross-check analysis for the $\tau_\mathrm{e}\tau_\mathrm{h}$ and $\tau_\mu\tau_\mathrm{h}$ final states, described in Sec. 8.3.5, are compatible within uncertainties.

Limits are also obtained for the simulation-based cross-check analysis in the $\tau_\mathrm{e}\tau_\mathrm{h}$ and $\tau_\mu\tau_\mathrm{h}$ final states, as described in Sec. 8.3.5. The upper limits are compatible within uncertainties.

Likelihood Scan in the $\mathrm{gg}\phi - \mathrm{bb}\phi$ Plane

The above presented 95% CL upper limits provide a tool to study one of the two production processes independently of the other. To test the compatibility of BSM scenarios with the results of this analysis, additional likelihood scans are performed in the $\mathrm{gg}\phi - \mathrm{bb}\phi$ plane referring to the 2D plane that is spanned for every mass point by the product of cross section times branching ratio of ggF and b-association production ($\sigma \cdot \mathcal{B}$). This is achieved by evaluating the likelihood value for each pair of $\sigma(\mathrm{gg}\phi) \cdot \mathcal{B}(\phi \to \tau\tau)$ and $\sigma(\mathrm{bb}\phi) \cdot \mathcal{B}(\phi \to \tau\tau)$.

The fit is performed assuming a background prediction that includes the SM Higgs
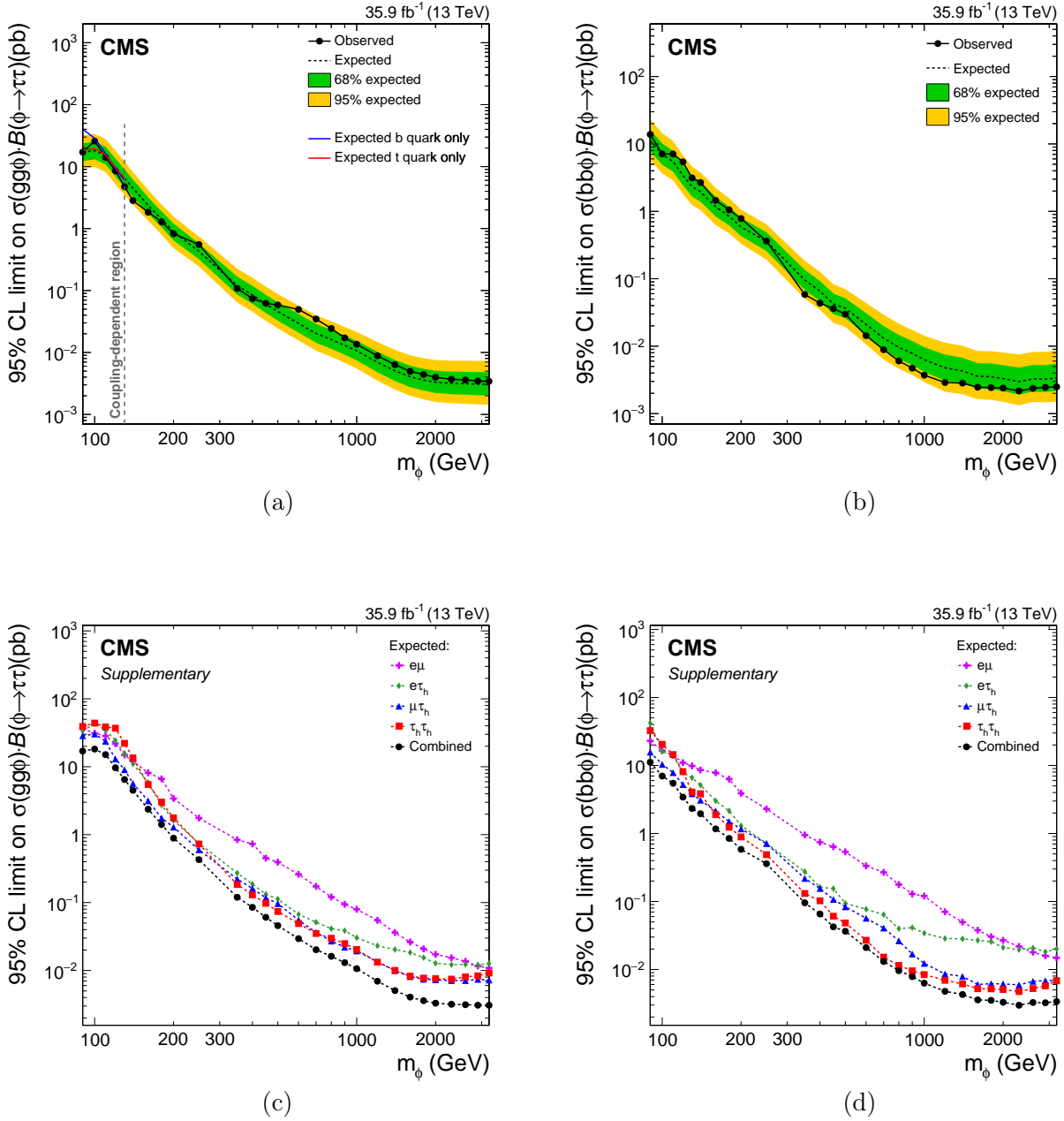
Figure 8.11: Expected and observed 95% CL upper limits for the production of a single narrow resonance ϕ with a mass between 90 GeV and 3.2 GeV in the ττ final state [143]. For these limits the SM Higgs boson has been included in the background. Limits are obtained for ggF production (a) and for production in association with b quarks (b). Also shown are the expected 95% CL upper limits split by final states for ggF (c) and b-associated production (d).

boson. A representative result for six exemplary mass points is shown in Fig. 8.12. The observed values are compatible with the background-only hypothesis that is indicated by the origin in the 2D planes. Additionally, the 68% and 95% CLs are indicated in the figures. For nearly all mass points the origin is well within the 68% CL of the best-fit value. The largest deviation is observed for $m_\phi = 700$ GeV with the SM expectation slightly outside the 68% CL.

Model-Dependent Exclusion Limits

For further interpretation exclusion contours in the m_A-$\tan\beta$ plane are obtained for two representative MSSM benchmark scenarios: the m_h^{mod+} and the hMSSM scenario, as introduced in Sec. 2.6.2.

In order to obtain exclusion limits in the m_A-$\tan\beta$ plane, the test statistic q_μ is modified to compare two fixed values of μ against each other, $\mu = 1$ and $\mu = 0$. Here, $\mu = 1$ describes the signal prediction for given values of m_A and $\tan\beta$, and $\mu = 0$ corresponds to the background-only prediction, i.e. no signal strength is included. The SM Higgs boson is added to the SM background in the likelihood ratio, and the MSSM signal-template combines 3 Higgs-signals (h,H,A).

The probability distribution functions for the test statistic are generated by pseudo-experiments. In principle, corresponding distributions need to be derived for every parameter point in the m_A-$\tan\beta$ plane. However, in order to reduce the computational efforts the points in the m_A-$\tan\beta$ plane are chosen such that the highest density is close to the expected exclusion limit and only few points are probed farther away. For parameter points in between the results are interpolated.

In Fig. 8.13, the observed and expected 95% CL exclusion contours are shown for the MSSM m_h^{mod+} and the hMSSM scenarios. For values $m_A \lesssim 250$ GeV the contours in both scenarios exclude values above $\tan\beta \approx 6$. The observed and expected exclusion limits agree over the whole mass range. The largest deviations are still contained in the 95% CI. In Fig. 8.14, the obtained 95% CL exclusion contours in the MSSM m_h^{mod+} scenario are compared to previous CMS publications. The obtained exclusion contours reach up to 1.6 TeV, extending the previously excluded mass range by almost a factor two in m_A. In the low-mass region, the exclusion contours are similar to the previous ones. This can be ascribed to three main factors: in the $\tau_e\tau_h$ and $\tau_\mu\tau_h$ final states, the increased instantaneous luminosity requires higher p_T thresholds at trigger level and as a result the signal acceptance is reduced; the discriminating variable m_T^{tot} is designed to provide more sensitivity for high-mass points, but in return provides less sensitivity to

the low-mass points; the improved signal prediction at NLO shows a softer p_T spectrum for the ggF production mode, which dominates at low $\tan\beta$ values.

In Fig. 8.14b, expected and observed 95% CL exclusion contours in the MSSM $m_\mathrm{h}^\mathrm{mod+}$ scenario of CMS and ATLAS results are compared. Both results are obtained using the full set of 2016 collision data. The ATLAS exclusion limit corresponds to the limit shown in Fig. 6.3c [127].
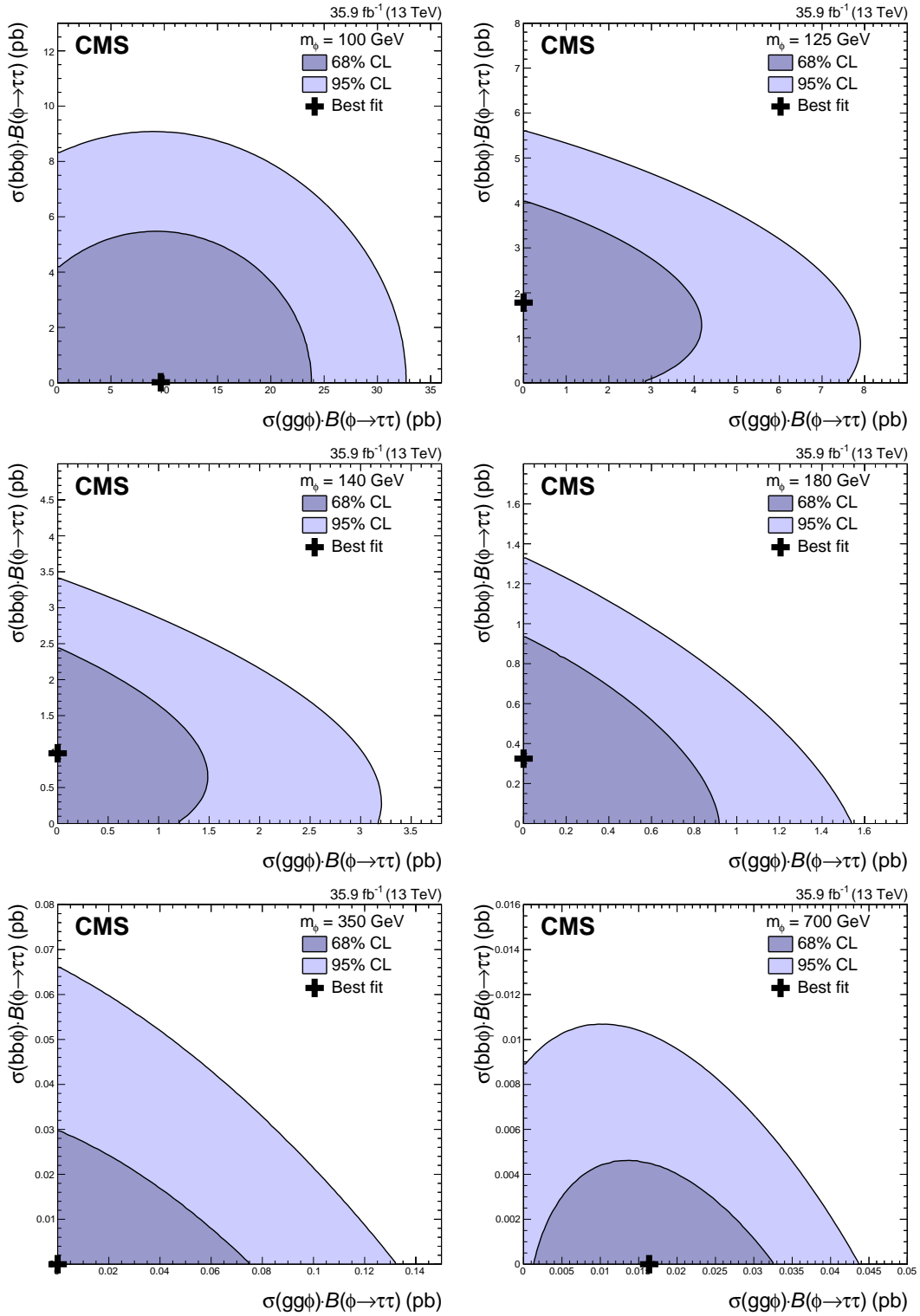
Figure 8.12: Likelihood scan for the search for a narrow width resonance produced via ggF or in association with b quarks in the $\tau\tau$ final state [143]. A representative subset of the tested mass points is shown.
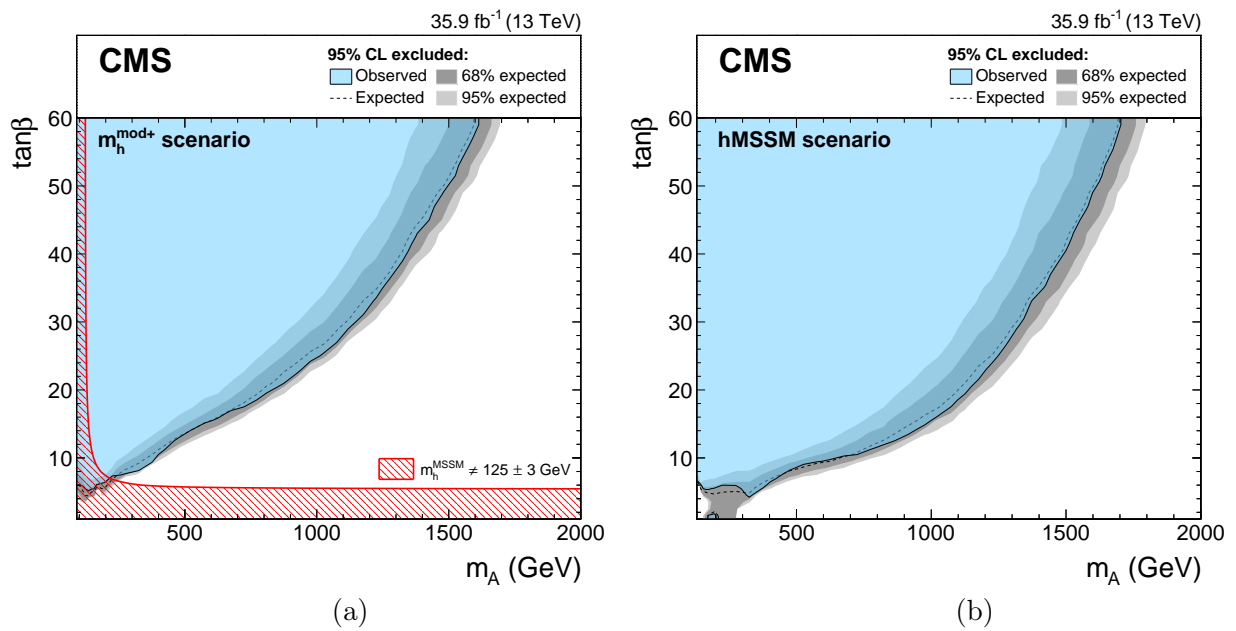
Figure 8.13: Expected and observed 95% CL exclusion contours in the m_A-$\tan\beta$ plane in the MSSM $m_h^{\mathrm{mod}+}$ scenario (a) and in the hMSSM scenario (b) [143].
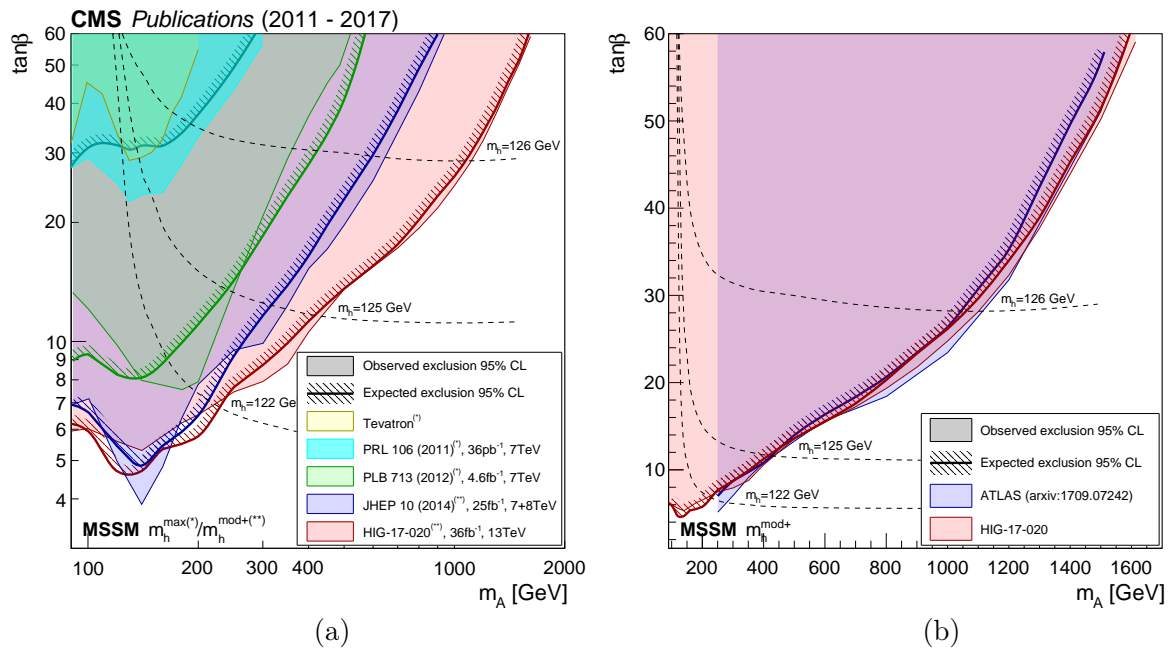
Figure 8.14: Expected and observed 95% CL exclusion contours in the m_A-$\tan\beta$ plane comprising CMS publications during the years 2011 till 2017 (a) [143]. The exclusion contours are shown in the MSSM $m_h^{\max}$ and $m_h^{\mathrm{mod}+}$ scenario. ATLAS and CMS exclusion limit comparison in the MSSM $m_h^{\mathrm{mod}+}$ scenario (b). The ATLAS exclusion is taken from Ref. [127].

Conclusions

Two analyses based on proton-proton collision data recorded by the CMS detector and CMS upgrade plans for the HL-LHC era have been presented in this thesis. The inclusive $Z/\gamma^* \to \tau\tau$ cross section measurement and the search for additional neutral Higgs bosons share a similar baseline selection and common analysis techniques.

The $Z/\gamma^* \to \tau\tau$ cross section has been measured for the first time at a center-of-mass energy of 13 TeV, using 2015 proton-proton collision data, corresponding to an integrated luminosity of 2.3 fb^{-1}. The product of cross section times branching fraction, $\sigma(\text{pp} \to Z/\gamma^* + X) \times \mathcal{B}(Z/\gamma^* \to \tau\tau)$, amounts to $1848 \pm 12(\text{stat.}) \pm 67(\text{syst.+lumi.})$ pb, in agreement with the SM expectation. The signal yield has been obtained in a simultaneous ML fit to the mass distribution, $m_{\tau\tau}$, in five di-tau final states: $\tau_\text{e}\tau_\text{h}$, $\tau_\mu\tau_\text{h}$, $\tau_\text{h}\tau_\text{h}$, $\tau_\text{e}\tau_\mu$ and $\tau_\mu\tau_\mu$. Furthermore, the τ_h reconstruction and ID efficiency and the τ_h ES have been determined. The resulting scale factors amount to 0.979 ± 0.022 and 0.986 ± 0.009 for the τ_h ID efficiency and for the τ_h ES, respectively.

A search for heavy neutral Higgs bosons decaying into pairs of tau leptons has been performed in the context of the MSSM, using 2016 proton-proton collision data corresponding to an integrated luminosity of 35.9 fb^{-1}. The analysis exploits the $\tau_\text{e}\tau_\text{h}$, $\tau_\mu\tau_\text{h}$, $\tau_\text{h}\tau_\text{h}$ and $\tau_\text{e}\tau_\mu$ final states, and uses 16 signal categories and three complementary background control regions. The categorization targets ggF and b-associated production motivated by the potential enhancement of the coupling of heavy neutral Higgs bosons to down-type fermions. The total transverse mass, m_T^tot, is chosen as discriminating variable and a simultaneous ML fit is performed to all signal categories and background control regions. No excess of events with respect to the SM expectation has been observed. Model-independent cross section limits have been set for ggF and b-associated production. Likelihood scans in the ggϕ-bbϕ plane have been provided, showing compatibility with the background only hypothesis. The results are supple-

mented by exclusion contours of two representative MSSM benchmark scenarios, i.e. the $m_\mathrm{h}^\mathrm{mod+}$ and the hMSSM scenario. Both scenarios exclude a heavy neutral MSSM Higgs boson of $m_\mathrm{A} \lesssim 250$ GeV for values of $\tan\beta$ above 6. For values of $\tan\beta < 60$ the exclusion contours reach values up to 1.6 GeV.

The fake factor method is introduced in the $\tau_\mathrm{e}\tau_\mathrm{h}$, $\tau_\mu\tau_\mathrm{h}$ and $\tau_\mathrm{h}\tau_\mathrm{h}$ final states to estimate backgrounds arising from events in which a quark or gluon jet is misidentified as τ_h, dominantly the W+jets, QCD multijet, $t\bar{t}$ backgrounds. The main processes contributing to this background contain specific mixtures of gluon-, light-quark and heavy-quark-initiated jets, which have different probabilities to be misidentified as τ_h decay. An unbiased modeling of the misidentified-τ_h background is achieved by independently deriving fake factors for the W+jets, QCD multijet and $t\bar{t}$ backgrounds and subsequently combining these fake factors based on the relative misidentified-τ_h background content in the application region.

The fake factor method is deployed for the first time in the $\mathrm{Z}/\gamma^* \to \tau\tau$ cross section measurement and extended within the scope of the search for a neutral MSSM Higgs boson. In both analyses, the method has been able to successfully model the misidentified-τ_h background in all three final states and in all subcategories. Dedicated cross checks have been performed which further validate the method.

The fake factor method is designed such that it can be used in similar (future) analyses. Since it relies almost entirely on collision data, simulation-related uncertainties become negligible. Hence, the statistical power of the method scales directly with the collected luminosity. In the light of the expected strong increase of collision data provided by the LHC, even larger simulation samples are needed to avoid prohibitively large statistical uncertainties of the modeling. The fake factor method provides an appealing alternative to simulation-based background estimation and is designed to completely substitute them for misidentified-τ_h backgrounds in the $\tau_\mathrm{e}\tau_\mathrm{h}$, $\tau_\mu\tau_\mathrm{h}$ and $\tau_\mathrm{h}\tau_\mathrm{h}$ final states.

Acknowledgements

Appendix

A.1 Measurement of the $Z/\gamma^* \to \tau\tau$ Cross Section in pp Collisions at $\sqrt{s} = 13$ TeV and Validation of τ Lepton Analysis Techniques - Supplementary Information

A.1.1 Fake Factor Corrections in the $\tau_e\tau_h$ Final State

(a)

(b)

(c)

(d)

(e)
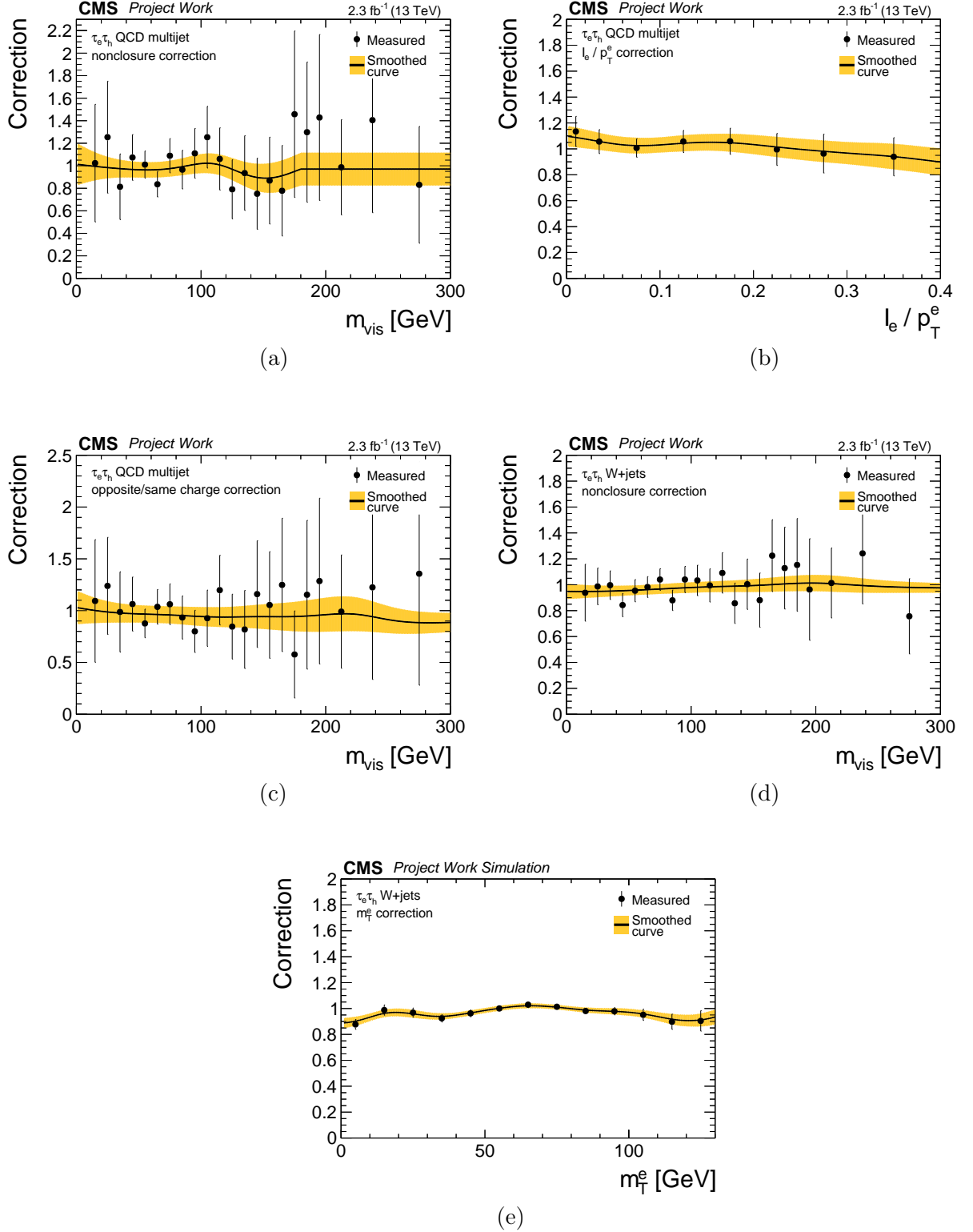
Figure A.1: Fake factor corrections in the $\tau_e\tau_h$ final state containing corrections for the raw FF_{QCD}: nonclosure correction in m_{vis} (a), I^e/p_T^e correction (b) and opposite/same charge correction (c) and corrections for the raw FF_{Wjets}: nonclosure correction in m_{vis} (d) and m_T^e correction (e).

A.1.2 Fake Factor Corrections in the $\tau_h\tau_h$ Final State

(a)   (b)
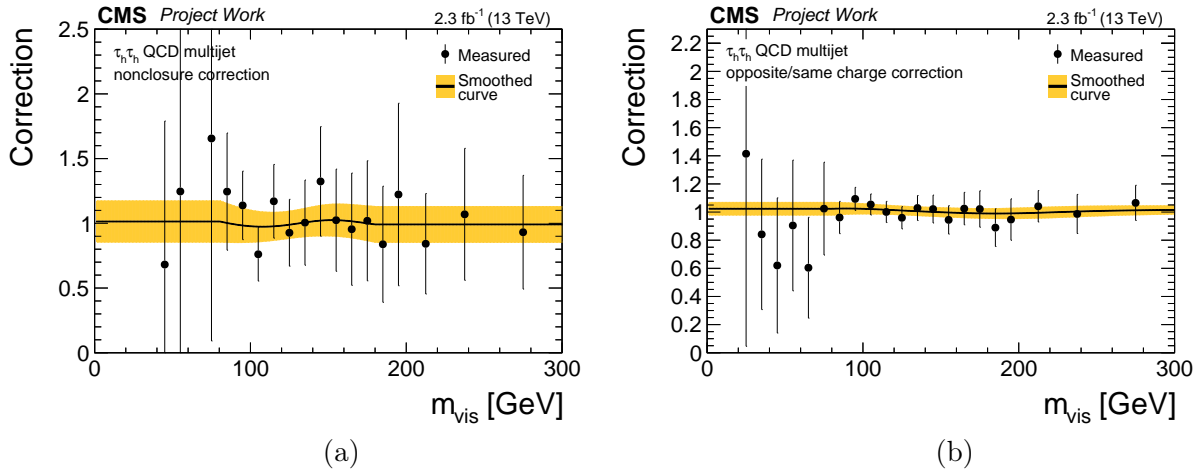
Figure A.2:   Fake factor corrections in the $\tau_e\tau_h$ final state containing corrections for the raw FF_{QCD}: nonclosure correction in m_{vis} (a) and a opposite-sign/same-sign electric charge correction (b).

A.1.3 Validation of Fake Factor Estimate in $\tau_e\tau_h$ Categories
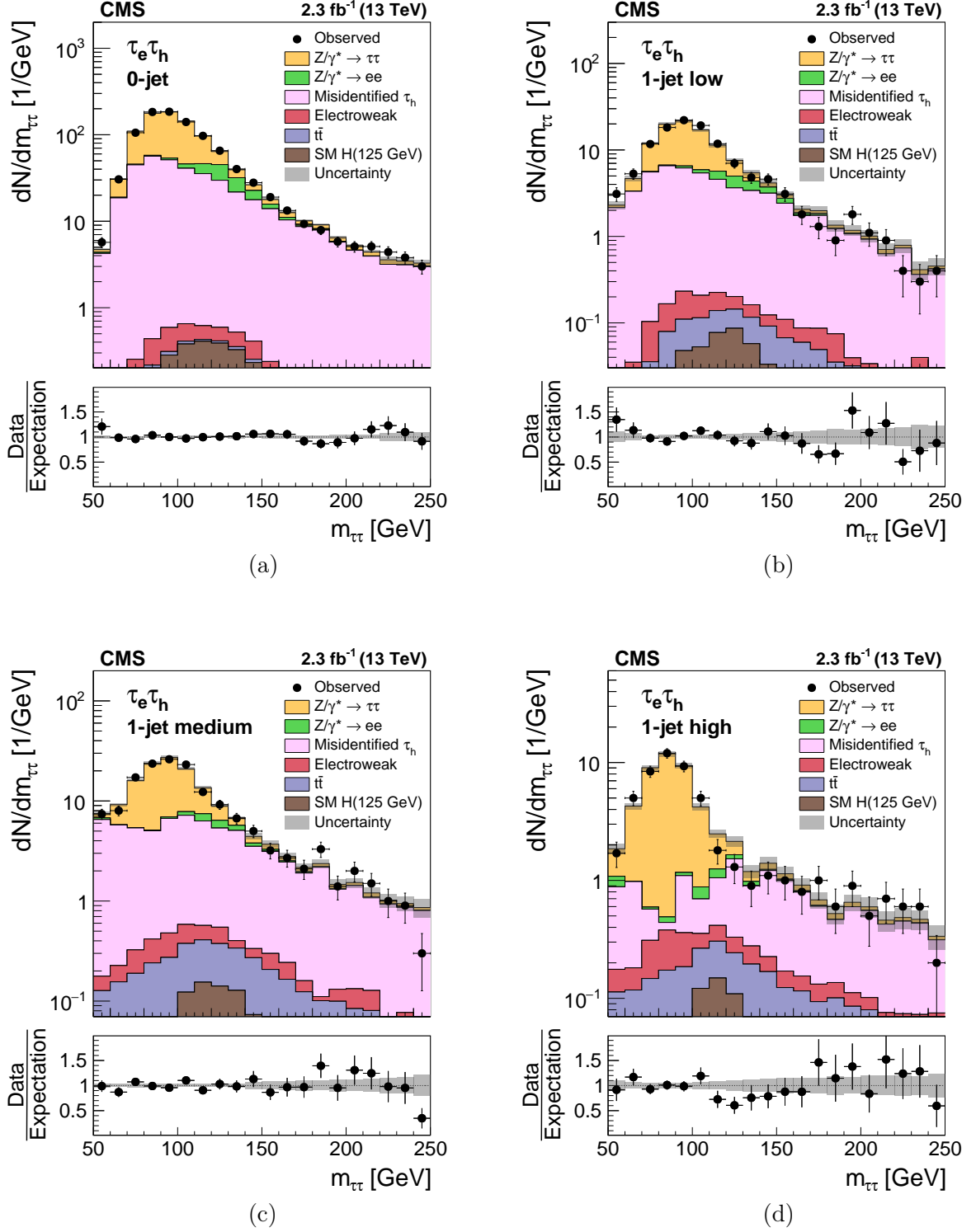
Figure A.3: Post-fit distributions of $m_{\tau\tau}$ in different exclusive event categories in the $\tau_e\tau_h$ final state: 0-jet (a), 1-jet low (b), 1-jet medium (c) and 1-jet high Z boson p_T (d) [128].
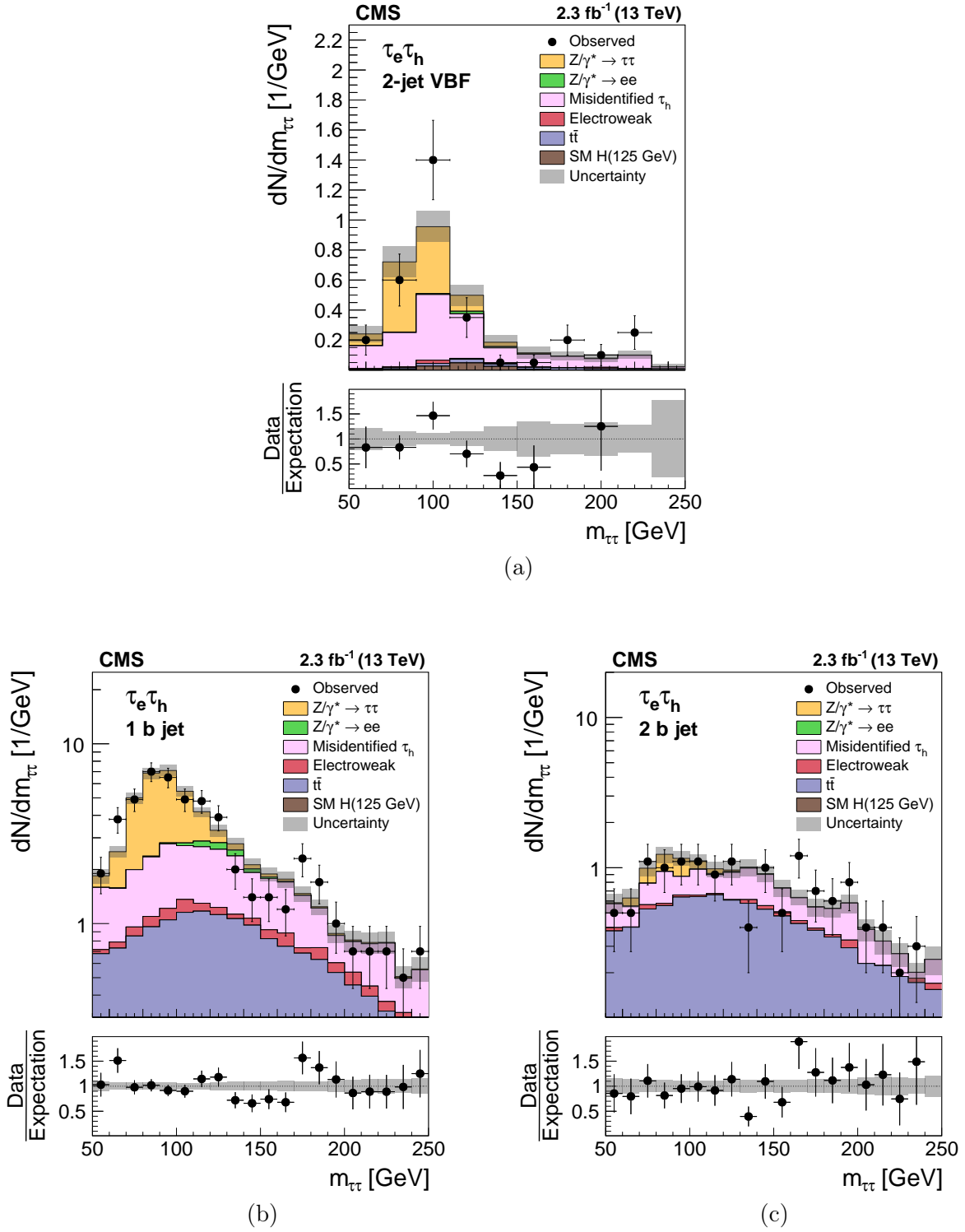
Figure A.4: Post-fit distributions of $m_{\tau\tau}$ in different exclusive event categories in the $\tau_e\tau_h$ final state: 2-jet VBF (a), 1 b jet (b) and 2 b jet (c) [128].

A.1.4 Validation of Fake Factor Estimate in $\tau_h\tau_h$ Categories
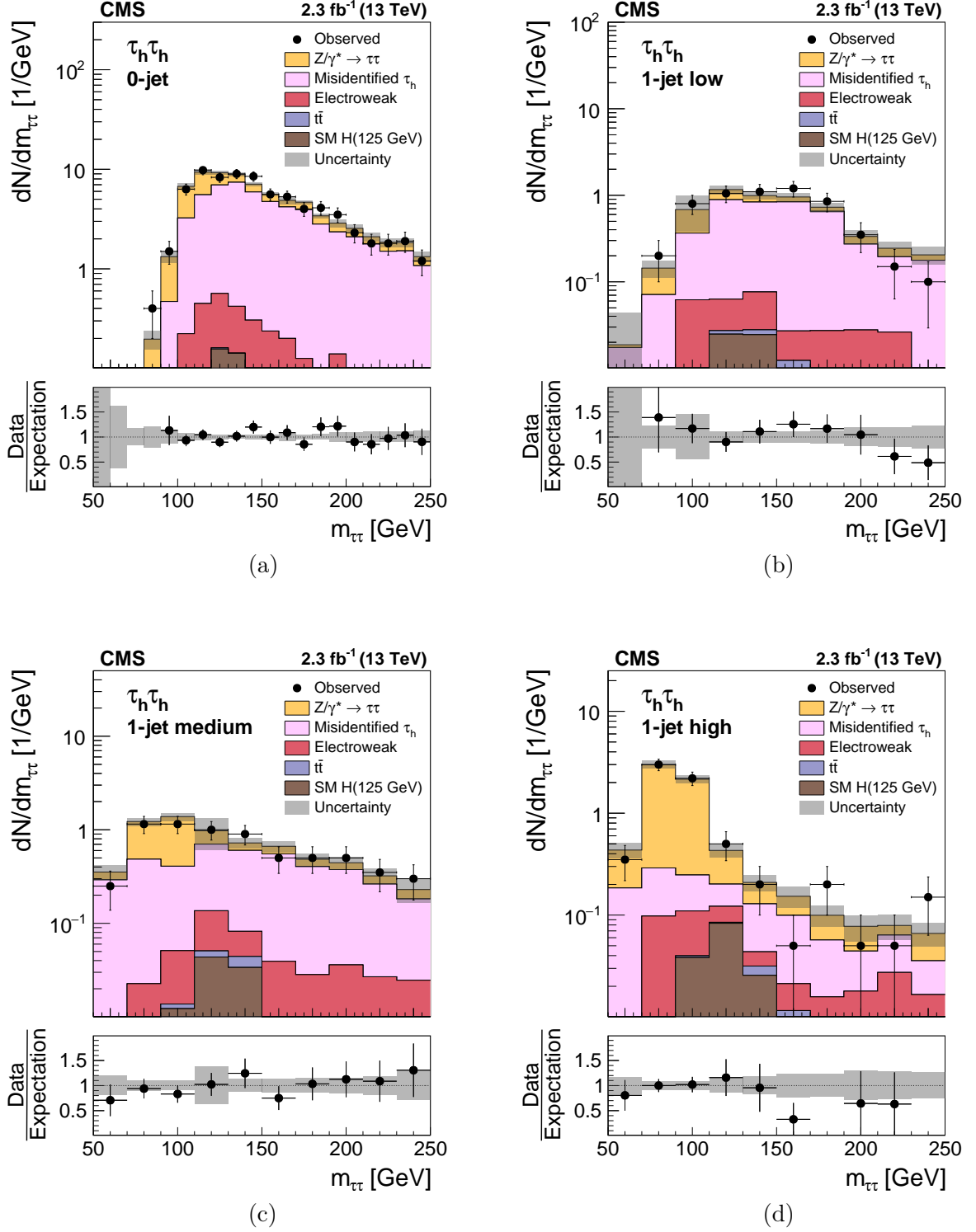
Figure A.5: Post-fit distributions of $m_{\tau\tau}$ in different exclusive event categories in the $\tau_h\tau_h$ final state: 0-jet (a), 1-jet low (b), 1-jet medium (c) and 1-jet high Z boson p_T (d) [128].
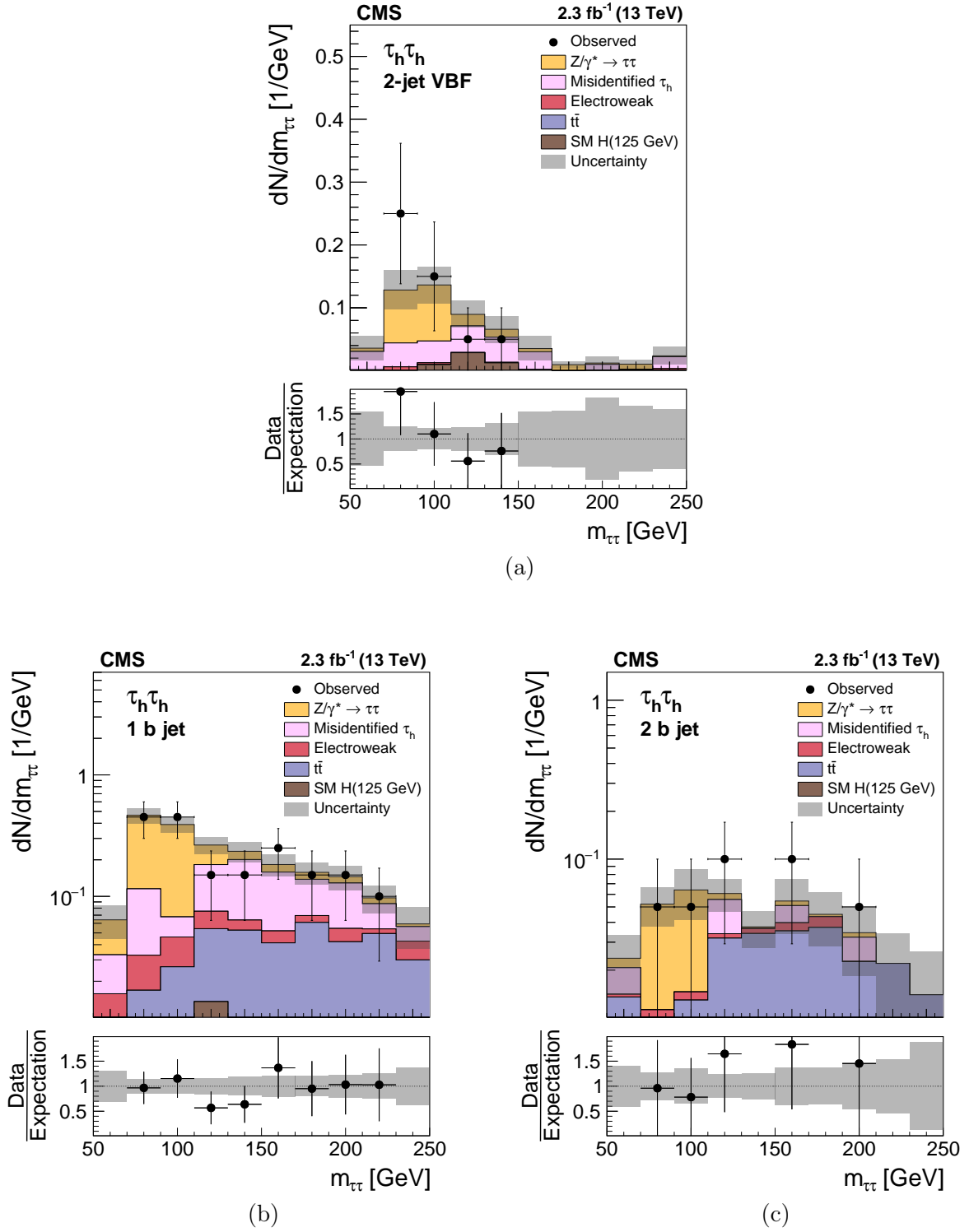
Figure A.6: Post-fit distributions of $m_{\tau\tau}$ in different exclusive event categories in the $\tau_h\tau_h$ final state: 2-jet VBF (a), 1 b jet (b), and 2 b jet (c) [128].

A.1.5 Signal and Background Yields

Process	$\tau_e\tau_h$	$\tau_\mu\tau_h$	$\tau_h\tau_h$
$Z/\gamma^* \to \tau\tau$	$7\,160 \pm 130$	$20\,020 \pm 220$	415 ± 32
Jets misidentified as τ_h	$5\,690 \pm 160$	$10\,550 \pm 220$	770 ± 49
$t\bar{t}$	354 ± 26	639 ± 47	17 ± 2
$Z/\gamma^* \to$ ee, $\mu\mu$ (e or μ misidentified as τ_h)	718 ± 96	840 ± 130	-
Electroweak	93 ± 13	183 ± 28	40 ± 6
SM H	49 ± 11	103 ± 23	13 ± 3
Total expected background	$6\,900 \pm 130$	$12\,310 \pm 180$	841 ± 46
Total SM expectation	$14\,060 \pm 120$	$32\,340 \pm 180$	$1\,255 \pm 40$
Observed data	$14\,063$	$32\,350$	$1\,255$

Process	$\tau_e\tau_\mu$	$\tau_\mu\tau_\mu$
$Z/\gamma^* \to \tau\tau$	$13\,600 \pm 220$	$2\,067 \pm 34$
QCD Multijet	$4\,620 \pm 240$	710 ± 110
$Z/\gamma^* \to$ ee, $\mu\mu$	-	$8\,010 \pm 170$
$t\bar{t}$	$3\,500 \pm 140$	$1\,239 \pm 79$
Electroweak	$1\,146 \pm 98$	293 ± 30
SM H	57 ± 12	18 ± 4
Total expected background	$9\,300 \pm 210$	$10\,270 \pm 120$
Total SM expectation	$22\,930 \pm 130$	$12\,340 \pm 120$
Observed data	$22\,930$	$12\,327$

Table A.1: Yields in $Z/\gamma^* \to \tau\tau$ signal events and backgrounds in the $\tau_e\tau_h$, $\tau_\mu\tau_h$, $\tau_h\tau_h$, $\tau_e\tau_\mu$, and $\tau_\mu\tau_\mu$ final states, obtained from the ML fit described in Section 7.6.1 [128]. The yields and uncertainties are rounded to a precision of two significant digits on the uncertainty.

A.2 Search for Additional Neutral MSSM Higgs Bosons in the Tau Tau Final State in Proton-Proton Collisions at $\sqrt{s} = 13$ TeV - Supplementary Information

A.2.1 Fraction of Misidentified-τ_h backgrounds in the AR in the $\tau_e\tau_h$ and $\tau_h\tau_h$ Final States
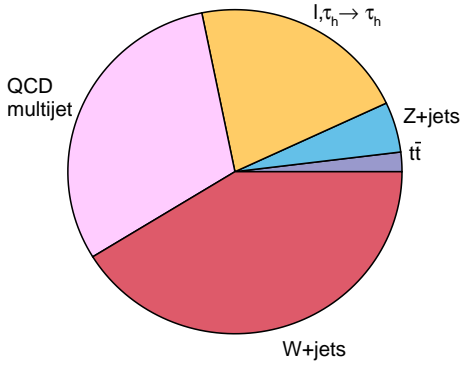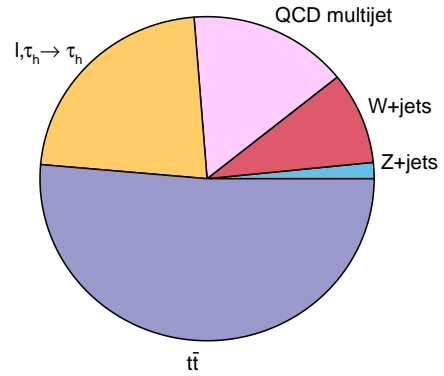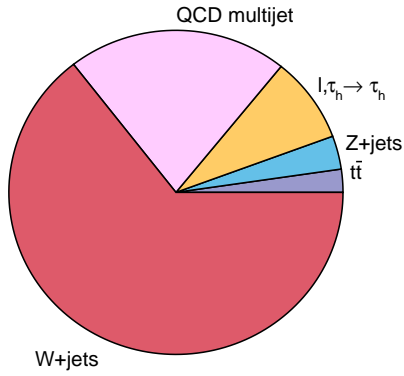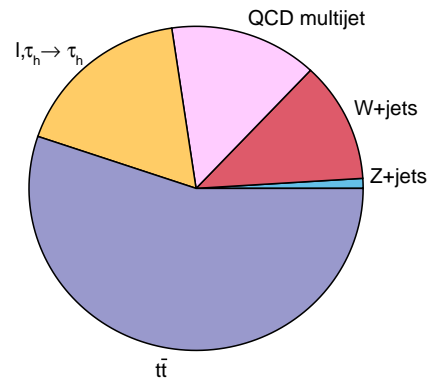
Figure A.7: Fraction of misidentified-τ_h backgrounds in the AR in four exclusive event categories in the $\tau_e\tau_h$ final state [143]. Backgrounds in the AR are due to QCD multijet, W+jets, $Z/\gamma^* \to \ell\ell +$ jets, and $t\bar{t}$ production. The yellow part displays the contributions from events with genuine τ_h decays or misidentified electrons or muons.
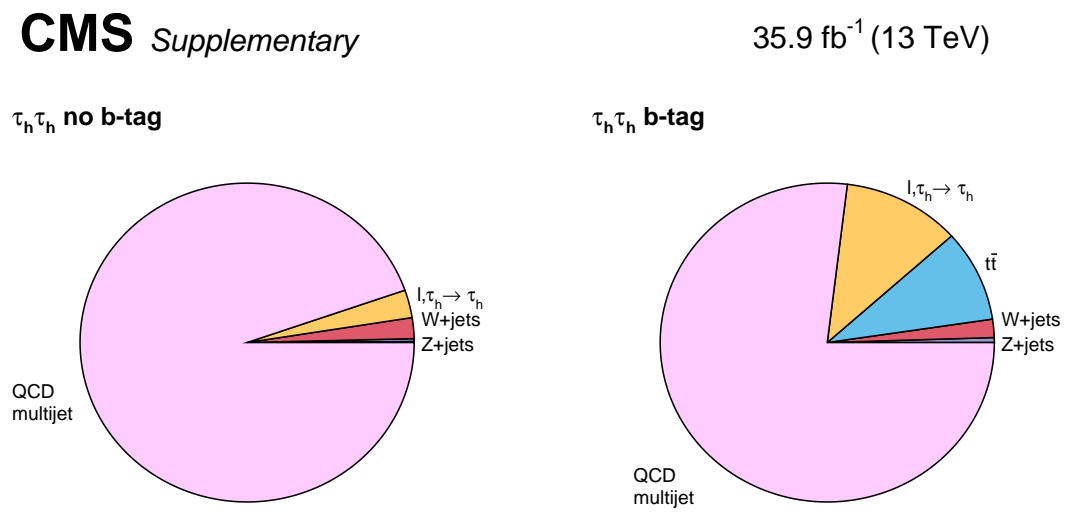
Figure A.8: Fraction of misidentified-τ_h backgrounds in the AR in two exclusive event categories in the $\tau_h\tau_h$ final state [143]. Backgrounds in the AR are due to QCD multijet, W+jets, $Z/\gamma^* \rightarrow \ell\ell +$ jets, and $t\bar{t}$ production. The yellow part displays the contributions from events with genuine τ_h decays or misidentified electrons or muons.

A.2.2 Simulation-based cross-check - Less sensitive event subcategories
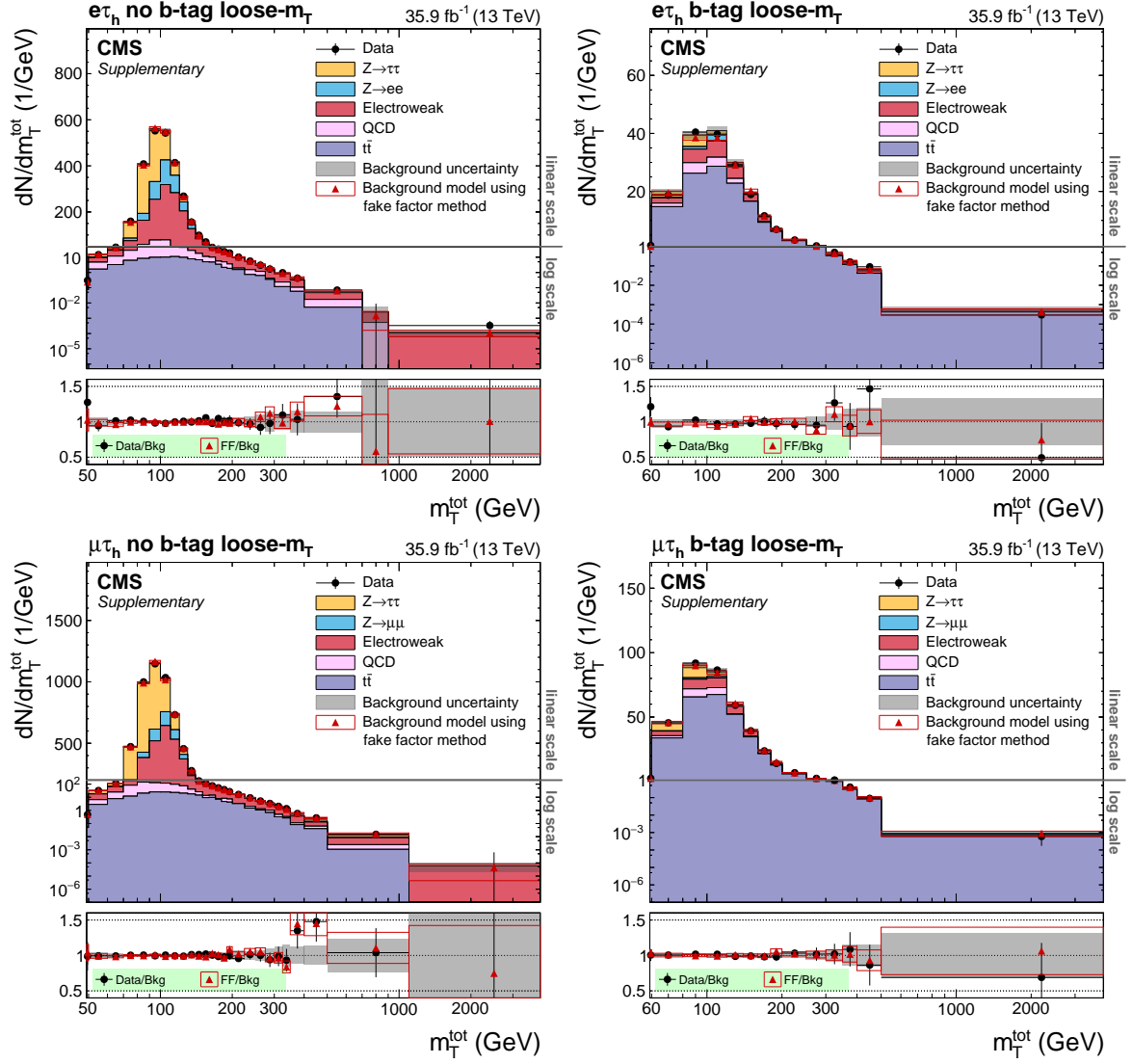
Figure A.9: Post-fit distributions of m_T^{tot} in the $\tau_e\tau_h$ (top) and $\tau_\mu\tau_h$ (bottom) final states, using the simulation-based cross-check [143]. For both final states the less sensitive loose-m_T event subcategories are shown. The triangles correspond to the background estimate obtained when the fake factor method is used.

A.2.3 Distribution of m_T^{tot} in the $\tau_e\tau_h$ and $\tau_\mu\tau_h$ final states - Less sensitive event subcategories

Figure A.10: Post-fit distribution of m_T^{tot} in the $\tau_e\tau_h$ (top) and $\tau_\mu\tau_h$ (bottom) final state [143]. For both final states the less sensitive Loose-m_T event subcategories are shown. The change from logarithmic to linear scale on the vertical axis is indicated by the gray horizontal line.

A.2.4 Distribution of m_T^{tot} in the $\tau_e\tau_\mu$ final state - Less sensitive event subcategories
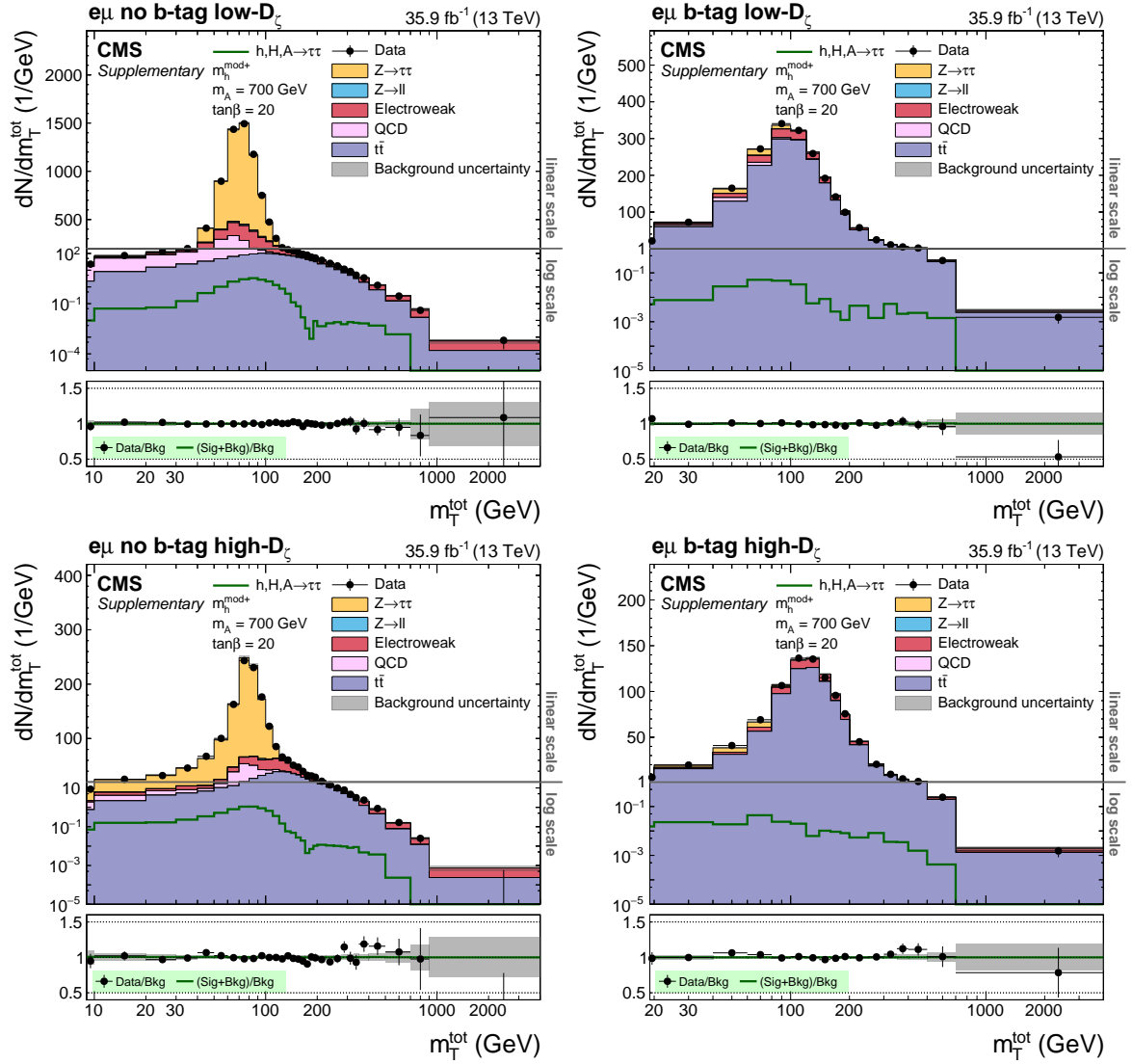
Figure A.11: Post-fit distribution of m_T^{tot} in the $\tau_\mu\tau_e$ final state [143]. The less sensitive Low-D_ζ (top) and High-D_ζ (bottom) event subcategories are shown. The change from logarithmic to linear scale on the vertical axis is indicated by the gray horizontal line..

A.2.5 Model Independent Exclusion Limits - No SM Higgs boson in the SM Background
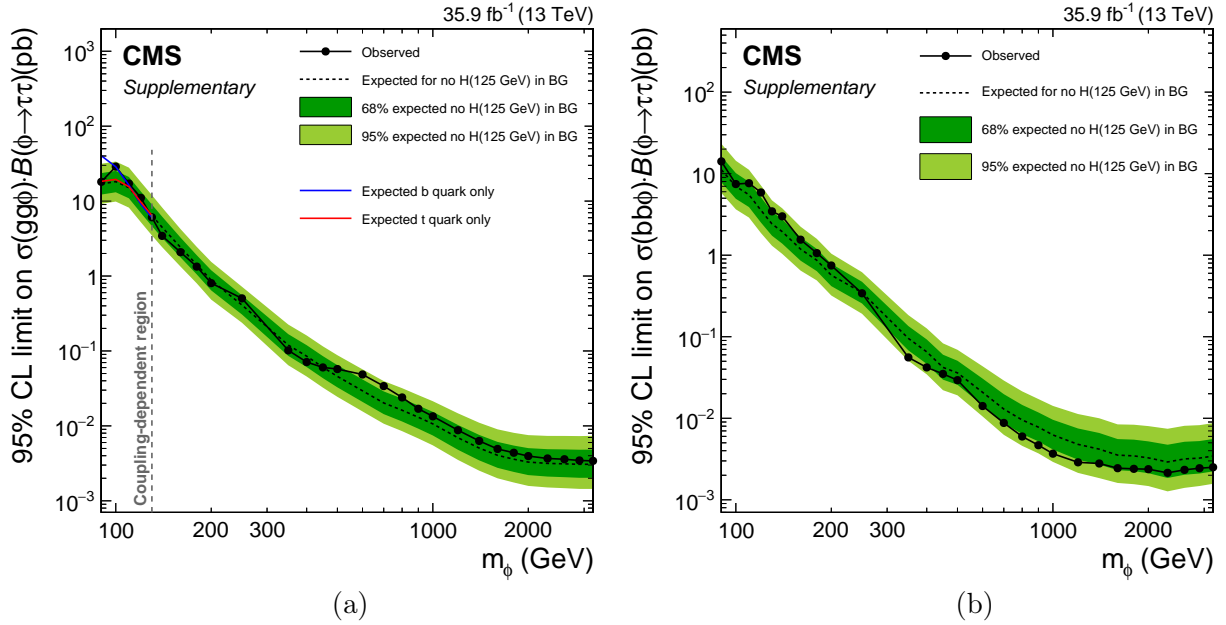
Figure A.12: Expected and observed 95% CL upper limits for the production of a single narrow resonance, ϕ, with a mass between 90 GeV and 3.2 GeV in the $\tau\tau$ final state [143]. For these limits the SM Higgs boson has not been added to the SM background. Limits are obtained for ggF production (a) and for production in association with b quarks (b). For ggF production also shown are the expected exclusion limits for the cases where only the b quark (blue continuous line) and only the t quark (red continuous line) are taken into account in the ggF loop.

A.2.6 Events numbers per subcategory

		Category	N_{Data}	$H \to \tau\tau$ (SM)	$Z \to \tau\tau$	$Z \to ll$	Diboson+single t	$t\bar{t}$	W + jets	QCD
$\tau_e\tau_\mu$	No b-tag	Low-D_ζ	85816	0.24	49.55	1.06	11.50	15.73	6.03	15.88
		Medium-D_ζ	102143	0.37	69.90	0.75	4.97	8.22	1.94	13.85
		High-D_ζ	18364	0.50	45.66	0.38	11.95	32.59	1.94	6.99
	b-tag	Low-D_ζ	42870	0.01	2.08	0.08	6.88	89.19	0.27	1.49
		Medium-D_ζ	27803	0.03	4.37	0.12	6.57	86.63	0.14	2.14
		High-D_ζ	20208	0.03	1.72	0.01	7.00	91.09	0.16	> 0.01

		Category	N_{Data}	$H \to \tau\tau$ (SM)	$Z \to \tau\tau$	$Z \to ll$†	Diboson+single t†	$t\bar{t}$†	jet $\to \tau_h$
$\tau_e\tau_h$	No b-tag	Tight-m_T	49120	0.66	55.82	12.72	0.95	1.24	28.61
		Loose-m_T	29108	0.35	28.41	11.71	1.70	2.32	55.50
	b-tag	Tight-m_T	3886	0.28	17.21	2.08	4.97	50.45	25.01
		Loose-m_T	3657	0.10	5.58	1.65	5.65	57.51	29.52
$\tau_\mu\tau_h$	No b-tag	Tight-m_T	124707	0.64	67.72	4.64	0.88	1.11	25.01
		Loose-m_T	58534	0.38	34.62	5.77	1.96	2.57	54.70
	b-tag	Tight-m_T	8778	0.28	19.33	0.98	4.80	50.11	24.50
		Loose-m_T	7887	0.08	5.86	0.59	5.55	59.65	28.28
$\tau_h\tau_h$	No b-tag		105545	0.45	14.94	2.08	0.28	0.23	82.02
	b-tag		3416	0.52	20.80	1.03	2.65	18.75	56.25

Table A.2: Observed number of selected events (N_{Data}) and the relative contribution of the expected backgrounds to the selected events in all event categories in the $\tau_e\tau_\mu$, $\tau_e\tau_h$, $\tau_\mu\tau_h$, and $\tau_h\tau_h$ final states [143]. The relative contribution of the expected backgrounds to the selected events is given in %, including the contribution of a SM Higgs boson with a mass of 125 GeV, and prior to the fit used for the signal extraction. In all but the $\tau_e\tau_\mu$ final state those events of a given processes, where a jet is misidentified as a hadronic τ lepton decay are subsumed into a common jet $\to \tau_h$ background class which is estimated from data.

† Excluding events with jets misidentified as τ_h candidates.

List of Figures

List of Tables

Acronyms and Abbreviations

AR	Application region
ATLAS	A Toroidal LHC Apparatus
BDT	Boosted Decision Tree
BS	Beam spot
BSM	Beyond the standard model
CERN	European Organization for Nuclear Research
CI	Confidence interval
CKM	Cabbibo-Kobayashi-Maskawa
CL	Confidence level
CMS	Compact Muon Solenoid
CP	Charge - parity
CPT	Charge - parity - time
CR	Control region
CSV	Combined Secondary Vertex
DAQ	Data acquisition
ECAL	Electromagnetic calorimeter
ES	Energy scale
FF	Fake factor

ggF	Gluon-gluon fusion
HCAL	Hadron calorimeter
HL-LHC	High Luminosity LHC
HLT	High-level trigger
HPS	Hadrons+strips
ID	Identification
IP	Interaction point
L1	Level-1
LEP	Large Electron-Positron Collider
LHC	Large Hadron Collider
LO	Leading order
MC	Monte Carlo
ML	Maximum likelihood
MR	Measurement region
MSSM	Minimal supersymmetric extension of the standard model
MVA	Multivariate
NLO	Next-to-leading order
NNLO	Next-to-next-to-leading order
OS	Opposite-sign
PF	Particle-flow
PLR	Profile Likelihood Ratio
POI	Parameter of interest
PU	Pileup
PV	Primary vertex
QCD	Quantum Chromodynamics
SM	Standard model of particle physics
SPS	Super Proton Synchroton
SR	Signal region

SR	Signal region
SS	Same-sign
SV	Secondary vertex
VBF	Vector boson fusion
WLCG	Worldwide LHC Computing Grid
WP	Working point

Bibliography

[1] ATLAS Collaboration, Observation of a new particle in the search for the Standard Model Higgs boson with the ATLAS detector at the LHC, *Phys. Lett.*, vol. B716, pp. 1–29, 2012, arXiv:1207.7214. doi: 10.1016/j.physletb.2012.08.020

[2] CMS Collaboration, Observation of a new boson at a mass of 125 GeV with the CMS experiment at the LHC, *Phys. Lett.*, vol. B716, pp. 30–61, 2012, arXiv:1207.7235. doi: 10.1016/j.physletb.2012.08.021

[3] M. E. Peskin and D. V. Schroeder, An Introduction To Quantum Field Theory. New York: Westview Press, 1995. ISBN 081-3-345-43X-

[4] D. Griffiths, Introduction to elementary particles, 2008. ISBN 9783527406012

[5] W. Cottingham and D. Greenwood, An introduction to the standard model of particle Physics. Cambridge Univ. Press, 2007. ISBN 9780521621960

[6] S. Weinberg, Recent progress in gauge theories of the weak, electromagnetic and strong interactions, *Rev. Mod. Phys.*, vol. 46, pp. 255–277, 1974, [J. Phys. Colloq.34,no.C1,45(1973)]. doi: 10.1051/jphyscol:1973103

[7] B. Hall, Lie Groups, Lie Algebras and Representations. Springer Science & Business Media, 2003. ISBN 0387401229, 9780387401225

[8] D. H. Perkins, Introduction to high energy physics. Cambridge Univ. Press, 2000. ISBN 9780521621960

[9] Gargamelle Neutrino Collaboration, Observation of Neutrino Like Interactions without Muon or Electron in the Gargamelle Neutrino Experiment, *Nucl. Phys.*, vol. B73, pp. 1–22, 1974. doi: 10.1016/0550-3213(74)90038-8

[10] UA1 Collaboration, Experimental Observation of Isolated Large Transverse Energy Electrons with Associated Missing Energy at s**(1/2) = 540-GeV, *Phys. Lett.*, vol. 122B, pp. 103–116, 1983, [,611(1983)]. doi: 10.1016/0370-2693(83)91177-2

[11] UA2 Collaboration, Observation of Single Isolated Electrons of High Transverse Momentum in Events with Missing Transverse Energy at the CERN anti-p p Collider, *Phys. Lett.*, vol. 122B, pp. 476–485, 1983. doi: 10.1016/0370-2693(83)91605-2

[12] UA1 Collaboration, Experimental Observation of Lepton Pairs of Invariant Mass Around 95-GeV/c**2 at the CERN SPS Collider, *Phys. Lett.*, vol. 126B, pp. 398–410, 1983. doi: 10.1016/0370-2693(83)90188-0

[13] UA2 Collaboration, Evidence for Z0 —> e+ e- at the CERN anti-p p Collider, *Phys. Lett.*, vol. 129B, pp. 130–140, 1983. doi: 10.1016/0370-2693(83)90744-X

[14] C. S. Wu, E. Ambler, R. W. Hayward, D. D. Hoppes, and R. P. Hudson, Experimental Test of Parity Conservation in Beta Decay, *Phys. Rev.*, vol. 105, pp. 1413–1414, 1957. doi: 10.1103/PhysRev.105.1413

[15] M. Goldhaber, L. Grodzins, and A. W. Sunyar, Helicity of Neutrinos, *Phys. Rev.*, vol. 109, pp. 1015–1017, 1958. doi: 10.1103/PhysRev.109.1015

[16] C. Patrignani *et al.*, Review of Particle Physics, *Chin. Phys.*, vol. C40, no. 10, p. 100001, 2016. doi: 10.1088/1674-1137/40/10/100001

[17] P. W. Higgs, Broken Symmetries and the Masses of Gauge Bosons, *Phys. Rev. Lett.*, vol. 13, pp. 508–509, 1964. doi: 10.1103/PhysRevLett.13.508

[18] F. Englert and R. Brout, Broken Symmetry and the Mass of Gauge Vector Mesons, *Phys. Rev. Lett.*, vol. 13, pp. 321–323, 1964. doi: 10.1103/PhysRevLett.13.321

[19] G. S. Guralnik, C. R. Hagen, and T. W. B. Kibble, Global Conservation Laws and Massless Particles, *Phys. Rev. Lett.*, vol. 13, pp. 585–587, 1964. doi: 10.1103/PhysRevLett.13.585

[20] J. Goldstone, Field Theories with Superconductor Solutions, *Nuovo Cim.*, vol. 19, pp. 154–164, 1961. doi: 10.1007/BF02812722

[21] A. Djouadi, *The Anatomy of electro-weak symmetry breaking. I: The Higgs boson in the standard model*, *Phys. Rept.*, vol. 457, pp. 1–216, 2008, arXiv:hep-ph/0503172. doi: 10.1016/j.physrep.2007.10.004

[22] LEP Working Group for Higgs boson searches, OPAL Collaboration, DELPHI Collaboration, ALEPH Collaboration, L3 Collaboration, *Search for the standard model Higgs boson at LEP*, *Phys. Lett.*, vol. B565, pp. 61–75, 2003, arXiv:hep-ex/0306033. doi: 10.1016/S0370-2693(03)00614-2

[23] Tevatron New Physics Higgs Working Group, CDF Collaboration, D0 Collaboration, *Updated Combination of CDF and D0 Searches for Standard Model Higgs Boson Production with up to 10.0 fb^{-1} of Data*, 2012, FERMILAB-CONF-12-318-E, CDF-NOTE-10884, D0-NOTE-6348, arXiv:1207.0449.

[24] CMS Collaboration, *Observation of the diphoton decay of the Higgs boson and measurement of its properties*, *Eur. Phys. J.*, vol. C74, no. 10, p. 3076, 2014, arXiv:1407.0558. doi: 10.1140/epjc/s10052-014-3076-z

[25] CMS Collaboration, *Measurement of the properties of a Higgs boson in the four-lepton final state*, *Phys. Rev.*, vol. D89, no. 9, p. 092007, 2014, arXiv:1312.5353. doi: 10.1103/PhysRevD.89.092007

[26] ATLAS Collaboration, *Measurement of Higgs boson production in the diphoton decay channel in pp collisions at center-of-mass energies of 7 and 8 TeV with the ATLAS detector*, *Phys. Rev.*, vol. D90, no. 11, p. 112015, 2014, arXiv:1408.7084. doi: 10.1103/PhysRevD.90.112015

[27] ATLAS Collaboration, *Measurements of Higgs boson production and couplings in the four-lepton channel in pp collisions at center-of-mass energies of 7 and 8 TeV with the ATLAS detector*, *Phys. Rev.*, vol. D91, no. 1, p. 012006, 2015, arXiv:1408.5191. doi: 10.1103/PhysRevD.91.012006

[28] LHC Higgs Cross Section Working Group, *Handbook of LHC Higgs Cross Sections: 4. Deciphering the Nature of the Higgs Sector*, 2016, arXiv:1610.07922. doi: 10.23731/CYRM-2017-002

[29] ATLAS Collaboration, CMS Collaboration, *Measurements of the Higgs boson production and decay rates and constraints on its couplings from a combined ATLAS and CMS analysis of the LHC pp collision data at $\sqrt{s} = 7$ and 8 TeV*, *JHEP*, vol. 08, p. 045, 2016, arXiv:1606.02266. doi: 10.1007/JHEP08(2016)045

[30] CMS Collaboration, Observation of the SM scalar boson decaying to a pair of τ leptons with the CMS experiment at the LHC, 2017, CMS-PAS-HIG-16-043, arXiv:1708.00373, Accepted by Phys. Lett. B.

[31] ATLAS Collaboration, Observation and measurement of Higgs boson decays to WW* with the ATLAS detector, *Phys. Rev.*, vol. D92, no. 1, p. 012006, 2015, arXiv:1412.2641. doi: 10.1103/PhysRevD.92.012006

[32] ATLAS Collaboration, Study of the spin and parity of the Higgs boson in diboson decays with the ATLAS detector, *Eur. Phys. J.*, vol. C75, no. 10, p. 476, 2015, arXiv:1506.05669.

[33] CMS Collaboration, Constraints on the spin-parity and anomalous HVV couplings of the Higgs boson in proton collisions at 7 and 8 TeV, *Phys. Rev.*, vol. D92, no. 1, p. 012004, 2015, arXiv:1411.3441. doi: 10.1103/PhysRevD.92.012004

[34] S. D. Drell and T.-M. Yan, Massive Lepton Pair Production in Hadron-Hadron Collisions at High-Energies, *Phys. Rev. Lett.*, vol. 25, pp. 316–320, 1970, [Erratum: Phys. Rev. Lett.25,902(1970)]. doi: 10.1103/PhysRevLett.25.316

[35] M. L. Perl *et al.*, Evidence for Anomalous Lepton Production in e+ - e- Annihilation, *Phys. Rev. Lett.*, vol. 35, pp. 1489–1492, 1975. doi: 10.1103/PhysRevLett.35.1489

[36] D. Clowe, M. Bradac, A. H. Gonzalez, M. Markevitch, S. W. Randall, C. Jones, and D. Zaritsky, A direct empirical proof of the existence of dark matter, *Astrophys. J.*, vol. 648, pp. L109–L113, 2006, arXiv:astro-ph/0608407. doi: 10.1086/508162

[37] Y. Fukuda *et al.*, Evidence for oscillation of atmospheric neutrinos, *Phys. Rev. Lett.*, vol. 81, pp. 1562–1567, 1998, arXiv:hep-ex/9807003. doi: 10.1103/PhysRevLett.81.1562

[38] Q. R. Ahmad *et al.*, Measurement of the rate of $\nu_e + d \rightarrow p + p + e^-$ interactions produced by ^8B solar neutrinos at the Sudbury Neutrino Observatory, *Phys. Rev. Lett.*, vol. 87, p. 071301, 2001, arXiv:nucl-ex/0106015. doi: 10.1103/PhysRevLett.87.071301

[39] J. Wess and B. Zumino, Supergauge Transformations in Four-Dimensions, *Nucl. Phys.*, vol. B70, pp. 39–50, 1974. doi: 10.1016/0550-3213(74)90355-1

[40] R. Haag, J. T. Lopuszanski, and M. Sohnius, *All Possible Generators of Supersymmetries of the s Matrix*, *Nucl. Phys.*, vol. B88, p. 257, 1975. doi: 10.1016/0550-3213(75)90279-5

[41] P. Fayet, *Supergauge Invariant Extension of the Higgs Mechanism and a Model for the electron and Its Neutrino*, *Nucl. Phys.*, vol. B90, pp. 104–124, 1975. doi: 10.1016/0550-3213(75)90636-7

[42] P. Fayet, *Spontaneously Broken Supersymmetric Theories of Weak, Electromagnetic and Strong Interactions*, *Phys. Lett.*, vol. 69B, p. 489, 1977. doi: 10.1016/0370-2693(77)90852-8

[43] M. Carena and H. E. Haber, *Higgs boson theory and phenomenology*, *Prog. Part. Nucl. Phys.*, vol. 50, pp. 63–152, 2003, arXiv:hep-ph/0208209. doi: 10.1016/S0146-6410(02)00177-1

[44] M. Carena, S. Heinemeyer, O. Stål, C. E. M. Wagner, and G. Weiglein, *MSSM Higgs Boson Searches at the LHC: Benchmark Scenarios after the Discovery of a Higgs-like Particle*, *Eur. Phys. J.*, vol. C73, no. 9, p. 2552, 2013, arXiv:1302.7033. doi: 10.1140/epjc/s10052-013-2552-1

[45] A. Djouadi, L. Maiani, G. Moreau, A. Polosa, J. Quevillon, and V. Riquer, *The post-Higgs MSSM scenario: Habemus MSSM?*, *Eur. Phys. J.*, vol. C73, p. 2650, 2013, arXiv:1307.5205. doi: 10.1140/epjc/s10052-013-2650-0

[46] E. Bagnaschi, F. Frensch, S. Heinemeyer, G. Lee, S. R. Liebler, M. Muhlleitner, A. R. Mc Carn, J. Quevillon, N. Rompotis, P. Slavich, M. Spira, C. Wagner, and R. Wolf, *Benchmark scenarios for low tan β in the MSSM*, CERN, Geneva, Tech. Rep., Aug 2015, LHCHXSWG-2015-002, https://cds.cern.ch/record/2039911.

[47] O. S. Brüning, P. Collier, P. Lebrun, S. Myers, R. Ostojic, J. Poole, and P. Proudlock, *LHC Design Report*, ser. CERN Yellow Reports: Monographs. Geneva: CERN, 2004, https://cds.cern.ch/record/782076.

[48] CMS Collaboration, *The CMS Experiment at the CERN LHC*, *JINST*, vol. 3, p. S08004, 2008. doi: 10.1088/1748-0221/3/08/S08004

[49] ATLAS Collaboration, *The ATLAS Experiment at the CERN Large Hadron Collider*, *JINST*, vol. 3, p. S08003, 2008. doi: 10.1088/1748-0221/3/08/S08003

[50] ALICE Collaboration, The ALICE experiment at the CERN LHC, *JINST*, vol. 3, p. S08002, 2008. doi: 10.1088/1748-0221/3/08/S08002

[51] LHCb Collaboration, The LHCb Detector at the LHC, *JINST*, vol. 3, p. S08005, 2008. doi: 10.1088/1748-0221/3/08/S08005

[52] CMS Collaboration, Public CMS Luminosity Information, *Public CMS Wiki*, 2016, https://twiki.cern.ch/twiki/bin/view/CMSPublic/LumiPublicResults.

[53] CMS Collaboration, CMS physics: Technical design report, *CERN-LHCC-2006-001*, 2006, https://cds.cern.ch/record/922757.

[54] CMS Collaboration, Description and performance of track and primary-vertex reconstruction with the CMS tracker, *JINST*, vol. 9, no. 10, p. P10009, 2014, arXiv:1405.6569. doi: 10.1088/1748-0221/9/10/P10009

[55] CMS Collaboration, Performance of Photon Reconstruction and Identification with the CMS Detector in Proton-Proton Collisions at $\sqrt{s} = 8$ TeV, *JINST*, vol. 10, no. 08, p. P08010, 2015, arXiv:1502.02702. doi: 10.1088/1748-0221/10/08/P08010

[56] CMS Collaboration, Performance of Electron Reconstruction and Selection with the CMS Detector in Proton-Proton Collisions at $\sqrt{s} = 8$ TeV, *JINST*, vol. 10, no. 06, p. P06005, 2015, arXiv:1502.02701. doi: 10.1088/1748-0221/10/06/P06005

[57] CMS Collaboration, Particle-flow reconstruction and global event description with the CMS detector, *JINST*, vol. 12, no. 10, p. P10003, 2017, arXiv:1706.04965. doi: 10.1088/1748-0221/12/10/P10003

[58] CMS Collaboration, The CMS barrel calorimeter response to particle beams from 2-GeV/c to 350-GeV/c, *Eur. Phys. J.*, vol. C60, pp. 359–373, 2009, [Erratum: Eur. Phys. J.C61,353(2009)]. doi: 10.1140/epjc/s10052-009-0959-5

[59] CMS Collaboration, Performance of CMS muon reconstruction in *pp* collision events at $\sqrt{s} = 7$ TeV, *JINST*, vol. 7, p. P10002, 2012, arXiv:1206.4071. doi: 10.1088/1748-0221/7/10/P10002

[60] CMS Collaboration, The CMS trigger system, *JINST*, vol. 12, no. 01, p. P01020, 2017, arXiv:1609.02366. doi: 10.1088/1748-0221/12/01/P01020

[61] Worldwide LHC Computing Grid, https://wlcg-public.web.cern.ch/.

[62] Weinzierl, Stefan, Introduction to Monte Carlo methods, 2000, arXiv:hep-ph/0006269. arXiv: hep-ph/0006269

[63] Collins, John C. and Soper, Davison E., The Theorems of Perturbative QCD, *Ann. Rev. Nucl. Part. Sci.*, vol. 37, pp. 383–409, 1987. doi: 10.1146/annurev.ns.37.120187.002123

[64] T. Gleisberg, S. Hoeche, F. Krauss, M. Schonherr, S. Schumann, F. Siegert, and J. Winter, Event generation with SHERPA 1.1, *JHEP*, vol. 02, p. 007, 2009, arXiv:0811.4622. doi: 10.1088/1126-6708/2009/02/007

[65] C. T. Sachrajda, APPLICATIONS OF PERTURBATIVE QCD TO HARD SCATTERING PROCESSES, in *10th International GIFT Seminar on Theoretical Physics: Quantum Chromodynamics Jaca, Spain, June 4-9, 1979*, 1979, pp. 137–230.

[66] T. Sjöstrand, S. Ask, J. R. Christiansen, R. Corke, N. Desai, P. Ilten, S. Mrenna, S. Prestel, C. O. Rasmussen, and P. Z. Skands, An Introduction to PYTHIA 8.2, *Comput. Phys. Commun.*, vol. 191, pp. 159–177, 2015, arXiv:1410.3012. doi: 10.1016/j.cpc.2015.01.024

[67] M. Bahr *et al.*, Herwig++ Physics and Manual, *Eur. Phys. J.*, vol. C58, pp. 639–707, 2008, arXiv:0803.0883. doi: 10.1140/epjc/s10052-008-0798-9

[68] J. Alwall, M. Herquet, F. Maltoni, O. Mattelaer, and T. Stelzer, MadGraph 5 : Going Beyond, *JHEP*, vol. 06, p. 128, 2011, arXiv:1106.0522. doi: 10.1007/JHEP06(2011)128

[69] P. Nason, A New method for combining NLO QCD with shower Monte Carlo algorithms, *JHEP*, vol. 11, p. 040, 2004, arXiv:hep-ph/0409146. doi: 10.1088/1126-6708/2004/11/040

[70] S. Frixione, P. Nason, and C. Oleari, Matching NLO QCD computations with Parton Shower simulations: the POWHEG method, *JHEP*, vol. 11, p. 070, 2007, arXiv:0709.2092. doi: 10.1088/1126-6708/2007/11/070

[71] S. Alioli, P. Nason, C. Oleari, and E. Re, A general framework for implementing NLO calculations in shower Monte Carlo programs: the POWHEG BOX, *JHEP*, vol. 06, p. 043, 2010, arXiv:1002.2581. doi: 10.1007/JHEP06(2010)043

[72] S. Frixione, P. Nason, and G. Ridolfi, A Positive-weight next-to-leading-order Monte Carlo for heavy flavour hadroproduction, *JHEP*, vol. 09, p. 126, 2007, arXiv:0707.3088. doi: 10.1088/1126-6708/2007/09/126

[73] S. Alioli, P. Nason, C. Oleari, and E. Re, NLO single-top production matched with shower in POWHEG: s- and t-channel contributions, *JHEP*, vol. 09, p. 111, 2009, [Erratum: JHEP02,011(2010)]. doi: 10.1007/JHEP02(2010)011

[74] S. Frixione, F. Stoeckli, P. Torrielli, B. R. Webber, and C. D. White, The MCaNLO 4.0 Event Generator, 2010, arXiv:1010.0819.

[75] J. Alwall, R. Frederix, S. Frixione, V. Hirschi, F. Maltoni, O. Mattelaer, H. S. Shao, T. Stelzer, P. Torrielli, and M. Zaro, The automated computation of tree-level and next-to-leading order differential cross sections, and their matching to parton shower simulations, *JHEP*, vol. 07, p. 079, 2014, arXiv:1405.0301. doi: 10.1007/JHEP07(2014)079

[76] A. Buckley *et al.*, General-purpose event generators for LHC physics, *Phys. Rept.*, vol. 504, pp. 145–233, 2011, arXiv:1101.2599. doi: 10.1016/j.physrep.2011.03.005

[77] J. Winter, S. Hoeche, H. Hoeth, F. Krauss, M. Schonherr, K. Zapp, S. Schumann, and F. Siegert, Systematic improvement of QCD parton showers, *Frascati Phys. Ser.*, vol. 54, pp. 336–355, 2012, arXiv:1204.5668.

[78] D. J. Lange, The EvtGen particle decay simulation package, *Nucl. Instrum. Meth.*, vol. A462, pp. 152–155, 2001. doi: 10.1016/S0168-9002(01)00089-4

[79] S. Jadach, Z. Was, R. Decker, and J. H. Kuhn, The tau decay library TAUOLA: Version 2.4, *Comput. Phys. Commun.*, vol. 76, pp. 361–380, 1993. doi: 10.1016/0010-4655(93)90061-G

[80] S. Agostinelli *et al.*, GEANT4: A Simulation toolkit, *Nucl. Instrum. Meth.*, vol. A506, pp. 250–303, 2003. doi: 10.1016/S0168-9002(03)01368-8

[81] W.Adam,B. Mangano,T. Speer,T.Todorov, Track reconstruction in the CMS tracker, 2006, CMS-NOTE-2006-041, https://cds.cern.ch/record/934067.

[82] R. Fruhwirth, Application of Kalman filtering to track and vertex fitting, *Nucl. Instrum. Meth.*, vol. A262, pp. 444–450, 1987. doi: 10.1016/0168-9002(87)90887-4

[83] K. Rose, Deterministic Annealing for Clustering, Compression, Classification, Regression, and Related Optimization Problems, in *Proceedings of the IEEE*, 1998. doi: 10.1109/5.726788 pp. 2210–2239.

[84] R. Fruhwirth, W. Waltenberger, and P. Vanlaer, Adaptive vertex fitting, *J. Phys.*, vol. G34, p. N343, 2007. doi: 10.1088/0954-3899/34/12/N01

[85] D. Buskulic *et al.*, Performance of the ALEPH detector at LEP, *Nucl. Instrum. Meth.*, vol. A360, pp. 481–506, 1995. doi: 10.1016/0168-9002(95)00138-7

[86] CMS Collaboration, Reconstruction and identification of τ lepton decays to hadrons and ν_τ at CMS, *JINST*, vol. 11, no. 01, p. P01019, 2016, arXiv:1510.07488. doi: 10.1088/1748-0221/11/01/P01019

[87] CMS Collaboration, Performance of tau-lepton reconstruction and identification in CMS, *JINST*, vol. 7, p. P01001, 2012, arXiv:1109.6034. doi: 10.1088/1748-0221/7/01/P01001

[88] CMS Collaboration, Performance of reconstruction and identification of tau leptons in their decays to hadrons and tau neutrino in LHC Run-2, 2016, CMS-PAS-TAU-16-002, https://cds.cern.ch/record/2196972.

[89] M. Cacciari, G. P. Salam, and G. Soyez, The Anti-k(t) jet clustering algorithm, *JHEP*, vol. 04, p. 063, 2008, arXiv:0802.1189. doi: 10.1088/1126-6708/2008/04/063

[90] CMS Collaboration, Jet algorithms performance in 13 TeV data, 2017, CMS-PAS-JME-16-003, https://cds.cern.ch/record/2256875.

[91] CMS Collaboration, Jet energy scale and resolution in the CMS experiment in pp collisions at 8 TeV, *JINST*, vol. 12, no. 02, p. P02014, 2017, arXiv:1607.03663. doi: 10.1088/1748-0221/12/02/P02014

[92] CMS Collaboration, Identification of b-quark jets with the CMS experiment, *JINST*, vol. 8, p. P04013, 2013, arXiv:1211.4462. doi: 10.1088/1748-0221/8/04/P04013

[93] CMS Collaboration, Identification of heavy-flavour jets with the CMS detector in pp collisions at 13 TeV, 2017, arXiv:1712.07158, Submitted to JINST.

[94] CMS Collaboration, Performance of the CMS missing transverse momentum reconstruction in pp data at $\sqrt{s}$ = 8 TeV, *JINST*, vol. 10, no. 02, p. P02006, 2015, arXiv:1411.0511. doi: 10.1088/1748-0221/10/02/P02006

[95] CMS Collaboration, Technical Proposal for the Phase-II Upgrade of the CMS Detector, Jun 2015, CERN-LHCC-2015-010, LHCC-P-008, CMS-TDR-15-02, https://cds.cern.ch/record/2020886.

[96] J. Butler, D. Contardo, M. Klute, J. Mans, L. Silvestris, and C. on behalf of the CMS, CMS Phase II Upgrade Scope Document, Sep 2015, CERN-LHCC-2015-019, https://cds.cern.ch/record/2055167.

[97] CMS Collaboration, Technical proposal for the upgrade of the CMS detector through 2020, Jun 2011, CERN-LHCC-2011-006, https://cds.cern.ch/record/1355706.

[98] A. Martelli, The CMS HGCAL detector for HL-LHC upgrade, in *5th Large Hadron Collider Physics Conference (LHCP 2017) Shanghai, China, May 15-20, 2017*, 2017, http://inspirehep.net/record/1620207/files/arXiv:1708.08234.pdf.

[99] D0 Collaboration, First measurement of σ ($p\bar{p} \rightarrow Z$) . Br ($Z \rightarrow \tau\tau$) at $\sqrt{s}$ = 1.96- TeV, *Phys. Rev.*, vol. D71, p. 072004, 2005, [Erratum: Phys. Rev.D77,039901(2008)]. doi: 10.1103/PhysRevD.77.039901

[100] D0 Collaboration, Measurement of $\sigma(p\bar{p} \rightarrow Z + X)$ Br($Z \rightarrow \tau^+\tau^-$) at $\sqrt{s}$ = 1.96-TeV, *Phys. Lett.*, vol. B670, pp. 292–299, 2009, arXiv:0808.1306. doi: 10.1016/j.physletb.2008.11.010

[101] CDF Collaboration, Measurement of $\sigma(p\bar{p} \rightarrow Z)$.Br($Z \rightarrow 2\tau$) in $p\bar{p}$ collisions at $\sqrt{s}$ = 1.96 TeV, *Phys. Rev.*, vol. D75, p. 092004, 2007. doi: 10.1103/PhysRevD.75.092004

[102] CMS Collaboration, Measurement of the Inclusive Z Cross Section via Decays to Tau Pairs in pp Collisions at $\sqrt{s}$ = 7 TeV, *JHEP*, vol. 08, p. 117, 2011, arXiv:1104.1617. doi: 10.1007/JHEP08(2011)117

[103] ATLAS Collaboration, Measurement of the Z to tau tau Cross Section with the ATLAS Detector, *Phys. Rev.*, vol. D84, p. 112006, 2011, arXiv:1108.2016. doi: 10.1103/PhysRevD.84.112006

[104] CMS Collaboration, Measurement of inclusive W and Z boson production cross sections in pp collisions at sqrt(s)=13 TeV, 2015, CMS-PAS-SMP-15-004, https://cds.cern.ch/record/2093537.

[105] CMS Collaboration, Measurements of inclusive and differential Z boson production cross sections in pp collisions at $\sqrt{s} = 13$ TeV, 2016, CMS-PAS-SMP-15-011, https://cds.cern.ch/record/2140105.

[106] ATLAS Collaboration, Measurement of $W^{\pm}$ and Z-boson production cross sections in pp collisions at $\sqrt{s} = 13$ TeV with the ATLAS detector, *Phys. Lett.*, vol. B759, pp. 601–621, 2016, arXiv:1603.09222. doi: 10.1016/j.physletb.2016.06.023

[107] R. Gavin, Y. Li, F. Petriello, and S. Quackenbush, FEWZ 2.0: A code for hadronic Z production at next-to-next-to-leading order, *Comput. Phys. Commun.*, vol. 182, pp. 2388–2403, 2011, arXiv:1011.3540. doi: 10.1016/j.cpc.2011.06.008

[108] R. Gavin, Y. Li, F. Petriello, and S. Quackenbush, W Physics at the LHC with FEWZ 2.1, *Comput. Phys. Commun.*, vol. 184, pp. 208–214, 2013, arXiv:1201.5896. doi: 10.1016/j.cpc.2012.09.005

[109] DELPHI Collaboration, OPAL Collaboration, ALEPH Collaboration, L3 Collaboration, LEP Working Group for Higgs Boson Searches, Search for neutral MSSM Higgs bosons at LEP, *Eur. Phys. J.*, vol. C47, pp. 547–587, 2006, arXiv:hep-ex/0602042. doi: 10.1140/epjc/s2006-02569-7

[110] CDF Collaboration, Search for Higgs bosons predicted in two-Higgs-doublet models via decays to tau lepton pairs in 1.96-TeV p anti-p collisions, *Phys. Rev. Lett.*, vol. 103, p. 201801, 2009, arXiv:0906.1014. doi: 10.1103/PhysRevLett.103.201801

[111] CDF Collaboration, Search for Higgs Bosons Produced in Association with b-quarks, *Phys. Rev.*, vol. D85, p. 032005, 2012, arXiv:1106.4782. doi: 10.1103/PhysRevD.85.032005

[112] D0 Collaboration, Search for neutral Higgs bosons in the multi-b-jet topology in 5.2fb^{-1} of $p\bar{p}$ collisions at $\sqrt{s} = 1.96$ TeV, *Phys. Lett.*, vol. B698, pp. 97–104, 2011, arXiv:1011.1931. doi: 10.1016/j.physletb.2011.02.062

[113] D0 Collaboration, Search for Higgs bosons decaying to $\tau\tau$ pairs in $p\bar{p}$ collisions at $\sqrt{s} = 1.96$ TeV, *Phys. Lett.*, vol. B707, pp. 323–329, 2012, arXiv:1106.4555. doi: 10.1016/j.physletb.2011.12.050

[114] CMS Collaboration, Search for a Higgs boson decaying into a b-quark pair and produced in association with b quarks in proton–proton collisions at 7 TeV, *Phys. Lett.*, vol. B722, pp. 207–232, 2013, arXiv:1302.2892. doi: 10.1016/j.physletb.2013.04.017

[115] CMS Collaboration, Search for neutral MSSM Higgs bosons decaying into a pair of bottom quarks, *JHEP*, vol. 11, p. 071, 2015, arXiv:1506.08329. doi: 10.1007/JHEP11(2015)071

[116] ATLAS Collaboration, Search for the neutral Higgs bosons of the Minimal Supersymmetric Standard Model in pp collisions at $\sqrt{s} = 7$ TeV with the ATLAS detector, *JHEP*, vol. 02, p. 095, 2013, arXiv:1211.6956. doi: 10.1007/JHEP02(2013)095

[117] CMS Collaboration, Search for neutral MSSM Higgs bosons decaying to $\mu^+\mu^-$ in pp collisions at $\sqrt{s} = 7$ and 8 TeV, *Phys. Lett.*, vol. B752, pp. 221–246, 2016, arXiv:1508.01437. doi: 10.1016/j.physletb.2015.11.042

[118] ATLAS Collaboration, Search for neutral Higgs bosons of the minimal supersymmetric standard model in pp collisions at $\sqrt{s} = 8$ TeV with the ATLAS detector, *JHEP*, vol. 11, p. 056, 2014, arXiv:1409.6064. doi: 10.1007/JHEP11(2014)056

[119] CMS Collaboration, Search for Neutral MSSM Higgs Bosons Decaying to Tau Pairs in pp Collisions at $\sqrt{s} = 7$ TeV, *Phys. Rev. Lett.*, vol. 106, p. 231801, 2011, arXiv:1104.1619. doi: 10.1103/PhysRevLett.106.231801

[120] CMS Collaboration, Search for neutral Higgs bosons decaying to tau pairs in pp collisions at $\sqrt{s} = 7$ TeV, *Phys. Lett.*, vol. B713, pp. 68–90, 2012, arXiv:1202.4083. doi: 10.1016/j.physletb.2012.05.028

[121] CMS Collaboration, Search for neutral MSSM Higgs bosons decaying to a pair of tau leptons in pp collisions, *JHEP*, vol. 10, p. 160, 2014, arXiv:1408.3316. doi: 10.1007/JHEP10(2014)160

[122] CMS Collaboration, Search for additional neutral Higgs bosons decaying to a pair of tau leptons in pp collisions at $\sqrt{s} = 7$ and 8 TeV, CERN, Geneva, Tech. Rep., 2015, CMS-PAS-HIG-14-029, https://cds.cern.ch/record/2041463.

[123] CMS Collaboration, Summary results of high mass BSM Higgs searches using CMS run-I data, 2016, CMS-PAS-HIG-16-007, https://cds.cern.ch/record/2142432.

[124] ATLAS Collaboration, Search for Minimal Supersymmetric Standard Model Higgs bosons H/A and for a Z' boson in the $\tau\tau$ final state produced in pp collisions at $\sqrt{s} = 13$ TeV with the ATLAS Detector, *Eur. Phys. J.*, vol. C76, no. 11, p. 585, 2016, arXiv:1608.00890. doi: 10.1140/epjc/s10052-016-4400-6

[125] CMS Collaboration, Search for a neutral MSSM Higgs boson decaying into tautau at 13 TeV, CERN, Geneva, Tech. Rep., 2016, CMS-PAS-HIG-16-006, https://cds.cern.ch/record/2160252.

[126] CMS Collaboration, Search for a neutral MSSM Higgs boson decaying into $\tau\tau$ with 12.9 fb^{-1} of data at $\sqrt{s} = 13$ TeV, CERN, Geneva, Tech. Rep. CMS-PAS-HIG-16-037, 2016, https://cds.cern.ch/record/2231507.

[127] ATLAS Collaboration, Search for additional heavy neutral Higgs and gauge bosons in the ditau final state produced in 36 fb^{-1} of pp collisions at $\sqrt{s} = 13$ TeV with the ATLAS detector, 2017, CERN-EP-2017-199, arXiv:1709.07242.

[128] CMS Collaboration, Measurement of the $Z\gamma^* \to \tau\tau$ cross section in pp collisions at $\sqrt{s} = 13$ TeV and validation of τ lepton analysis techniques, 2018, CMS-HIG-15-007, CERN-EP-2017-307, arXiv:1801.03535, Submitted to EPJC.

[129] CMS Collaboration, Evidence for the 125 GeV Higgs boson decaying to a pair of τ leptons, *JHEP*, vol. 05, p. 104, 2014, arXiv:1401.5041. doi: 10.1007/JHEP05(2014)104

[130] L. Bianchini, J. Conway, E. K. Friis, and C. Veelken, Reconstruction of the Higgs mass in $H \to \tau\tau$ Events by Dynamical Likelihood techniques, *J. Phys. Conf. Ser.*, vol. 513, p. 022035, 2014. doi: 10.1088/1742-6596/513/2/022035

[131] R. D. Ball, V. Bertone, S. Carrazza, L. Del Debbio, S. Forte, A. Guffanti, N. P. Hartland, and J. Rojo, Parton distributions with QED corrections, *Nucl. Phys.*, vol. B877, pp. 290–320, 2013, arXiv:1308.0598. doi: 10.1016/j.nuclphysb.2013.10.010

[132] R. D. Ball, V. Bertone, F. Cerutti, L. Del Debbio, S. Forte, A. Guffanti, J. I. Latorre, J. Rojo, and M. Ubiali, Unbiased global determination of parton distributions and their uncertainties at NNLO and at LO, *Nucl. Phys.*, vol. B855, pp. 153–221, 2012, arXiv:1107.2652. doi: 10.1016/j.nuclphysb.2011.09.024

[133] R. D. Ball *et al.*, Parton distributions for the LHC Run II, *JHEP*, vol. 04, p. 040, 2015, arXiv:1410.8849. doi: 10.1007/JHEP04(2015)040

[134] CMS Collaboration, Event generator tunes obtained from underlying event and multiparton scattering measurements, *Eur. Phys. J.*, vol. C76, no. 3, p. 155, 2016, arXiv:1512.00815. doi: 10.1140/epjc/s10052-016-3988-x

[135] CMS Collaboration, Measurements of Inclusive W and Z Cross Sections in pp Collisions at $\sqrt{s} = 7$ TeV, *JHEP*, vol. 01, p. 080, 2011, arXiv:1012.2466. doi: 10.1007/JHEP01(2011)080

[136] CMS Collaboration, Measurement of differential top-quark pair production cross sections in pp colisions at $\sqrt{s} = 7$ TeV, *Eur. Phys. J.*, vol. C73, no. 3, p. 2339, 2013, arXiv:1211.2220. doi: 10.1140/epjc/s10052-013-2339-4

[137] CMS Collaboration, Measurement of the differential cross section for top quark pair production in pp collisions at $\sqrt{s} = 8$ TeV, *Eur. Phys. J.*, vol. C75, no. 11, p. 542, 2015, arXiv:1505.04480. doi: 10.1140/epjc/s10052-015-3709-x

[138] ATLAS Collaboration, CMS Collaboration, CMS luminosity measurement for the 2015 data-taking period, CERN, Geneva, Tech. Rep., 2015, CMS-PAS-LUM-15-001, http://cds.cern.ch/record/2138682.

[139] CMS Collaboration, Procedure for the LHC Higgs boson search combination in Summer 2011, CERN, Geneva, Tech. Rep., 2015, CMS-NOTE-2011-005, ATL-PHYS-PUB-2011-11, https://cds.cern.ch/record/1379837.

[140] CMS Collaboration, Combined results of searches for the standard model Higgs boson in pp collisions at $\sqrt{s} = 7$ TeV, *Phys. Lett.*, vol. B710, pp. 26–48, 2012, arXiv:1202.1488. doi: 10.1016/j.physletb.2012.02.064

[141] J. S. Conway, Incorporating Nuisance Parameters in Likelihoods for Multisource Spectra, in *Proceedings, PHYSTAT 2011 Workshop on Statistical Issues Related to Discovery Claims in Search Experiments and Unfolding, CERN,Geneva, Switzerland 17-20 January 2011*, 2011. doi: 10.5170/CERN-2011-006.115 pp. 115–120, arXiv:1103.0354.

[142] Y. Li and F. Petriello, Combining QCD and electroweak corrections to dilepton production in FEWZ, *Phys. Rev.*, vol. D86, p. 094034, 2012, arXiv:11208.5967. doi: 10.1103/PhysRevD.86.094034

[143] CMS Collaboration, Search for additional neutral MSSM Higgs bosons in the $\tau\tau$ final state in proton-proton collisions at $\sqrt{s} = 13$ TeV, 2018, CMS-HIG-17-020, arXiv:1803.06553, Submitted to JHEP.

[144] E. Bagnaschi, R. V. Harlander, H. Mantler, A. Vicini, and M. Wiesemann, Resummation ambiguities in the Higgs transverse-momentum spectrum in the Standard Model and beyond, *JHEP*, vol. 01, p. 090, 2016, arXiv:1510.08850. doi: 10.1007/JHEP01(2016)090

[145] E. Bagnaschi and A. Vicini, The Higgs transverse momentum distribution in gluon fusion as a multiscale problem, *JHEP*, vol. 01, p. 056, 2016, arXiv:1505.00735. doi: 10.1007/JHEP01(2016)056

[146] R. V. Harlander, H. Mantler, and M. Wiesemann, Transverse momentum resummation for Higgs production via gluon fusion in the MSSM, *JHEP*, vol. 11, p. 116, 2014, arXiv:1409.0531. doi: 10.1007/JHEP11(2014)116

[147] ATLAS Collaboration, Modelling $Z \to \tau\tau$ processes in ATLAS with τ-embedded $Z \to \mu\mu$ data, *JINST*, vol. 10, no. 09, p. P09018, 2015, arXiv:1506.05623. doi: 10.1088/1748-0221/10/09/P09018, 10.1088/1748-0221/2015/9/P09018

[148] CMS Collaboration, CMS Luminosity Measurements for the 2016 Data Taking Period, 2017, CMS-PAS-LUM-17-001, https://cds.cern.ch/record/2257069.

[149] A. D. Martin, W. J. Stirling, R. S. Thorne, and G. Watt, Parton distributions for the LHC, *Eur. Phys. J.*, vol. C63, pp. 189–285, 2009, arXiv:0901.0002. doi: 10.1140/epjc/s10052-009-1072-5

[150] A. D. Martin, W. J. Stirling, R. S. Thorne, and G. Watt, Uncertainties on alpha(S) in global PDF analyses and implications for predicted hadronic cross sections, *Eur. Phys. J.*, vol. C64, pp. 653–680, 2009, arXiv:0905.3531. doi: 10.1140/epjc/s10052-009-1164-2

[151] T. Junk, Confidence level computation for combining searches with small statistics, *Nucl. Instrum. Meth.*, vol. A434, pp. 435–443, 1999, arXiv:hep-ex/9902006. doi: 10.1016/S0168-9002(99)00498-2

[152] A. L. Read, Presentation of search results: The CL(s) technique, *J. Phys.*, vol. G28, pp. 2693–2704, 2002, [,11(2002)]. doi: 10.1088/0954-3899/28/10/313

Johannes **Brandstetter**

PHYSICIST · DATA ANALYST

DoB: September 25, 1989
Bubing 113, 4782 St.Florian, AUSTRIA

(+) 43-6767314617 | j.brandstetter89@gmail.com

Education

Doctoral program in Technical Sciences Technical Physics　　　　*Jan. 2015 - PRESENT*

- TU Wien (Dr.tech./Ph.D.)
- Doctoral Thesis '*Neutral Higgs Boson and Z Boson Decays Into Pairs of Tau Leptons with the CMS Detector*', supervisor: Jochen Schieck

Master Program Technical Physics　　　　*Oct. 2012 - Nov. 2014*

- TU Wien (Dipl.-Ing./MSc., with distinction)
- Master Thesis '*Understanding Muon Detection Efficiencies for Quarkonium Polarization Measurements at the Compact Muon Solenoid*', supervisor: Claudia Wulz

Bachelor Program Technical Physics　　　　*Oct. 2009 - Jul. 2012*

- TU Wien (BSc., with distinction)
- Bachelor Thesis at Stefan-Meyer Institute Vienna (Mar. - Jul. 2012): '*Design of a Polarized Hydrogen Beam*', supervisor: Eberhard Widmann

Bundesgymnasium Schärding　　　　*2000 - 2008*

- Matura, with distinction

Community Service　　　　*Aug. 2008 - Apr. 2009*

- Austrian Civil Service at *Rotes Kreuz* Schärding

Research Experience

Junior Researcher at Institute of High Energy Physics, Vienna　　　　*Nov. 2013 - PRESENT*

- Member of the CMS experiment, CERN
- Research for Doctoral and Master Thesis
- Development and application of physics analysis and complex statistical methods
- Collaboration with internationally highly recognized universities
- Several short- and mid-range stays at CERN
- Co-supervision of bachelor and master students
- Presentation of results in several international seminars and meetings

Research project at CERN　　　　*Jul. 2013 - Aug.2013*

- '*Improvement of the Communication Interface of High-Level-Trigger and Level-1 Trigger*'
- Development of common web interface

Research project at Institute of Applied Physics Vienna　　　　*Sep. 2013 - Nov.2013*

- '*Electronic Structure of Diamonds with Nitrogen Impurities*'
- Simulation of diamond lattices, statistical analysis

Skills

Programming	C++, Python, C, Fortran
Operation Systems	Mac OS, Linux, Windows
Tools	Git, ROOT, LaTeX, Matlab, SVN
Language Skills	*German* (Mother tongue), *English* (Excellent level), *French* (Basic level)

Further Training

CERN School of Computing 2017 *Aug. 2017 - Sep. 2017*
- Universidad Politécnica de Madrid

MLHEP Summer School on Machine Learning in High Energy Physics *Aug. 2015*
- St. Petersburg Academic University

ATHENS Program - Information Extraction Techniques and the Semantic Web *Mar. 2014*
- Télécom ParisTech

Tutor at the Institute of Solid State Physics, TU Wien *Oct. 2012 - Jun. 2013*
- Supervising laboratory exercises

Seminar Subatomic Physics *Feb. 2012*
- University of Jyväskylä

Internships

EVGroup, St.Florian/Inn *Jul. 2012 - Sep. 2012*
- Simulating and analyzing heat dependencies in wafer bonding processes

Frauscher Sensortechnik, St.Marienkirchen/Schärding *Jul. 2011 - Aug. 2011*
- Analyzing applications of inductive railway sensor technology processes

Fill Metallbau, Hohenzell/Ried *August. 2010 - Sep. 2010*
- Various metalworking tasks

Tennis Instructor *2005 - 2012*
- Responsibility for small groups of children of various age groups

Contributions to Publications and Conferences

Scientific Publications

- CMS Collaboration, ´*Search for singly produced third-generation leptoquarks decaying to a tau lepton and a b quark in proton-proton collisions at $\sqrt{s} = 13$ TeV*', CMS-PAS-EXO-17-029
- CMS Collaboration, ´*Search for additional neutral Higgs bosons in the tau tau final state in proton-proton collision at $\sqrt{s} = 13$ TeV*', CMS-PAS-HIG-17-020, https://cds.cern.ch/record/2296333 ,
- CMS Collaboration, ´*Measurement of the $Z\gamma^* \to \tau\tau$ cross section in pp collisions at $\sqrt{s} = 13$ TeV and validation of τ lepton analysis techniques*', arXiv:1801.03535, Submitted to Eur. Phys. J. C.
- CMS Collaboration, ´*Observation of the Higgs boson decay to a pair of tau leptons*', arXiv:1708.00373, Accepted by Phys. Lett. B.
- CMS Collaboration, ´*Technical proposal for the Phase-II Upgrade of the Compact Muon Solenoid*', CMS-TDR-15-002, CERN-LHCC-2015-010, https://cds.cern.ch/record/2020886
- CMS Collaboration, ´*CMS Phase II Upgrade Scope Document*', CERN-LHCC-2015-019, https://cds.cern.ch/record/2055167
- CMS Collaboration, ´*Jet algorithms performance in 13 TeV data*', CMS-PAS-JME-16-003, http://cds.cern.ch/record/2256875
- CMS Collaboration, ´*J/psi and psi(2S) prompt double-differential cross sections in pp collisions at 7 TeV*', CMS-PAS-BPH-14-001, https://cds.cern.ch/record/1744914
- Johannes Brandstetter, ´*Higgs boson results on couplings to fermions, CP parameters and perspectives for HL-LHC (ATLAS AND CMS)*', Talk presented at the International Workshop on Future Linear Colliders (LCWS2017), Strasbourg, France, 23-27 October 2017. C17-10-23.2, arXiv:1801.07926
- Johannes Brandstetter, ´*Higgs properties*', PoS(FPCP2016)025
- Johannes Brandstetter, ´*Higgs boson properties and tests of the Standard Model at CMS*', Nuclear and Particle Physics Proceedings, Volumes 270-272, January-March 2016, p.222-226, https://doi.org/10.1016/j.nuclphysbps.2016.02.044

Contributions to Conferences

- ´*Searches for additional Higgs bosons at CMS with Run2 data*', DIS 2018, Kobe, Japan, Apr. 2018
- ´*Higgs boson results on couplings to fermions, CP parameters and perspectives for HL-LHC (ATLAS AND CMS)*', LCWS 2017, Strasbourg, France, Oct.2017
- ´*Higgs boson and standard model physics in the tautau final state*', ALPS 2017, Obergurgl, Austria, Apr. 2017
- ´*Tau Identification Studies for High-Luminosity LHC Upgrade*', OePG 2016, Vienna, Austria, Sep. 2016
- ´*Higgs properties*', FPCP 2016, California Institute of Technology, Pasadena, USA, Jun. 2016
- ´*Results and prospects for the measurement of Higgs boson decays to pairs of tau leptons with the CMS experiment*', SPG-OePG 2015, Vienna, Austria, Sep. 2015
- ´*Higgs boson properties and tests of the Standard Model at CMS*', QCD 2015, Montpellier, France, Jun. 2015
- ´*Measurements of Quarkonia Production Cross Section at CMS*', OePG 2015, Pöllau, Austria, Sep. 2014